GMTS | GRUPO DE MAQUINAS Y MOTORES TERMICOS DE SEVILLA

Design of supercritical carbon dioxide centrifugal compressors

PhD Thesis

Seville, March 2014

PhD Candidate: Benjamín Monge Brenes

Supervisor: Tomás Sánchez Lencero

Co-supervisor: David Sánchez Martínez

This page left intentionally blank

AGRADECIMIENTOS (ACKNOWLEDGEMENTS)

Al final de mi periodo de doctorado, me enfrento probablemente a la tarea más complicada de las que he realizado durante estos 4 años: los agradecimientos. Y es que es imposible expresar en una sola página mi gratitud hacia quienes me han brindado esta oportunidad de desarrollo profesional, pero sobre todo; y es lo mejor que me llevo; personal.

En primer lugar deseo manifestar también mi agradecimiento a la Consejería de Economía, Innovación, Ciencia y Empleo de la Junta de Andalucía por haber financiado el proyecto de excelencia "Desarrollo de turbocompresores centrífugos de dióxido de carbono supercrítico para implementación en sistemas de producción de potencia limpios y con alta eficiencia" (referencia TEP09-5300) en la convocatoria 2009. Esta tesis se ha desarrollo en el seno de dicho proyecto". Y por supuesto, agradecer a la Universidad de Sevilla el haberme concedido la beca de Plan Propio que he gozado y al Grupo de Máquinas y Motores Térmicos por confiar en mí como alumno aspirante. Especial agradecimiento merecen el director de dicho grupo, el Prof. Dr. D. Tomás Sánchez Lencero y el Prof. Dr. D. David Sánchez Martínez, tutor y co-tutor respectivos de esta tesis. La guía basada en su experiencia y conocimiento ha sido la clave en muchas ocasiones para el desarrollo de esta tesis. Por supuesto no me puedo olvidar del Prof. Dr. D. Ricardo Chacartegui Ramírez, cuyo asesoramiento y ayuda han sido fundamentales en el proceso de aprendizaje de mi doctorado, además de enriquecedores en otros trabajos conjuntos.

Sin salir del terreno universitario, quiero expresar mi reconocimiento a la Cranfield University (Reino Unido) y en especial a los Prof. Pilidis y Savill, con quienes compartí un periodo breve, pero productivo y muy determinante para la elaboración de esta tesis.

No puedo terminar mis agradecimientos en la Universidad de Sevilla sin nombrar a quienes me han aguantado en el día a día durante estos años: Los compañeros, pero sobre todo, amigos de los laboratorios. En especial a José Muñoz de Escalona, gracias a cuyo trabajo el mío ha resultado más fácil y fructífero. Además de sentirme un privilegiado por formar parte de este inmenso grupo humano, considero haber hallado con ellos algo tan valioso como esta propia tesis doctoral.

Y ahora quiero mostrar mi agradecimiento a las personas que me han hecho posible encontrar esta posibilidad. Esas personas que con su apoyo, esfuerzo material e inmaterial y sobre todo su amor, le han dado y le siguen dando sentido y motivación a mi vida. Hablo por supuesto de mi familia:

De la única mujer de mi vida, Lola, con quien llevo más de 14 años de vida compartidos y aún sigue impresionándome por las muestras de amor, cariño y sobre todo comprensión hacia mí.

De mis padres, Manolo y Consuelo, y de mi hermana, Natalia, quienes me han inculcado los valores de humildad, compromiso y amor por la familia de los que espero nunca desprenderme. Gracias a que ellos me han procurado siempre lo mejor, he podido llegar hasta este punto.

Hablo también de mis fieles amigos de toda la vida, porque ellos también han aportado a mi currículum para lograr este objetivo. Especialmente mi primo político, el único, el inigualable Tirado con su primo y su hermano.

Y por último, esa otra gran parte de mi vida: Mi Banda, donde puedo desarrollar mi pasión por la música y la docencia a la vez.

A toda mi familia…

…a los que ya no están, a los que están y a los que estarán.

This page left intentionally blank

Contents

Figures

Tables

CHAPTER 1. Introductory concepts

The Thermal Power Group (GMTS, Grupo de Máquinas y Motores Térmicos) at the University of Seville focuses on looking for power cycles that, operating at a modest turbine inlet temperature (TIT) in the order of 700 ºC, exhibit as high as possible efficiency. A cycle like that would better fit concentrated solar power (CSP) applications, thus being put forth as an ideal candidate to substitute the current steam turbines running at either 380ºC peak temperature in parabolic trough facilities (Cleveland, 2004) or 540 ºC for central receiver plant such as Gemasolar® (Torresol Energy Investments, S.A., 2010). Moreover, these systems could be employed for energy recovery on waste heat streams and would also be adequate for its integration into hybrid systems as bottoming cycles for high temperature fuel cell. Because of the interest that solar power production raises in the region of Andalucía, home to the University of Seville, a detailed analysis of the main difficulties and constraints related to solar technologies nowadays is presented in first place below; issues that the alternative power cycle presented in this study should resolve on the other hand.

1.1 Scope of work

Over the last decades, several factors have caused the rise of solar technologies in the energy sector, in particular concentrated solar power (CSP). Initially, the scarcity of fossil fuels pointed out by several authors from different areas of society woke up the interest in alternative energy sources like hydro, wind and solar. Specifically, in the region of Andalusia (south of Spain), where the available direct insolation is higher than 2000 kWh/m^2·a (Junta de Andalucía, 2014), the solar source has gained especial attention both within the research community and the industry. Also global warming problems and the consciousness on sustainable sources has favoured the deployment of solar technologies. Conventional technologies based on coal or gas generate greenhouse gas emissions between 150 and 1100 g CO_2 per kWh produced approximately, depending upon whether CCS systems are employed or not (Houses of Parliament, 2011). On the contrary, this emission ratio ranges from 1 to 170 g CO_2/kWh for renewable energies.

The main drawback of these sustainable energy systems is their economic performance, since the maturity of conventional technologies provides them with much lower costs as opposed to solar technologies which are perceived as having a higher risk nowadays. Nonetheless, some CSP technologies, mainly parabolic trough and central receiver; have experienced important progress, consequently reducing the costs down to acceptable values, which are expected to be even lower in the following years thanks to the impulse of some governmental initiatives (Commission, 2013) (NREL, 2012).

Another interesting aspect of solar technologies that is also demanded by the new electricity grid is modularity. In contrast with larger power plants operating at base load, which are typically inefficient in part-load operation, solar systems can be designed for low rated outputs, thus enabling distributed generation concepts that adapt better to a variable demand. At the same time, CSP is dependent upon meteorological conditions, which brings about a problem of a fluctuating production of electricity and the subsequent mismatch between supply and demand. This challenge has originated the deployment of thermal energy storage technologies.

So far, the development of solar power plants has relied on steam turbine technology, where the receiver typically operates at some 550ºC. Higher temperature are to be expected in the near future though, in particular if gas turbines become a feasible alternative for the power block, given that the theoretical concentration capacity of state-of-the-art solar field technology is capable of achieving more

than 1000ºC with reduced heat losses. However, it must also be acknowledged that a technology enabling the current turbine inlet temperature levels of modern gas turbines (1500ºC) is not envisaged in the near future and, therefore, auxiliary firing will have to be implemented if high efficiencies are sought. In this context, the reference supercritical carbon dioxide power cycle considered in this work may contribute to fill the gap between steam and gas turbines, offering competitive thermodynamic performance, modularity and applicability in renewable energy systems but, currently, at a prohibitively high cost.

1.2 Main constraints of CSP technologies

Transforming solar power into electricity requires an initial process of concentration, whose aim is generating high quality energy available for the prime mover or, widely, system that carries out the different steps of the energy conversion process: solar to heat to mechanical to, eventually, electrical energy. A higher concentring capacity brings about a higher receiver temperature and consequently a higher efficiency potentially attainable by the power conversion system. It is therefore an important parameter for the characterisation of solar facilities the so-called geometric concentration ratio, $CR = A_{rec}/A_{col}$, which is simply the ratio between receiver aperture area and collector aperture area.

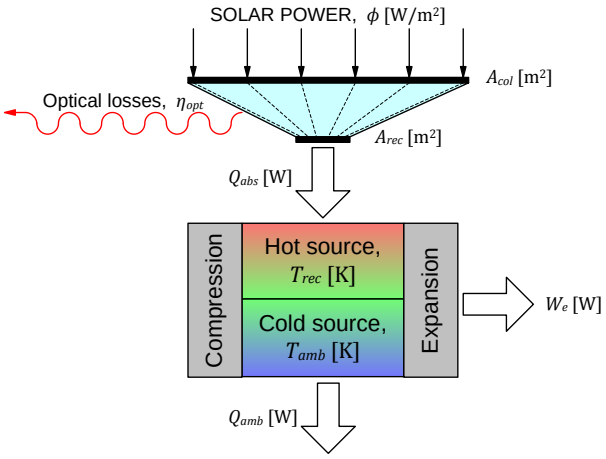

Figure 1. Scheme of a Concentrating Solar Power (CSP) system.

The heat transferred to the fluid per unit of receiver surface (Q_{abs}/A_{abs}) is given by applying the energy conservation law (Romero-Álvarez & Zarza, May 2007)*:*

$$Q_{abs}/A_{abs} = \alpha \cdot CR \cdot \phi \cdot \eta_{opt} - \sigma \cdot \varepsilon(T_{rec}^4 - T_{amb}^4) \qquad \text{[Equation 1.1]}$$

This heat is thus a function of the absorptivity (α) and emissivity (ε) of the receiver, the temperatures of the hot source (T_{rec}) and cold sink (T_{amb}) and the specific thermal power (per unit area) impinging the receiver from the collector field, $\phi \cdot \eta_{opt}$, where ϕ is the normal direct irradiation [W/m²] and η_{opt} the optical efficiency of the facility, which accounts for the losses taking place from the solar energy striking the solar field to that hitting the receiver surface. The receiver efficiency is thus expressed as:

$$\eta_{abs} = \frac{\text{Power absorbed}}{\text{Power received}} = \frac{Q_{abs}/A_{abs}}{CR \cdot \phi \cdot \eta_{opt}} = \alpha - \frac{\sigma \cdot \varepsilon(T_{rec}^4 - T_{amb}^4)}{CR \cdot \phi \cdot \eta_{opt}} \qquad \text{[Equation 1.2]}$$

The power absorbed by the receiver is converted into electrical energy (in a series of energy conversion processes) by a power block operating between a hot source and a cold sink. As known, given a hot and cold temperatures for these source and sink, the practical heat to mechanical energy conversion efficiency is limited by that of the Carnot Cycle: $\eta_{CARNOT} = (T_{rec} - T_{amb})/T_{amb}$. Thus, the total ideal efficiency of the receiver and (ideal) power block is expressed as the product of both, $\eta_{syst} = \eta_{rec} \cdot$

η_{CARNOT}, making it evident that for given irradiation and optical efficiency, increasing the receiver temperature (peak temperature of the working fluid) has counteracting effects on the global efficiency of the plant. On one hand, it increases the thermal efficiency of the power cycle while, on the other, it also increases the radiation losses from the receiver (i.e. heat radiated from the receiver surface to the surroundings). This combined effect is shown in figure 2 where, for a concentration ratio, an optimum receiver temperature is found in terms of global efficiency. For temperatures higher than the optimum one, the receiver radiation losses are not compensated for by the higher cycle efficiency.

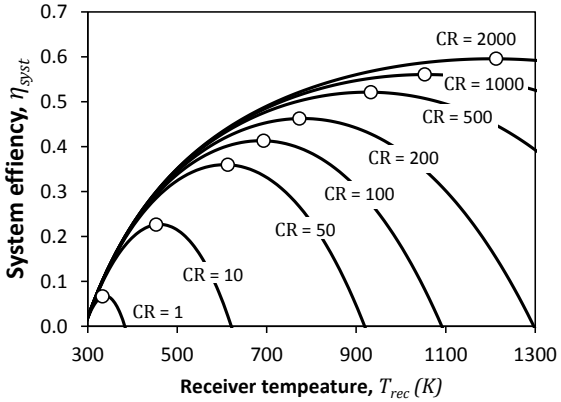

Figure 2. Influence of receiver temperature (T_{rec}) on system efficiency (η_{syst}) for different geometric concentration ratios (CR), considering an irradiation of ϕ=1000 W/m², an optical efficiency of η_{opt}=0.8, an ambient temperature of T_{abm}=20 ºC and emissivity and absorptivity of $\alpha = \varepsilon$=0.85.

For the most developed solar technologies, geometric concentration ratios vary between 30 and 80 for parabolic trough and between 200 and 1000 for central receiver plants, which limits the system efficiency to values below 60 % even if the cycle works ideally, as shown in figure 2. Moreover, the real power blocks operate very far from Carnot efficiency so their global performance is further reduced. Consequently, in terms of project economics, the Levelised Cost Of Electricity (LCOE in €/kWh) measuring the cost of each unit electrical energy obtained, all lifelong capital and operating expenditures of the plant into account, departs from that of the hypothetical ideal plant.

LCOE values around 0.12-0.15 €/kWh for parabolic trough (Turchi, et al., 2010) and 0.09-0.12 €/kWh for central receiver plants (Prior, 2011) have been reported. These account for all the expenditures and investment costs that need to be faced along the plant lifetime operation, $LCOE = (\sum Investment + \sum Expenses)/\sum Production$, and it is therefore an important parameter to appraise the economic feasibility of a project. In a simple model, one can express:

- The capital investment as the product of the specific capital cost and the power installed: $\sum Investment = c_{inv} \cdot \dot{W}$,
- The operational expenditures as the sum of financial (debt services), operating and fuel cost, the latter being null for a purely solar application (no fuel hybridisation): $\sum Expenses = X_{debt} \cdot \sum Investment + k_1 \cdot c_{OP\&M} \cdot \sum Production$,
- And the production as a function of the lifetime (N in years), plant load factor (f_{load}) and rated output ($\dot{W}$): $\sum Production = 8760 \cdot k_2 \cdot N \cdot f_{load} \cdot \dot{W}$.

Manipulating the previous expressions, LCOE can be expressed as:

$$\mathrm{LCOE} = \frac{c_{inv} \cdot (1 + X_{debt})}{8760 \cdot k_2 \cdot N \cdot f_{load} \cdot \dot{W}} + k_1 \cdot c_{OP\&M} \qquad \text{[Equation 1.3]}$$

Where c_{inv} and $c_{O\&M}$ are the specific investment and operational/maintenance costs in €/kW and €/kWh respectively, k_1 and k_2 are constant coefficients that bring both maintenance costs and production to their present values at the initial moment of the project and X_{debt} the ratio between the total financial expenses and the initial investment. The new proposal can only influence the specific costs in a partial way, since a large portion of costs is related not to the power block but to the solar field (where there would be a reduction only if the efficiency of the power block were higher). It is acknowledged here that costs depend largely on the maturity of the technology and hence commercial development is necessary for these costs to be accurate; nevertheless, attention must also be paid to other aspects that permit reducing the LCOE: simplicity and compactness of equipment and layouts, possibility of integrating energy storage systems and good partial load performance are some of them.

The last limitation to highlight regarding solar power plants based on Rankine cycles is the dependence on water, necessary for cooling (note that air cooled condenser reduce the consumption of water but at the expense of a lower efficiency and therefore larger solar field) and also for cycle make up. Typical yearly water consumptions for Rankine power plants are around 2 L/kWh (Walker, et al., 2013), establishing an important handicap for the location of these plants in desert areas, where the solar resource is highest but hardly any water is available.

1.3 Open simple Brayton cycle as an alternative for solar power production

The use of Brayton instead of Rankine cycles could offer some advantages such as no water consumption, a plant footprint considerably reduced thanks to its higher specific power, a priori similar thermal efficiency to state-of-the-art Rankine-based plants. However, both efficiency and specific work are preconditioned by the working fluid and operating parameters: pressure ratio and TIT mainly.

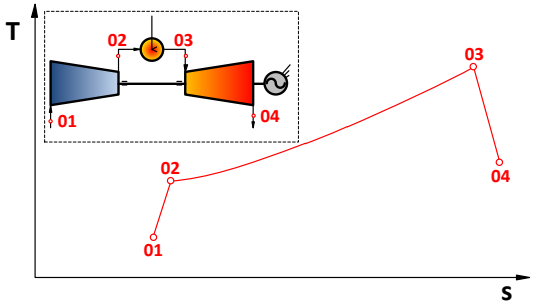

Figure 3. Temperature- Entropy diagram of a conventional open Brayton cycle.

Figure 3 shows the four characteristic stagnation points of a conventional Brayton cycle in a temperature-entropy diagram. The heat injected per unit mass is $Q = h_{03} - h_{02}$ and the gross specific shaft work $W = (h_{03} - h_{04}) - (h_{02} - h_{01})$, both in J/kg. The efficiency is the quotient of both ($\eta = W/Q$) and it can be expressed as shown in [equation 1.4] by using the definition of the pseudo-pressure ratio $\delta = \rho^{(\gamma-1)/\gamma}$ and the temperature ratio $\theta = T_{03}/T_{01}$, where ρ is the pressure ratio and it has been assumed ideal gas and no pressure drops.

$$\eta = \frac{\frac{\theta}{\delta}\eta_C\eta_T - 1}{\frac{\theta - 1}{\delta - 1}\eta_C - 1} \qquad \text{[Equation 1.4]}$$

$$W = \frac{C_p T_{01}(\delta - 1)}{\eta_C}\left(\frac{\theta}{\delta}\eta_C\eta_T - 1\right) \qquad \text{[Equation 1.5]}$$

The equations above are obtained for an ideal cycle under the following assumptions:

- The working fluid in the entire cycle is air which is also assumed to behave ideally.

- There are no pressure drops.
- The fuel flow rate is negligible with respect to air one.
- Non-isentropic behaviour of compressor and turbine.

This simple model yields two well-known general conclusions for Brayton cycles (Figure 4):

- There exist two different optimum pressure ratios for a given temperature ratio: one for highest efficiency and another for highest specific work, the former being always higher than the latter. The choice of one of these options depends on the application.
- The achievable efficiency is upper limited by the temperature ratio, increasing in a directly proportional manner.

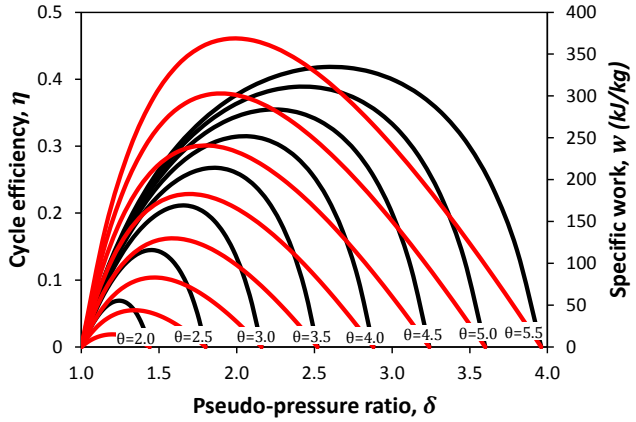

Figure 4. Effects of pseudo-presure ratio (δ) and temperature ratio (θ) on cycle efficiency (η, in black) and specific work (W, in red) for an ideal gas with γ=1.4, compressor inlet temperature of T_{01}=300 K and compressor and turbine isentropic efficiencies of 80 and 90 % respectively.

It is worth noting that the curves in Figure 4 do only apply to the rated operating conditions; i.e. they are not valid for varying operating conditions at part-load or off-design operation. Thus, for the characteristic range of TIT in solar applications, cycle efficiency is restricted to values under 30 % for temperature ratios not higher than 3.5 (TIT<1050 K), which is under the expectation of the new proposal. This can be improved by implementing several modifications in the conventional Brayton cycle lay-out, or by using a combustion chamber in series with the solar receiver to increase the temperature from receiver outlet to turbine inlet. However, this second option contradicts the renewable nature of any solar facility and it is therefore discarded. There exits two other options worth considering though: the first one is to make the cycle recuperative (Section 1.4) and the second one is the possibility to change the working fluid in order to operate near its critical points, giving place to supercritical Brayton cycles (Section 1.5).

1.4 Open recuperative Brayton cycle as an alternative for solar power production

The recuperator located between compressor and heater recovers part of the heat content of the turbine exhaust which is used to heat up the compressor delivery air (Figure 5). Consequently, the heat required to reach a certain TIT decreases and therefore, the cycle efficiency is improved.

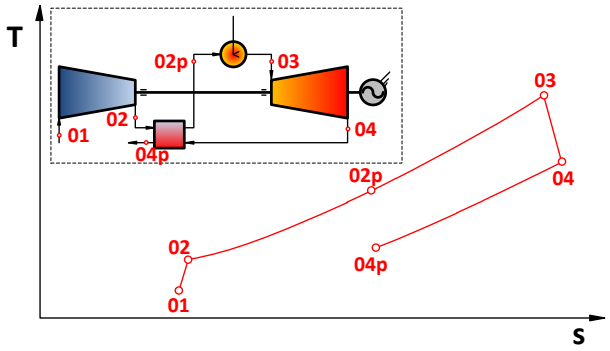

Figure 5. Temperature- Entropy diagram of an open simple recuperative Brayton cycle.

Points 02p and 04p represent the high and low pressure outlet streams of the recuperator and, based on them, the recuperator effectiveness can be defined As $\varepsilon_{rec} = (h_{02p} - h_{02})/Q_{max}$ or $\varepsilon_{rec} = (h_{04} - h_{04p})/Q_{max}$, since due to energy conservation $(h_{02p} - h_{02}) = (h_{04} - h_{04p})$. The maximum heat is simply calculated as $Q_{max} = h_{02} - h_{04}$ for substances with constant specific heat such as ideal gases or liquids. However, if the specific heat varies strongly from across each side of the heat exchanger, as it happens with supercritical fluids; the maximum heat is generally calculated as exposed by (Dostal, et al., March, 2004):

$$Q_{max} = MIN\{(h_{04} - h_{04^*}), (h_{02^*} - h_{02})\} \qquad \text{[Equation 1.6]}$$

Where point 02* is at same pressure as 02p and at the temperature of point 04, and equivalently point 04* is at same pressure as than 04p and at the temperature of 02. Therefore, these points imply thermal equilibrium at one of the two recuperator ends (that with lower specific heat).

If the effectiveness of the recuperator is now combined with the aforementioned non-dimensional parameters δ and θ, the new cycle efficiency is defined as in [equation 1.7] from which [equation 1.4] is obtained for the non-recuperated cycle (ε_{rec}=0). On the contrary, the equation yielding the specific work of the cycle does not vary with respect to the previous expression [Equation 1.5] as long as the simplifying assumptions are still considered.

$$\eta = \frac{\frac{\theta}{\delta}\eta_C\eta_T - 1}{\frac{\theta - 1}{\delta - 1}\eta_C - 1 - \frac{\varepsilon_{rec}(\theta - \delta^2)}{\delta(\delta - 1)}\eta_C} \qquad \text{[Equation 1.7]}$$

A parametric representation of this expression is presented in figure 6, where a recuperator effectiveness equal to 85 % is considered (which is a technological value for air recuperator effectiveness according to literature review (Muñoz de Escalona, et al., 2010)). In addition to a cycle efficiency enhancement with respect to the simple cycle (Figure 4), another effect of recuperation is the displacement of the pressure ratio for maximum efficiency towards lower values, because increasing the pressure ratio in such configuration implies (for a given TIT) reducing the recuperative potential as the temperature gap between 04 and 02 decreases. As shown, it is possible to exceed 35 % of efficiency with this level of recuperation (Figure 6), a value that is close to the expectations for a gas turbine based application even though another alternative is still studied in the next section: the supercritical Brayton cycle.

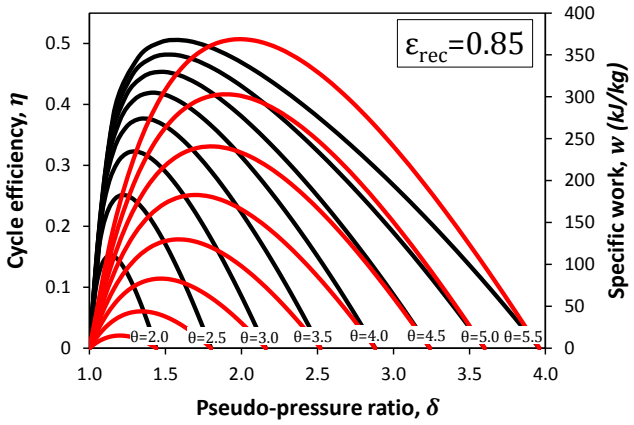

Figure 6. Effects of pseudo-presure ratio (δ) and temperature ratio (θ) on cycle efficiency (η, in black) and specific work (w, in red) for an ideal gas with γ=1.4 in a recuperative cycle with ε_{rec}=0.85, compressor inlet temperature of T_{01}=300 K and compressor and turbine isentropic efficiencies of 80 and 90 % respectively.

1.5 Why supercritical carbon dioxide Brayton cycle for solar power production?

Non-conventional fluids in supercritical or transcritical cycles are usually linked to closed or externally heated configurations as shown in Figure 7. A cooling system is therefore needed which is a non-desirable feature for the new proposal as long as it involves water consumption. Nevertheless, the motivation of using supercritical cycles is mainly twofold:

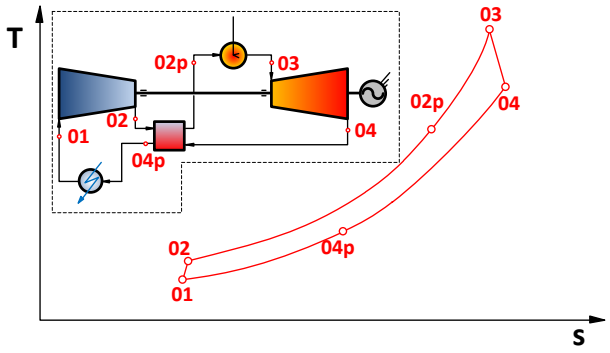

Figure 7. Temperature- Entropy diagram of a Supercritical Brayton cycle

- On one hand, the real gas behaviour provides the fluid with a lower compressibility factor that makes the compression process less energy-consuming. In fact, even with a lower expansion work at the turbine, the net power output of still high as it is compensated for by the reduction in compression work. The cycle thus becomes the only practical alternative to improve cycle efficiency under the peak temperature limitation found in solar applications (without significantly affecting the layout of the plant).
- On other hand, the highly pressurised conditions in the system reduce the footprint of the power block. In fact, the graphical comparison shown in (Dostal, et al., March, 2004) exposes very clearly the size reduction attainable with supercritical CO_2 turbomachinery in comparison to air (Brayton) and water (Rankine) turbines. The first supercritical CO_2 turbomachinery design (Figure 8) came to demonstrate the surprising size reduction that supercritical technologies can make possible in relation to conventional systems. This is a

very important aspect, since it should bring about cost reductions in a future scenario of technical maturity and, at the same time, the expected compactness can make it very suitable for modular applications (so common in renewable and waste energy applications).

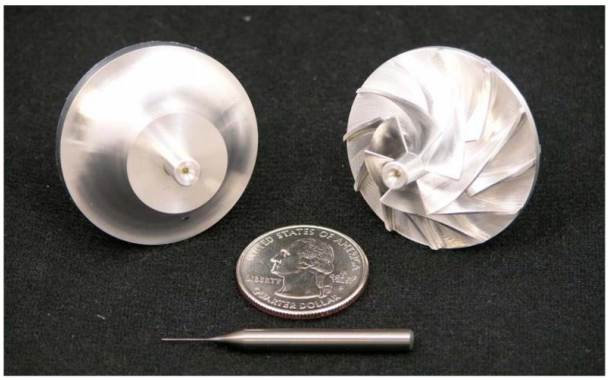

Figure 8. Supercritical CO_2 compressor impeller. Designed and manufactured by Barber Nichols Inc. for SANDIA National Laboratories facilities (Wright, et al., September 2010).

One of the first individuals to research the supercritical cycle was Feher (Feher, 1968). This author demonstrated the need to adopt recuperative configurations to reach high efficiencies, since the heat recovery between high and low pressure streams can be performed with high effectiveness. However, recuperation finds a particular problem in supercritical cycles called the *pinch problem*, which is associated to the enormous differences in isobaric specific heat that can exist between the cold and hot ends and the high and low pressure sides of the recuperator. Feher also exposed it very clearly in an enthalpy-temperature diagram, which was later manipulated by Dostal (Dostal, et al., March, 2004) to present the effect of this circumstance on the effectiveness of the recuperator (Figure 9). Even if the minimum temperature difference is set to 0ºC at one recuperator end, there is still a region, called the *pinch-point region* by Dostal, where the effectiveness is lower and does not attain 100%.

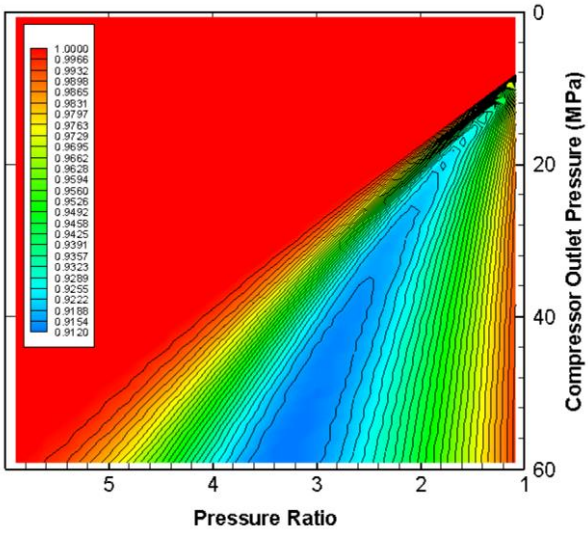

Figure 9. Recuperator effectiveness in different conditions in a recuperative supercritical carbon dioxide Brayton cycle for thermal equilibrium (Dostal, et al., March, 2004).

This particular performance of the working fluid in the heat exchangers at low temperature (close to the critical point) brings about a subsequent penalisation on cycle efficiency. Therefore, compact and highly efficient recuperators are mandatory in order not to incur in an excessive deterioration of the global efficiency of the system though this issue does not represent a technological barrier today. In effect,

printed circuit heat exchangers (PCHE) can achieve efficiencies of up to 95% easily (Muñoz de Escalona, et al., 2010), in particular for CO_2 which is a very advantageous fluid for supercritical cycles thanks to its critical conditions (31ºC, 73.8 bar), Table 1.

Fluid	Critical temperature (K)	Critical pressure (bar)
Air	132.5	37.9
Water (H_2O)	647.1	220.6
Ammonia (NH_3)	405.4	113.3
Carbon dioxide (CO_2)	304.1	73.8
Perfluoropropane (C_3F_8)	345.0	2.6
Sulfur dioxide (SO_2)	430.6	7.9
Sulfur hexafluoride (SF_6)	318.7	3.8
Xenon (Xe)	289.7	5.8
Propane (C_3H_8)	369.9	42.5
n-Butane (C_4H_{10})	425.1	38.0
Isopentane (C_5H_{12})	460.4	33.8

Table 1. Critical properties of different fluids (Lemmon, et al., 2010).

There is a second aspect that needs to be studied in addition to the selection of the working fluid. Depending on the pressure range, (Brayton) power cycles can be differentiated in transcritical, when the critical pressure of the working fluid is met somewhere in the compression process, and supercritical, when the compression process starts at a pressure above the critical point[1]. In the transcritical layout, a new classification is needed depending on whether the working fluid is in liquid state at the inlet to the compression device (pump in this case) or if it is in gaseous state (compressor). The former case is usually termed as the supercritical condensation cycle which was extensively studied by Prof. Angelino in his seminal work (Angelino, July 1968) which where through a complete evaluation of several layouts this author presented a body of knowledge so as to which supercritical cycle is more efficient and where the inefficiencies are located. Figures 11 and 12 are taken from the aforecited reference and show the different layouts studied by Angelino.

Angelino pointed out that most of the cycle's irreversibility is found in the recuperator, as a result from the fact that heat transfer occurs between streams with different heat capacities (Angelino, July 1968). Thus, this author proposed different layouts aiming at reducing these sources of efficiency drops. The most important contribution of that work is the recompression cycle (Cycle A in

Figure *11*), which manages to reduce the difference between heat capacities in this process. To that aim, this layout comprises two compressors (main and recompression) and two recuperators (high and low temperature recuperator, HTR and LTR). Differences in specific heats between both sides of the HTR are negligible, since the real behaviour of the gas tends to disappear at elevated temperature. Therefore, similar heat capacities will be obtained as long as mass flow rates are kept equal in both sides of the HTR. However, in the LTR, due to more noticeable differences in the specific heat between streams, the hot outflow of the LTR is split: a fraction is directed to recompression and the remaining flows to the condenser, thus attaining similar heat capacities in both sides of the LTR.

Irreversibility reductions are verified in Figure 10, where cumulative efficiency drops are represented for the different equipment of the cycle and their consequent losses, taking the Carnot

[1] *This concept can be extended to temperature (supercritical cycles being those operating at a higher than critical temperature) though this is not common.*

efficiency between maximum and minimum cycle temperatures ($\eta_{CARNOT} = 1 - T_{min}/T_{max}$) as a reference. Same conditions and cycle parameters as in (Angelino, July 1968) are considered for this calculation and it is confirmed that Angelinos's recompression cycle manages to reduce the overall cycle irreversibility noticeably.

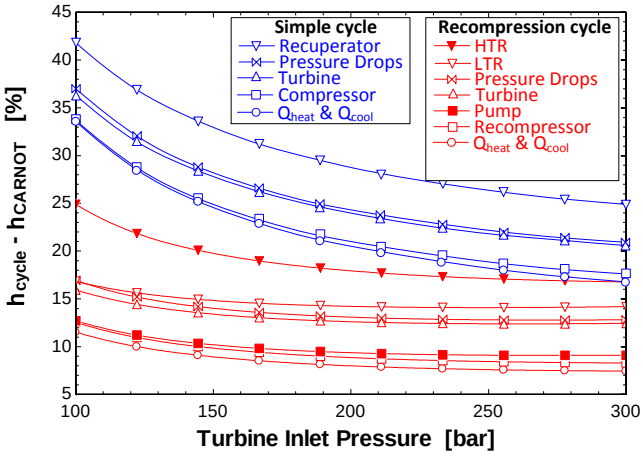

Figure 10. Cumulative efficiency drops due to different equipment for both the simple cycle (in blue) and the recompression one (in red).

Starting off from this layout, other cycle configurations were suggested by Angelino with the objective of further reducing irreversibilities as well as avoiding other technical problems. Cycle layout B is the pre-cooling cycle and makes the turbine exhaust pressure independent from condensation pressure. This layout comprises an additional cooling process from points 9 to 10, which provides additional waste heat available for integration opportunities. Layout C belongs to the reheating cycle, and presents another alternative to layout A which reduces the stresses in the high temperature devices. The pre-compression cycle (layout D) is a last option similar to the pre-cooling cycle but without additional cooling. In this case, the pre-compression enhances the potential to recuperate heat in the LTR due to the temperature increase of point 10, however this cycle does not contain any recompression.

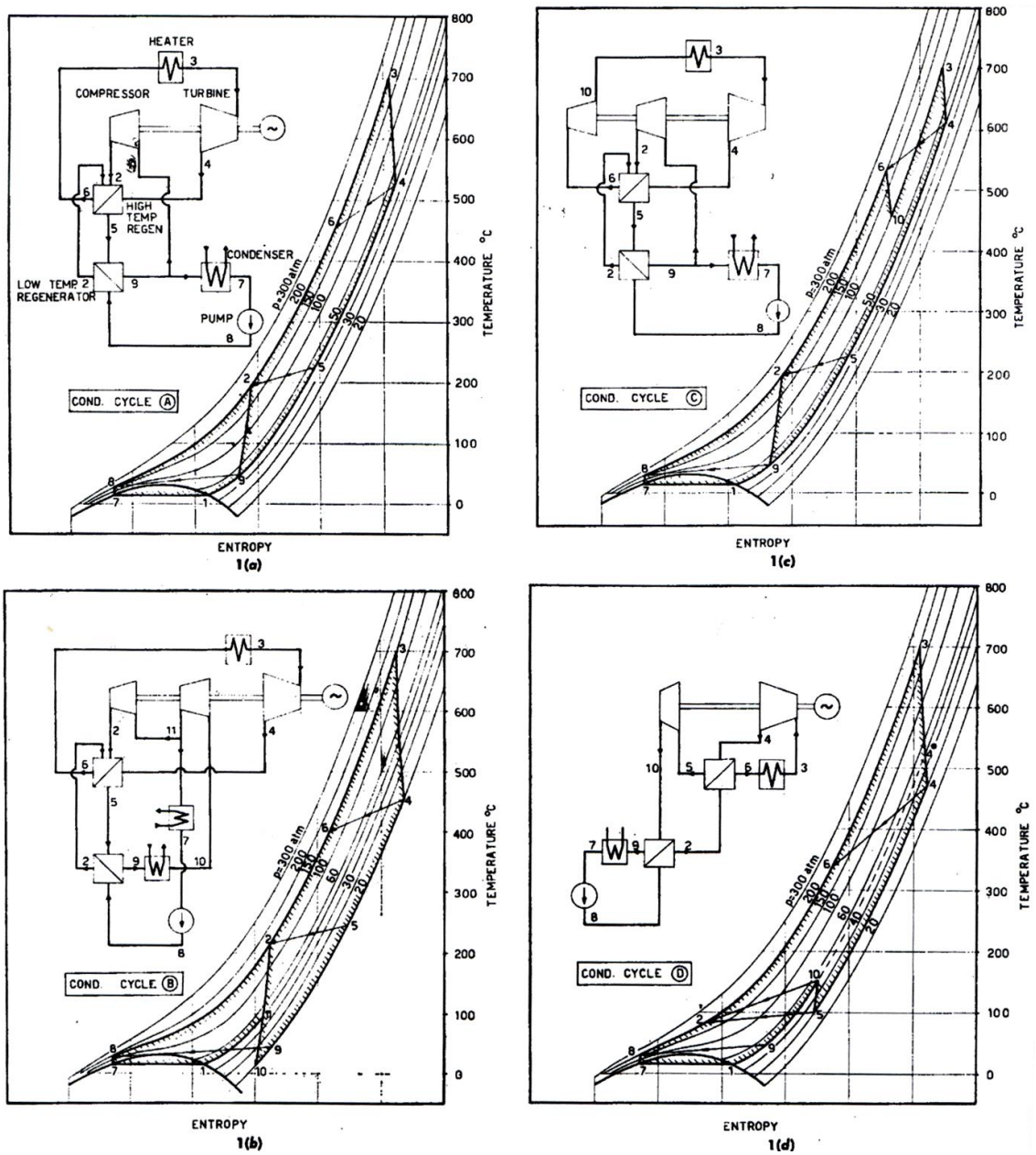

Figure 11. S-CO2 cycle configurations studied by Angelino in 1968 (Angelino, July 1968).

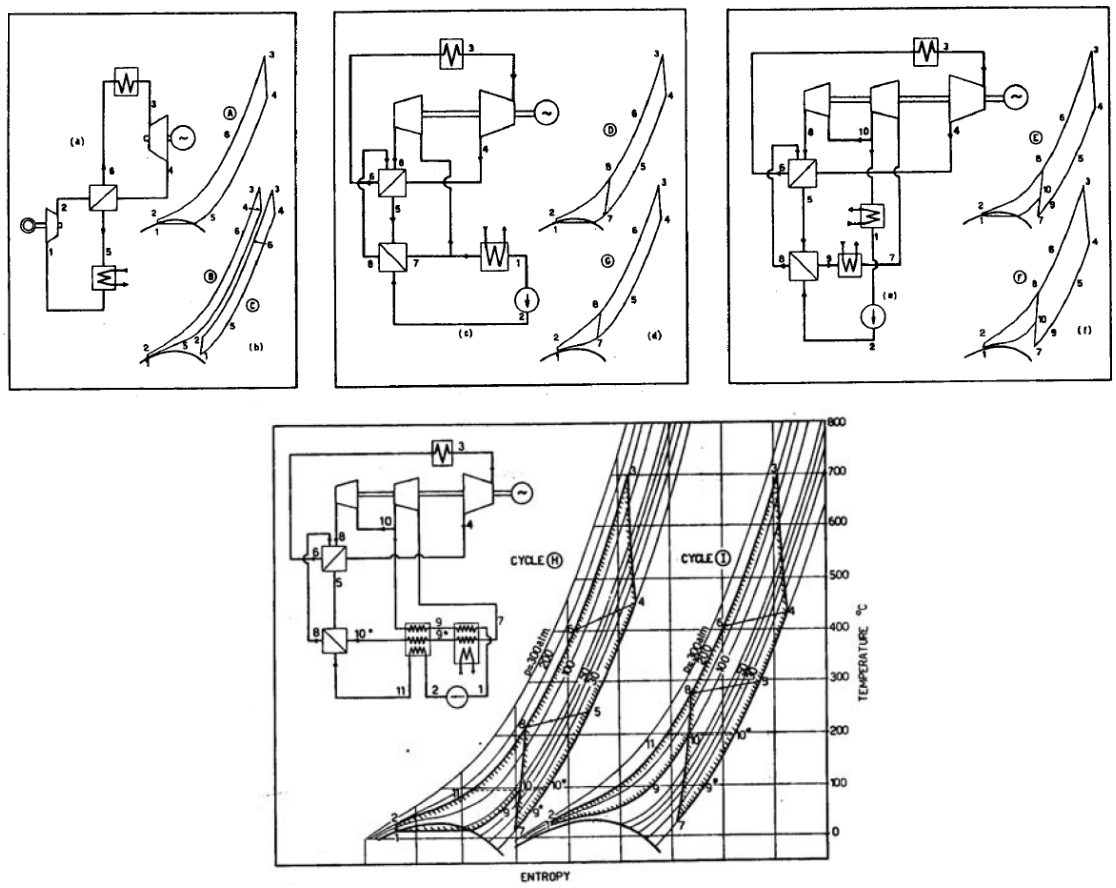

Figure 12. S-CO2 cycle configurations studied by Angelino in 1969 (Angelino, 1969).

As a conclusion of these analyses, the reheat recompression cycle resulted to be the most advantageous configuration in terms of thermodynamic performance. Unfortunately, this is achieved at the cost of a higher complexity since each equipment is doubled: double heater, double compressor (one pump and one compressor for transcritical cycles), double turbine and also double recuperator, which makes it undoubtedly a much more expensive option. Nevertheless, it must be acknowledged that the efficiency can be increased up to 10 percentage points in comparison with the simple recuperative cycle (Figure 13).

Supercritical carbon dioxide technology is not still developed due to its incipient maturity. Although noteworthy advances have been done with compact heat exchanger existing nowadays, turbomachinery still needs to be reinvented. A new development based on existing turbomachinery for conventional fluids has to be developed for CO_2 (Ulizar & Pilidis, 2000) given the substantial differences that are to be expected from the substitution of the working fluid (Monje, et al., 2012). Under these uncertainties, the simplest case is selected for the development of the present work: the simple recuperative S-CO_2 cycle, offering high efficiency (around 40%) in the modest temperature range selected and the possibility of ambient air cooling. Additionally, the existence of only one compressor in simple configurations, avoids smaller and less efficient compressors as the recompression one, where secondary losses associated to reduced section may become dominant.

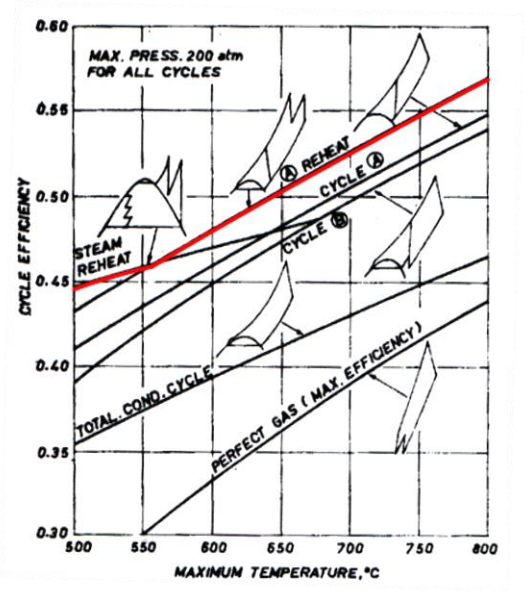

Figure 13. Efficiency comparison amongst the supercritical cycle configurations studied by Angelino (Angelino, July 1968).

1.6 The fluid: Carbon Dioxide

The first question that arises regarding a proper design of the compressor inserted in the aforementioned cycle is: how does the fluid behave? Is it a compressible or incompressible fluid? And accordingly, can the compressor be designed according to the well-established guidelines for pumps or ideal gas compressors or, on the contrary, is this machine somewhere in between and therefore it requires the development of a new theory? The parameter commonly employed to discuss this question is the compressibility factor: $Z = Pv/(RT)$, defined as the ratio between the actual specific volume of the fluid and the one that the fluid would have in the case of ideal gas behaviour. Thus, a value of compressibility factor near unity means ideal gas behaviour, becoming real gas effects more and more important when Z decreases down to approximately 0.2 near the critical point (Figure 14).

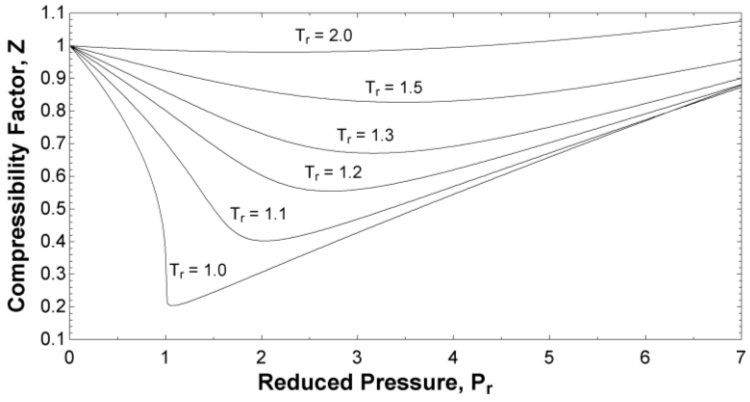

Figure 14. Generalised compressibility factor diagram.

For instance, atmospheric air flowing through the compressor of a gas turbine with 18:1 pressure ratio and 85 % isentropic efficiency hardly has any change in compressibility. The working fluid does accordingly fit well to the ideal gas behaviour along the whole compressor. On other hand, a booster pump can feed the boiler of a steam power plant at 200 bar with a negligible water temperature increase, changing the compressibility factor of the fluid from $7.3 \cdot 10^{-4}$ to 0.145, where the variation is mainly due

to pressure changes as the specific volume remains fairly constant (Figure 15). In between them, neither density nor compressibility factor of carbon dioxide remain constant at supercritical conditions when flowing through the compressor, and therefore both the liquid (vertical line at $\rho/\rho_0 = 1$ in figure 15) and ideal gas (horizontal line at $Z = 1$ in figure 15) approaches are incorrect. The thermodynamic path followed by carbon dioxide is a consequence of the particular variation of its density with pressure and temperature near the critical point.

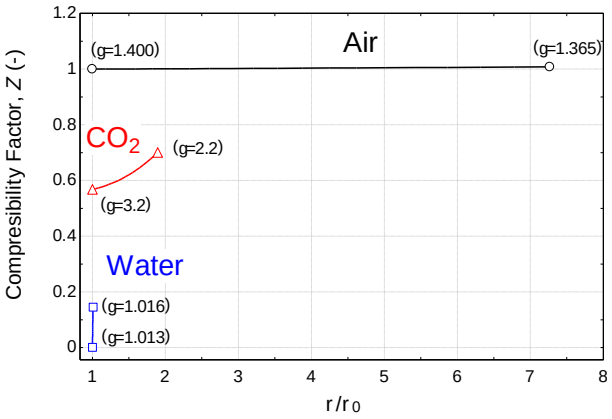

Figure 15. Compressibility factor variation vs. density ratio with respect to the inlet conditions in compression processes for air water and supercritical CO_2.

In the main, any fluid property can be expressed as a summation of its value as an ideal gas and a deviation term which depends on the thermodynamic state (P and T) as well as on some fluid other properties, mainly molecular weight (MW) and complexity (taken as the number of activated degrees of freedom[2], N). Moreover, the evolution of any fluid property with respect to the thermodynamic state is strongly linked to the fluid nature (MW and N). In comparison to other fluids, CO_2 can be classified as a low-molecular-complexity substance, which explains why the temperature dependence of its properties differs largely from some other more complex organic fluids such as syloxanes and other refrigerants.

The critical point of a substance could simply be defined as the highest temperature which can hold liquid-vapour equilibrium during phase change and, therefore, at higher temperatures gas and liquid states do not coexist. In other words, conventional vaporisation does not exist above the critical temperature and, consequently, the concept of vaporisation enthalpy makes no sense. The transition between liquid-vapour equilibrium in the supercritical region produces a very sharp discontinuity in the value of specific heats, indicating that temperature increases in isobaric conditions are very energy-consuming, recalling the aforecited vaporisations processes. Figure 16 shows that the higher the pressure, the lower the specific heat peak, but also the higher the temperature at which they are achieved. All the temperatures for which a peak of specific heat are achieved at supercritical pressures conform the so-called pseudo-critical points, which confer to the fluid a behaviour similar to the critical point but attenuated as pressure increases. Coming back to the thermodynamic cycle, this fact is likely to cause the pinch problem: if a pseudo-critical point is achieved inside the recuperator, the energy that the low pressure fluid requires for cooling down can lead to thermal equilibrium between both fluids with effectiveness lower than 100 %.

More formally, the critical point is defined as that point where the isotherm has a deflection point in a pressure-volume diagram. Therefore, mathematically:

[2] *The degrees of freedom in a molecule are associated to translations, rotations and vibrations plus the different electronic configuration possible in the molecule, the latter being negligible for the majority of applications given that the temperature threshold that activates this contribution is in the order of 10^4 K. The number of degrees of freedom activated is a function of temperature, but the maximum limit satisfies: $N_{trans}^{max} = 3$, $N_{rot}^{max} = 2 + \epsilon$ and $N_{vib}^{max} = 3n_a - 5 - \epsilon$, where ϵ =-2, 0 and 1 for monoatomic, linear polyatomic and non-linear polyatomic substances and n_a is the number of atoms in the molecule* (Harink, et al., 2009).

$$\left(\frac{\partial P}{\partial v}\right)_{T_c} = \left(\frac{\partial^2 P}{\partial v^2}\right)_{T_c} = 0 \qquad \text{[Equation 1.8]}$$

As density is the inverse of specific volume, the previous expression implies that $\partial\rho/\partial P \to \infty$ in the critical point, what in practical terms means that a pronounced increase in density takes place when pressure increases. This is an important difference to be highlighted in comparison with conventional fluids (whether water or air) which will presumably affect turbomachinery design (Section 1.7). Figure 16 shows this and other peculiarities of carbon dioxide in the supercritical region.

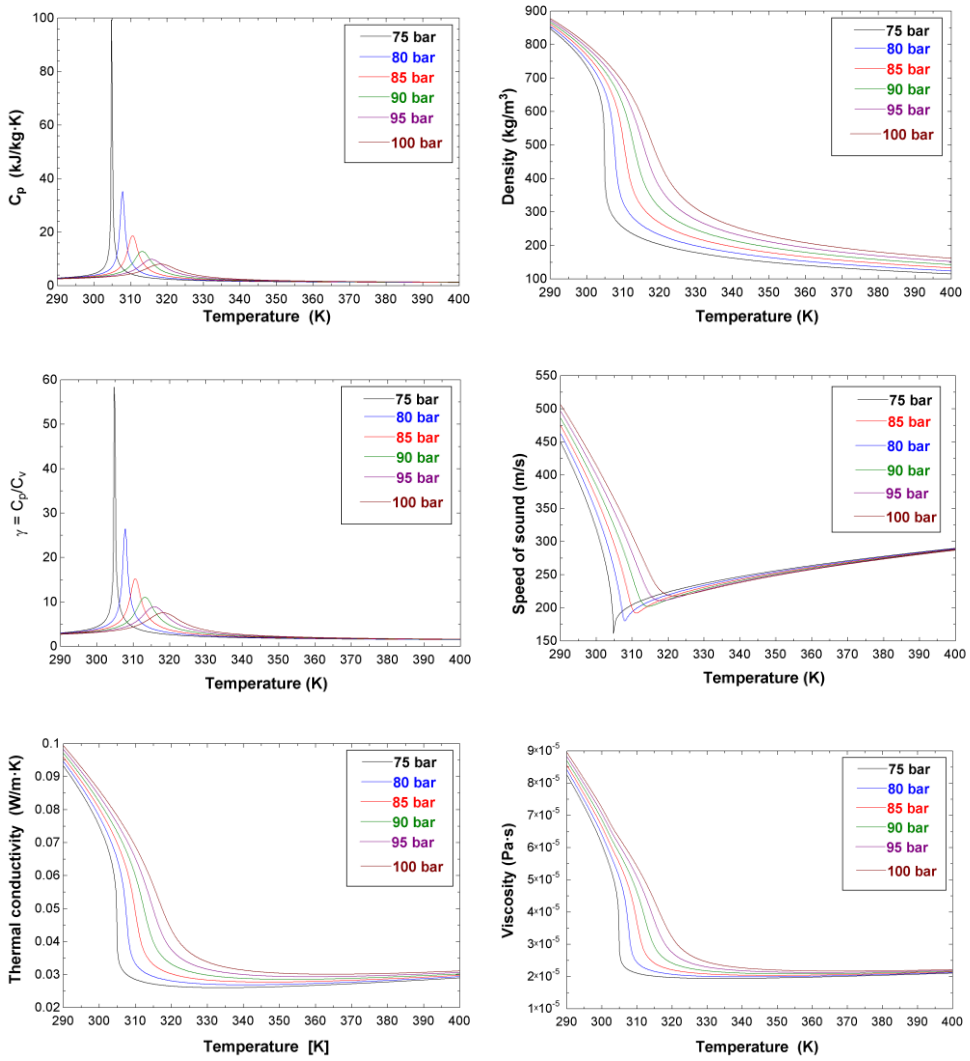

Figure 16. Carbon dioxide properties vs. temperature as a function of pressure.

1.7 The turbomachinery issue

The previous sections have shown that supercritical carbon dioxide exhibits some particularities never considered before in turbomachinery design, such as the strong variation in the ratio of specific heats as well as the low compressibility factor of the gas. This, at least, puts into question the validity of some experimental expressions obtained for air turbomachinery; Weisner's expression for calculating the slip factor in a radial impeller (Wiesner, 1967) and the expression developed by Aungier (Aungier, 1995) for the tip blockage factor are just some examples of this. Regarding axial turbomachinery, the seminal

works by Lieblein for compressors (Lieblein, 1965) and Ainley & Mathieson for turbines (Ainley & R Mathieson, 1955), which provide empirical equations both for losses and deviation in cascades, were also obtained by analysing air cascades experimentally. However, these expressions can be theoretically extended to other ideal gases by changing the specific constants which define the working fluid, basically the ratio of specific heats (γ) and molecular weight (MW). Nevertheless, since there is not a single value of γ for carbon dioxide in the compressor of a supercritical power cycle (i.e., γ changes substantially between inlet and outlet) the question that rises up is whether or not the application of these expressions in a discrete way in the range of variation of γ is valid. Moreover, bearing in mind that the compressibility factor carbon dioxide in the system considered are between the typical values for gas and liquid, it could be thought that expressions developed for liquids, as the guide presented by Balje (Balje, 1981), could also be valid for this particular application. In fact, the pioneer supercritical impeller designed by Fuller et al. at Barber Nichols (Figure 8) is based on recommendations for hydraulic machinery. But these are actually the two ends of the whole range of design choices, which might as well not be valid for the majority of cases for supercritical CO_2 and, as pointed out by some other authors (Ulizar & Pilidis, 2000), it is necessary to develop a new theory for the specific characteristic of the fluid. This work aims to contribute to this request.

1.8 International research and commercial interest in S-CO2 technology

Since the revival of the interest in the S-CO2 cycle early in the 21th century, with works such as the one from M.I.T. (Dostal, et al., March, 2004) or the one from the Czech Technical University in Prague (Petr, et al., 1999), relevant research institutes have stepped forward by constructing different experimental facilities.

1.8.1 Czech Republic institutes

There exist four research centres in the Czech Republic working in the S-CO2 cycle nowadays (Dostal & Kulhanec, 2009): Prague Czech Technical University (CTU), Řež Nuclear Research Institute, Běchovice Research Institute and the Technical University of Brno. It is worth highlighting the experimental facility located in the Běchovice Research Institute (Figure 17), whose main purpose is to study the stability of compression and expansion processes with volumetric machines. Additionally, it is now planned the construction of another facility at the Řež Nuclear Research Institute for the development of turbomachinery in power cycles of between 2 and 3 MW.

Figure 17. Experimental loop at Běchovice research institute.

1.8.2 Tokyo Institute of Technology

The research team led by Prof. Motoaki Utamura created a small scale S-CO_2 cycle facility that works at turbine inlet temperatures up to 550 K (Tokyo Institute of Technology, 2011), whose design

concept is presented in (Utamura, et al., 2010). However, because of scale effects, the generated power is almost completely offset by the mechanical and electrical losses, yielding a net output of some hundreds of kilowatts, far from the gross value of 18 kW. In the line of this work, special attention is paid to the compressor of this facility described in the reference (Utamura, 2012), where the authors concluded that "*compressor performance in the supercritical liquid-like phase achieved the highest performance in both experiments and predictions by the simulation program*". An image of the aforementioned compressor is shown in Figure 18.

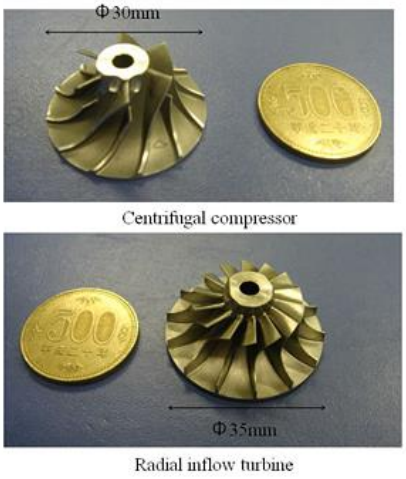

Figure 18. Radial impeller of the S-CO2 cycle experimental facility at the Tokyo Institute of Technology.

1.8.3 SANDIA National Laboratories

Since May 2008, SANDIA National Laboratories (SNL) have a small scale S-CO_2 compression test loop, aimed at validating models employed in turbomachinery and heat exchanger design for nuclear applications (Wright, et al., September 2010). The facility was designed by SNL and Barber-Nichols Inc. and originally comprised a 50 kWe motor-driven compressor, a gas chiller to avoid the heating up of the fluid along the loop and an orifice valve which expands the fluid down to the compressor inlet pressure. A small turbine (1.2 inch diameter) was added in a later revamping in January 2009 in order to obtain S-CO_2 cycle experimental data with a maximum turbine inlet temperature of 537 ºC (Figure 19).

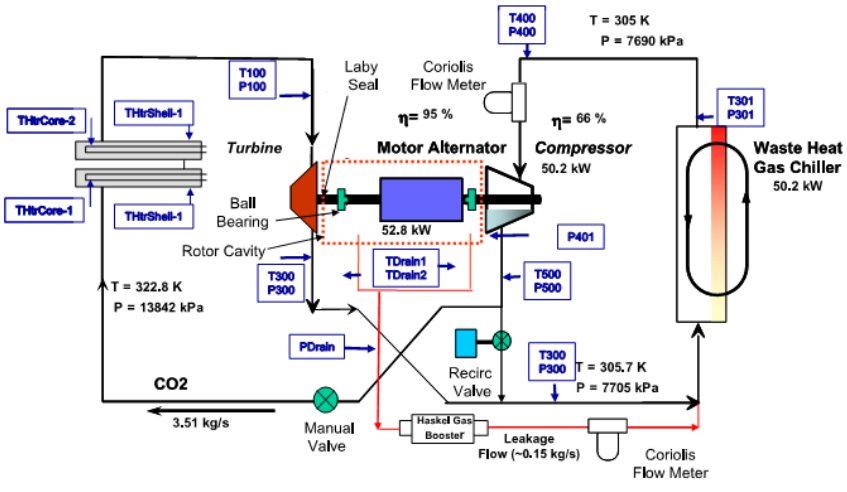

Figure 19. Flow diagram of the closed compression test loop of SANDIA National Laboratories.

1.8.4 National Renewable Energy laboratory

In 2010, the National Renewable Energy laboratory (NREL) started working in this field (Ma & Turchi, 2011) and nowadays, the Head of the CSP department at NREL, Dr. Craig Turchi, is world-widely acknowledged as an active leader of the S-CO_2 community. NREL is participating in the development of a 16 M$ Project financed by the Department Of Energy (DOE) of the US in the scope of the Sunshot initiative (NREL, 2012) (see section 1.8.7).

1.8.5 Argonne National Laboratory

The Argonne National Laboratory (ANL) from the U.S. Department of Energy is actively working on the S-CO_2 cycle oriented to nuclear applications. Heat transfer studies were initially done in the facility shown in Figure 20, which has two separated S-CO_2 loops thermally linked by the heat exchanger: the lower pressure loop operates at around 80 bar and the higher pressure loop at up to 200 bar. CO_2/CO_2 and water/CO_2 heat transfer phenomena were studied aimed at developing design techniques for the recuperator and the cooler of the S-CO_2 power cycle.

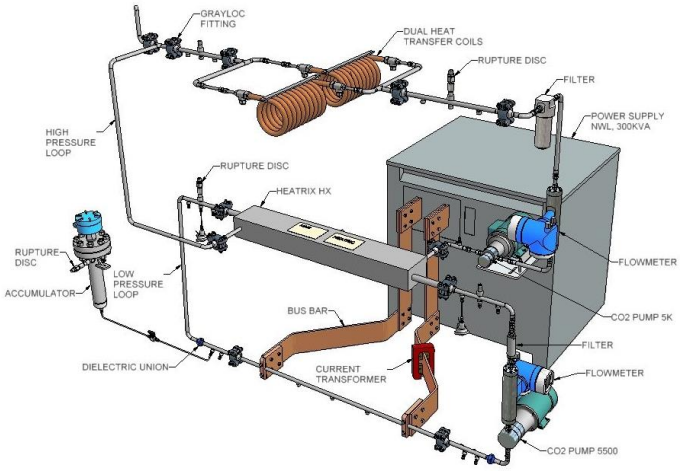

Figure 20. Scheme of a S-CO2 experimental loop at Argonne National Laboratory for heat transfer studies. Not in operation nowadays.

After these heat transfer studies, ANL is currently developing an experimental project on Sodium-Cooled Fast Reactors (SFR) in a consortium with Commissariat a l'Energie Atomique (CEA) of France and Japan Nuclear Cycle Development Institute (JNC) (Chang, et al., 2005). This type of advanced nuclear reactor is nowadays conceived as one of the most promising options in the mid-long term beyond 2020 and this project would cover all the experimental stages regarding equipment for the S-CO_2 cycle oriented to nuclear applications. The Idaho National Laboratory is also contributing to this project by investigating the material compatibility for the so-called Very High Temperature Reactors (VHTR) (Chang, et al., 2006).

1.8.6 The University of Queensland, Australia

In 2009, the Queensland government founded the Queensland Geothermal Energy Centre of Excellence (QGECE) with an initial investment of 15 M$. Amongst their different initiatives, the development of turbines for supercritical fluids, CO_2 amongst them (Haghshenas Fard, et al., 2010), is worth mentioning. In this case, the application studied consists of an advanced geothermal system based on a CO_2 geo-thermosiphon that extracts heat from rock layers at a depth of 5 km, thus heating up a fluid that is later expanded in the turbine, cooled down and pumped again towards the hot zone in the subsoil.

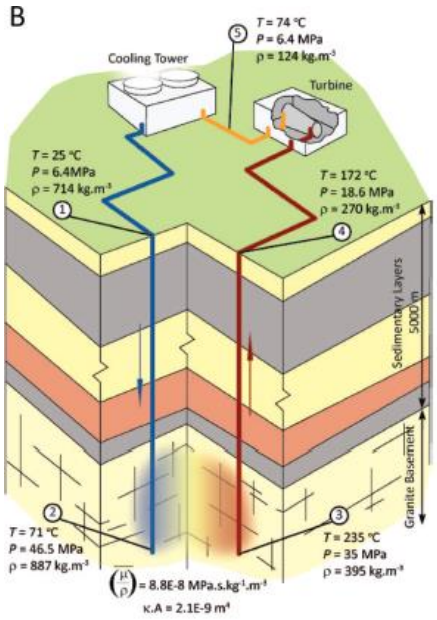

Figure 21. Scheme of a geo-thermosiphon based on S-CO2 cycle, object of study at the QGECE.

1.8.7 International diffusion and investments

In terms of dissemination of research, important achievements must also be highlighted such as the Supercritical CO_2 Power Cycle Symposium, organised every two years by the S-CO_2 community, as well as the creation of the technical committee number 34, Supercritical CO_2 power within the International Gas Turbine Institute (IGTI) of ASME. In addition to that, the ASME-IGTI decided to take on the organisation of the *2nd International Symposium on ORC Power Systems*, which resulted from a recent European initiative driven by Professor Piero Colonna (Technical University of Delft, Netherlands). This event took place last October in Rotterdam.

Nowadays, it seems that this intense investigation of the S-CO2 cycle has provided sufficient knowledge and gathered enough interest to start thinking about addressing its commercial deployment, in order to which important governmental support plans are being put forth in this field. In this sense, the SunShot Initiative promoted by the Department of Energy of the United States has fixed the objective of the reducing the cost of electricity to $0.06/kWh for Concentrating Solar Power (CSP) technologies, for which 21 projects totalling an investment of $54.7 million have been put in place for. Amongst this, $8 million are being devoted to the construction of a S-CO_2 power cycle by the National Renewable Energy Laboratory, NREL (NREL, 2012).

1.8.8 Grupo de Máquinas y Motores Térmicos de la Universidad de Sevilla (GMTS)

In this scope, GMTS is trying to contribute to the supercritical carbon dioxide community, not only with theoretical and numerical studies, but also by participating in experimental projects such as the one developed in consortium with ALTRAN TECHNOLOGIES, S.A. and aimed at designing a wind tunnel with pressurised CO_2 and a S-CO_2 modular design where both simple and recuperative cycle will be possible to analyse as well as radial compressor stages in stand-alone loops.

CHAPTER 2. Considerations about the CFD simulation of supercritical carbon dioxide in turbomachinery

Computational Fluid Dynamics (CFD) can be defined as a mathematical technique to obtain more or less realistic solutions to real problems involving physical-chemical fluid phenomena. The realism of the solution depends not only upon the validity of the models employed, but also on the skills from the user, solely acquired by experience on simulation.

Although experiments must be seen as the most creditable method to get data, CFD is increasingly becoming more widely implemented in industry whether as part of the design processes or for research, as it exhibits advantages with respect to high-quality experimental facilities. The following are worth noting:

- Although investment costs of a high-performance computing facility (both for acquiring CFD software and computing hardware) are not negligible, they can be drastically reduced with respect to test rigs. Moreover, a reduction of more than an order of magnitude must be expected for large systems (for instance, gas turbine engines)
- State-of-the-art numerical codes are versatile and allow for the implementation of multiple physical phenomena (aerodynamic, hydrodynamic, chemical reactions, heat transfer, etc.), the so-called multi-physics, thus recreating the real operating conditions of the experimental facility but in a virtual environment.
- Tests of the system in hazardous operating conditions can be developed without personal or material danger.
- Thanks to the great level of detail with which results can be obtained, CFD allows obtaining data where, perhaps, instrumentation could never have been installed.

Based on these advantages, which are even more important in the scenario of economic crisis that we are currently going through, CFD simulation in ANSYS FLUENT® has been employed as the principal tool to develop this project, since supercritical carbon dioxide experimental facilities are nowadays extremely costly. Nonetheless, the few experimental results available in the field are considered as references for validation.

2.1 Basics of CFD

It is well-acknowledged that commercial CFD software, including ANSYS FLUENT®, employs the finite volume method (Versteeg & Malalasekera, 2007), which forms part of the finite differences techniques and consists of solving the flow conservation equations in the differential control volumes that compose the entire continuum. This is carried out by the solver and it is just a part of the problem since CFD also involves other two additional stages: pre-processing and post-processing which take place and after the solver completes the calculations.

2.1.1 Pre-processing

Pre-processing comprises all the stages previous to the calculation, accordingly defining the necessary inputs, models and methods to use by the solver.

- **Geometry:** creation of the computational domain by using CAD software.
- **Mesh** generation: discretization of the geometry into elementary cells.
- Selection of physical-chemical **models** in accordance with the phenomena of interest: turbulence, radiation, chemical reaction, multiphase flow, etc.
- **Material:** specification of properties.
- Definition of the **boundary conditions**.
- Setting up the **numerical** aspect to be used by the solver in a way that they do not have an effect on the final solution but, on the contrary, only help to improve the computation process. However, this can become crucial for convergence in highly complex problems such as the precise case of the majority of supercritical carbon dioxide simulations.

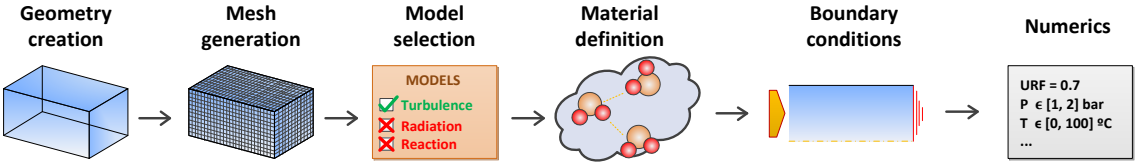

Figure 22. Stages in pre-processing.

2.1.2 The solver

Resolution is obviously the heart of CFD and, as said before, the software employed uses the finite volume method, whose algorithm is based on the following steps: (i) Integration of the conservation equations on each cell, (ii) discretisation of equations and (iii) resolution of the algebraic equation system in an iterative manner (for more details on solver operation (Versteeg & Malalasekera, 2007), (Ferziger & Peric, 2002)).

2.1.3 Post-processing

Once a solution has converged to an acceptable level, all the relevant magnitudes of the flow field are available to be screened in a number of formats: numerical reports, contour and vector plots, 2D graphs, streamlines and even animation when the case is time-dependent. While experimental facilities require high-quality instrumentation that are specific for each magnitude and only acquire data for a particular location, post-processing a CFD solution is so powerful that permits getting any data at any location within the flow domain. Moreover, this is done without perturbing the flow as the instrument would do. On the negative side tough, it must be noted that the fidelity of these outputs is strongly dependent on how the pre-processing is done so that an incorrect pre-processing brings about unreal post-processing outputs.

2.2 Modelling material properties: equations of state

The real behaviour of the fluid through the compressor (see section 1.6) manifests as low compressibility factors (see Figure 15), meaning that ideal gas models do not describe the state of the fluid accurately. In this context, real gas effects with compressibility factors slightly lower than unity can be modelled accurately enough with surrogate ideal gas models (Takagi, et al., 2010), i.e. modifying the molar mass of the gases in order to adjust density to its actual value. Should a stronger real gas behaviour occur, this could be modelled by a cubic Equation Of State (EOS) for certain ranges of pressure and temperature, but still they fail to evaluate the properties of the fluid in the vicinity of the critical point. Modelling the flow in this region usually requires a dedicated EOS (for each fluid).

Several attempts to model carbon dioxide have been made since 1970. A compendium of them is presented in (Span & Wagner, 1996) and summarised in table 2.

Authors	Year	Temperature range (K)	Pressure range (MPa)
Bender	1970	216-1076	0-50
Altunin and Gadetskii	1971	215-1300	0-300
Stein	1972	Non published	Non published
Starling et al.	1972	243-413	0-48
Meyer-Pittroff	1973	200-1273	0-60
Angus et al.	1976	220-1100	0-100
Huang et al.	1985	216-423	0-310
Ely	1986	216-1023	0-300
Ely et al.	1987	216-1023	0-300
Pitzer and Schreiber	1988	230-1030	0-100
Ely et al.	1989	216-1023	0-316
Pitzer and Sterner	1994	220-2000	0-10000

Table 2. Equations of state developed for carbon dioxide. Extracted from (Span & Wagner, 1996).

Since 1996, it is worldwide accepted that the most precise EOS for modelling carbon dioxide is the one developed by Span and Wagner (Span & Wagner, 1996).This equation is based on Helmholtz energy (A) as a function of density (ρ) and temperature (T) in their dimensionless forms: $\phi = A/RT$, $\delta = \rho/\rho_c$ and $\tau = T_c/T$ respectively. As a function of these three variables and its partial derivatives, Span & Wagner presented all the functions and coefficients necessary to calculate the following list of thermodynamic properties: pressure, entropy, enthalpy, internal energy, isochoric and isobaric heat capacity, saturated liquid heat capacity, speed of sound, Joule-Thompson coefficient, fugacity and second and third virial coefficients. Nonetheless, the EOS solves part of the problem, as transport properties need to be modelled as well, especially viscosity and conductivity, both of which participate in the CFD simulation through the momentum and energy equations. There exists consensus also for this and thus complementary information to Span & Wagner's EOS are needed; for instance the works by Fenghour et al. (Fenghour, et al., 1998) and Vesovic et al. (Vesovic, et al., 1990).

This set of models is recommended by the National Institute of Standard and Technology (NIST) in its Standard Reference Data (SRD) (NIST, Nov. 2012) for modelling carbon dioxide properties. This approach is employed by REFPROP®, the reference software for the simulation of fluid properties developed by this institution.

The implementation of this set of equation into ANSYS Fluent® can be complex and tedious and thus some researchers have opted for parametric (or look-up) tables which have been employed mostly in proprietary codes. Amongst this, the works by Colonna's team stands out (Pecnik, et al., 2012). Parametric tables constitute powerful tool given the considerable reduction in elapsed time that can be achieved given that they only involve polynomial interpolations in 2D. Fortunately enough for this work, ANSYS Fluent®, in addition to offering the possibility to use parametric tables by means of User Defined Real Gas Model (UDRGM) functions, also contains a database of 83 pure fluids modelled according to NIST (as included in REFPROP®). One of these fluids available is carbon dioxide which is modelled satisfactorily

in the ranges 200-100 K, 0-100 MPa[3]. This fluid model is activated in ANSYS Fluent by the following text command:

define/user-defined/real-gas-model/nist-real-gas-model/yes/"co2.fld"

NIST Real Gas Models (NRGM) has nonetheless limitations in ANSYS Fluent®, amongst which the impossibility to model two-phase flow must be cited. It must be noted this feature may have a significant impact on the project since condensation is a phenomenon likely to appear in supercritical fluid turbomachinery, as discussed by (Pecnik, et al., 2012).

Even though it might appear partial load operation, condensation is a priori a non-desirable phenomenon in turbomachinery design (as it is the case in an LP steam turbine). In consequence, from a design standpoint, no two-phase flow will need to be simulated as long as the design space is constrained to condensation-free regions.

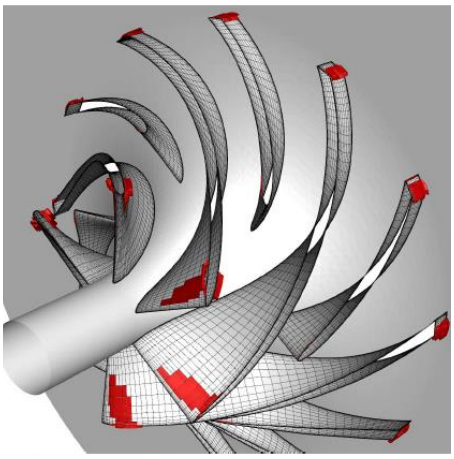

Figure 23. Results of the simulations of the SANDIA S-CO2 radial compressor by (Pecnik, et al., 2012). The points (cells) where vapour-liquid equilibrium conditions are found are shown in red.

In order to explore how the EOS affects the results, section 3.1.4.4 shows the evaluation of different options to model S-CO_2 in a conical diffuser (two-dimensional simulations). Even though small differences were found in the estimates of the representative performance parameters of the diffuser, such as blockage factor and pressure rise coefficient, much larger differences were observed in fluid properties like density and speed of sound, and consequently in Mach number. Therefore, it was concluded that cubic EOS are not appropriate for the purpose of designing turbomachinery where fluid properties play a crucial role. Consequently, the NRGM for carbon dioxide is employed for simulation.

2.3 Modelling physics: turbulent flow

As the majority of industrial applications of interest, conventional turbomachinery problems involve turbulence flows because of the typically high values of Reynolds number, which are still higher for supercritical carbon dioxide due to its high density in comparison with air (Figure 16). Therefore, turbulence is the main physical phenomenon to be concerned about in the CFD simulation of interest for this study. In nature, turbulent flow is non-steady and heterogeneous in the three spatial coordinates; in fact, Wilcox pointed out that "*it is characterized by the presence of a large range of excited length and*

[3] *These are the ranges of validity for the thermal conductivity model employed by (Vesovic, et al., 1990), which is the most restrictive one in this case.*

time scales". A simpler manner to describe turbulent flow is by the *Reynolds decomposition*, whereby each fluid dynamic variable at a certain position and time $\phi(\vec{x},t)$ is decomposed in a mean value $\bar{\phi}(\vec{x},t)$ and a fluctuating term $\phi'(\vec{x},t)$.

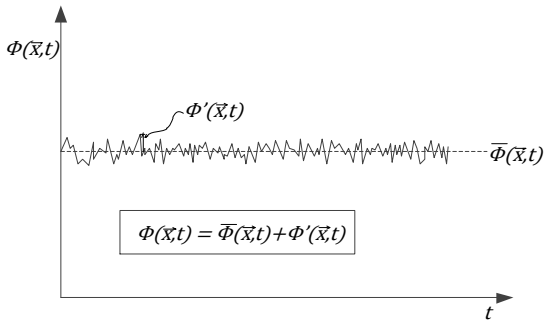

Figure 24.Illustration of a typical flow variable distribution in turbulent flow.

In the heterogeneous and unsteady nature of turbulent flows, there coexist eddies of different scales that interact between them and also with the mean flow. The largest eddies have characteristic length and velocity in the same order of magnitude of the problem itself, let them be l_0 and v_0 respectively, and they are dominated by inertia. Therefore the characteristic time at this scale is $\tau_0 = l_0/v_0$. Kolmogorov's Theory (Pope, 2000) postulates that:

- Large eddy velocities are in the order of magnitude of the turbulent intensity:

$$v_0 \propto v' = (2k/3)^{1/2} \qquad \text{[Equation 2.1]}$$

- Large eddies dissipate their energy along their characteristic time, for which the dissipation rate is:

$$\varepsilon \propto \frac{v_0^2/2}{\tau_0} \qquad \text{[Equation 2.2]}$$

Therefore the large eddy length scale, termed as the *integral scale*, is derived as:

$$l_0 \propto \frac{k^{3/2}}{\varepsilon} \qquad \text{[Equation 2.3]}$$

The Largest eddies interact with the mean flow, where the energy is produced and transferred to successively smaller scales until the energy is delivered to the smallest turbulence scales ~ 0.1-0.01 mm (*Kolmogorov scale*) (Versteeg & Malalasekera, 2007). Kolmogorov scales are dominated by viscosity, and consequently energy is finally transformed into thermal energy due to the action of viscous friction. Accordingly, kinetic energy flows from the energy containing to the dissipation range, passing through an intermediate range (*Taylor scale*) where inertial forces are predominant. In this energy flow; called *energy scale (*Figure 25*)*, there must exist a balance so that the energy extracted by large eddies from the mean flow is dissipated in thermal form by the smallest ones.

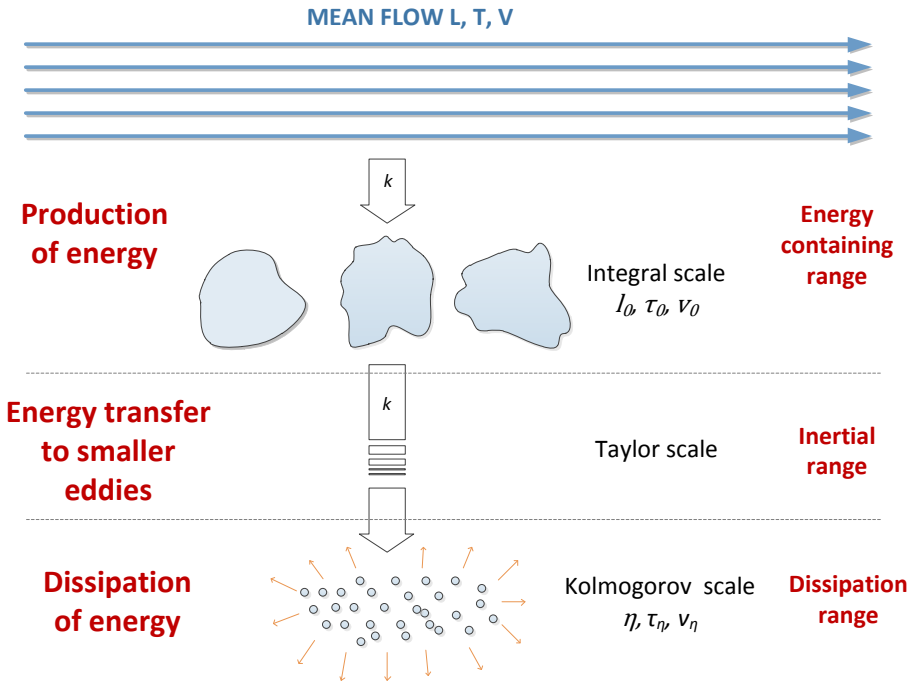

Figure 25. Energy cascade energy established in turbulent flows.

Evaluating the Kolmogorov scale for a certain problem can be done by assuming that Reynolds number is approximately unity, since viscosity is dominant in this region. Kolmogorov's velocity scale can be written as $v_\eta = \nu/\eta$, which together with the definition of dissipation rate, $\varepsilon_\eta = v_\eta^2/\tau_\eta$, and time scale, $\tau_\eta = \eta/v_\eta$, allow expressing the characteristic magnitudes for the Kolmogorov scale as functions of the fluid properties ($\nu = \mu/\rho$) and the nature of the problem (ε) (Tennekes & Lumley, 1972).

$$\eta = (\nu^3/\varepsilon)^{1/4}$$
$$v_\eta = (\varepsilon\nu)^{1/4} \qquad \text{[Equation 2.4]}$$
$$\tau_\eta = (\nu/\varepsilon)^{1/2}$$

From which ratios between integral and Kolmogorov scales can be deduced in a certain problem.

$$\frac{\eta}{l_0} = Re_L^{-3/4}$$
$$\frac{\tau_\eta}{\tau_0} = Re_L^{-1/2} \qquad \text{[Equation 2.5]}$$
$$\frac{v_\eta}{v_0} = Re_L^{-1/4}$$

The turbulent spectrum scales were also established by Kolmogorov's theory and experimentally verified by several researchers (see figure 6.14 in (Pope, 2000)). The usual distribution of energy with respect to the eddy length scale (λ), expressed by means of the commonly employed wave number $\kappa = 2\pi/\lambda$, is represented in figure 26 (Pope, 2000), where it is possible to observe:

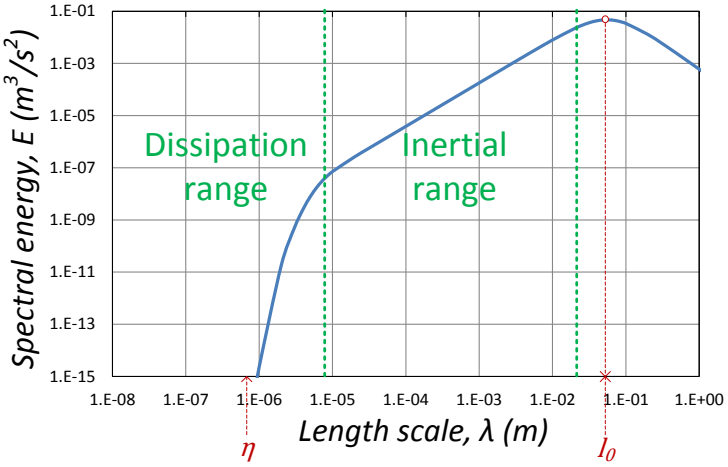

Figure 26. Spectrum distribution of the turbulent energy.

- The majority of the turbulent energy is contained in the largest eddies.
- The integral length scale, l_0, has the highest energy content.
- In the Taylor scales, energy decreases linearly in a double logarithm system with a slope of -5/3 (Kolmogorov's 5/3 Law).
- There exists a length scale that separates inertial from dissipation ranges, below which the energy content decreases sharply.

2.3.1 Turbulent flow treatment in CFD

Considering a temporal interval sufficiently longer than the longest time scale of the problem, it is possible to average the fluid motion equations giving place to the *Reynolds-Averaged Navier-Stokes* (RANS) equations, presented next:

- Mass conservation:

$$\nabla \cdot \vec{U} = 0 \qquad \text{[Equation 2.6]}$$

- Momentum conservation:

$$\frac{\partial \vec{U}}{\partial t} + \nabla \cdot \left(\vec{U}\vec{U}\right) = -\frac{1}{\rho}\overrightarrow{\nabla p} + \nu \Delta \vec{U} - \nabla \cdot \overrightarrow{\overline{v'v'}} + \vec{f}_m \qquad \text{[Equation 2.7]}$$

- Energy conservation:

$$\rho c \left(\frac{\partial T}{\partial t} + \vec{U} \cdot \overrightarrow{\nabla T}\right) = k\Delta T + \phi_{\vec{U}} + \phi_{\overrightarrow{v'}} - \rho c \nabla \cdot \overrightarrow{\overline{v'T'}} + Q \qquad \text{[Equation 2.8]}$$

This results in a system with 5 equations and 8 unknowns: velocities ($\vec{U}$), pressure (p) and temperature (T), the Reynolds stress tensor ($\tau_{ij} = \overrightarrow{\overline{v'v'}}$), the turbulent heat transport ($\overrightarrow{\overline{v'T'}}$) and the viscous dissipation due to turbulence ($\phi_{\overrightarrow{v'}}$) (Zamora Parra, 2008). The concept of *turbulent viscosity* (μ_t) introduced by Boussinesq (Boussinesq, 1877) allows to close the problem. Turbulent viscosity relates the stresses in the flow with mean flow velocity gradients and is dependent upon the nature of the problem:

$$\tau_{ij} = \mu_t \left(\frac{\partial U_i}{\partial x_j} + \frac{\partial U_j}{\partial x_i} \right)$$ [Equation 2.9]

Although μ_t is a function of the mean flow velocities, the problem is not still closed. For that, a turbulence model needs to be implemented. In decreasing order of complexity, turbulence models can be classified into:

- **Direct Numerical Simulation (DNS)** is the absence of turbulence model, meaning that Navier-Stokes equations are directly solved unsteadily and capturing the whole spectrum of scales. Very fine meshes are thus required in order to capture the flow phenomena in the Kolmogorov scale, which therefore poses a maximum cell size limit. The computational effort required by DNS is within the capacity of only some computers all over the world.
- **Large-Eddy Simulation (LES)** does include turbulence models but only for the smaller scales while the interaction of larger eddies is simulated. This is in consequence inherently unsteady and three-dimensional. LES was developed by Smagorinsky in 1963 (Smagorinsky, 1963) for studying the dynamics of general circulation in the atmosphere. In 1970, Deardorff (Deardorff, 1970) applied this proposal to Pouseuille flow at high Reynolds number, where wall-affected flows were analysed by advanced turbulence models. After that, LES was profusely extended to other industrial applications because of the good agreement to reality and the lower computational cost in comparison with DNS. LES philosophy is based on a low-pass filter that is applied to fluid motion equation so that Sub-Grid Scale (SGS) models are applied for scales smaller than the cell sizes, whereas above that the equations are solved directly. Although lower than DNS, the computational cost of performing LES is important, even more for S-CO_2 as it is characterised by a Reynolds number higher than air. Based on this, it is clear that LES is out of the scope of this project.
- **RANS equations**, as explained before, result from time averaging the Navier-Stokes equations. Thus, steady simulations can be performed easily and simplifications such as symmetric or periodic conditions can be applied. The system composed by equations 2.6-2.8 has 2 degrees of freedom and therefore RANS models require the implementation of additional turbulence models with one (Spallart-Allmaras (Spalart & Allmaras, 1992)), two ($k-\varepsilon$ (Launder & Spalding, 1972) and $k-\omega$ (Wilcox, 1994)) or even more equations. Theoretically, if DNS and LES results were time-averaged along long enough intervals of time they would coincide with results of the RANS model.

2.3.2 Turbulence model applied to S-CO_2 turbomachinery

Taking into account that no doubts exist regarding the EOS, the choice of a suitable turbulence model has the largest impact on the results, apart from numerical aspects such as discretisation, interpolation schemes and other solver features. Given the lack of experimental results in the field (only some results of the centrifugal compressor at SANDIA NL publically available (Wright, et al., September 2010)), an examination of the various turbulence models available in ANSYS Fluent® has been performed in order to help make the choice. It is also true that other numerical simulations have been carried out in the field of supercritical carbon dioxide turbomachinery ((Pecnik, et al., 2012), (Rinaldi, et al., 2013) and (Munroe, et al., 2009)) and heat exchangers (Van Abel, et al., 2011), which offer a sort of state-of-the-art in the field. These works confirm that two-equation models are the most common choice since, as stated by Wilcox "*They are, in fact, the simplest complete model of turbulence*" (Wilcox, 1994).

Within the usual constraints in computational capacity, whether use $k-\varepsilon$ or $k-\omega$ models is the most frequent question to answer. The $k-\omega$ model was initially proposed by Wilcox (Wilcox, 1988), but it was not till its Shear-Stress-Transport (SST) version was created by Menter (Menter, 1994), that its use was profusely extended across the industrial world (Menter, et al., 2003). Older than $k-\omega$, $k-\varepsilon$ models, originally introduced by Launder & Spalding (Launder & Spalding, 1972) are the alternative. These are especially suitable for fully turbulent (high Reynolds number) non-separated flows. However, its main

shortcoming as well-known by the CFD community is simulating flows under adverse pressure gradients and/or high streamline curvature. $k-\omega$ models, especially the SST form, improve the near wall treatment and also low Reynolds number flows. The SST model is the most widespread option for industrial applications in turbomachinery, the works (Pecnik, et al., 2012) and (Rinaldi, et al., 2013) being specific examples in the field of supercritical carbon dioxide turbomachinery (see meshes in Figure 28 and 8). The main drawback of this model is the requirement of mesh refinement near the wall, which can produce unaffordable meshes when the computational effort is limited. Some examples of using $k-\varepsilon$ models to simulate S-CO_2 turbomachinery are nevertheless found (Munroe, et al., 2009) (see mesh of Figure 27), with the caution of using proper wall functions for more precision in the near wall treatment.

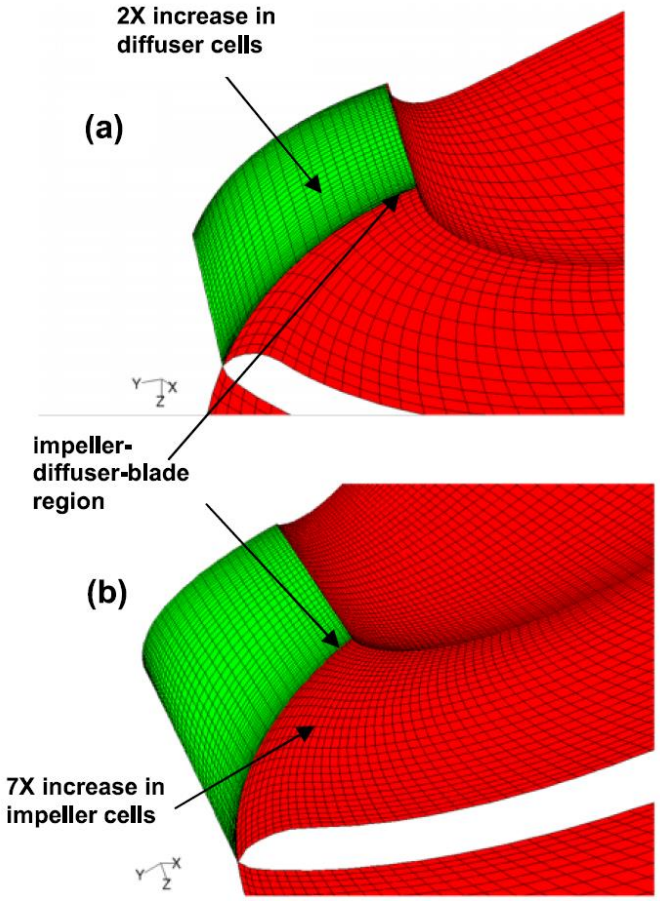

Figure 27. Computational mesh employed in (Munroe, et al., 2009), where a $k-\varepsilon$ model with enhanced wall functions is employed and, accordingly, no extremely near wall refinement is observed in the mesh.

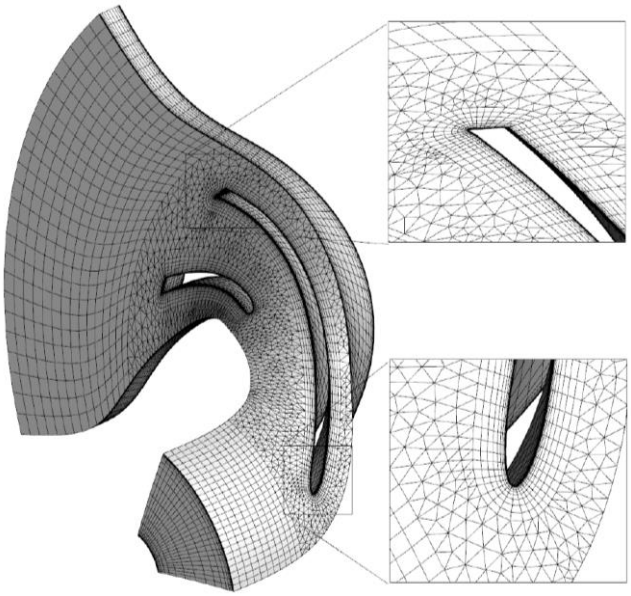

Figure 28. Computational mesh employed in (Pecnik, et al., 2012), where a $k-\omega$ model is employed. As observed, a stronger mesh refinement is performed near the wall.

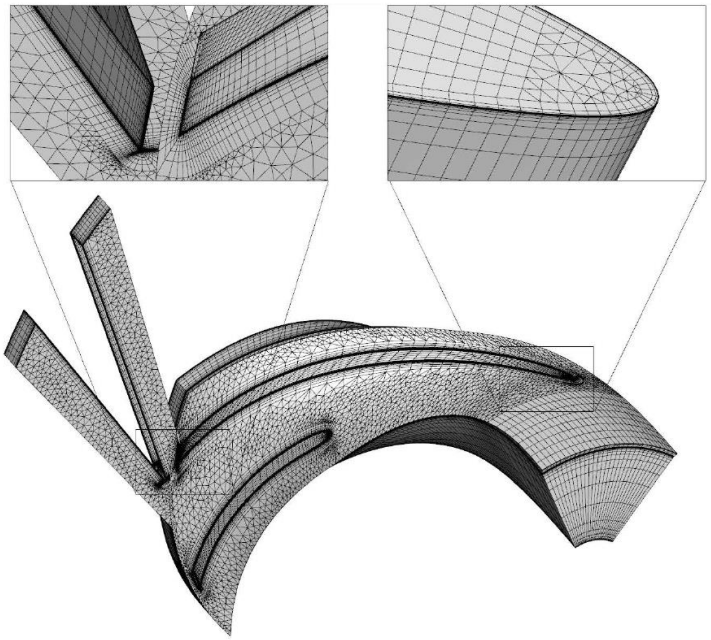

Figure 29. Computational mesh employed in (Rinaldi, et al., 2013), where a $k-\omega$ model is employed. As observed, a stronger mesh refinement is performed near the wall.

To sum up, and taking into account the industrial trends in CFD, the $k-\omega$ SST model is deemed the most appropriate option, as long as sufficient refinement is implemented near the wall. On the contrary, if coarser meshes need to be employed due to limitations of any type, the $k-\varepsilon$ model with wall functions would be preferred. In particular, the standard wall function is used, establishing:

$$U^* = \frac{1}{\kappa}\ln(Ey^*) \qquad \text{[Equation 2.10]}$$

Where U^* and y^* are the dimensionless velocity and length (ANSYS, 2011), E an empirical constant equal 9.793 and κ the Von Kármán constant (=0.4187).

2.4 Additional numerical considerations for S-CO_2 simulation

There are two features that make supercritical CO_2 simulations less stable than their equivalent for air: on one side, the pronounced variations that properties exhibit near the critical point and on other the risk of condensation if saturation conditions are met. These two facts require taking into account the following recommendations in order not to fail to converge:

- It is observed that using the *Coupled* algorithm for pressure-velocity coupling provides the only way to achieve convergence. Nevertheless, the SIMPLE algorithm (Semi-Implicit Method for Pressure-Linked Equations) (Patankar & Spalding, 1972) is set by default in ANSYS Fluent®. In this method, from a guessed pressure field, the velocity field is calculated from the momentum equation and then continuity is employed to obtain a pressure correction which modifies the pressure field in next iteration. As opposed to this, the Coupled algorithm solves the system of equations formed by mass and momentum conservation (Figure 30). Therefore, pressures and velocities satisfy conservation laws in every single cell for its given boundaries. This algorithm makes the calculation much more robust even though at the cost of taking longer to solve each iteration step.

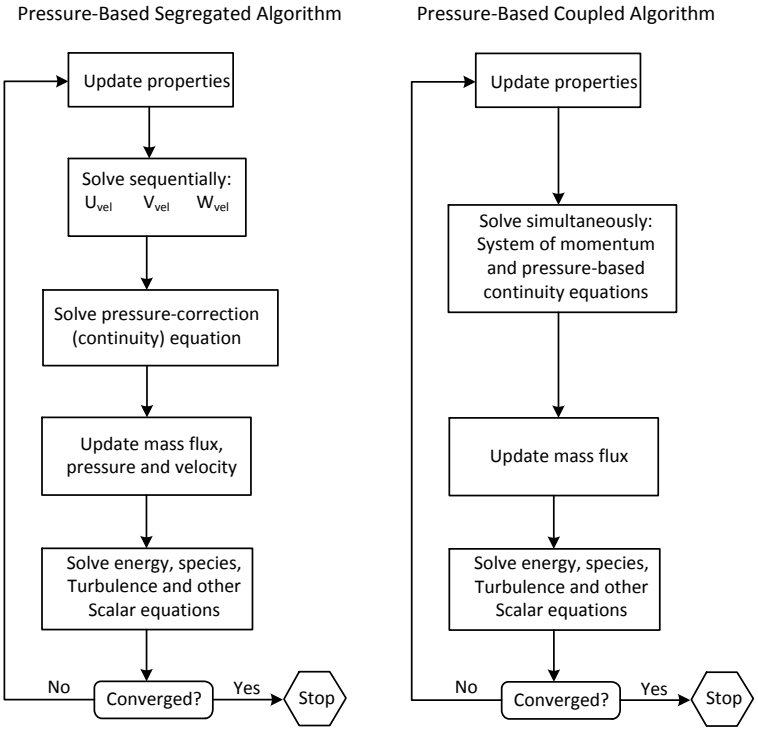

Figure 30. segregated vs. Coupled algorithms iteration loops (ANSYS, 2011).

- Adopting *first order upwind* (fou) interpolation schemes (Versteeg & Malalasekera, 2007) makes convergence faster. It might reduce the accuracy of the results though, since only one cell upstream is considered to affect every cell. However, the validation yields satisfactory enough results.
- It is crucial to set up lower *limits* of pressure and temperature sufficiently far from the critical values. This avoids entering the two-phase region while solving, what would immediately interrupt the calculation. From this point of view, upper limits are not necessary though they definitely help.
- Solving the *equations* progressively also gives stability to the calculation. When every case is run for the first time (before adjustments), the equations are solved one by one. Firstly

only flow equations (mass and momentum) are solved until low enough mass imbalance[4] is achieved. Then turbulence is activated and finally, when the residuals are considerably low ($\sim 10^{-3} - 10^{-4}$ depending on the case), the energy equation is incorporated.

2.5 Uncertainties associated to CFD simulation with S-CO_2

In addition to the uncertainties due to modelling (δ_M), whether be fluid nature or physics, numerical aspects also bring about errors to the solution (δ_N). In general, the error of a numerical solution with respect to the real value can be decomposed as (Stern, et al., 2006):

$$\delta = \delta_M + \delta_N = \delta_M + \delta_I + \delta_G + \delta_T + \delta_P \qquad \text{[Equation 2.11]}$$

The deviation between the numerical result and the true experimental value is the summation of: uncertainties due to modelling (δ_M), the number of iterations (δ_I), the spatial discretisation, i.e. the grid (δ_G), the temporal discretisation (δ_T), and the input parameters (δ_P). Uncertainty due to the time step (δ_T) is discarded in this project as simulations are stationary. On the other hand, the uncertainties owed to the input parameters (δ_P) are null for the majority of cases, since there are no experimental results to compare with. Consequently, once a suitable modelling is chosen for the physical process of interest, minimising errors means reducing errors due to iterations δ_I and mesh δ_G. While the later is analysed in detail by the Grid Convergence Index (GCI) methodology, the former is negligible since the convergence criteria is set to residuals values below 10^{-6} and therefore, the variation of the solution between iterations is much lower than the variations due to mesh size, as can be deduced from the proper definition of residual of a certain transport property ϕ.

The linearised form of any conservation equation is written for a cell i (Versteeg & Malalasekera, 2007) as follows:

$$a_i \phi_i = \sum_{ni} a_{ni} \phi_{ni} + b_i \qquad \text{[Equation 2.12]}$$

Where a_i is a characteristic coefficient of the cell of study, a_{ni} is characteristic of the neighbouring cells and b_i is a source term. In accordance with that, the residual of the magnitude ϕ is defined as the summation of imbalances on each cell through the entire computational domain (ANSYS, 2011)].

$$R_\phi = \frac{\sum_i |\sum_{ni} a_{ni} \phi_{ni} + b_i|}{\sum_i |a_i \phi_i|} \qquad \text{[Equation 2.13]}$$

Therefore, residuals lower than 10^{-6} implies very soft variations of the solution between successive iterations, verifying $\delta_I < 10^{-6}$ for all of the variable of interest (density, pressure, velocity components and turbulent variables k, ε and ω).

To sum up, amongst all the sources of uncertainties that need to be mitigated, it is the one due to the characteristic mesh size (for which the Grid Convergence Index (GCI) analysis (Celik, et al., 2008) is implemented) which needs to be accounted for only. Based on the Richardson Extrapolation (RE), the Grid Convergence Index method estimates an extrapolated value of the variable, ϕ_{ext}, corresponding to an infinitely fine mesh and finally calculates the deviations from the solution obtained. The methodology require simulating the same case in three different meshes with refinement ratio[5] ≥ 1.3, to which the RE is applied. A representative size is defined for two and three dimensional meshes by $h = \sqrt{S/N}$ and $h =$

[4] *Mass imbalance is defined as the difference in mass flow rate between the inlet and outlet sections.*

[5] *Refinement ratio for two meshes, always higher than unity, is defined as the ratio between the representative sizes of coarse to fine mesh.*

$\sqrt[3]{V/N}$ respectively, where S and V are the total extensions of the 2D and 3D domains and N the number of cells in the mesh.

Let ϕ_1 , ϕ_2 and ϕ_3 be the values of a key variable ϕ for the numerical analysis carried out in the three meshes, ranked from coarsest to finest. The absolute and relative errors can be defined as:

$$\varepsilon_{21} = \phi_2 - \phi_1 \; ; \; \varepsilon_{32} = \phi_3 - \phi_{2;} \qquad \text{[Equation 2.14]}$$

$$e_a^{21} = |(\phi_1 - \phi_2)/\phi_1| \; ; \; e_a^{32} = |(\phi_1 - \phi_2)/\phi_1| \qquad \text{[Equation 2.15]}$$

The apparent order of accuracy p is calculated with:

$$p = \frac{1}{ln(r_{21})} |ln|\varepsilon_{32}/\varepsilon_{21}| + q(p)| \qquad \text{[Equation 2.16]}$$

$$q(p) = ln\left(\left(r_{21}^p - s\right)/\left(r_{32}^p - s\right)\right) \qquad \text{[Equation 2.17]}$$

$$s = 1 \cdot sign(\varepsilon_{32}/\varepsilon_{21}) \qquad \text{[Equation 2.18]}$$

From these parameters, it is possible to estimate the value of the key variable ϕ when the representative size of the mesh tends to zero ($h \to 0$). This is done with [equation 2.19].

$$\phi_{ext}^{21} = \left(r_{21}^p \phi_1 - \phi_2\right)/\left(r_{21}^p - 1\right) \; ; \; \phi_{ext}^{32} = \left(r_{32}^p \phi_2 - \phi_3\right)/\left(r_{32}^p - 1\right) \qquad \text{[Equation 2.19]}$$

And extrapolated relative errors can also be defined:

$$e_{ext}^{21} = |(\phi_{ext}^{12} - \phi_1)/\phi_{ext}^{12}| \; ; \; e_{ext}^{32} = |(\phi_{ext}^{23} - \phi_2)/\phi_{ext}^{23}| \qquad \text{[Equation 2.20]}$$

Finally, the grid convergence index is calculated as:

$$GCI_{21} = F_S \cdot e_a^{21}/\left(r_{21}^p - 1\right) \; ; \; GCI_{32} = F_S \cdot e_a^{32}/\left(r_{32}^p - 1\right) \qquad \text{[Equation 2.21]}$$

Where F_S is a safety factor with the typical value of 1.25. The grid convergence index provides a confidence interval for the extrapolated solution. Hence, for a given parameter or function ϕ of interest, it is ensured that the converged solution lies within the interval $[\phi(1 - GCI), \phi(1 + GCI)]$.

This result must be distinguished from local analysis. In this regard Celik pointed out in (Celik, et al., 2008) that local values "*may not exhibit a smooth monotonic dependence on grid resolution, and in a time-dependent calculation*". Nevertheless, and also stated by the same author, this method "*is currently the most reliable method available for the prediction of numerical uncertainty*", it is in fact the only recommendation for accepted by NASA (Slater, 2008). In conclusion, although less reliable, this is the only widely accepted methodology within the CFD community for evaluating the local effects of mesh size (when an alternative method is used, it is usually required to provide report confirming that it can be accepted). Thus, instead of averaged extrapolated values, it is possible to calculate extrapolated profiles of a certain variable in a section, e.g. velocities. In these cases, an apparent order is calculated locally and then an averaged order ($\bar{p}$) is employed to calculate the extrapolated local values with [Equation 2.19], where the flow variable ϕ also takes the local value. Section 5.2.1.1 shows the results of applying GCI to velocity profiles locally.

2.6 Summary and conclusions

After an overview of the main steps in the CFD workflow, emphasis has been made on particular aspects related to S-CO_2 turbomachinery simulation: (i) the equation of state of the fluid and (ii) a proper physical modelling of the problem, i.e. turbulence.

With regard to the EOS, it is widely agreed that the best choice is the Span & Wagner equation, specifically developed for CO_2. Other options based on cubic EOS were evaluated in simple diffuser geometries but without success. As for the EOS, there is also consensus in the modelling of transport properties, Fenghour's model being suitable for viscosity and Vesovic's for conductivity. This system of models is used by the National Institute of Standard and Technology (NIST) to model CO_2 and accordingly it is included on REFPROP®. Interestingly enough, there is a link between ANSYS Fluent® and REFPROP® that allows loading NIST Real Gas Models (NRGM) for certain pure substances, CO_2 amongst them. The corresponding NRGM is employed for S-CO_2 simulations in this work, both for 2D diffuser (chapter 3) and 3D compressor (chapter 5). This function has the limitation of not being able to simulate two-phase flow. In consequence, some off-design simulations with likely appearance of condensation may not be performed (Pecnik, et al., 2012).

The main remarks of Kolmogorov's theory and earlier developments are presented after the EOS discussion in order to comprehend turbulence modelling in CFD. Although turbulence is intrinsically non-steady and heterogeneous, high fidelity turbulence models such as DNS and LES are discarded because of the computational cost implied, and two-equation RANS models are used instead. More specifically, $k-\varepsilon$ Realizable and $k-\omega$ SST are the models of choice, the latter being more precise than the former at simulating flows with adverse pressure gradients. On the contrary, the $k-\omega$ SST model requires heavier meshes, as near-wall refinement needs to be implemented, whereas the $k-\varepsilon$ Realizable does not given that it applies wall functions to model turbulence scales near the wall.

Finally, a discussion is done regarding numerical uncertainties in CFD, deducing that the only source of errors in the cases herein addressed is mesh refinement. Then, the Grid Convergence index (GCI) methodology is adopted in subsequent chapters. This methodology is based on the results obtained in 3 meshes of different characteristic cell size and to the extrapolation of the solution for the infinitely fine mesh, whose mean cell size tends to zero.

CHAPTER 3. Analysis of S-CO_2 flows in elementary diffusion processes

Turbocompressors are sophisticated machines that increase the total pressure of a certain inlet flow of gas by converting mechanical work at the rotor shaft into total enthalpy of the fluid at the exit. This energy conversion is a two-step process taking place in the rotor and stator rows of the machine. Thus, the rotor converts shaft work into kinetic energy (expressed in terms of absolute velocity) and enthalpy (i.e. pressure), delivering a flow at high speed to the static blade row where the gas decelerates and kinetic energy is converted into enthalpy giving place to a flow at high pressure and low/moderate velocity. The transformation of kinetic energy into pressure is called diffusion, after which the static blade row of a radial compressor is called the diffuser, and in subsonic adiabatic flow it requires increasing cross sectional area ducts.

Based on this rationale, the intersection between a stream surface in an axial compressor and the channels enclosed within two adjacent blades presents a two-dimensional divergent cross sectional area pitch-wise. However, this geometry must not be mistaken for the reduction in channel height span-wise which accommodates to the increasing density of the gas at constant mass flow rate. In an axial compressor, the higher the outlet to inlet area ratio, the higher the static pressure rise. This is all presented in the figure below (Bölcs & Tsamourtzis, 1991).

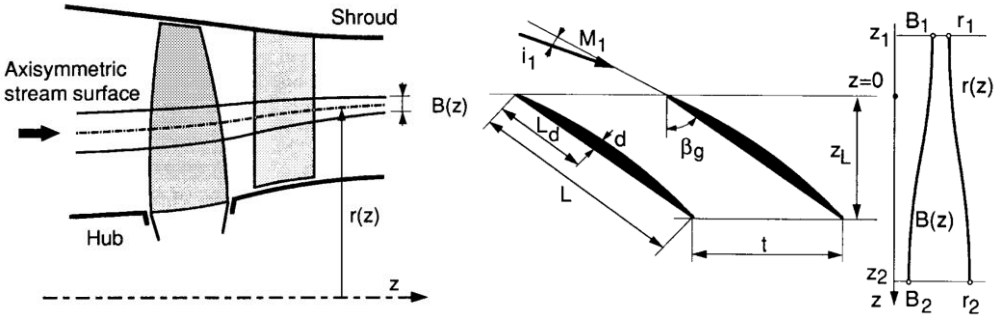

Figure 31. Details of turbomachinery geometry (Bölcs & Tsamourtzis, 1991).

The corresponding hub (bottom) and shroud (top) surfaces must increase their cross section area, both for rotor and stator, especially in axial machines, where the increment of fluid total pressure through the rotor is much lower than in radial machines. In the latters, centrifugal force allows for achieving higher rotor pressure ratio, bringing about marked density changes and so determining smaller outlet section areas. Nevertheless, independently on machine type (axial or radial) and blade row (rotor or stator), the relative flow to the blade is always diffused, accordingly decreasing relative velocity form inlet to outlet.

The afore discussed fundamentals apply both to axial and radial compressors. Nevertheless, in the latter, shaft work is converted into enthalpy (i.e. pressure) by virtue of the so called centrifugal forces. In effect, one feature that sets radial machines apart from axial ones is the noteworthy variation of blade speed. This velocity, which is assumed constant in virtually all the stages in an axial turbomachinery (in particular those stages with a hub-to-tip ratio higher than 0.7-0.75), almost triples from the inlet to the outlet of a centrifugal compressor impeller, thus allowing for a much larger energy transfer from the shaft to the fluid. This differential feature will eventually lead to a much higher stage pressure ratio.

Nevertheless, prior to addressing the whole centrifugal compressor problem, it is deemed convenient to begin with an analysis of elementary diffusers, since diffusion plays a crucial role in the turbomachinery. This is further confirmed by Japikse and Baines (Japikse & Baines, 1998) who pointed out that "*a change of 0.01 in pressure recovery can be equivalent to a few tenths of a point of stage efficiency*".

Conical diffusers involve simpler physical phenomena in comparison with the complex fluid dynamics of a full compression stage, what can help to comprehend how supercritical carbon dioxide flows behave in diffusion processes, which differences exhibit with respect to a conventional fluid (for instance air) and, in the light of these results, how the standard design rules can be customised in order to get highly efficient machines with the new working fluid. In this regard, an extensive study on conical diffusers is carried out in this chapter with the endeavour of estimating the impact of the main dimensionless parameters of influence in accordance with the available literature.

3.1 Definition and scope of the analysis

The analysis of diffusers was initiated by Gibson in 1910 (Gibson, 1910), who basically analysed the influence of some geometrical parameters on the performance of conical diffusers working with water for hydraulic applications. This work gave place to an intense activity in this topic between the 50's and 80's most of which considered air as the working fluid. Unexpectedly, some of the parameters that had been disregarded previously proved to have a noteworthy effect on system performance whereas others which were presumed to be dominant showed up to hardly have any influence, for instance Mach number as demonstrated in (Dolan & Runstadler, 1973). As a consequence of this research, a vast amount of information was generated, mainly in the form of performance maps that resulted very useful for turbomachinery design (Japikse, 1996) and contributed significantly to the development of gas turbines and aero engines.

In spite of a huge database of air diffuser performance being currently available, there is very little information of such devices operating on other less common fluids. This raises the following questions: is this database applicable to supercritical carbon dioxide diffusers? How large is the impact of the real gas behaviour on the performance of such diffuser? These are the two main questions that this chapter aims to answer. For this purpose, the parameters of influence are firstly presented in order to define the boundaries of the study. As a second step, the numerical tool on which the work bases is presented and validated against the available information for air diffusers. Finally, the results are presented for the different parameters considered and a number of conclusions about how to design efficient turbomachinery for S-CO_2 are drawn.

3.1.1 Diffuser operation

In spite of its usually simple geometry, the operation of a diffuser can become very complex due to the irreversibilities caused by diverging walls. As opposed to nozzles, where converging walls tend to practically remove the outflow boundary layer, in diffusers even isentropic flows at the inlet can become very distorted and unsteady at the outlet depending on geometry and inlet flow conditions. Several works done during the 50's and 60's focused on studying different operation regimes of diffusers and on the impact of flow features on performance: for instance inlet turbulence (Fox & Kline, 1962) (Moore & Kline, 1958) and aerodynamic blockage (Runstadler & Dolan, 1973) (Reneau, et al., 1967).

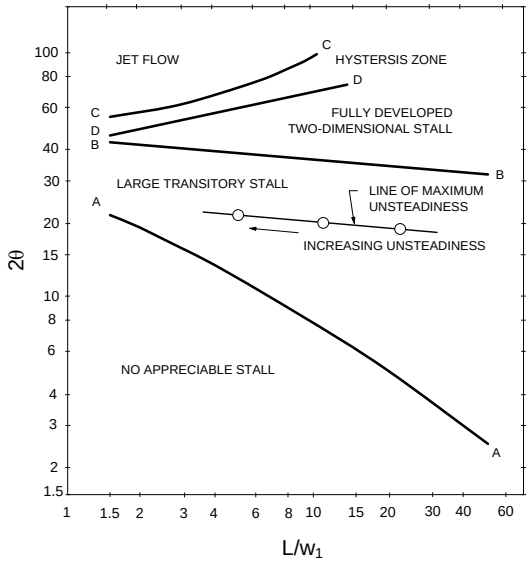

Figure 32. Operating regions of a straight line diffuser[6]. *(Smith, 1975)*

Even though figure 4 refers to channel diffusers, it is useful to illustrate all the possible regimes in which any diffuser can operate; this includes conical ones. The desired performance is *no appreciable stall* and it is achieved for moderate divergence angles (2θ) and non-dimensional lengths (L/w_1). On the contrary, *jet flow* appears when divergence is very high. In between these, two different stall phenomena are found. First, when divergence angle is increased starting from no stall operation, there is a certain and reproducible point where transient separation takes place (line AA). Bubbles are created locally on the diffuser walls, generating large and appreciable eddies which make the flow transient. For a given non-dimensional length, there is a certain and also reproducible divergence angle for which maximum transitory effects are noticed. If the divergence angle is further increased, a second transition to a new steady operation is observed (line BB) which is characterised by a two-dimensional steady flow completely detached from the wall. A visible stream tube travels through the diffuser with a nearly constant cross sectional area while a stagnant fluid fills the rest of the diffuser.

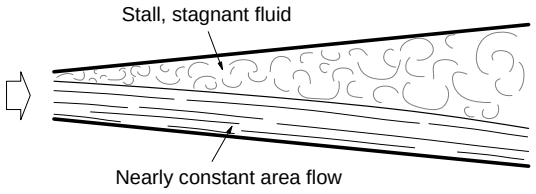

Figure 33. Diffuser operating in two-dimensional stall region.

When increasing divergence angle, the separation between two-dimensional stall and jet flow is represented by line CC in figure 32figure 4. However, if divergence angle is decreased from jet flow operation, transition to two-dimensional stall doesn't happen in the same line, but for a smaller angle in line DD, giving place to a hysteresis phenomenon.

[6] *The geometrical parameters participating in this figure are: the divergence angle (2θ) and the length to inlet width ratio (L/w_1). Linked to these two parameters, it could be used the area ratio, which is defined for straight line diffusers by* $AR = 1 + (L/w_1)\tan\theta$.

3.1.2 Parameters of influence in conical diffuser performance

Dimensional analyses provide useful information about which and how many parameters have an effect on the behaviour of a certain physical problem/system, the extent of which is then revealed by experiments. For diffusers, this has regularly been done over the years by a number of researchers. A complete review of this is presented in (Japikse & Baines, 1998), from where the following list of parameters is derived:

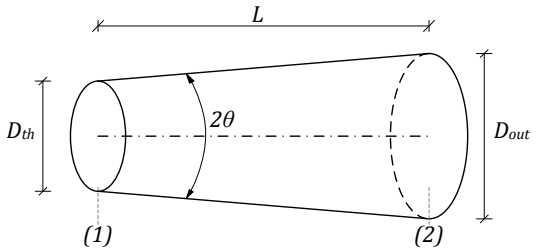

Figure 34. Diffuser geometry.

- *Non-dimensional length*, which is defined as the ratio from the length to the throat diameter of a conical diffuser.
- *Divergence angle*, i.e. 2θ, or equivalently area ratio between outlet and inlet. These geometric parameters are related as shown by [Equation 3.1] for conical diffusers.

$$AR = [1 + 2(L/D_{th}) \tan\theta]^2 \qquad \text{[Equation 3.1]}$$

- *Aerodynamic blockage* at the throat, defined as the fraction of cross sectional area that is occupied by the boundary layer. It can also be related with the ratio between actual and ideal mass flow rates and is directly linked to the boundary layer displacement thickness.

$$B_{th} = 1 - \frac{A_{eff}}{A} = 1 - \frac{\dot{m}}{\dot{m}_{id}} = 4\frac{\delta^*}{D_{th}}\left(1 - \frac{\delta^*}{D_{th}}\right) \qquad \text{[Equation 3.2]}$$

  Amongst all fluid dynamic parameters subsequently described, aerodynamic blockage is the most relevant one. Boundary layer displacement thickness was already investigated in the 60's by Stratford and Tubbs (Stratford & Tubbs, 1965), who found that it constrains the maximum pressure recovery in a diffuser (first with theoretical models and afterwards by comparison against experiments). Nearly a decade later, Dolan and Runstadler (Dolan & Runstadler, 1973) completed a detailed study on the effect of blockage and others aerodynamic parameters on diffuser performance. This is considered a seminal work in the topic and will be used here for validation purposes.

- Both *Mach* and *Reynolds* numbers are commonly taken into account in any fluid dynamic problem. However, although in the early stages of diffuser research they were considered critical, it was later confirmed experimentally that they have a rather soft impacts. As a matter of fact, virtually no influence of Reynolds number was observed beyond 10^5 in (Dolan & Runstadler, 1973), confirming the existence of a critical value of *Re* around that value, beyond which Reynolds number does not affect.
- Apart from that blockage, other features of the inlet velocity distribution have been studied in literature: *swirl* and *distortion*. Swirl refers to the angular velocity and is usually proportional to the radius. It modifies the development of both core and boundary layer flows through the diffuser, largely improving its performance as shown in figure 35. On the other hand, distortion affects to the axial component and it manifests as a momentum

defect/excess at certain locations of the diffuser throat. Three main studies were done in this field: (Srinivasan & Lakshmi Narasimhan, 1978) , (Sajben, et al., 1974) and (Shimizu, et al., 1982), where performance improvements were sometimes observed, even though not as noticeable as for swirl.

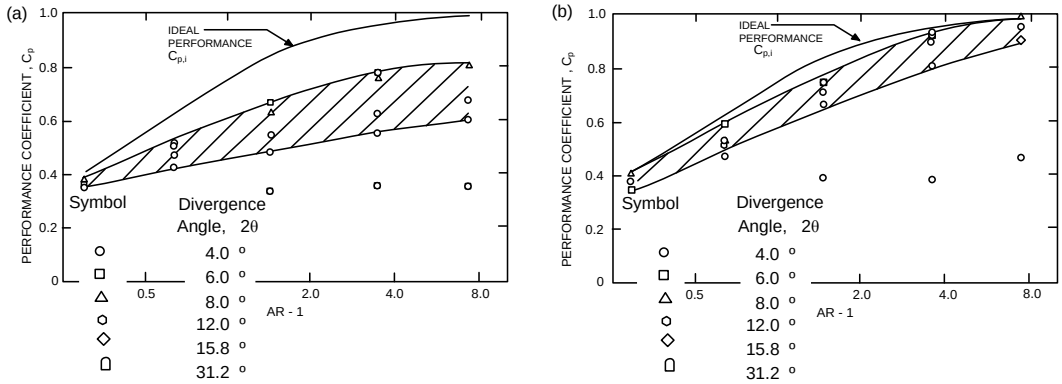

Figure 35. Comparison of conical diffuser performance without (a) and with (b) swirl effect found by (Mc Donald, et al., 1971)

- The influence of turbulence in conical diffuser performance can also be analysed by comparing the works available in literature even though it needs to be extrapolated from the results for other geometries. In this regard, the systematic study done by Hoffman for channel diffusers (Hoffman, 1981) is worth mentioning, figure 36.

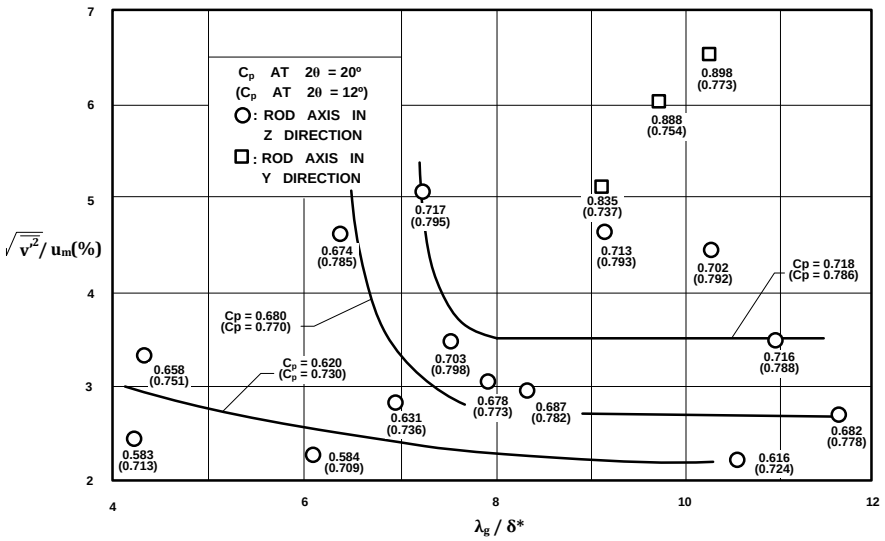

Figure 36. Turbulence intensity and turbulence length scale effects in channel diffusers (Hoffman, 1981)

As noticed, there is a critical value of the non-dimensional turbulence length scale beyond which this parameter has no effect (~8 in figure 36). And similarly, this figure suggests the existence of a critical turbulence intensity after which its effects disappear. Additionally, Hoffman pointed out that in addition to intensity and length scale having an impact on diffuser performance, the turbulence structure, i.e. whether it is isotropic or not, influences it.

- The real behaviour of CO_2 near the critical point suggests that the influence of the *compressibility factor* ($Z = pv/RT$) be studied. It must be highlighted that this is an

additional parameter never considered before because of the ideal behaviour of most working fluids in turbomachinery applications ($Z = 1$). In contrast, the fluid of interest in this works exhibits a very variable compressibility factor depending on the static pressure and temperature across the compressor.

- The parameters shown up to now are the most relevant ones because of the large impact that they have on diffuser performance as well as their variability from one diffuser application to another. Apart from them, some authors studied different aspects related to some specific diffuser applications such as the rotation of the diffuser, oscillatory inflows, etc… This effects that will not be considered in this work.

To sum up, after dimensional analysis, diffuser performance can be expressed as a function of 11 parameters: area ratio (AR), non-dimensional length (L/D_{th}), aerodynamic blockage (B_{th}), Mach (M_{th}) and Reynolds numbers (Re_{th}), dimensionless parameters for swirl (C_{swirl}) and distortion (C_{dist}), turbulence intensity (Tu_{th}), non-dimensional turbulence length scale (l_{th}/δ^*) and a parameter identifying the turbulence structure ($C_{t,est}$), i.e. its anisotropy. The compressibility factor (Z_{th}) is also added.

$$C_p = f\left(AR, L/D_{th}, B_{th}, M_{th}, Re_{th}, C_{swirl}, C_{dist}, Tu_{th}, l_{th}/\delta^*, C_{t,est}, Z_{th}\right) \qquad \text{[Equation 3.3]}$$

Given that the experiments are carried out by numerical simulation in ANSYS FLUENT®, and owing to the limited computational capacity at the disposal of this work, no analyses were done in terms of turbulence structure. In other words, the RANS approach is compulsory and this does not allow this type of analysis which would require *Large Eddy Simulation* (LES). Hence only the influence of the remaining parameters of influence was analysed.

3.1.3 Presentation of results and range of study

Once the key parameters have been exposed, the outputs and the format in which they are presented are described in this section. The most common diffuser performance indicator is the *static pressure rise coefficient* (C_p), defined as the ratio from static pressure rise to inlet dynamic head. This coefficient does not provide complete information about how efficiently the diffuser operates though. In effect, it is possible to achieve a high value of C_p in a rather irreversible and thus inefficient process (i.e. prohibitive total pressure losses) as long as diffuser geometry allows that level of pressure recovery. Therefore, the *diffuser effectiveness* (η_D), defined as the ratio between the actual and ideal values of C_p is needed to fully assess the optimality of the device, where the ideal is C_p obtained in isentropic conditions and only depends on area ratio: $C_{p,i} = 1 - AR^{-2}$. An additional performance parameter considered in this work, which is equivalent to the previous one, is the *total pressure loss coefficient* (K_D), defined as the ratio between total pressure losses and inlet dynamic head.

$$C_p = \frac{p_2 - p_1}{p_{01} - p_1} \qquad \text{[Equation 3.4]}$$

$$\eta_D = C_p / C_{p,i} \qquad \text{[Equation 3.5]}$$

$$K_D = \frac{p_{01} - p_{02}}{p_{01} - p_1} \qquad \text{[Equation 3.6]}$$

These parameters were measured for different fluid dynamic conditions in 30 diffuser geometries defined by red points in figure 37: AR = 3 - 8, L/D_{th} = 6 - 20 and 2θ = 4 - 10º. The effect of geometry was plotted by curves of constant C_p in the L/D_{th}- AR plane. Coordinates were selected to transform constant angle curves into lines, hence a double-logarithmic scale was chosen to represent the effect of geometry: $\log(L/D_{th})$ in abscissa and $\log\left(\sqrt{AR} - 1\right)$ in ordinate [equation 3.1].

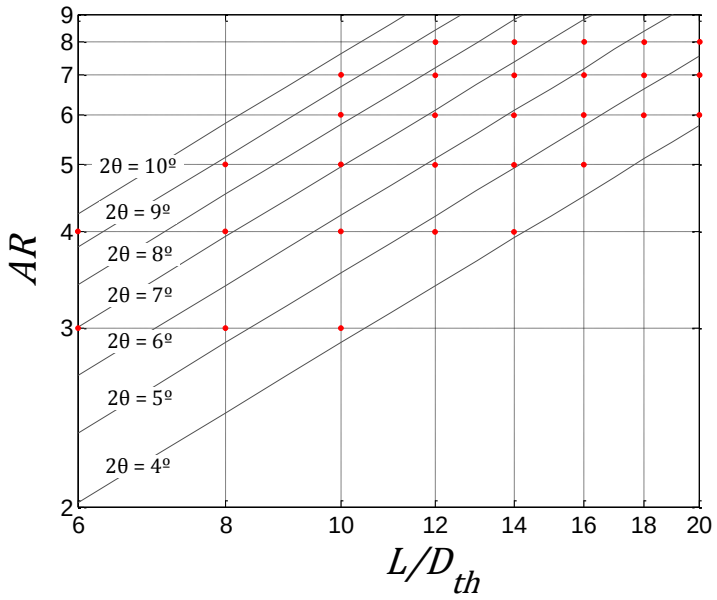

Figure 37. Typical performance map of a diffuser, showing the effect of geometry.

This is the standard map employed to represent the effects of geometry along with the so called *first order parameters*: B_{th}, M_{th} and Re_{th}. The influence of *second order parameters*, which are those related to velocity profile and turbulence, are available in closely related MSc thesis (López Florenciano, 2013) developed by fellow student at the GMTS - Department of Energy Engineering under the supervision of Prof. D. Sánchez. The main results of this complementary work are summarised in section 3.4.

3.1.4 The tool: definition, validation and verification

The heart of the tool employed for the analysis is a two-dimensional model created in ANSYS FLUENT® which comprises the *k-ω* SST model for turbulence, the Span and Wagner equation of state for supercritical CO_2 (Span & Wagner, 1996) and a mesh that accomplishes the required refinement level with $MAX(y^+) \leq 1$. This model acts as a slave and runs through journal files[7] (**.jou*), that are previously generated by a Matlab script, which is the master block commanding the previous one (see figure 38). The main loop controls every variable by modifying a certain input parameter of the model, therefore the following relations between manipulating and control variables can be established:

[7] *A journal file contains a sequence of ANSYS FLUENT® commands, arranged as they would be typed interactively in the program* (ANSYS, 2011).

Control variable	Manipulating variable
Aerodynamic blockage at throat	Parameter δ in the inlet flux profile
Mach number at throat	Static pressure at outlet boundary
Reynolds number at throat	Throat diameter
Swirl coefficient	Angular velocity profile
Distortion parameter	Type of inlet flux profile
Turbulence intensity	Turbulence intensity at inlet boundary
Dimensionless turbulence length scale	Turbulence length scale at inlet boundary
Compressibility factor	Stagnation temperature at inlet boundary
Wall y^+	Size of first element in prismatic layer

Table 3. Control and manipulating variables of the tool.

3.1.4.1 Simplified model (in EES)

For given influence parameters, a simplified model developed in EES calculates the geometry of the diffuser and the isentropic flow conditions at the inlet and outlet. Geometric results are used for geometry and mesh generation with ICEM CFD® while isentropic flow conditions are useful for initialising both the flow and boundary conditions (see section 3.1.4.4), some of which are manipulating variables that need to be changed along the calculation loop (Figure 38) in order to keep the control variables within the desired ranges.

As shown below, the model has been built by imposing mass and energy conservation along with no entropy generation.

$$h_0 = h + v^2/2$$
$$\dot{m} = \rho v \frac{\pi}{4} D^2 \qquad \text{[Equation 3.7]}$$
$$s_0 = s$$

The Span and Wagner equation of state for CO_2 closes the model when applied for static and stagnation conditions both at inlet and outlet together with the definitions of Mach and Reynolds numbers.

$$M = v/SS$$
$$Re = \frac{\rho v D}{\mu} \qquad \text{[Equation 3.8]}$$

Where the properties of interest are: enthalpy (h), entropy (s), density (ρ), speed of sound (SS) and viscosity (μ).

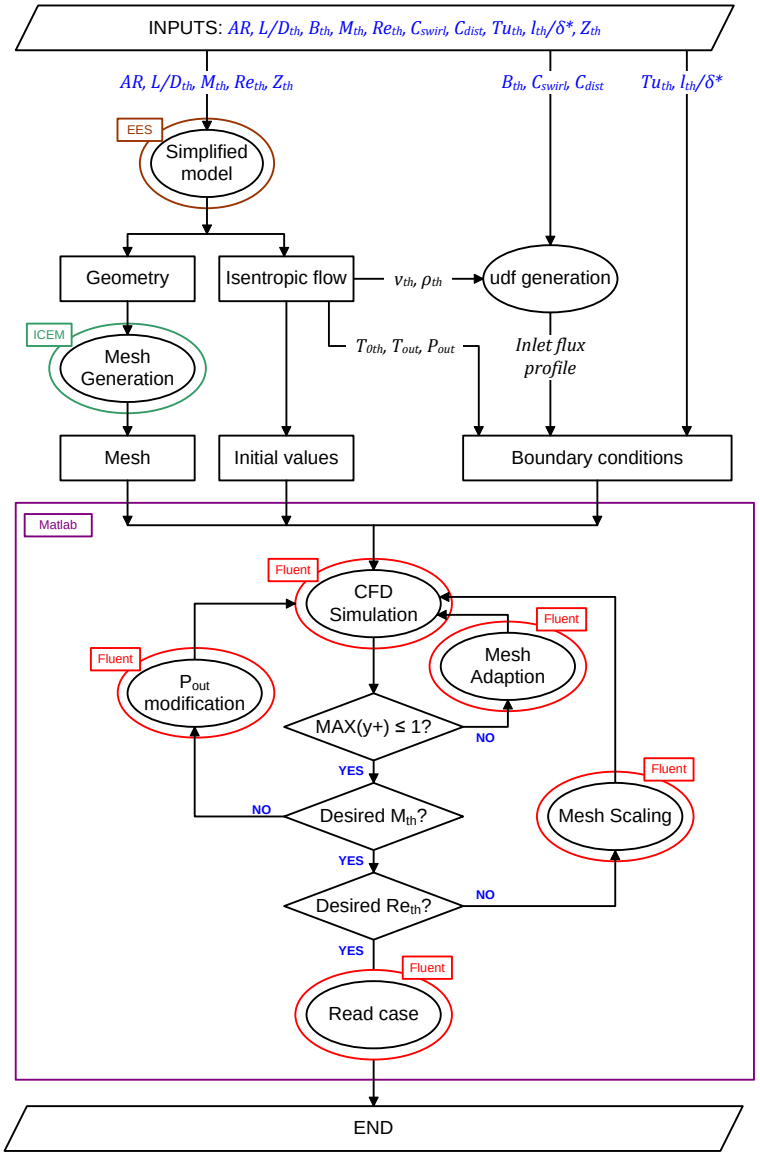

Figure 38. Block diagram of the numerical tool.

Given the geometrical parameters and fluid dynamic conditions at the throat, it is possible to calculate the dimensions of the diffuser as well as the thermodynamic conditions (pressures and temperatures) at inlet and outlet. Therefore, geometry and mesh can be constructed. Simulations require defining initial values, which are taken from the outputs of the simplified model, and boundary conditions, some of them specified from the beginning and others obtained from the simplified model. Once the simulation is run, wall y+ is checked to be lower than one. If this is not accomplised, a mesh adaption is performed and the simulation launched again. If wall y+ <1, the throat Mach number is adjusted by modifying the static pressure outlet (the lower this pressure, the higher the Mach number). Then, if the Reynolds number obtained is far from the target value, the problem is scaled up/down in order to modify the throat diameter. Finally, once all parameters have converged, Fluent is open for last time to read the values of interest.

3.1.4.2 Flux profile adjustment

As presented in section 3.1.4.4, a mass flow inlet boundary is imposed at the diffuser throat, for which a flux profile (mass flow rate per unit area, ρv) can be specified in lieu of a total mass flow rate. This allows changing the velocity profile thus playing with blockage, swirl and distortion independently. Though some variations were done for distortion analysis (section 3.4.1), the basic flux profile for blockage modifications is composed by a constant value in the core flow and a parabola in a *virtual boundary layer*[8] with zero flux in the wall and peak flux in the vertex (Figure 39).

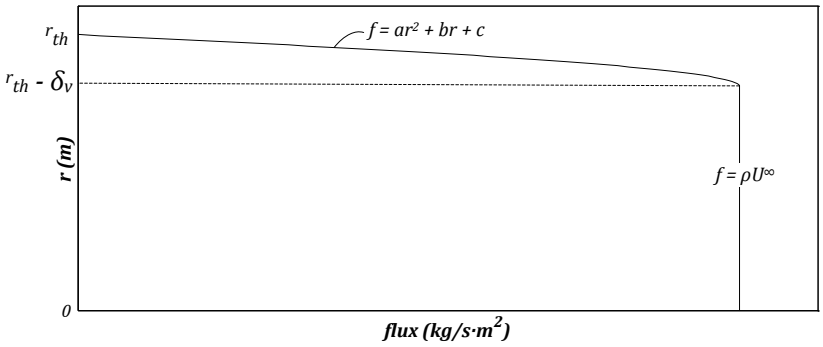

Figure 39. Flux profile at diffuser throat, imposed as boundary condition.

Density (ρ), core velocity (U^∞) and throat radius (r_{th}) are known when the influence parameters are given, so the following conditions are required to determine the parabola constants (a, b and c) and the *virtual thickness* δ_v.

- Null flux on the wall because of the non-slip conditions fixed in the CFD model.

$$a \cdot r_{th}^2 + b \cdot r_{th} + c = 0 \qquad \text{[Equation 3.9]}$$

- Continuity of the flux function at the virtual boundary layer edge.

$$a \cdot (r_{th} - \delta_v)^2 + b \cdot (r_{th} - \delta_v) + c = \rho \cdot U^\infty \qquad \text{[Equation 3.10]}$$

- Maximum flux at the virtual boundary layer edge, $[df/dr]_{r=r_{th}-\delta_v} = 0$, which results in:

$$2a \cdot (r_{th} - \delta_v)^2 + b = 0 \qquad \text{[Equation 3.11]}$$

- Specified value of the virtual aerodynamic blockage, which is directly related to the virtual thickness.

$$\delta_v = r_{th}\left(1 - \sqrt{1 - B_{th,v}}\right) \qquad \text{[Equation 3.12]}$$

8 The term "virtual" is used herein because δ will not coincide with the displacement boundary layer thickness obtained after simulation, as explained in section 3.1.4 later.

Once the structure of the profile is known, some adjustments need to be done in order to reach the desired values of both Mach number, i.e. velocity, and aerodynamic blockage, i.e. displacement boundary layer thickness:

- Mach is first adjusted by setting density and core velocity equal to the mass-averaged values measured in the CFD simulation. This requires iterating but, after convergence and given that density depends on the static conditions, its value does not change unless the compressibility factor changes. Furthermore, the core velocity reached upon convergence is proportionally affected by the Mach number of study, what means that if velocity is adjusted for a reference Mach number $M_{th,ref}$, any simulation for the same static conditions (same compressibility factor) can be performed if the core velocity is multiplied by the ratio $M_{th}/M_{th,ref}$.
- A second and more time-consuming adjustment is required for blockage. After simulation, values of virtual and measured aerodynamic blockages do not match at all (Figure 40). The reasons are that the actual velocity profile is not parabolic and density is not uniform at diffuser throat either, which were the assumption of the initial profile. Therefore, a correlation need to be found between virtual and measured blockages. To this aim, different diffuser geometries were simulated in a range of blockages, finding the following correlation:

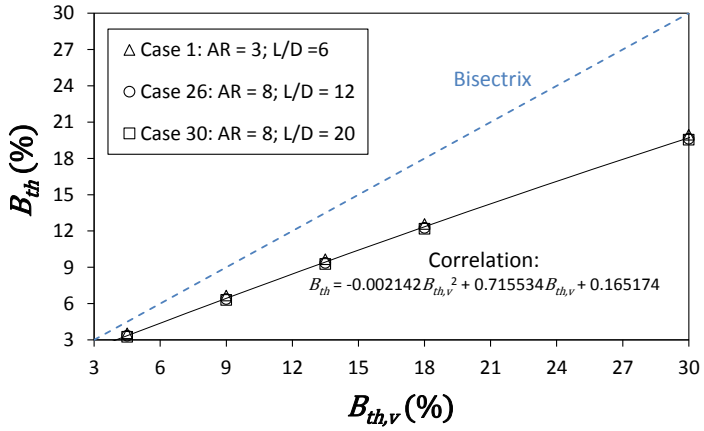

Figure 40. Virtual vs. measured aerodynamic blockages fitting. Done for three different geometries with $M_{th} = 0.2$, $Re_{th} = 7.4 \cdot 10^6$ and $Z_{th} = 0.3$.

Finally, a flux function is created as a *c* file (**.c*) to be loaded by Fluent® as a boundary condition. In addition to the profile expressions previously presented, the correlation in figure 40 is included and therefore accurate enough aerodynamic blockages are obtained after the simulation.

3.1.4.3 Mesh generation

As presented later, axial symmetry are used for simulations. It brings about a trapezoidal domain in two dimensions with different lengths of their sides depending upon area ratio and non-dimensional length. Because of the simplicity of the geometry, structured meshes (quadratic elements) are selected, with increasing size from the wall to the axis and the first element between $2.7 \cdot 10^{-9}$ and $2.4 \cdot 10^{-8}$ m in height. Due to these small values, wall y+ lower than unity is usually obtained and consequently no mesh adaptions are required at the same time that the computational cost remains affordable.

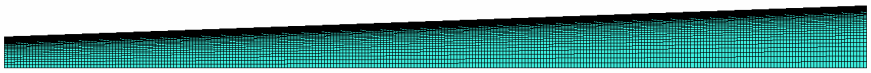

Figure 41. Example of computational mesh.

A mesh is created for each one of the 30 cases with a common throat radius of 6.35 m (250'') by using script files (**.rpl*) in ICEM CFD®. Them, depending on the desired throat diameter (i.e. on the target Reynolds number), scale factors are applied after reading the mesh in ANSYS FLUENT®. If necessary, as the block diagram expresses (Figure 38), a mesh adaption is done by splitting the first element next to the wall into four parts.

Finally, a *grid convergence index* (GCI) analysis is performed for same cases aiming to verify to which extent the mesh affects the solution and to assess how this uncertainty is propagated to the outputs parameters (see section 3.1.4.5).

3.1.4.4 Definition of the CFD model

Due to the original behaviour of the fluid, simulating supercritical carbon dioxide flows in ANSYS FLUENT® involves some issues which do not appear with conventional fluids, for instance atmospheric air. At least in the range of study, these problems are solved by taking into account some numerical considerations explained in this section, which may as well not suffice for others case studies involving the same working fluid. This special complexity has driven some authors to create CFD codes specifically adapted for CO_2 simulation and examples of that have been presented at some international events (Pecnik & Colonna, 2011) (Pecnik, et al., 2012). Nonetheless, there is also a number of authors who have adopted a commercial code like for instance ANSYS FLUENT® code (Munroe, et al., 2009). This latter approach is used in this thesis.

Since fluid dynamics are the only physics involved in diffuser operation (note that the diffuser is considered adiabatic), the model is fully constructed with the appropriate turbulence model and equation of state. Before selecting each one of them, two separate sensitivity analyses are presented in order to evaluate how these choices can affect the results.

3.1.4.4.1 Effect of turbulence model choice

Given the lack of experimental results for supercritical CO_2 diffusion processes against which the CFD model could be validated, the same case is run with all the (RANS) turbulence models available in ANSYS FLUENT®. This reference case comprises a pipe with a length of 200 mm and a diameter of 0.5'' through which supercritical CO_2 flows. Total inlet pressure and temperature are 96 bar and 315 K the inlet Mach number is 0.2.

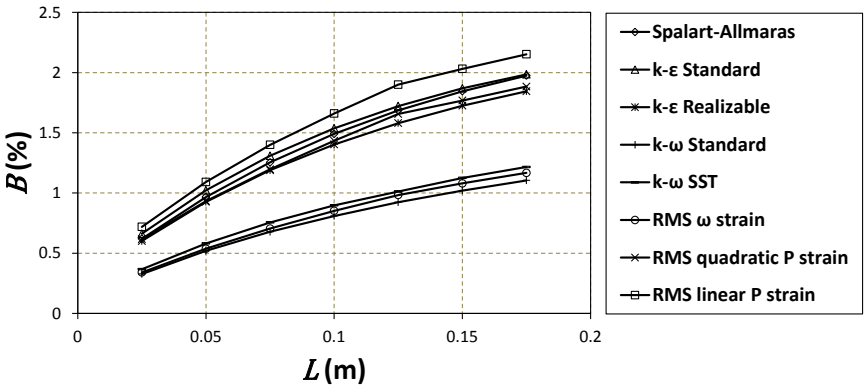

Figure 42. Effect of some RANS turbulence models in S-CO_2 flow through a pipe.

In the light figure 42, two turbulence model categories are identified: on one hand, those that use the turbulent kinetic energy dissipation rate (ω) and, on the other, the remaining ones. Such differences are easily observed in the evolution of aerodynamic blockage along the pipe, achieving lower values for the first category. Taking into account the comparison in (Van Abel, et al., 2011), previous works done in the turbomachinery field in Delft University of Technology (Pecnik, et al., 2012) (Pecnik & Colonna, 2011) and recommendations in ANSYS documentation (ANSYS, 2011), the k-ω SST (Shear Stress Transport) (Wilcox, 1993) model is adopted. This is a two-equation model widely used in turbomachinery (both in academia and industry) thanks in particular to its precision when solving boundary layers in adverse pressure gradients.

3.1.4.4.2 Effect of equation of state choice

Apart from the commonly known cubic real-gas equations of state, ANSYS FLUENT® incorporates a useful fluid database from REFPROP v7.0, which provides properties of a total of 83 pure fluids created by NIST (National Institute of Standards and Technology); carbon dioxide is available in this database as modelled by (Span & Wagner, 1996). Nonetheless, in order to explore the differences, simulations with all the real gas cubic equations of state available (Redlich-Kwong, its modification by Aungier, and the Soave and Peng-Robinson model) are performed, yielding the following conclusions:

- Deviations between -10 and -14.18 % in density and between -46 and -50 % in the speed of sound are experienced when cubic EOS's are used. Accordingly, a twofold increase in Mach numbers is experienced for the same boundary conditions.
- In spite of different mean velocities, similar velocity distributions are observed, bringing about similar aerodynamic blockage factors.
- Above all, since blockage is of paramount importance for pressure rise coefficient, errors around 1 % are found.

Globally, though similarities are found in terms of blockage and pressure rise coefficient, much larger differences are observed for the fluid properties. Therefore, it is concluded that cubic EOS are inappropriate for SCO2 turbomachinery design, where fluid properties play a crucial role, and thus NIST real gas model is selected instead. This implies additional though affordable computational cost.

3.1.4.4.3 Boundary conditions

Only boundary conditions that are adequate for compressible fluid can be set up when a NIST real gas model is activated in Fluent, even at low velocity flows. Therefore, a *pressure outlet* boundary must be set at the outlet and two options are possible for the inlet: *mass flow inlet* and *pressure inlet*; given that velocity profiles need to be specified at the throat, the first option is chosen. The axial symmetry of the model requires an axis boundary condition and finally, a non-moving wall completes the set of boundary definition.

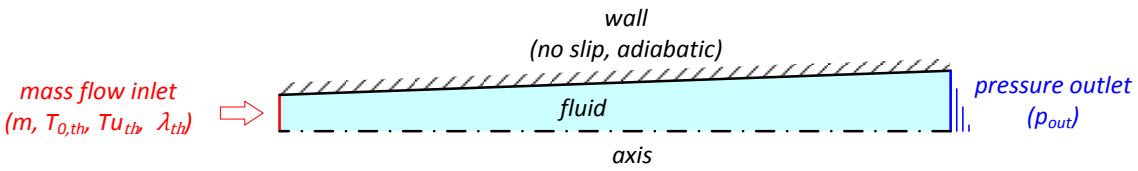

Figure 43. Boundary conditions.

The definition of the inlet boundary is completed with the stagnation temperature and two turbulence parameters which, for diffusers, are turbulence intensity and length scale. These seem to be most appropriate according to the parameters of influence. In the outlet boundary, turbulence parameters and a static temperature are defined as well to be used only for those cells with backflow; this has a negligible impact on the results though given the absence of backflow. The adiabatic wall boundary is defined by the non-slip conditions and smooth surfaces in fluid dynamic terms which add to

the no heat transfer feature. Setting up the axis boundary and activating the axial symmetry completes the definition of all the boundary conditions.

3.1.4.4.4 Some numerical considerations

The are two aspects that make supercritical CO_2 simulations be less stable than their equivalent with air: on one hand, the pronounced variations that the properties exhibit near the critical point and, on the other, the risk of condensation if saturation conditions are met. These two facts require taking into account the following recommendations in order not to fail to converge:

- The *Coupled* algorithm for pressure-velocity coupling seems to provide the only effective path to convergence. The SIMPLE algorithm (Semi-Implicit Method for Pressure-Linked Equations) (Patankar & Spalding, 1972) is nevertheless set by default in ANSYS Fluent®. In this latter method, from a guessed pressure distribution, the velocity field is calculated from the momentum equation and, then, continuity is employed to calculate a pressure correction factor which modifies the pressure field in the next iteration. As opposed to this, the *Coupled* algorithm solves the system of equations formed by mass and momentum conservation simultaneously. Therefore, pressures and velocities satisfy the conservation laws in every single cell for its given boundaries. This algorithm makes the calculation much more robust, with the drawback of taking longer in each iteration step.
- Similarly, first order upwind (fou) interpolation schemes (Versteeg & Malalasekera, 2007) allow for a faster convergence. It must be acknowledged though that this approach can reduce the accuracy of the results since only one cell upstream is considered when calculating the variables of a particular cell. However, the validation results are satisfactory enough to conclude that this approach is acceptable.
- Another aspect is the importance of setting lower limits of pressure and temperature which are sufficiently far from their critical values. This avoids penetrating the two-phase region while running the solver, since this would immediately stop the calculation. From this point of view, upper limits are not necessary though they definitely help.
- Solving the equations progressively is another means to gain stability in the calculation process. When a case is run for the first time (before adjustments), the equations are solved one by one. The flow equations (mass and momentum) are solved initially until a low enough mass imbalance[9] is achieved; turbulence is then activated and finally, when the residuals are considerably low ($\sim 10^{-3} - 10^{-4}$ depending on the case), the energy equation is incorporated.

3.1.4.5 Validation

This work faces a hurdle that is very difficult to overcome, since a proper experimental validation cannot be done for supercritical CO_2. This is a common problem experienced by all the researchers in the field. Still, the work by Dolan and Runstadler (Dolan & Runstadler, 1973) is taken as a reference to validate the methodology, at least for air. These authors studied the effects of aerodynamic blockage and Mach and Reynolds numbers on air diffuser performance and therefore constitutes a benchmark against which models can be calibrated. In the present work, and due to the most important influence of blockage, the proposed numerical methodology is applied to replicate Dolan & Runstadler's cases with 3, 6, 9 and 12 % blockage, 0.2 Mach number and $6 \cdot 10^4$ Reynolds number. The comparison between the experimental and numerical values is shown in figure 44.

[9] *Mass imbalance is defined as the difference in mass flow rate between inlet and outlet sections.*

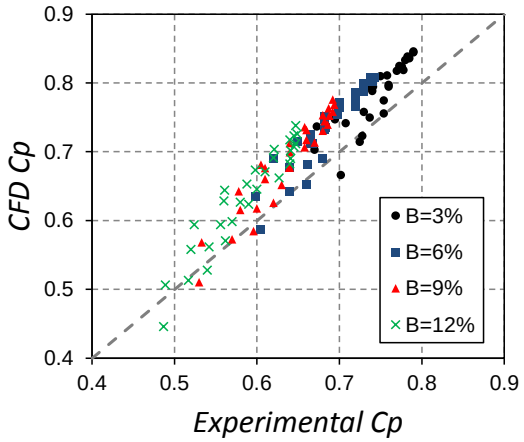

Figure 44. Validation of the methodology in air diffusers with B_{th} = 3, 6, 9, 12 %, M_{th} = 0.2 and Re_{th} = 6·10⁴.

According to the cited figure, the CFD model tends to overpredict the performance of the diffuser by 4.6 % on average, which is deemed satisfactory if the following additional limitations of the lab tests are considered:

- Very high experimental uncertainty in the blockage factor measurement, with values up to 51 % for B_{th}= 3% and 12 % for B_{th}= 12 %.
- Fluid dynamics are affected by a 1.27 mm diameter cylindrical pressure probe located at the axis of the diffusers.
- Total pressure is assumed constant along the inlet nozzle which is not the case in practice (see figure 45).
- Non-specified turbulence parameters.

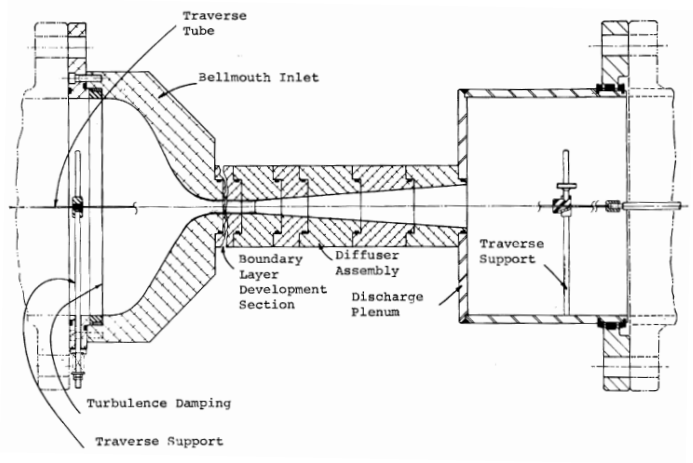

Figure 45. Experimental rig for diffusers analysis by (Dolan & Runstadler, 1973).

3.1.4.6 Verification

Once the methodology is validated for air, one could assume that an appropriate (correctly constructed) CFD model for CO_2 would offers results sufficiently close to experiments. Nonetheless, an additional source of inaccuracy in the CFD model still needs to be assessed when supercritical CO_2 is used: the mesh, considered in global terms and not limited to local effects such as the near wall regions. An

infinitely fine mesh ideally is expected to reproduce the experimental values as long as the models employed are realistic, whereas a very rough mesh will most likely offer unreliable results. Within this range, it is necessary to evaluate how fine the mesh must be in order to get results that are not affected by the representative mesh size. In other words, the extent to which the results are influenced by a certain mesh needs to be assessed. The method widely accepted by the CFD community to assess this effect is the *Grid Index Convergence* (GCI) analysis (Celik, et al., 2008), presented in the previous chapter.

This analysis is applied to several geometries considering total and static pressures, static temperature and velocity at the throat as key variables. Representative grid convergence indexes of the analysis are shown in table 4 for a certain case, confirming that even with the coarsest mesh satisfactory results are obtained (GCI_{21}<<1%).

	Mesh sizes				**Grid Convergence Index**	
	0.223 mm	**0.149 mm**	**0.099 mm**	$h \to 0$	GCI_{21} (%)	GCI_{32} (%)
$\overline{P_{0,th}}$ (Pa)	9493348	9496353	9498433	9503110	0.089	0.062
$\overline{P_{th}}$ (Pa)	9031615	9033361	9034625	9037939	0.063	0.046
$\overline{T_{th}}$ (K)	312.7215	312.7271	312.7318	312.7547	0.011	0.009
$\overline{v_{th}}$ (m/s)	42.0619	42.1197	42.1581	42.2338	0.339	0.225

Table 4. Results of the GCI analysis for a S-CO_2 case with AR=4, L/D_{th}=6 and B_{th}=3% at M_{th}=0.2 and Re_{th}=7.4·10⁶.

From these results, the effect of mesh refinement on C_p can be evaluated by error propagation according to the following expression [Equation 3.4]:

$$\mathrm{d}C_p = \frac{\partial C_p}{\partial P_{th}}\,\mathrm{d}P_{th} + \frac{\partial C_p}{\partial P_{0,th}}\,\mathrm{d}P_{0,th} \qquad \text{[Equation 3.13]}$$

This equation assumes that the outlet static pressure does not influence the error since it is set as a boundary condition in the simulation, therefore having a constant value. If the parameter uncertainties ($\mathrm{d}P_{th}$ and $\mathrm{d}P_{0,th}$) are taken as their corresponding *GCI* in absolute terms (which is actually the meaning of *GCI*), the following expression is obtained:

$$\mathrm{d}C_p = \frac{\left(\mathrm{GCI}_{P_{th}} \cdot P_{th}\right)\left(P_{out} - P_{0,th}\right) + \left(\mathrm{GCI}_{P_{0,th}} \cdot P_{0,th}\right)\left(P_{th} - P_{out}\right)}{\left(P_{0,th} - P_{th}\right)^2} \qquad \text{[Equation 3.14]}$$

For the case in table 4, the variation in C_p that comes about because of the mesh size is 0.0168, representing a -2.26% of its value (0.7407). This is considered acceptable from an accuracy vs. computational burden standpoint.

3.2 Effect of geometry

As already presented in section 3.1.3, the effect of geometry is presented in formatted maps, figure 37, where constant-C_p and constant divergence angle curves are drawn in red and blue respectively. A comparison between maps obtained for supercritical carbon dioxide (numerical) and air (experimental, taken from (Dolan & Runstadler, 1973)) is firstly presented. In this regard, it must be noted that, although no specifications about turbulence parameters appear in the reference work, all maps in this section are

obtained for a 1 % turbulence intensity and non-dimensional turbulence length scale equal to 10. Blockage and Mach number are set to the same values for air and supercritical CO_2 whereas, on the contrary, Reynolds number differs from one fluid to another due to the very different fluid properties, density in particular (more than 400 times higher for CO_2). Nevertheless, as stated in (Dolan & Runstadler, 1973), the effect of Re on diffuser performance is negligible in the range of study.

The maps in figure 46 comprise curves for S-CO_2 (simulation) in red and air (experiments) in green. The particular (fluid dynamic) boundary conditions appear at the top of each single map for CO_2 and on a green square at the bottom for air. Both C_p surfaces intersect in the dashed purple line, which divides every map into two regions: (i) one where air has better performance (shadowed in green) and (ii) one where supercritical carbon dioxide performs better (shadowed in red).

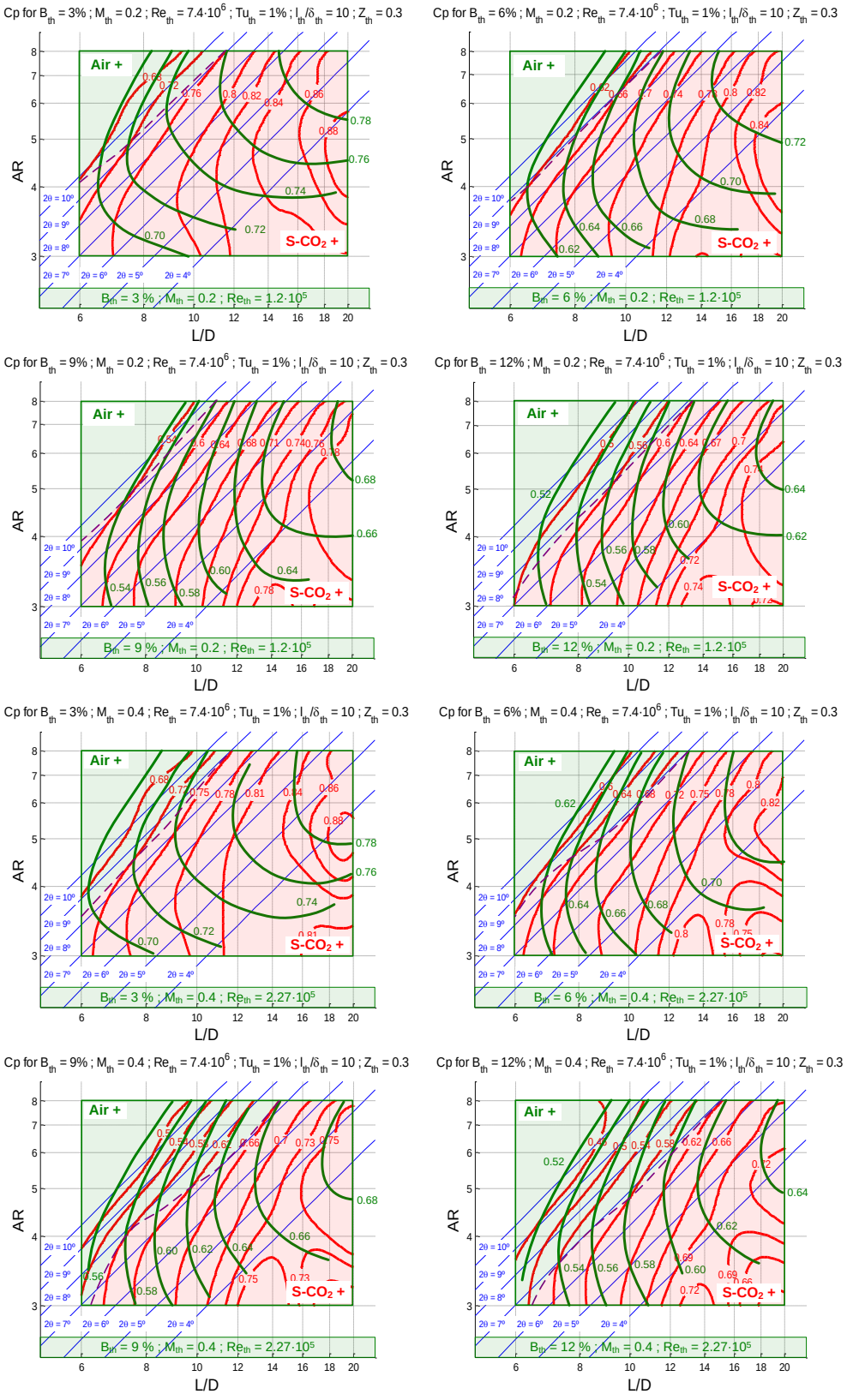

Figure 46. Comparative performance maps for CO_2 and air. Results for CO2 are numerical whilst air data are taken from (Dolan & Runstadler, 1973).

By observing the previous maps, the first conclusion is that CO_2 performs better than air in a wider region of the range considered, this region being larger when blockage decreases. The shapes of the curves are also different for each fluid. The green lines present a wide region where the area ratio hardly affects the performance (constant C_p are almost vertical) while this zone does not even exist for CO_2in many cases. This means that for certain combinations of operating conditions, the cone diffuser operating with air seems to be more resistant to high divergence angles and thus to flow detachment. In other words, high C_p's can be sought by increasing both the area ratio and the non-dimensional length. On the contrary, S-CO_2 is less resistant to flow detachment and hence needs an increment of dimensionless length at limited area ratio in order to improve the performance.

The previous comparison shows experimental data for air and numerical results for carbon dioxide. Apart from this comparison, simulations have also been carried out with air as working fluid (see maps in figure 49), whose validation is shown in section 3.1.4.5. For these simulations, similitude regarding turbulence parameters and equal blockage factor and Mach number are considered and, indeed, it comes to show the improvement in performance when CO_2 is used as well as the fact that varying the area ratio can be favourable for air but rarely for carbon dioxide. Additional information about this effect will later be shown in section 3.3.1.

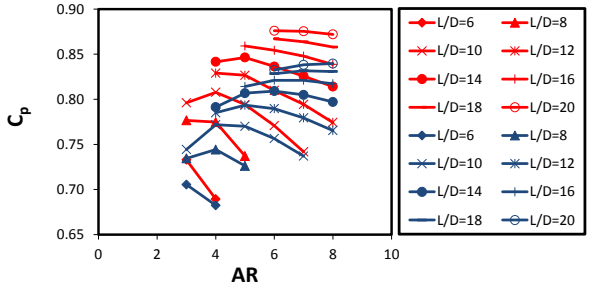

Figure 47. Comparison between air (blue) and S-CO_2 (red): effect of area ratio onto diffuser performance at constant non-dimensional length, $M_{th} = 0.2$ and $B_{th} = 3$ %.

This result evidences that the supercritical fluid adapts better to longer diffusers with lower divergence angles, which was actually to be expected given the much higher Reynolds number characteristic of S-CO_2. As latter explained in section 3.3.1, the dominant effect of inertia over friction incurs a lower capability of the flow to attach to the wall and hence the flow is very sensitive to an increase in cross sectional area. In order to further explain the observed behaviour, a comparison between air and S-CO_2 flows at M_{th}=0.2 and B_{th}=6 % are shown for three different geometries: cases 3, 20 and 25. Cases 3 and 20 have the same non-dimensional lengths, cases 20 and 25 have the same area ratios and cases 3 and 25 have similar divergence angles.

From the comparison of diffusers with the same non-dimensional length (Figure 48Figure 61 top), it is concluded that the wider the divergence angle, the faster the boundary layer growth in the entry region (near the throat) for S-CO_2. This evidences that air adapts better to area changes. However, when diffusers with same area ratios but different lengths are compared (Figure 48 centre), it is observed that the aerodynamic blockage tends to converge to a common value as the flow develops along the diffuser. Furthermore, the blockage factor is even lower for S-CO_2 if the diffuser is long enough, as observed for case 25. Therefore, near the throat, carbon dioxide separates from the walls because of inertia but, as velocity decreases and the significance of viscosity forces increases, the velocity profiles become more uniform in such a way that the boundary layer at the outlet is thinner for the supercritical fluid if the diffuser is long enough. Finally, a comparison of diffusers with similar divergence angles (Figure 48 bottom) shows that the aerodynamic blockage develops similarly streamwise. When the length is increased, the region where viscous forces are more important is proportionally longer and, in consequence, the velocity profiles are more homogeneous and the blockage factor is reduced. On the negative side, this increases the effect of wall friction though this is attenuated for the supercritical fluid thanks to the higher Reynolds number of CO_2 with respect to air. This explains why high non-dimensional lengths benefit CO_2 in terms of diffuser performance.

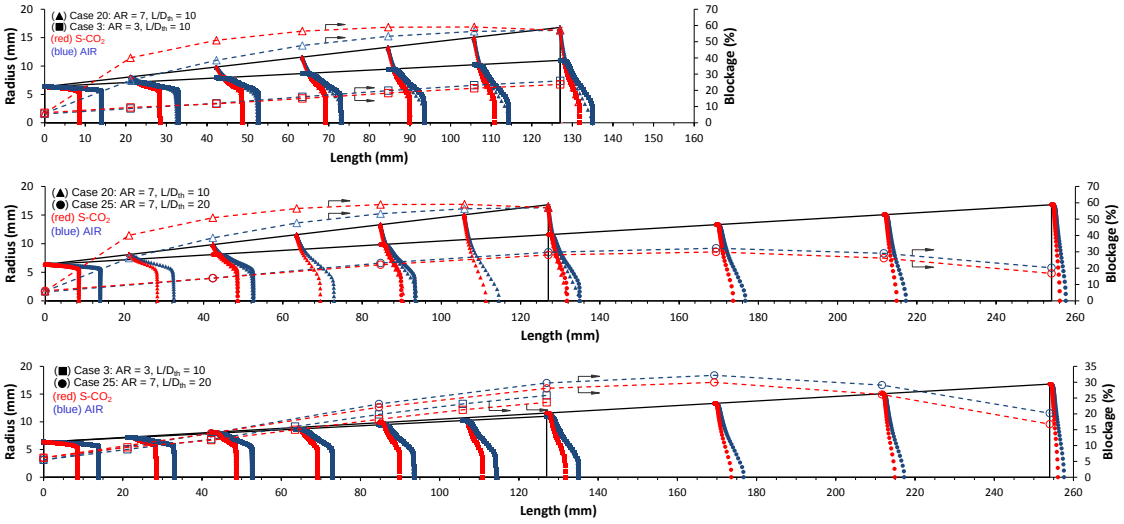

Figure 48. Development of blockage (dashed lines) and velocity profile (solid symbols) along various diffusers for air (blue) and S-CO_2 (red). Constant non-dimensional length (top), constant area ratio (middle) and similar divergence angle (bottom).

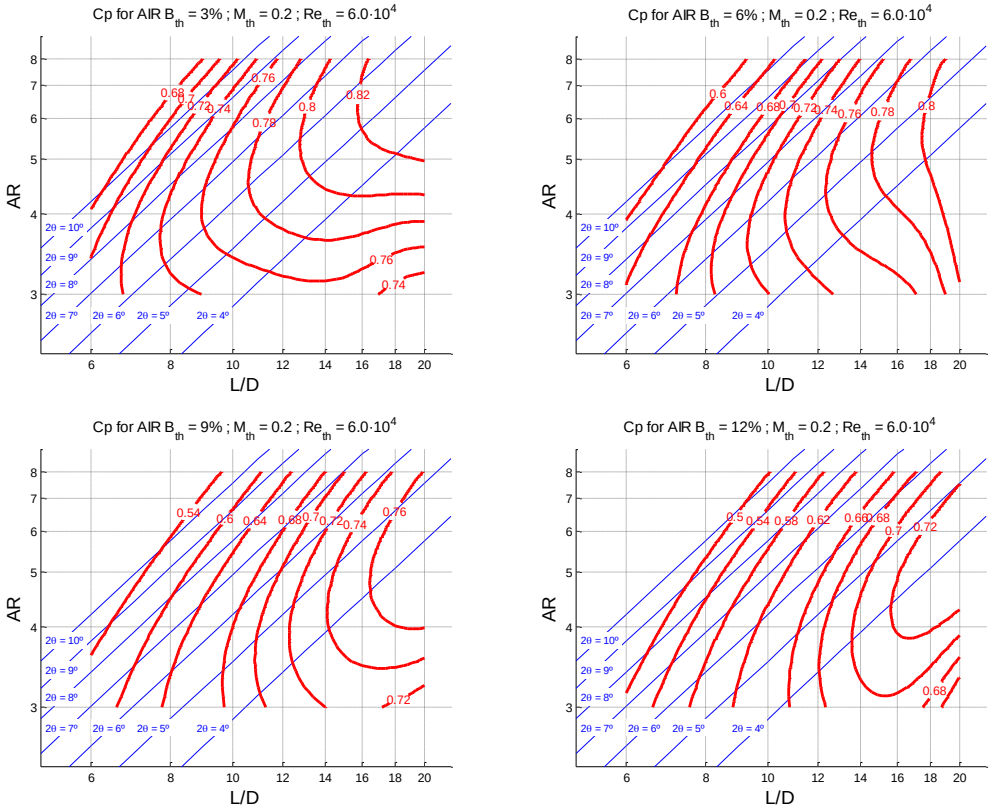

Figure 49. Air diffuser maps obtained numerically.

A last set of figures is now presented to confirm the beneficial effect of non-dimensional length on the performance of supercritical carbon dioxide diffusers. In effect, even though blockage factor somehow transforms the shape of constant-L/D_{th} curves, constant-AR curves in the figures below always exhibit the same trends, definitely confirming that increasing the non-dimensional length brings about better diffuser performance.

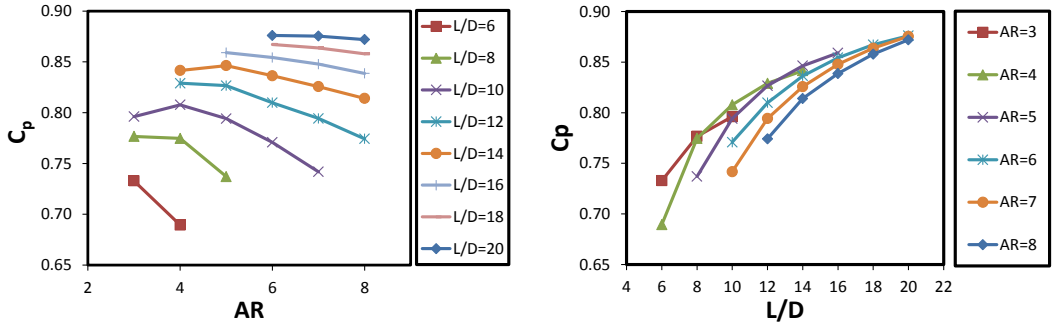

Figure 50. Pressure rise coefficient vs. area ratio (left) and non-dimensional length (right) for S-CO_2 at $B_{th} = 3$ %, $M_{th} = 0.2$, $Re_{th} = 7.4{\cdot}10^6$.

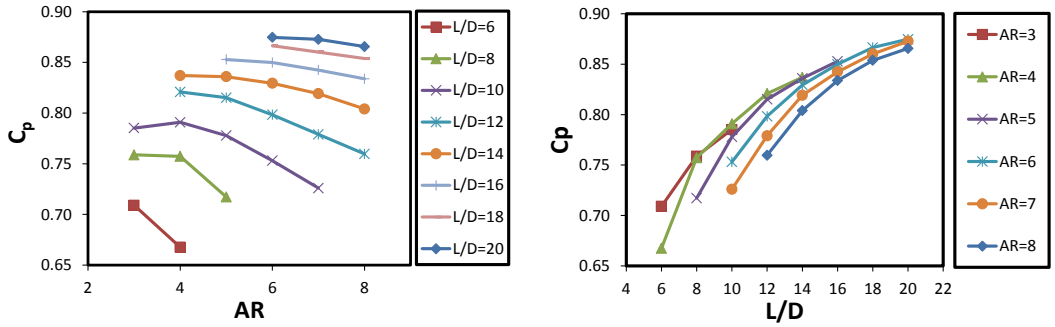

Figure 51. Pressure rise coefficient vs. area ratio (left) and non-dimensional length (right) for S-CO_2 at $B_{th} = 3$ %, $M_{th} = 0.4$, $Re_{th} = 1.6{\cdot}10^7$.

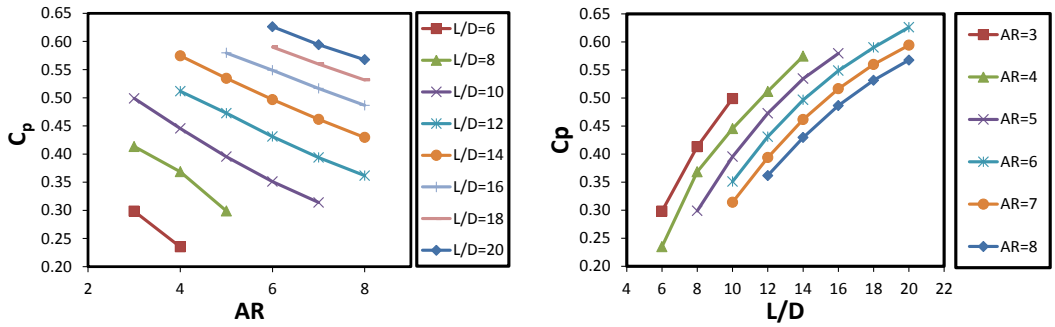

Figure 52. Pressure rise coefficient vs. area ratio (left) and non-dimensional length (right) for S-CO_2 at $B_{th} = 15$ %, $M_{th} = 0.2$, $Re_{th} = 1.6{\cdot}10^7$.

In order to complete this section on the effect of geometry, all the maps obtained numerically for carbon dioxide are presented below.

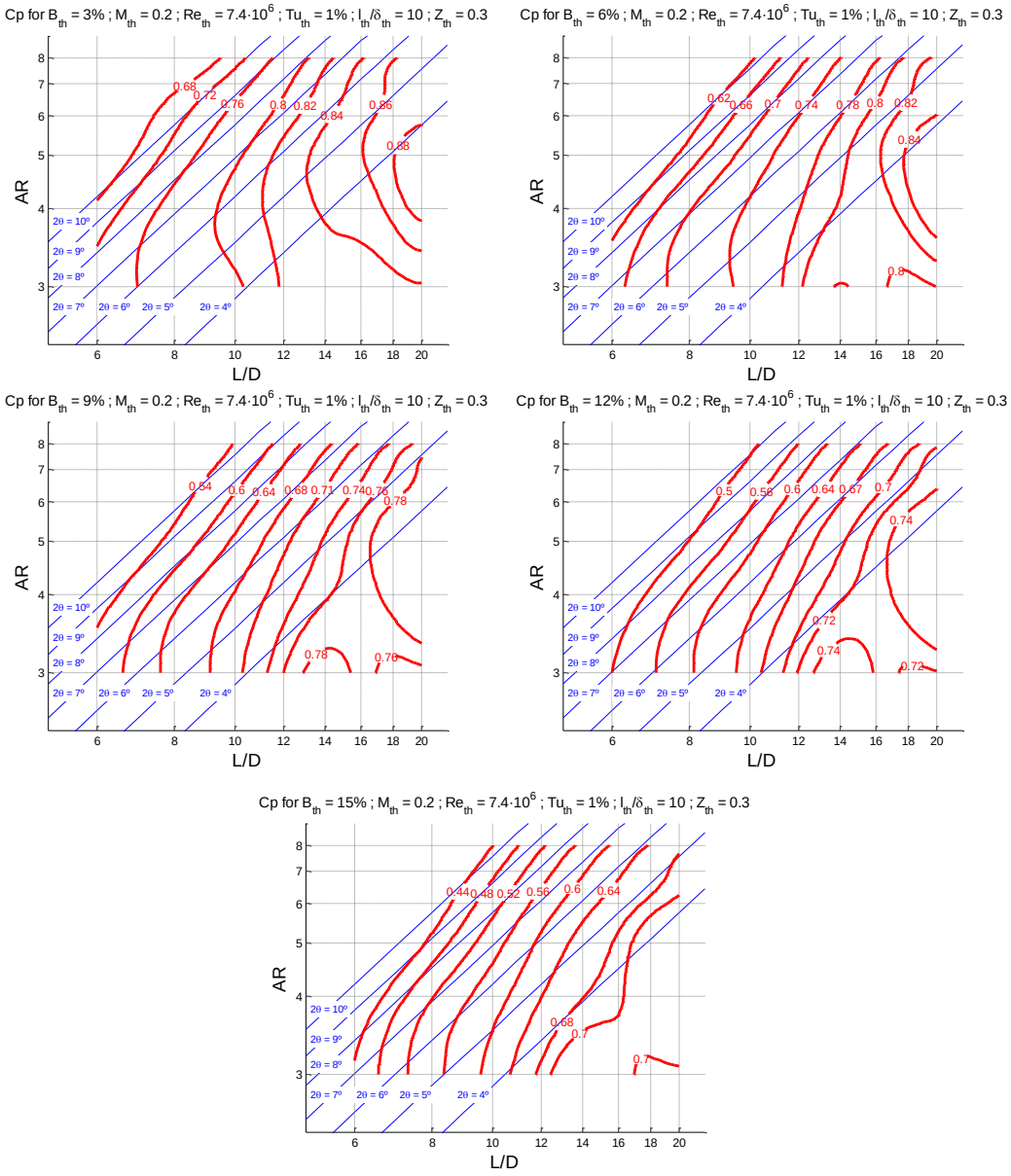

Figure 53. Diffuser maps for S-CO₂ at $M_{th} = 0.2$, $Re_{th} = 7.4{\cdot}10^6$, $Tu_{th} = 1\ \%$, $l_{th}/\delta_{th} = 10$, $Z_{th} = 0.3$.

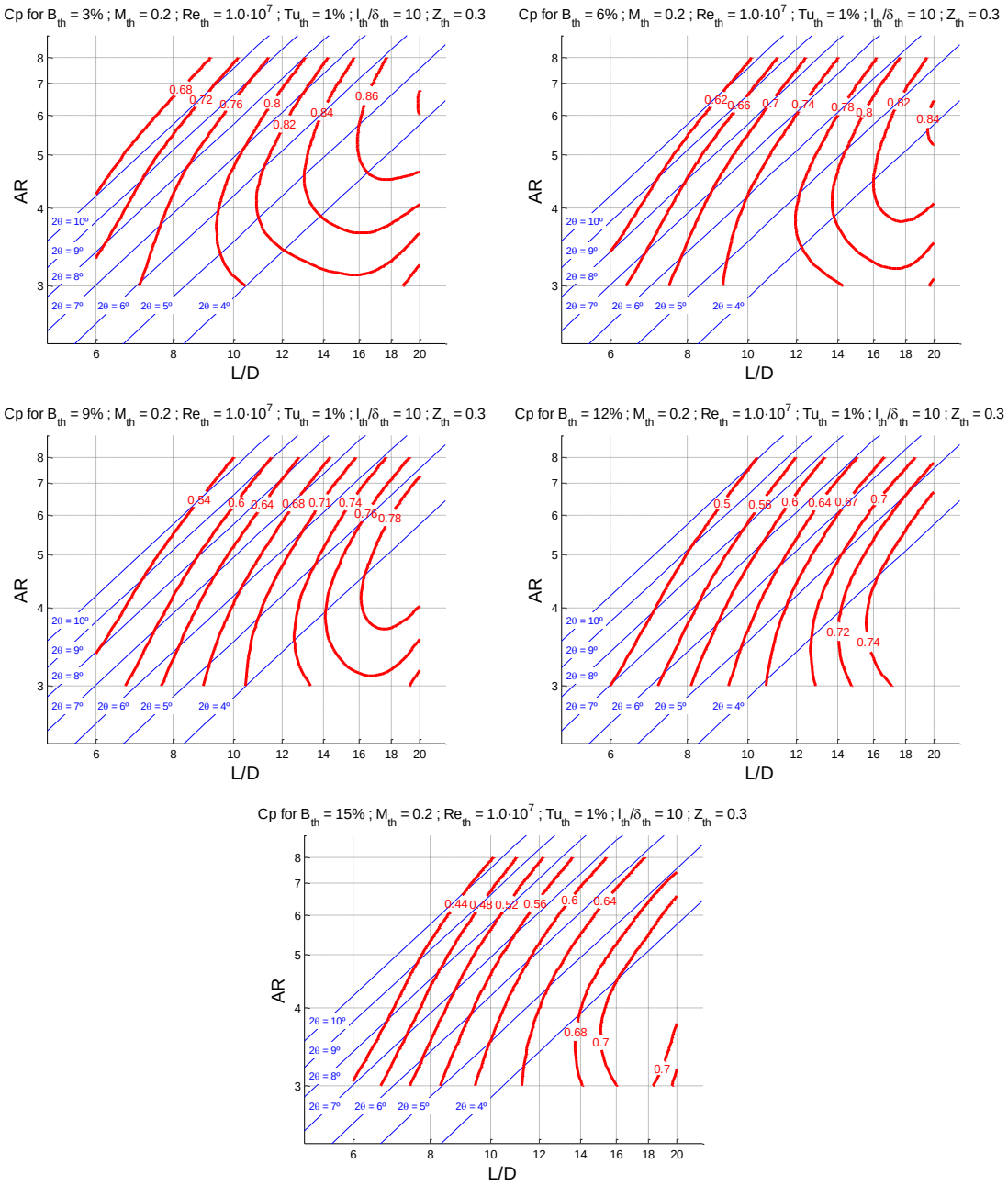

Figure 54. Diffuser maps for S-CO₂ at $M_{th} = 0.2$, $Re_{th} = 1.0{\cdot}10^7$, $Tu_{th} = 1\,\%$, $l_{th}/\delta_{th} = 10$, $Z_{th} = 0.3$.

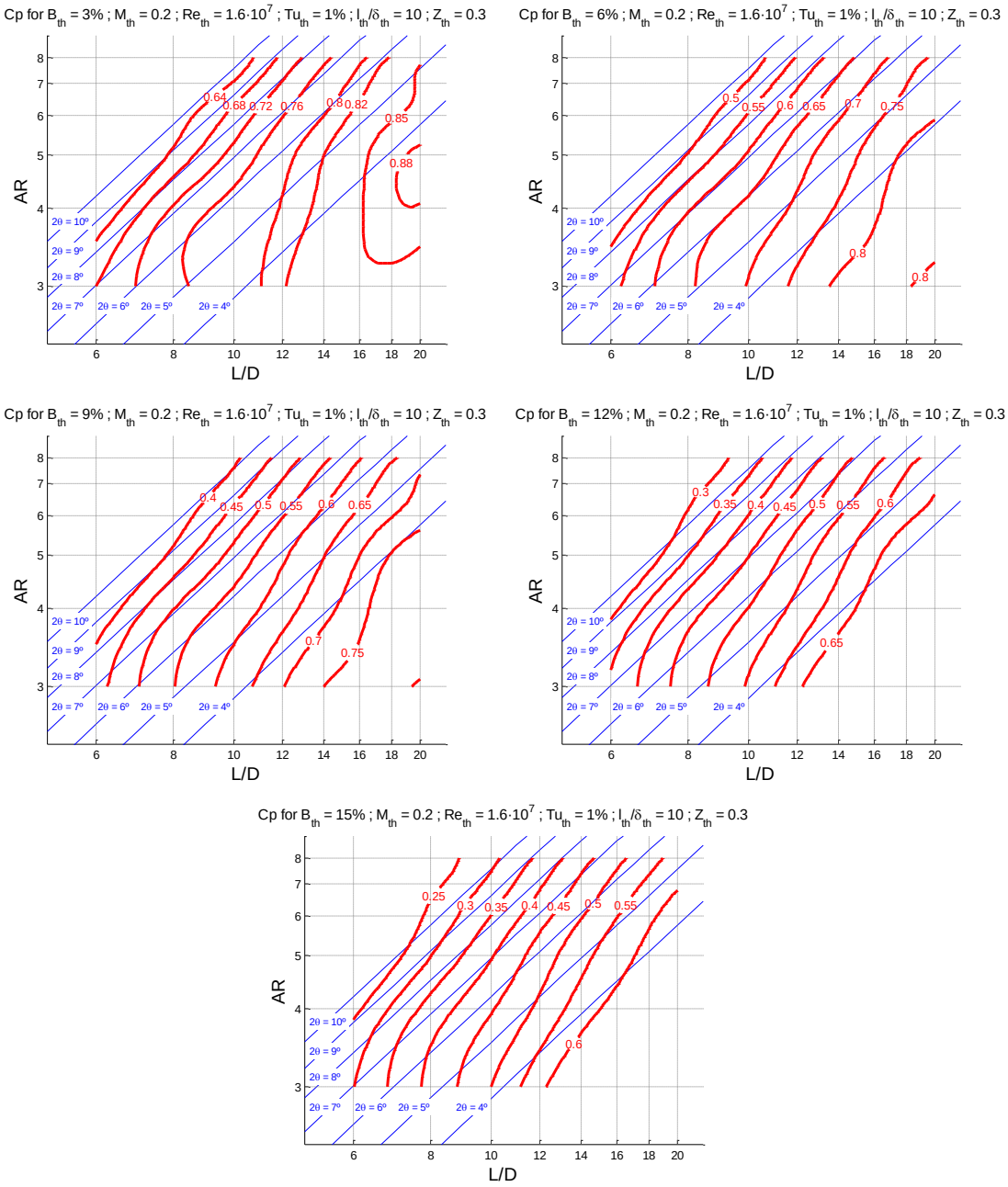

Figure 55. Diffuser maps for S-CO₂ at $M_{th} = 0.2$, $Re_{th} = 1.6{\cdot}10^7$, $Tu_{th} = 1\ \%$, $l_{th}/\delta_{th} = 10$, $Z_{th} = 0.3$.

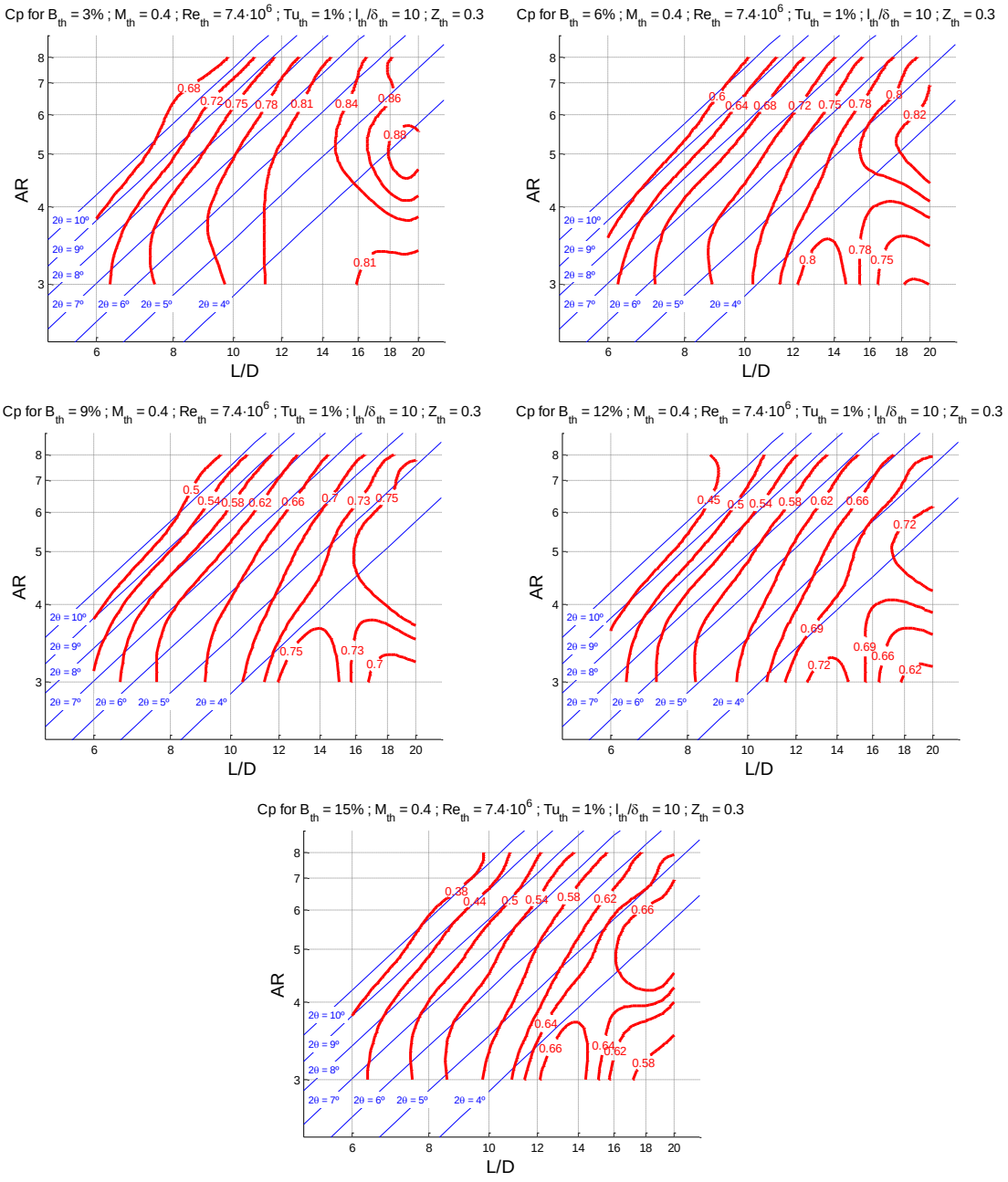

Figure 56. Diffuser maps for S-CO₂ at $M_{th} = 0.4$, $Re_{th} = 7.4{\cdot}10^6$, $Tu_{th} = 1\ \%$, $l_{th}/\delta_{th} = 10$, $Z_{th} = 0.3$.

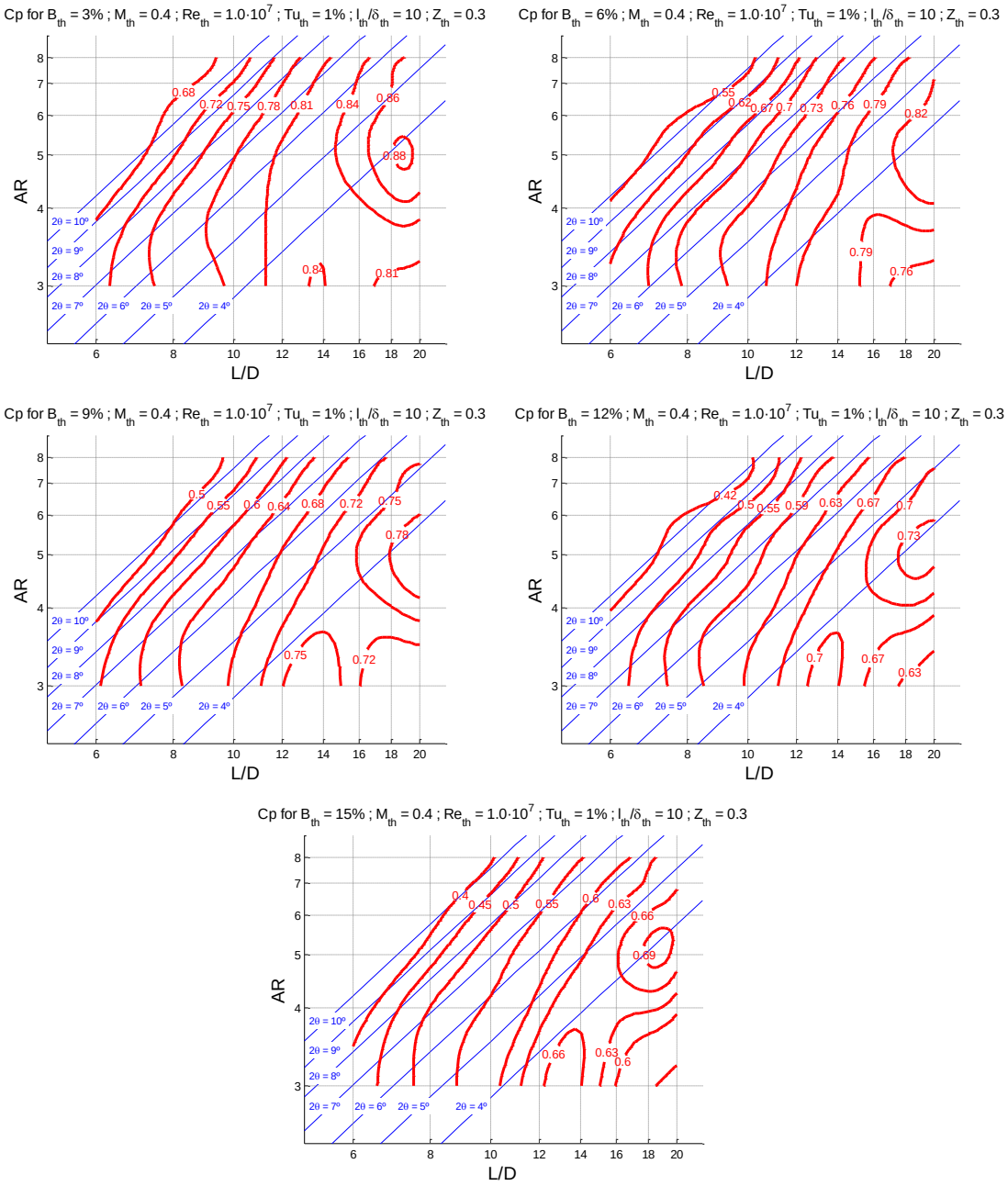

Figure 57. Diffuser maps for S-CO₂ at $M_{th} = 0.4$, $Re_{th} = 1.0{\cdot}10^7$, $Tu_{th} = 1\,\%$, $l_{th}/\delta_{th} = 10$, $Z_{th} = 0.3$.

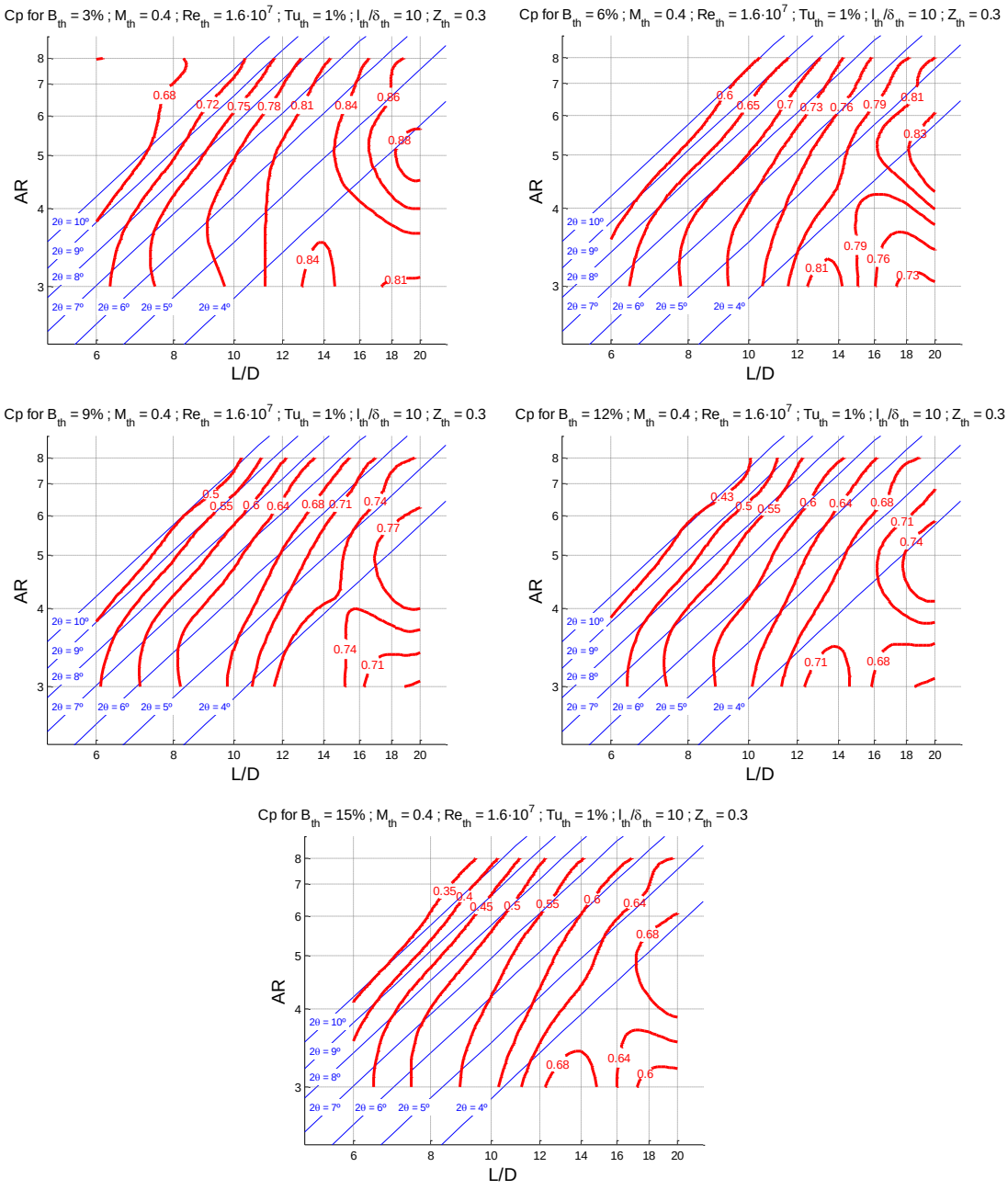

Figure 58. Diffuser maps for S-CO₂ at $M_{th} = 0.4$, $Re_{th} = 1.6{\cdot}10^7$, $Tu_{th} = 1\ \%$, $l_{th}/\delta_{th} = 10$, $Z_{th} = 0.3$.

3.3 Effect of first order parameters

Aerodynamic blockage factor and Mach and Reynolds numbers are herein called "*first order parameters*" because they are transversal variables, very common in the majority of fluid dynamic studies and above all, they were the first parameters on which the original works on diffuser focused. In this regard, several investigators pointed out that aerodynamic blockage is the most relevant fluid dynamic parameter affecting diffuser performance. In contrast, Reynolds number is a very weak parameter, with an unclear effect on diffuser performance, at least in the range of study since there are certain conditions where Reynolds can be influential (Japikse & Baines, 1998). On the other hand, it has been demonstrated experimentally that Mach number at diffuser throat hardly has any effect on conical diffuser performance. This is not clear though, since studies done by Dolan and Runstadler (Runstadler & Dolan, 1973) suggested an important effect of Mach number in channel diffusers when the throat aspect ratio is lower than 1.

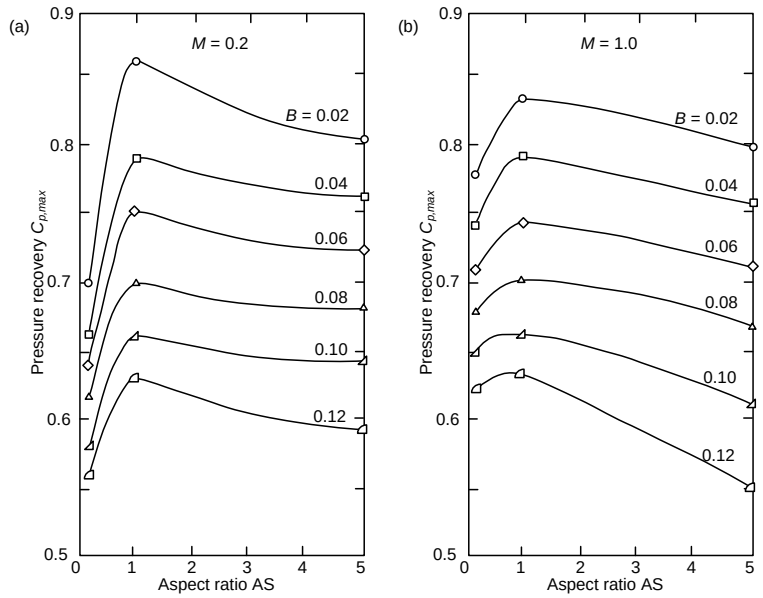

Figure 59. Pressure recovery versus aspect ratio for channel diffuser (Runstadler & Dolan, 1973).

Since this work concentrates on conical diffuser, the influence of Mach number is partially omitted even though cases at Mach number equal 0.2 and 0.4 are analysed, one on incompressible and another on compressible flow conditions. Moreover, the proposed methodology seems to fail when running cases above around $M_{th} = 0.55$ because of numerical problems in ANSYS Fluent®. This is thought to be due to the thermodynamic state of the fluid entering the saturation dome (note that the inlet boundary conditions are of the total pressure/temperature plus mass flow rate type; i.e. the static conditions are not specified directly and depend on flow velocity largely). Modifications not covered in this work are currently being implemented in the methodology in order to be able to run cases with Mach number equal to 0.6.

3.3.1 Effect of aerodynamic blockage

According to its definition (see section 3.1.2), calculating the aerodynamic blockage factor requires defining the isentropic conditions in the section of interest (denoted with the subscript "*id*" in [equation 3.15]). The ideal mass flow rate (and thus the blockage factor) is estimated from these conditions by solving the following system of equations.

$$\left.\begin{aligned} B_{th} &= 1 - \dot{m}/\dot{m}_{id} \\ \dot{m}_{id} &= \rho_{id} \cdot v_{id} \cdot A_{th} \\ h_0 &= h_{id} + v_{id}^2/2 \\ s_0(P_{0th}, T_{0th}) &= s(P_{th}, T_{id}) \\ h_0 &= h(P_{0th}, T_{0th}) \\ h_{id} &= h(P_{th}, T_{id}) \\ \rho_{id} &= \rho(P_{th}, T_{id}) \end{aligned}\right\} \qquad \text{[Equation 3.15]}$$

This system is solved with EES®, which contains the desired equation of state for CO_2 and requires the following inputs: static pressure and total conditions at the throat as well as the actual mass flow rate and the throat cross sectional area.

Once blockage factor and static pressure rise coefficient are calculated for all the cases of interest, they can are plotted conveniently (Figure 60) to confirm that the maximum pressure recovery decreases with blockage regardless of the working fluid and, also, that higher C_p can be achieved with supercritical carbon dioxide, especially at low blockage factors. Air is only simulated with blockage factors up to 12 % while 15 % was reached for CO_2. It was found that the points associated to S-CO_2 are more disperse.

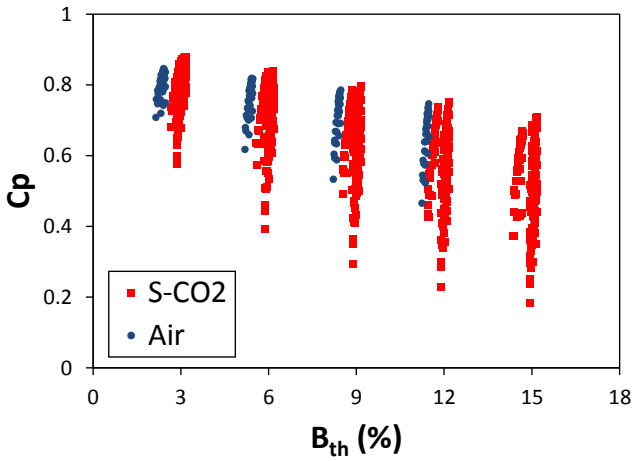

Figure 60. C_p versus B_{th} for all the simulation cases, both for air and carbon dioxide.

The following figures, along with figure 47 , present the differential effect of blockage on diffuser performance in a clearer way. The negative effect that area ratio has on CO_2 diffuser performance is again observed though, at the same time that for air cases, area ratio increments become more and more detrimental when blockage increases. The joint effect of these trends is that differences between fluid behaviours tend to disappear when blockage augments.

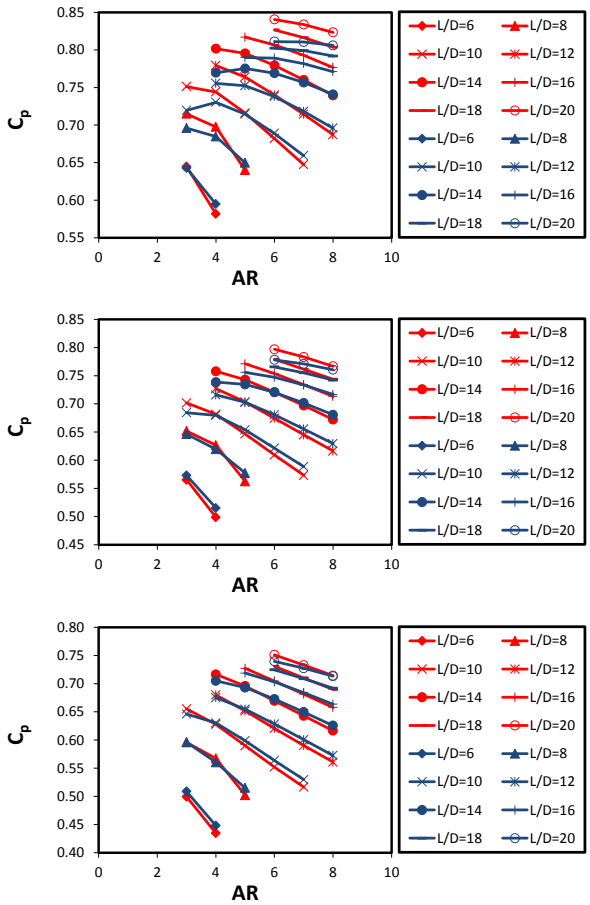

Figure 61. Effect of area ratio onto diffuser performance at curves with constant non-dimensional length, $M_{th} = 0.2$ and $B_{th} = 6$ % (top) , 9 % (centre) and 12 % (bottom). Comparison between air (blue) and S-CO_2 (red)

The following figures show that increasing the aerodynamic blockage factor makes the geometrical parameters more and more determinant: area ratio becomes more detrimental and non-dimensional length more beneficial. Figure 62 compares the influence of blockage on the relative effects of area ratio (left) and non-dimensional length (right). For instance, it is observed that, at constant length (left) and a blockage of 3 %, a modification of area ratio from 6 to 8 hardly reduce C_p whereas this coefficient drops from 0.708 to 0.668 if blockage is 15 %, meaning a reduction of 5.6 %. At constant area ratio, increasing the non-dimensional length from 10 to 20 improves C_p by 13.6 % when blockage is 3% and by 40 % when blockage is 15 %.

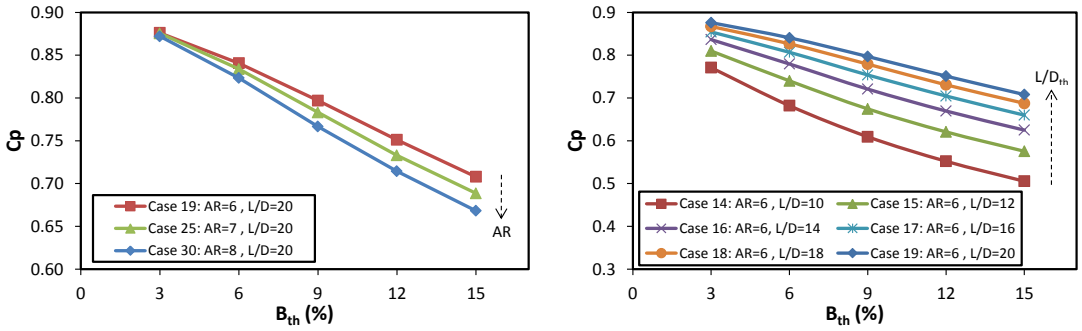

Figure 62. Effect of B_{th} on C_p at M_{th} =0.2 and $Re_{th} = 7.4{\cdot}10^6$.

3.3.2 Effect of Mach and Reynolds numbers

Due to the little effect of these parameters on diffuser performance in comparison with others, their respective analyses start off from the investigations done in the 60s and 70s, in particular the work developed at NASA by Dolan and Runstadler (Dolan & Runstadler, 1973) which confirm the quasi-negligible effects of *M* and *Re*. Regarding Reynolds number, the early works by McDonald and Fox (Mc Donald & Fox, 1966) on incompressible flow in diffusers demonstrated that the influence of *Re* vanishes above $7.5 \cdot 10^4$ as the water flow enters the throat at fully developed turbulent regime (Figure 63). In continuation to this study and incorporating compressible flows, Van Dewoestine and Fox (Van Dewoestine & Fox, 1966) analysed Mach number effects focusing on the appreciable stall line, concluding that this line remains mostly unchanged regardless of the Mach number. Moreover, they found that the pressure recovery of a diffuser with a specific geometry is only slightly affected by Mach number and, as expected, in opposed directions depending on geometry: when M_{th} increases, C_p also increases if the diffuser geometry is under the appreciable stall line; if, on the contrary, the geometry is beyond this line, the opposite effect on C_p is observed.

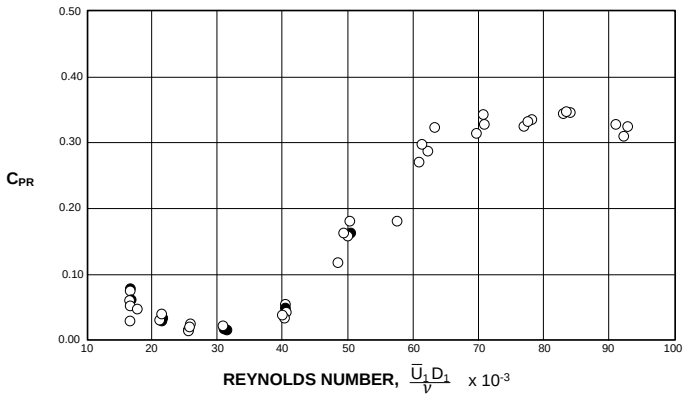

Figure 63. Effect of Re_{th} on C_p as obtained experimentally by McDonald and Fox. (Mc Donald & Fox, 1966)

Since little effects are expected to be obtained, specific rather than systematic studies are initially considered with respect to these parameters with carbon dioxide, covering the ranges M_{th}= [0.2, 0.4] and Re_{th}=[$7.4 \cdot 10^6$, 10^7, $1.6 \cdot 10^7$]. The results obtained are as expected for compressible flow (i.e. M_{th}= 0.4), while at the lower Mach number no stabilisation of C_p with respect to Reynolds number is observed.

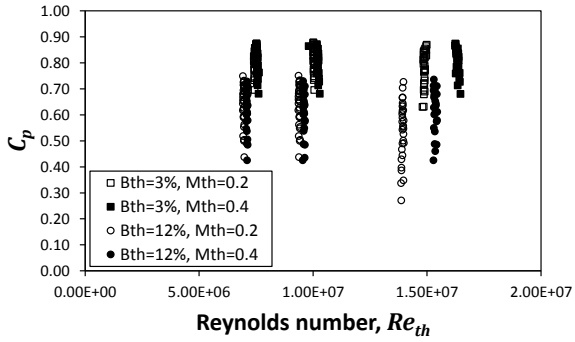

Figure 64. Effect of Re_{th} on C_p for S-CO₂.

Figure 64 shows a wider variation of C_p varies at the highest Re_{th} but only if M_{th}= 0.2; i.e. more widespread distribution of points vertical-wise at low M_{th} whereas at higher Mach number the range of C_p is similar at M_{th}= 0.2 and M_{th}= 0.4. This different pattern suggests that there is an influence of Mach number on the particular value of the critical Reynolds number beyond which no further effect of Re_{th} is observed.

3.4 Effect of second order parameters

In order to organise the information and because of the higher specificity of the parameters considered in this section, they are called "*second order parameters*" and refer to the velocity distribution and turbulence characteristics at the throat: distortion, swirl and turbulence. The analysis of these parameters has been done in the scope of the same project developed by the Thermal Power Group at the Department of Energy Engineering of the University of Seville, by means of a MSc thesis (López Florenciano, 2013), whose main findings are summarised in the next sections as a compendium.

3.4.1 Effect of inlet distortion (velocity profile)

Different distorted velocity profiles have been historically examined by the scientific community researching the performance of diffusers. Small obstacles and local flow injections were the practical artifices for developing experiments, giving place to momentum deficit or excess where needed. CFD simulation makes this task much easier, since the inlet velocity profile is simply modified by an analytical function implemented as a udf. In this sense, the profiles considered (Figure 65) have been taken from previous experimental works and later applied to both S-CO2 and air in different geometries. The tip jet profile, studied by (Padilla, et al., 2011), is derived from the flow around the tip clearance in turbomachinery while the linearly distorted profile (Wolf & Johnston, 1969) and the asymmetric parabola (Mahalakshmi, 2007) are somehow related to the flow at the outlet from a radial impeller, where a momentum deficit exists at the suction side with respect to the pressure side. Symmetric profiles like the jet flow type (Wolf & Johnston, 1969) was also studied. These are all shown in the figure below.

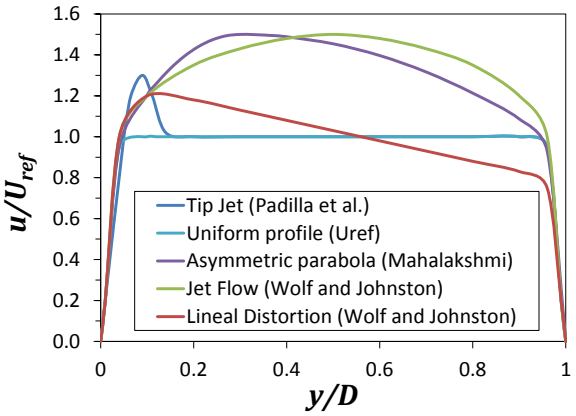

Figure 65. Velocity profiles considered for the analysis of inlet distortion.

The type and extent of distortion is defined by the parameters α and λ, defined by [Equation 3.16] and [Equation 3.15]. The former is a measure of how sharp the profile is, and takes the value 1 for completely flat profiles; whereas the latter quantifies the asymmetry of the profile and is taken ≥ 1 for convenience. By definition, α itself is closely related to blockage factor, hence conditioning the value of the latter strongly and making it fairly difficult to perform systematic analyses (as both α and M_{th} vary simultenaously). On the contrary, the distortion factor λ seems adequate and it is therefore selected for this application.

$$\alpha = \frac{\int_{A_{th}} v^3(r) dA}{\bar{v}^3 \cdot A_{th}} \qquad \text{[Equation 3.16]}$$

$$\lambda = \frac{\int_{A_u} v\, dA}{\int_{A_b} v\, dA} \qquad \text{[Equation 3.17]}$$

The next bullet points along with the results in Table 5 summarise the results with respect to the effect of distortion as obtained in the aforementioned thesis (López Florenciano, 2013):

- Regardless of the operating fluid, the diffuser has an amplifying effect on distortion, evidenced by an increase in λ as the fluid flows through the diffuser.
- This amplifying effect is stronger for air and it is found to be accentuated with the asymmetry of the velocity profile.
- Supercritical carbon dioxide exhibits a slightly higher pressure rise coefficient, the differences between fluids being emphasised for those inlet profiles for which the radial velocity gradients are higher.

	Air			Carbon dioxide		
D_1/D_2	C_p	λ_{in}	λ_{out}	C_p	λ_{in}	λ_{out}
1.5/0.8	0.502	1.065	1.608	0.517	1.094	1.401
1.5/0.5	0.509	1.054	1.479	0.528	1.072	1.307
1.5/0.3	0.520	1.036	1.397	0.541	1.056	1.207
1.5/0.0.	0.540	1.006	1.021	0.569	1.042	1.044

Table 5. Summary of the effect of distortion on diffuser performance for AR=4, L/D_{th}=12 (López Florenciano, 2013).

3.4.2 Effect of swirl component

Swirl modifies the flow structure inside the diffuser both in the core flow and in the boundary layer, bringing about important beneficial effects on pressure recovery, as well as in other engineering fields such as fuel-air mixing in reciprocating engines or homogenisation in coal combustion in boilers. These effects have also been evaluated numerically in (López Florenciano, 2013), making use of the flexibility of ANSYS Fluent for 2D axisymmetric swirl simulation. To this aim, the angular component of velocity is modelled to vary proportional to the radius by means of a *udf* and this is then added to the axial velocity distribution described in section 3.4.1 before.

Although complex parameters have historically been defined to quantify the intensity of swirl [Equation 3.18] (Mc Donald, et al., 1971), the results are here presented as a function of the maximum swirl angle at the throat, Figure 66.

$$m = \frac{Angular\ momentum}{Axial\ momentum} = \frac{\int_0^R v_m v_\theta r^2\, dr}{R\int_0^R v_m^2\, r dr} \qquad \text{[Equation 3.18]}$$

$$\theta_{max} = \max\left[\operatorname{atan}\left(\frac{v_\theta}{v_{axial}}\right)\right] \qquad \text{[Equation 3.19]}$$

As opposed to the effect of inlet distortion, only soft differences were observed in the influence of swirl for each fluid. A very close look at figure 66 would only evidence that the swirl angle for peak

pressure rise is slightly higher for supercritical carbon dioxide than for air (24.5 vs. 23.5) as so is the improvement in C_p (0.10 vs, 0.09), though the patterns are just alike, representing an improvement of 10 %.

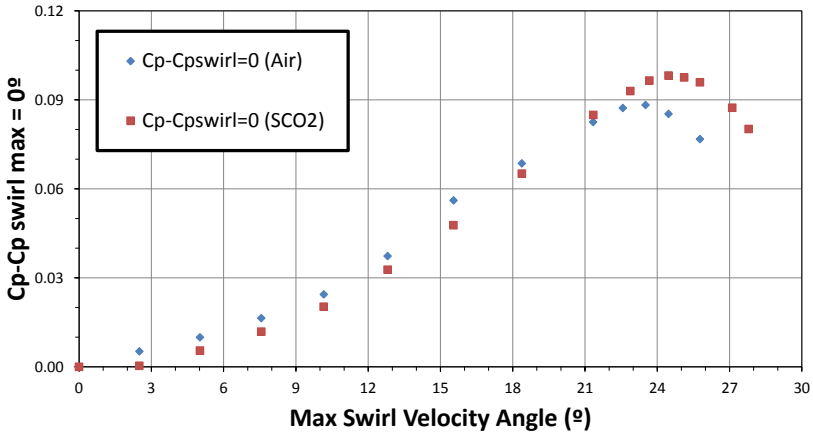

Figure 66. Summary of the effect of swirl on diffuser performance for the geometry AR=5, L/D_{th}=14 at B_{th} = 6%, M_{th}=0.2, Re_{th}=7.4·10⁶ (López Florenciano, 2013).

Additionally, the aforementioned effect of the swirl into the boundary layer flow structure causes in some cases even a null velocity in the axis at diffuser outlet.

3.4.3 Effect of turbulence

There are various features of turbulence that have an effect on diffuser performance: intensity, length scale and structure (i.e. anisotropy), the first two of which were found to present critical values beyond which no further influence is to be expected in a channel diffuser, Figure 5 in (Hoffman, 1981). Unfortunately, no systematic studies on turbulence have been done in the field of conical diffusers to date, even if Klein (Klein, 1981) carried out a complete compendium on the effect of turbulence amongst other parameters. In this work, the author concluded that *"The effect of increasing inlet turbulence intensity is to increase pressure recovery"*, which is true until a certain limit because, as reported in (Hoffman, 1981), there seems to exists a value of intensity beyond which diffuser performance stabilises as shown in figure 67. Apart from this, this figure shows a slightly higher improvement of C_p when L/D_{th} is increased for S-CO2. This comes about because of the beneficial effect that higher lengths have on S-CO2 diffuser performance.

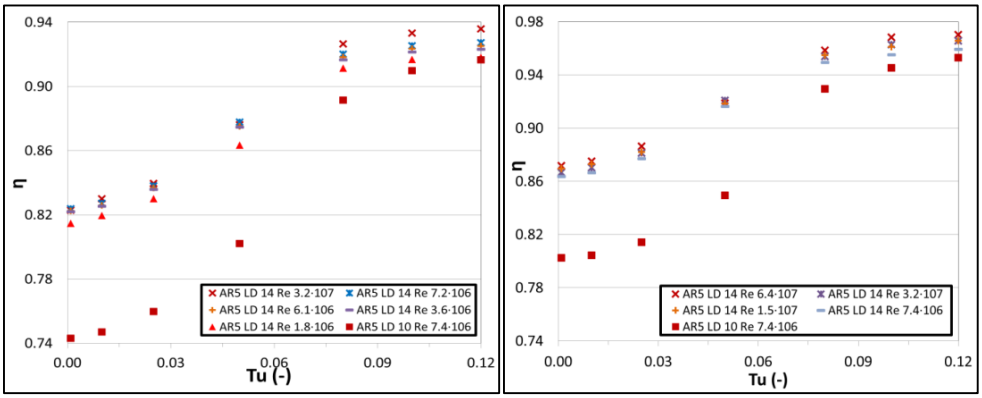

Figure 67. Effect of turbulence intensity at the throat for S-CO_2 (left) and air (right) for different geometries and Reynolds numbers (López Florenciano, 2013).

A critical value of non-dimensional turbulence length scale is easily identified in figure 68, which is in agreement with the results presented by Hoffman (Hoffman, 1981) for channel diffusers. This critical value is around 100, meaning that the characteristic length scale of the turbulence phenomenon is in the order of magnitude of the throat diameter. Regarding the effect of fluid nature, no important differences are worth noting.

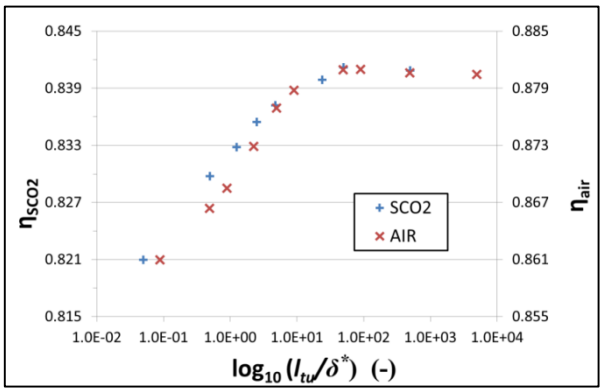

Figure 68. Effect of non-dimensional turbulence length scale at throat for S-CO2 (left) and air (right) (López Florenciano, 2013).

3.5 Summary and conclusions

Conical diffuser operation has been comparatively analysed for S-CO_2 and atmospheric air by CFD simulation in ANSYS Fluent®. For that, an integral tool has been created by combining the CFD software with a mesh generator (ICEM CFD®) and also Matlab® and EES®. This tool permits to modify any parameter of influence in conical diffuser operation, not unlimited but till a certain extent. Nonetheless, for the range of analysis, the tool has been validated for air, since no experimental results are available for S-CO_2 in this field. Therefore, an analysis of uncertainties has been performed for S-CO2 by considering different EOS and turbulence models in addition to apply the GCI analysis in order to determine numerical uncertainties due to the grid, the only source of errors.

Although at the beginning it seems to exist huge differences between atmospheric air and S-CO_2 in regard to conical diffuser operation, the development of this study has shown also the existence of important similitudes between both fluids.

From a geometrical standpoint, the main difference to highlight is diffuser performance is enhanced only by lowering the divergence angle if S-CO_2 is the working fluid, while for air it is possible to increase the pressure rise coefficient by increasing the area ratio. This is herein attributed to the much higher Reynolds number that characterizes S-CO_2, as the higher inertia of this flow penalizes it adaption to divergent walls. However, this tendency is affected by the blockage factor, in such a way that this difference disappear at a 12 % blockage. It means that, at this level of analysis, the influence of fluid nature disappear in considerably distorted flows.

It is another similitude the fact that blockage is the parameter with stronger influence. Moreover, as for air, Mach and Reynolds number have virtually no effect on the pressure rise coefficient.

From the study on inlet velocity profiles, it was observed that: (i) air experiences a more pronounced distortion that the supercritical fluid, and by other side (ii) for those profiles with higher gradient of radial velocity, the operation with S-CO_2 will be improved at higher extent in relation to air because of the lower weight of viscous forces.

Finally, in regard to turbulence and swirl parameters, there weren't observed important differences between both fluids.

3.6 Further calculations towards more reliable turbulence modelling

Under the lack of experimental results in the field for the fluid of interest, the numerical approach employed in this project was compared against another one based on a more complex turbulence model, in contrast to the RANS turbulence models herein considered. DNS was discarded whereas focus was put on LES. However, since S-CO2 diffuser involves high Reynolds number and wall bounded flows, computational efforts are very strong in comparison with free flow simulations. In consequence, the Wall-Modeled Large Eddy Simulation (WMLES) (Shur, et al., 2008) approach was used for the comparison.

WMLES belongs to the ELES (Embedded Large Eddy Simulation) approach, where two different zones are distinguished in the computational mesh: one where turbulent scales are modelled by using RANS models, and another one where turbulent scales are solved by Large Eddy Simulation. It is therefore a hybrid method that permits using 2-equation models in the near wall region, while the core flow can be directly solved by LES. Thus, three diffuser cases were run on WMLES computational models, requiring a total of around between 35,000 and 55,300 CPU hours per case, which would require 1 year and 7 months of just computational time if these calculations were performed with the GMTS computers and the academic licenses available. Therefore, this work was subcontracted to ANSYS, Inc, in parallel to the development of other tasks of this project.

In general terms, the main conclusion was that results with RANS and WMLES were very similar, showing noticeable differences near the end of the cone, where stall flow becomes more likely. Next, details of ANSYS WMLES calculation are provided for the case 1 only, being the remaining cases very similar to the on presented here with results qualitatively identical.

Case	AR	L/D_{th}	M_{th}	Re_{th}	B_{th}	Comments
1	3	8	0.4	$7.4 \cdot 10^6$	0.03	Max. C_p @ low B_{th}
2	5	8	0.4	$7.4 \cdot 10^6$	0.12	Max. C_p @ high B_{th}
3	3	10	0.2	$7.4 \cdot 10^6$	0.03	High 2θ (near stall)

Table 6.Cases analysed in the ANSYS WMLES study.

Six profiles were measured along each diffuser at 0, 20, 40, 60, 80 and 100 % of their lengths and velocity, pressure and temperature profiles were extracted and plotted in the table below, both for RANS (solid lines) and WMLES (dashed lines) calculations. As observed, results start differing apart from 80 % of the length, i.e. where stall flow may happen. However, mean values of pressures are very similar in both cases, offering very similar diffuser performance coefficients, C_p.

	RANS	WMLES
Velocities	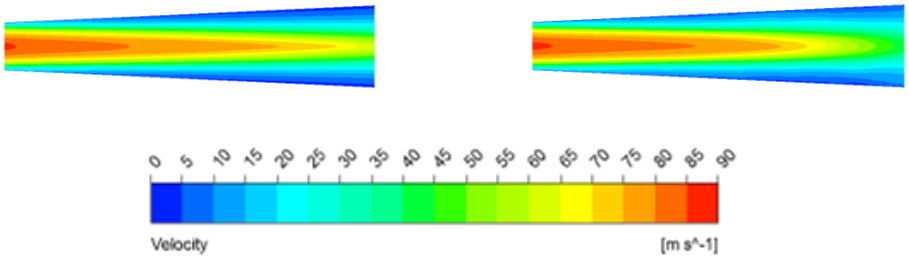	
Pressures	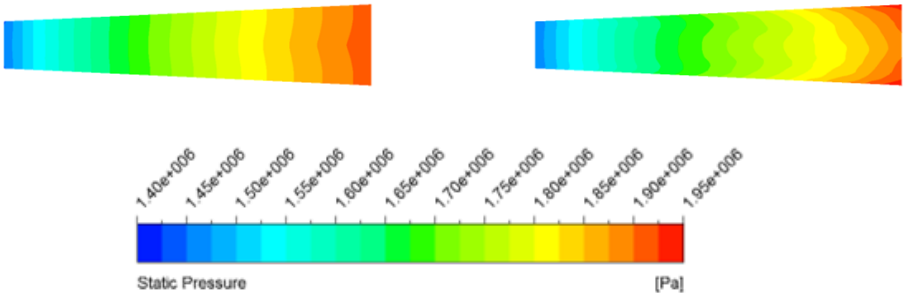	
Temperatures	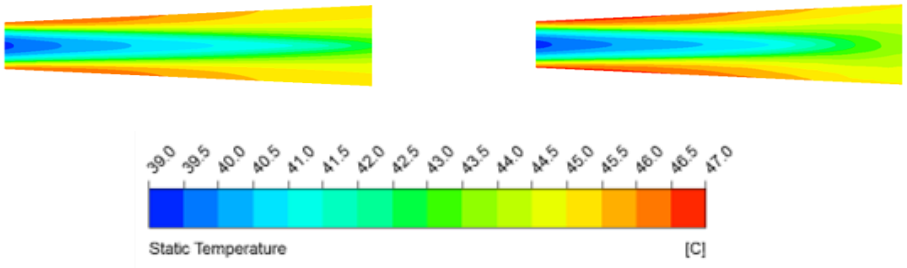	

Table 7.RANS vs. WMLES for case 1.

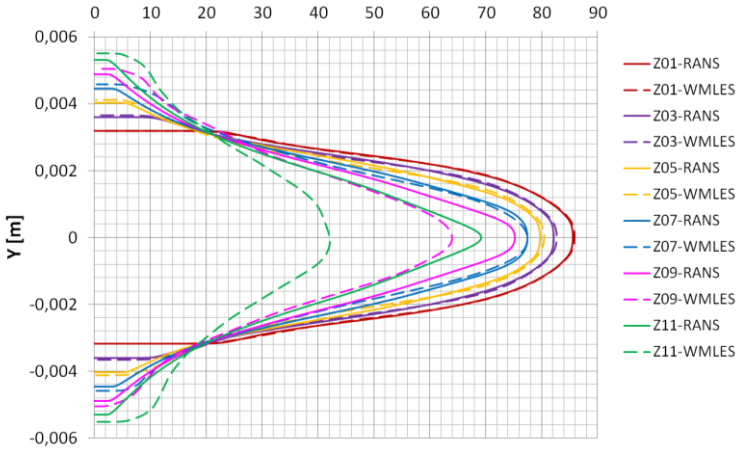

Figure 69. Velocity magnitude (in m/s) profiles comparison for case 1.RANS vs. WMLES comparison.

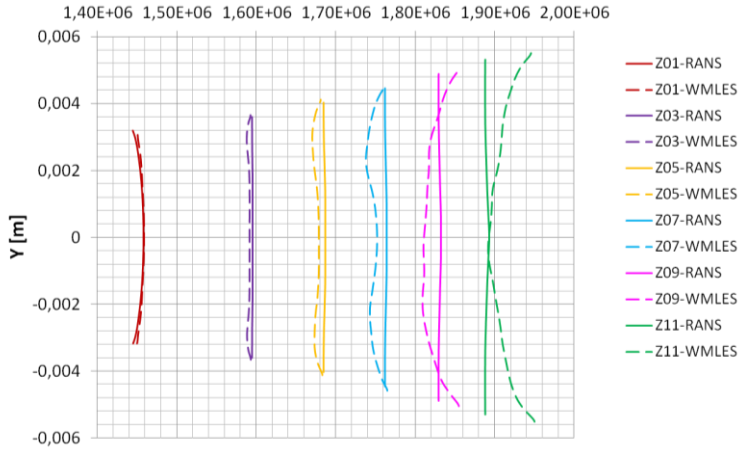

Figure 70. Static pressure (in Pa) profiles comparison for case 1. RANS vs. WMLES comparison. NOTE: Operating pressure of reference: $7.5 \cdot 10^6$ Pa.

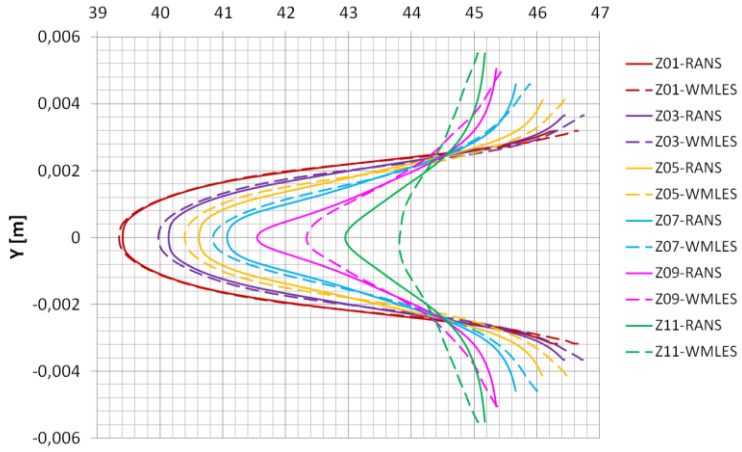

Figure 71. Static temperature (in ºC) profiles comparison for case 1. RANS vs. WMLES comparison.

Two main conclusions were extracted from this analysis:

- Mean values of interest, i.e. static pressure to calculate afterwards performance coefficient; are very similar for both approaches. Therefore, diffuser maps obtained with the RANS-2D tool are considered numerically satisfactory, being still pending the corresponding empirical validation.
- On the other hand, local values are noticeably different between both models, especially apart from the 60 % of the diffuser length. In consequence, measurements related to that such as peaks of velocity, wall shear stresses, etc. are not reliable in the 2D tool.

From the light of these results, it could be deduced that RANS simulation provides satisfactory results for cases operating in the non-appreciable stall region (Figure 32), not being an accurate tool for predicting stall flow.

CHAPTER 4. One-dimensional model of supercritical carbon dioxide centrifugal compressors

In spite of the powerful simulation tools existing nowadays, one-dimensional techniques still constitute an essential part in the design process of a turbomachinery (Aungier, 1995). As an example, Dr. D. Japikse recommends the flow diagram of figure 72 for turbomachinery design (Japikse, 1996), where everything starts with one-dimensional (also called quasi-two-dimensional) evaluations. Moreover, because of their simplicity, these tools allow for quick evaluations of how a specific design would perform at given conditions, whether it be on or off-design operation.

In addition to conservation laws, 1D models require experimental correlations for the evaluation of key performance parameters such as pressure loss coefficients and deviation angles amongst others. Nevertheless, it seems that, as far as supercritical carbon dioxide is concerned, there is not a body of knowledge which ensures the successful design of turbomachinery. This observation is based on the fact that the expected design efficiencies are not being reached by the very few existing machines at SANDIA National Laboratories, Bechtel Marine Propulsion Corporation and Tokyo Institute of Technology. In fact, a number of researchers have pointed out the need to develop a new design theory specific for supercritical carbon dioxide turbomachinery (Ulizar & Pilidis, 2000) (Wang, et al., 2004). In consequence, new proposals are included in this chapter aiming to contribute to fulfilling this gap.

A literature review is first presented in section 4.1. Then the one-dimensional performance analysis is presented in detail (direct problem) and validated in the following section. Once the validity of the tool is confirmed to the extent possible (validation against experimental data), the equations of the performance model are re-organised to solve the indirect problem, which is presented in section 4.4. Finally, the main conclusions are exposed together with a summary of the chapter.

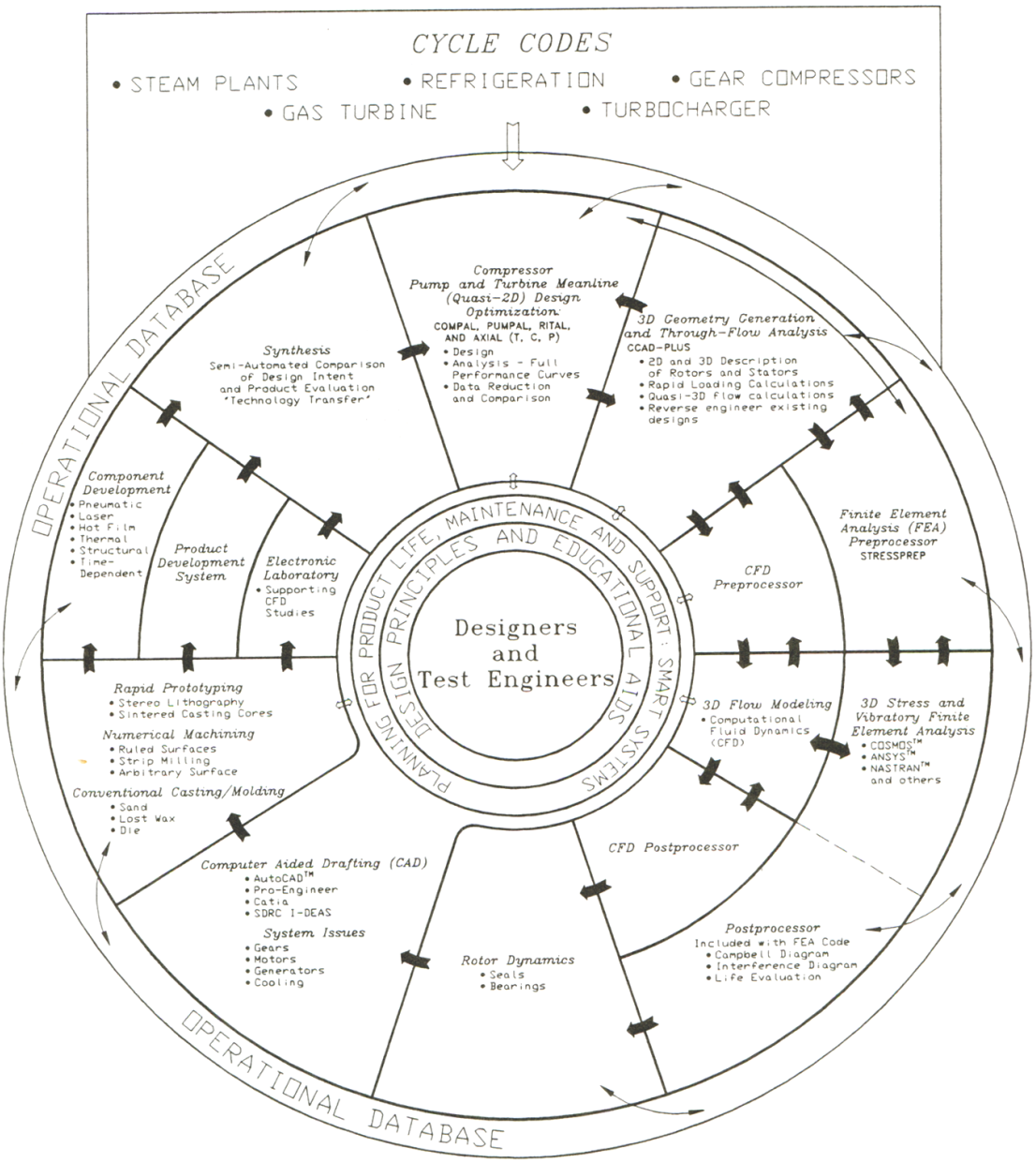

Figure 72. Design strategy proposed by D. Japikse (Japikse, 1996).

4.1 Review of one-dimensional centrifugal compressor models

A one-dimensional model is a numerical tool which solves for the thermo-fluid dynamic state of the gas/liquid at the interface between the different elements comprised by the turbomachinery under analysis. As such, the flow is characterised by the mean values of the relevant properties at each station of interest. Obviously, conservation laws of mass, momentum and energy, along with the equation of state must be taken into account by the model. Nevertheless, there exist several approaches to model the physics inside each compressor element, all of them potentially valid as long as its comparison against experiment shows good agreement.

An author to highlight in the field of radial turbomachinery is *Dr. David Japikse*, whose work is a remarkable contribution to illustrate the physical phenomena that occur inside each turbomachinery

component. In addition, he has provided methods and tools both for solving the direct (analysis) and the indirect (design) problems. All this work has been managed through Concepts ETI Inc., created in 1980, which is nowadays one of the leading software developers for turbomachinery design worldwide. And not only this, the books by Dr. Japikse and co-workers, for instance (Japikse, 1996), are very illustrative and provide valuable graphical information about different aspect of turbomachinery.

Focusing on one-dimensional models, Dr. Japikse pays particular attention to the two-zone model originally developed by (Dean & Senoo, 1960), which is based on splitting the flow at the impeller exit into an isentropic core flow (*jet*) and a non-isentropic distorted flow (*wake*) where all the impeller losses occur. There are two main parameters that characterise this model: the ratio of secondary to total mass flow rates χ and the secondary regime area fraction ε, the dependency between which is correlated in figure 73. The model is closed by assuming a value of χ depending on the application, typically between 0.02 and 0.25 for efficient and poor design cases respectively. Implementing the two-zone model requires the assumption of χ which is well controlled for standard turbomachinery with conventional fluids but incurs large uncertainty when it comes to using supercritical carbon dioxide (since no experimental data exist). Concluding with this model, the flow is mixed after the impeller by applying mass, momentum and energy conservation. Therefore, as the author himself states, "*the concept of using a blockage parameter at the rotor exit is fundamentally inconsistent*".

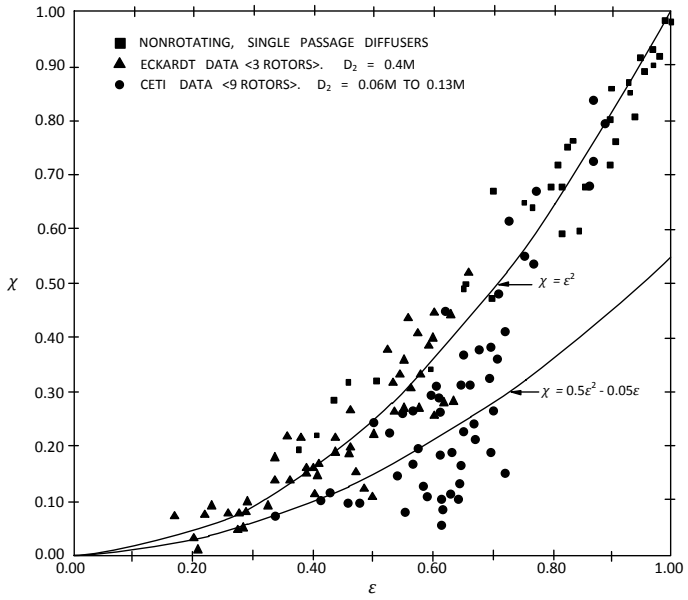

Figure 73. Two-zone model results (Japikse, 1996).

The Two-Elements-In-Series (TEIS) model is an alternative approach to compressor design (Japikse, 1996). This model assumes that the impeller channel can be modelled as two simple elements (see Figure 74) in series, the first one of which might be a nozzle or a diffuser, depending on the flow regime (high or low flow respectively), whilst the second one is always a diffuser. The performance of each separated device is affected by the parameters exposed in chapter 3, making it evident that the geometry and flow features at the inlet to both elements need to be identified in order to calculate their performances, whether by static pressure rise coefficients ($C_{p,a}$ and $C_{p,b}$) or equivalent efficiencies (η_a and η_b). Again, experience plays a crucial role for closing this model as the elements' performance parameters are fixed according to sizes and applications. From the point of view of supercritical carbon dioxide, serious doubts arise once more due to the limited database available. In this sense, chapter 3 tries to contribute to overcoming this lack of knowledge so that a complete set of information for the new fluid of interest is available in the future. In contrast to the two-zone model, the impeller outflow in the TEIS model is characterised by a blockage factor, as it is the case in diffuser theory.

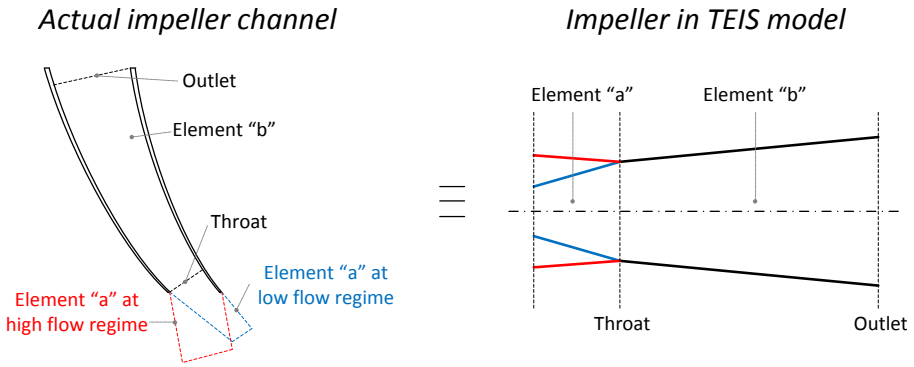

Figure 74. Two-Elements-In-Series (TEIS) conceptual model.

Slip is another fundamental feature of a radial impeller and it is conceptually similar to deviation in axial machinery. The formation of a bubble on the suction side at the outlet makes the streamlines deviate from the pressure to the suction side, bringing about a difference between blade and flow angles at the trailing edge of the blade. This fact has been investigated by several authors amongst which Dr. Japikse suggests using the one by Eckardt (Eckardt, 1980), expressed in [Equation 4.1].

$$1 - \sigma_{slip} = \frac{v_{2u}}{u_2}\left(\frac{1}{\sigma'_{slip}} - 1\right) \qquad \text{[Equation 4.1]}$$

Similar to Japikse (Japikse, 1996), Cumpsty's work (Cumpsty, 1989) makes a complete review of the models available for compressor design, where a compendium of the different approaches from one-dimensional concepts such as the Jet and Wake and other loss-based models, to two-dimensional blade-to-blade and hub-to-shroud calculations is gathered. Additionally, this book contains design recommendations that applicable to conventional turbomachinery and also an important set of impeller flow measurements. Therefore, this reference emerges as an important source of information to find physical validation of the results of this project rather than as a specific guide for radial machinery analysis or design.

Another work of relevance in the field of radial turbomachinery is the one developed by *Ronald H. Aungier* (Aungier, 2000). Throughout his carrier, R. H. Aungier has created methodologies both for turbomachinery analysis and design with methods based on loss models rather than two-zone models as it was the case for Japikse, approaches shared by several authors in the field (Yahya, 2005), (Balje, 1981), (Schobeiri, 2005). The main flaw of this approach is nevertheless that is virtually impossible to measure all loss terms in each turbomachinery element individually what, in turn, makes it impossible to validate them if not from a global standpoint. However, as it can be later seen, most loss models rely on the physics of the flow which makes them less dependent on fluid nature. This becomes a considerable advantage for the particular case of this project as the fluid is not conventional. Aside from conservation laws, Aungier's models are based on the calculation of several loss contributions to finally calculate a total pressure drop coefficient for each element. These are all one-zone models, so no distinction between secondary and primary zones is made. Instead, aerodynamic blockage factor are considered at each station.

As opposed to Japikse, who adopted Eckardt's approach, Aungier developed a somewhat new slip factor expression by modifying the original work by Wiesner (Wiesner, 1967). His book (Aungier, 2000) is a compendium of all his work on radial compressors and constitutes a complete guide the aerodynamic design of centrifugal compressors, from the initial concept to the final three-dimensional geometry optimisation.

Although more design-oriented, the work presented by A. Whitfield and N.C. Baines (Whitfield & Baines, 1990) also provides guidelines for the performance analysis of both for turbines and compressors. The approach is similar to Aungier's but, in lieu of pressure loss coefficients, Whitfield and Baines's proposal is based on entropy gain contributions, defined as $\sigma = \ln\left(-\Delta s/R_g\right)$ and calculated by empirical

correlations; this approach is also found in (Denton, 1993),. These authors dedicate a chapter to remark special features of separated flows in impellers by using one and two-zone models, where the non-experimental nature of the two-zone models is again noted given by the fact that it is based on assuming a somewhat arbitrary mass flow ratio between primary (jet) and secondary (wake) flow regime. Regarding performance, the section dedicated to separation and based on the study by Frigne and Van den Braembussche (Frigne & Van Den Braembussche, 1979) must be highlighted. From this, some features of the flow pattern can be obtained (see Figure 75).

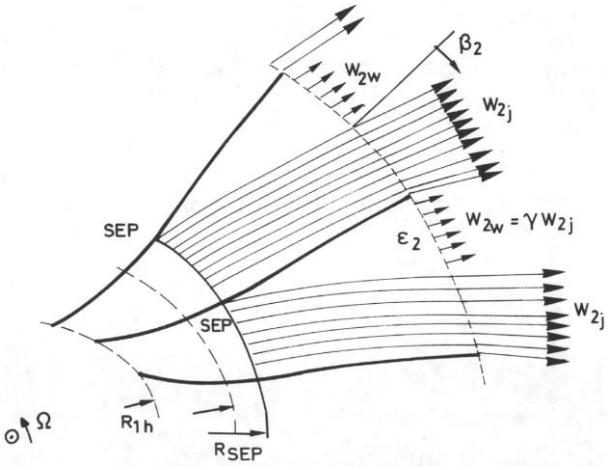

Figure 75. Streamlines after separation in the impeller according to (Frigne & Van Den Braembussche, 1979).

Balje also proposes a loss-based model in (Balje, 1981) previously in (Balje, 1970) , putting especial emphasis on the boundary layer theory. Balje's loss model is based on a more or less precise evaluation of both displacement and momentum boundary layer thicknesses, δ and θ respectively, the ratio between which is called the boundary layer shape factor: $H = \delta/\theta$. This author makes an analysis of the development (growth/reduction) of the boundary layer across an element of interest, progressively increasing the complexity of this element: the flow next to a wall first and through a cascade later (supersonic, radial, etc…). Thus, once the boundary layer is characterised, a total loss coefficient is calculated mainly as a function of Reynolds and Hagen[10] numbers, geometrical magnitudes and a reference free stream velocity. Unlike other loss-based approaches, such as (Aungier, 2000) (Whitfield & Baines, 1990), this proposal does not separate all loss contribution but only the three principal mechanisms: profile, end-wall and clearance gap losses (note that diffusers comprise the first two contributions only).

From a different perspective, it is also worth mentioning the dimensional analysis presented in (Balje, 1981) and based on specific speed (N_S) and diameter (D_s). Balje managed to create a general map applicable to all the different types of turbomachinery (compressors and turbines, radial and axial, etc.) and relating these two non-dimensional parameters with efficiency and other easy to obtain features (Reynolds number, some geometrical parameters…). These maps still constitute a powerful tool for the preliminary design of turbomachinery, since they provide initial estimations of some design parameters on the basis of target efficiency. More specifically in the field of S-CO_2 turbomachinery, these maps have gained particular importance due to their use in the methodology proposed by Barber-Nichols Inc.(R) (Fuller, et al., 2012), pioneering company in designing S-CO_2 turbomachinery. In fact, the design methodology herein proposed is also based on these maps in the initial stages.

Back in the 50's, these dimensionless terms (N_S and D_s) were discussed in (Sheperd, 1956), where the author presented in a simple way a dimensional/similarity analysis of turbomachinery based on the application of the Π-Theorem. Sheperd also suggested a pressure loss pressure model to provide a

[10] *The Hagen number is defined as the ratio between pressure and viscosity forces:* $\mathrm{Ha} = \frac{(\mathrm{dp/dx})\delta^*}{\tau_{\mathrm{wall}}}$, *where* δ^* *is the boundary layer thickness.*

qualitative explication of turbomachinery performance. Special attention was paid to the slip factor, a distinguishing feature of radial compressors with respect to axial. More focused on qualitative descriptions and design aspects of all types of turbomachinery, this work proposed design rules and analysis methods generally applicable in conventional turbomachinery even nowadays. Some of them have been applied herein, even if they have proved invalid for supercritical carbon dioxide. As a clear example, Sheperd pointed out that "*The pressure ratio of radial flow compressors is governed largely by stress limitations at high tip speed*"; however, S-CO_2 turbomachinery is found to be more constrained by the risk of condensation which enforces a reduction in the overall pressure ratio (see section 4.4.1).

4.2 Model of performance of supercritical CO_2 centrifugal compressors: direct problem

Aiming to produce a design tool, a model of performance is created to solve the direct problem first. Then, once validated (section 4.2.6.1), a one-dimensional design tool is also developed by combining the same equations in a different manner (section 4.4), hence solving the inverse problem. Matlab® is the software of choice to implement this tool.

The model is a one-zone type, mainly because of the limited empirical information available for supercritical carbon dioxide. Hence, the required assumptions such as the secondary regime mass fraction in two-zone models or the efficiencies of the elements in TEIS models are avoided, the precision of the tool relying on the fidelity of each individual physical model. The concept of the model is consequently based on individual pressure loss coefficients that affect different elements of the compressor to finally close analysis with the conservation laws of mass, momentum and energy. It is therefore what D. Japikse called a data-driven physical model in (Japikse, 2009), as opposed to a data-driven global model which works by means of empirical correlation statically obtained and involving overall performance parameters of the turbomachinery only.

As shown in previous chapters, supercritical carbon dioxide has densities around 300-500 kg/m^3 at compressor inlet, bringing about very low volume flow rates for a considerable power production. Due to the reduced dimensions of turbomachinery, no inlet guide vanes (IGV) are included in the model as it would penalise the performance. As sketched in figure 76, the model does comprise impeller, vaneless space, vaned diffuser and volute. Additionally, the inducer is also indicated which comprises from the inlet section to the impeller throat. Given that the impeller throat presents the smallest cross sectional area in the compressor, its precise modelling offers decisive information, especially for the case of supercritical CO_2 and not only for the direct problem but also for the inverse one (section 4.4).

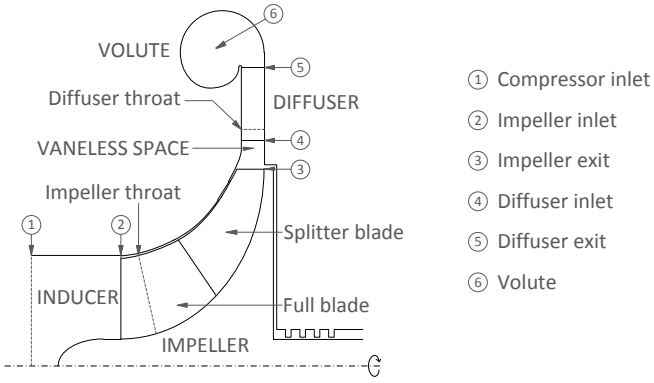

Figure 76. Elements of the centrifugal compressor modelled (Meridional view).

The model (for the direct problem) yields the outlet flow conditions and other performance parameters related to the internal flow as a result: slip factor, aerodynamic blockage, recirculating and gap flows and disk friction among others. To this aim, it needs to be fed with: total conditions at the inlet, mass flow rate, shaft speed and full geometry (not to say the fluid, which it carbon dioxide).

Finally, because of its conceptual approach and also for his clarity and accessible information, Aungier's book (Aungier, 2000) is considered as the reference work. Nonetheless, some modifications have been implemented in the model in an attempt to make it more precise for supercritical carbon dioxide applications.

4.2.1 Fundamentals of the model

The flow is studied in two different reference frames as usual: absolute and relative, the later rotating around the impeller shaft and at the same speed. The usual curvilinear coordinate system (m,n,θ) is employed, where m is the meridional coordinate along a *stream surface*[11], n is the coordinate normal to the cited *stream surface* and θ is the angular coordinate, as it is in a cylindrical system. As a meanline model, each section normal to the meridional direction is characterised by mean values that are constant along the n and θ coordinates. In consequence, the analysis is entirely conducted along the stream surface located at midspan.

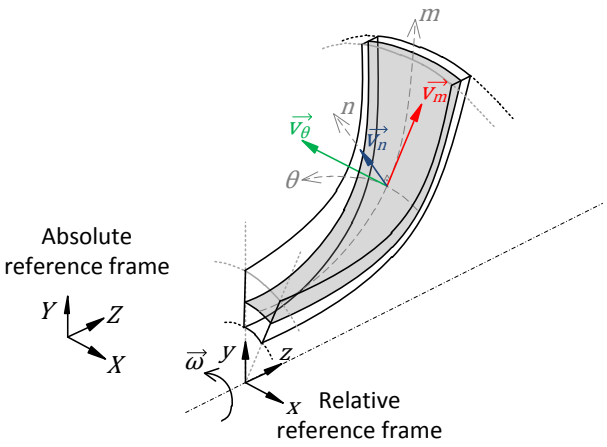

Figure 77. Coordinates and reference frames.

It is well known from the principles of relative motion that absolute velocity ($\vec{v}$) is the sum of relative velocity ($\vec{w}$), or velocity relative to the moving reference frame, and the velocity of the moving reference frame ($\vec{u}$). For the particular case of a rotating impeller, the latter turns into the tangential blade speed at the location of interest, see below. As observed, the angles are defined respect to the meridional direction, α and α' corresponding to the absolute and relative flow angles respectively, whereas β (not represented in figure 78) is used for the geometric or blade angles (the latter term used most frequently).

$$\vec{v} = \vec{w} + \vec{u} = \vec{w} + \vec{\omega} \times \vec{r} \qquad \text{[Equation 4.2]}$$

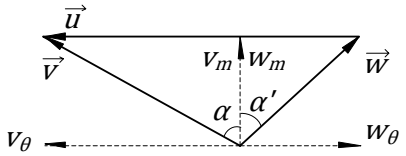

Figure 78. Velocity diagrams.

Mass conservation implies that $\rho \cdot v_m \cdot A$ is kept constant along the turbomachinery, A being the cross sectional area in the meridional direction. Furthermore, should the flow be isentropic spanwise (along n) and pitchwise (along θ) in section A, the boundary layer would not exist and the effective area would coincide with the geometric one. Otherwise, an aerodynamic blockage factor exists which brings

11 A stream surface is defined within the scope of this analysis as the locus of an infinite number of stream lines rooted at a constant radius arc; i.e. velocity is tangent at any location of the stream surface and therefore no normal velocity exists.

about a reduction in flow area. Given that a single zone model is used, this effect is taken into account with a certain blockage factor *B* which affects continuity as follows:

$$\dot{m} = \rho \cdot v_m \cdot A \cdot (1 - B) \qquad \text{[Equation 4.3]}$$

Though omitted so far, it is quite clear from the previous equation that the analysis is performed in steady state conditions, for which the first principle of Thermodynamics applied to a control volume is:

$$\dot{Q} + \dot{W} = \dot{m} \cdot \Delta\left(e + \frac{p}{\rho} + \frac{v^2}{2}\right) \qquad \text{[Equation 4.4]}$$

Where both thermal and mechanical power ($\dot{Q}$ and $\dot{W}$) if transferred or done on to the system. From the definition of static enthalpy ($h = e + p/\rho$), it is obvious that the amount in parenthesis is the total enthalpy. Due to the very small residence time of a fluid particle inside a turbomachinery and given the very large exchange of kinetic energy and mechanical work within it, it is commonly assumed that these equipment are adiabatic per unit mass. In consequence, energy conservation turns into $\Delta h_0 = 0$ across a stationary control volume (for instance vaneless space, diffuser and volute), whereas for the moving parts (for instance the impeller) $\dot{W} = \dot{m} \cdot \Delta h_0$.

Complementary to the first principle of Thermodynamics, the Euler equation [Equation 4.5], which results from applying the law of conservation of angular momentum in the impeller) is a fundamental tool to calculate the amount of work exchanged between impeller and fluid; this equation is usually termed the *Fundamental Law of Turbomachinery*:

$$h_{03} - h_{02} = v_{u3} \cdot u_3 - v_{u2} \cdot u_2 \qquad \text{[Equation 4.5]}$$

The second principle of Thermodynamics is applied by verifying that $\Delta s \geq 0$, which is done in practice by calculating the total pressure losses at each element as exposed in the following sections.

Finally, an appropriate equation of state closes the problem. Going back to chapter 2, it is now known that an accurate thermodynamic model for supercritical CO_2 is available in the refPROP® database which can be load into ANSYS Fluent® by calling the *co2.fld* file. The same file can also be called in Matlab® by the function refpropm.m (Lemmon, et al., 2010) which is utilised in this one dimensional model.

Before continuing with the description of the model, table 1 shows inputs and outputs of it.

Inputs	Outputs
• Fluid • Total temperature and pressure at inlet • Mass flow rate • Shaft speed • Geometry: radii, angles, thicknesses, number of blades and others	• Outlet conditions • Pressure ratio • Efficiencies • Other performance parameters: slip, blockages, losses and others.

Table 8. Inputs and outputs of the model of performance (direct problem).

4.2.2 Inducer model

Modelling the inducer consists in calculating the resulting inlet static conditions for the given total conditions and geometry and the available loss model in this component. It is normally a complicated task to measure the throat dimensions, both in the impeller and the diffuser since the throat is located very close to the leading edge of the blade. Its dimensions are thus computed by assuming:

- Same blade height than at the leading edge.
- The throat width is given by the following expression referred to figure 79.

$$W_{th} = \left(\frac{2\pi r_2}{z_{FB}} - t_2\right)\cos\beta_2 \qquad \text{[Equation 4.6]}$$

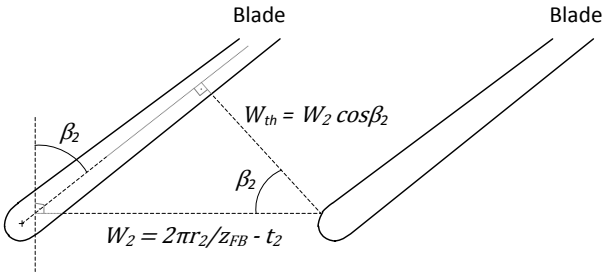

Figure 79. Throat geometry calculation.

This section of the impeller contains the portion of the blades comprised between the leading edge and the throat, where the incidence losses take place. In addition to this, another loss term is included to account for the reduction in flow area between sections 1 and 2 (Figure 76), which is implemented as a sudden contraction coefficient.

$$\varpi_{cont} = \left(1 - \frac{A_2}{A_1}\right)^2 = \left(\frac{r_{2h}}{r_{2s}}\right)^4 \qquad \text{[Equation 4.7]}$$

Incidence losses are located at the leading edge of the blades and arise due to the difference between (relative) flow and blade angles at the inlet to the channels. In a very intuitive way, (Conrad, et al., 1980) suggested to assume the incidence losses directly proportional to the difference in tangential velocities between the actual relative velocity and the ideal one at zero incidence:

$$\Delta h_{inc} = \frac{1}{2} f_{inc}\left(w_{u2,id} - w_{u2}\right)^2 \qquad \text{[Equation 4.8]}$$

The factor f_{inc} is calculated experimentally and, when unknown, values in the range 0.5-0.7 are suggested in (Conrad, et al., 1980).

Despite being reported in (Oh, et al., 1997) as the most accurate incidence loss model, this model is discarded here due to the lack of experimental data in the S-CO_2 field. As an alternative, Aungier's proposal is considered, where the following two contributions are taken into account in this loss term: (i) the destruction of tangential velocity owing to the different flow and blade angles at the leading edge, and (ii) the reduction in flow area produced by the blades themselves (Aungier, 2000). It is noted here that the latter is usually negligible.

$$\varpi_{inc} = 0.8\left(1 - \frac{v_{m2}}{w_2 \cos\beta_2}\right)^2 + \left(\frac{z_{FB}\, t_2}{2\pi r_2 \cos\beta_2}\right)^2 \qquad \text{[Equation 4.9]}$$

As proposed by (Aungier, 2000), the final incidence loss coefficient results from averaging the values calculated at the hub, mid-span and shroud with the following relative weights 1:10:1.

For some impellers, the diffusion of the relative flow between the leading edge and the throat is found to be not negligible and is thus taken into account by considering an additional *diffusion* loss term. Such term is computed as follows where it must be always ensured that $\varpi_{diff} \geq 0$ (Aungier, 2000);if not, this additional term is set to zero:

$$\varpi_{diff} = 0.8\left(1 - \frac{w_{th}}{w_2}\right)^2 - \varpi_{inc} \qquad \text{[Equation 4.10]}$$

Moreover, the diffusive effect between leading edge and throat has sometimes been observed to bring about stall and must thus be limited. The stall criterion suggested by Aungier to detect the onset of stall is $w_{2s}/w_{th} \geq 1.75$ (Aungier, 1995), after which diffusion losses are limited by [Equation 4.11], as found by (Kosuge, et al., 1982).

$$\varpi_{diff} \geq \left(\frac{w_{2s} - 1.75 w_{th}}{w_2}\right)^2 - \varpi_{inc} \qquad \text{[Equation 4.11]}$$

At the other end of the operating range, high flows are likely to bring about sonic conditions at the throat, giving place to additional choking losses. Let A^* be the area for which sonic conditions would theoretically be reached for the operating mass flow rate. Then the following pressure loss coefficient due to choking must be included:

$$\varpi_{CH} = \frac{1}{2}(0.05 \cdot X + X^7) \quad ; \quad if\ X = 11 - 10\frac{C_r\, A_{th}}{A^*} > 0 \qquad \text{[Equation 4.12]}$$

Where $C_r \cdot A_{th}$ is the effective throat area calculated from the following contraction ratio:

$$C_r = \sqrt{A_2 \cos\beta_2 / A_{th}} \qquad \text{[Equation 4.13]}$$

It is finally noted that no choking losses take place when the effective throat area is large enough ($\varpi_{CH} = 0$).

4.2.2.1 Algorithm

There is a mutual dependence of flow velocity upon thermodynamic state and viceversa for given total conditions and mass flow rate at the inducer inlet. More in particular, the velocity of the flow depends upon mass flow rate and static density for a certain throat area; this is usually expressed by the continuity equation in a simple manner. Unfortunately, the static properties of the fluid are calculated from the total inlet pressure and temperature, total pressure losses and flow velocity, thus making it necessary to follow an iterative scheme to solve the fluid dynamics and thermodynamics of the inducer and impeller.

As described before, contraction, incidence, diffusion and choking losses must be accounted for when solving the inducer numerically. Amongst these, contraction and incidence losses are calculated directly but the remaining loss terms make use of an iterative calculation based on energy conservation and pressure loss equation between impeller inlet and throat, Figure 76:

$$h_{0th} = h_{02}$$
$$P_{0th} = P_{02} - (P_{02} - P_2)\sum_{2\rightarrow th} \varpi_i \qquad \text{[Equation 4.14]}$$

A first estimate of the thermodynamic conditions at the throat is obtained by assuming no losses, i.e. isentropic flow. This makes it possible to re-compute the contribution of losses and compare them against the values of the previous iteration step (which, as said, is null for the first one). This routine continues until convergence is achieved, typically when the error between two consecutive values of the pressure loss coefficient is below 10^{-4} % (Figure 80).

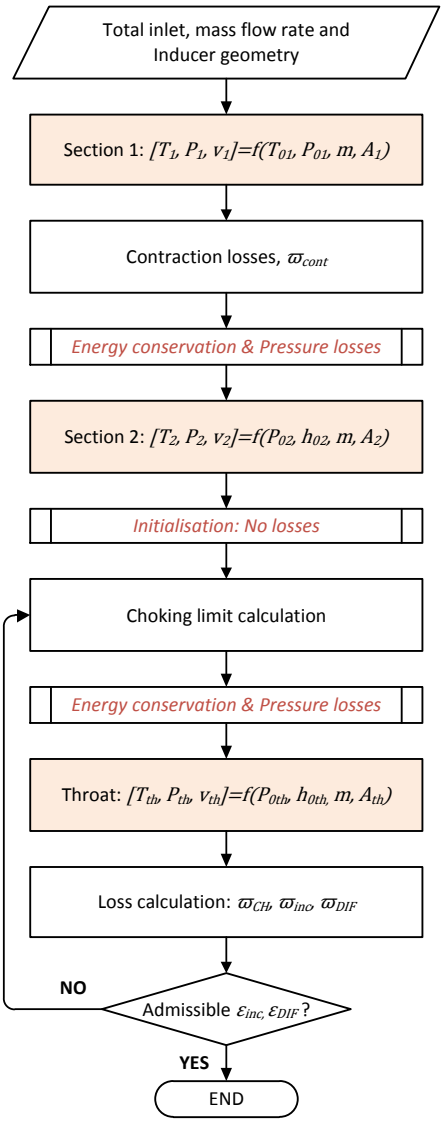

Figure 80. Flow diagram for the analysis of the inducer.

4.2.3 Impeller model

Following the philosophy of the project, the fluid dynamic model of the impeller is based on pressure loss coefficients, as it is for the inducer. The flow is analysed in the relative frame of reference, for which loss coefficients apply to the relative dynamic pressure across the element. Impeller losses are classified as internal and parasitic, the latter not existing in stationary elements as diffusers and volute. Internal losses refer to the irreversibilities originated due to the non-ideal behaviour of the flow, which produces an increase in entropy or, equivalently, a total pressure losses. In contrast, parasitic losses have a mechanical nature, reducing the total enthalpy increase of the fluid with respect to the mechanical work produced by the shaft. There are three different sources of parasitic losses: disk friction (I_{DF}), recirculation flow (I_R) and leakage flow (I_L) (see figure 81). Inducer loss coefficients and the ones explained in sections 4.2.3.1 to 4.2.3.5 refer to internal losses, while parasitic losses are modelled in sections 4.2.3.6 to 4.2.3.8 by means of work input coefficients (non-dimensionalised with respect to u_3^2).

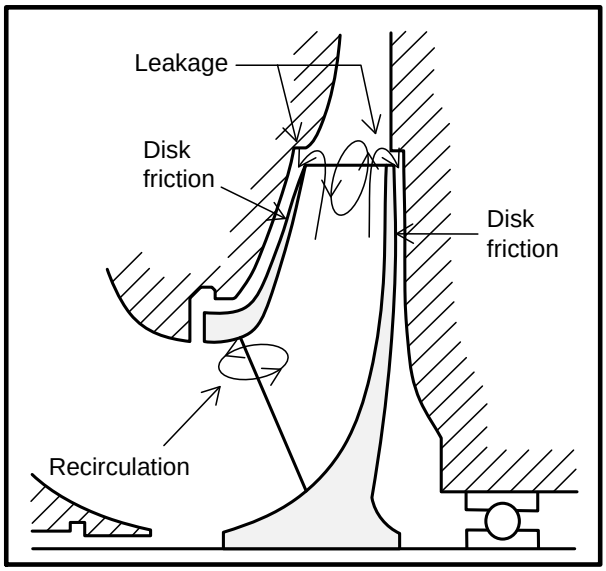

Figure 81. Parasitic losses (Japikse & Baines, 1997) .

4.2.3.1 Wall friction losses

Friction losses are evaluated with the model developed by (Schlichting, 1979), which provides a friction coefficient c_f as a function of the characteristic Reynolds number of the duct ($Re = \rho w d_H/\mu$, averaged between inlet and outlet) and relative roughness (ε/d_H) to be later applied in:

$$\varpi_{fr} = 4c_f \frac{L_B}{\overline{d}_H}\left(\frac{\overline{w}}{w_2}\right)^2 \qquad \text{[Equation 4.15]}$$

Where L_B is the impeller channel length and $\overline{d}_H$ the mean hydraulic diameter between impeller throat and exit. The mean relative velocity $\overline{w}$ is computed as $\overline{w} = \sqrt{(w_2^2 + w_3^2)/2}$, being $\overline{w} \geq \sqrt{(w_{th}^2 + w_3^2)/2}$ always. Two additional aspects must be noted with respect to the flow areas and the shape of the impeller channel (figure 82):

- The inlet and outlet sections are assumed normal to the relative flow: $A_{in,channel} = A_2 \cos\beta_2$ and $A_{out,channel} = A_3 \cos\beta_3$.
- In order to account for the influence of the splitter blades on these losses, A_3 is is calculated with respect to the total number of blades, $z_{FB} + z_{SB}$, when calculating hydraulic diameter.

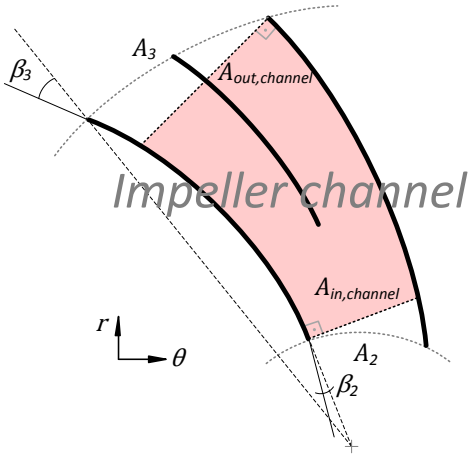

Figure 82. Impeller channel geometry.

This friction loss term considers the effect of the mean velocity of the fluid flow through the impeller channel. Therefore no local effects are considered, for which dedicated models are presented subsequently.

4.2.3.2 Aerodynamic loading losses

Blade loading losses come about because of the deflexion of streamlines inside the impeller channels, which causes the diffusion of the relative flow. Some authors describe them as "*the momentum loss due to boundary layer build-up*" (Jansen, 1967). Given the much higher density of the fluid in comparison with air, and based on the fact that these losses stem from the change in angular momentum of the flow, a significant contribution of this loss term is expected in S-CO_2 turbomachinery. Moreover, even if Its effect could be reduced by increasing the number of blades or reducing the blade curvature (i.e. flow deflexion), this would on the other hand penalise the performance of the impeller due to increased friction increase.

These losses are evaluated with the model proposed in (Aungier, 2000), which requires a simple model for the meridional (stream-wise) velocity distribution along the pressure and suction sides of the blades. A simple (close to ideal) velocity profile can be obtained from a simple irrotational flow analysis and is depicted in figure 83.

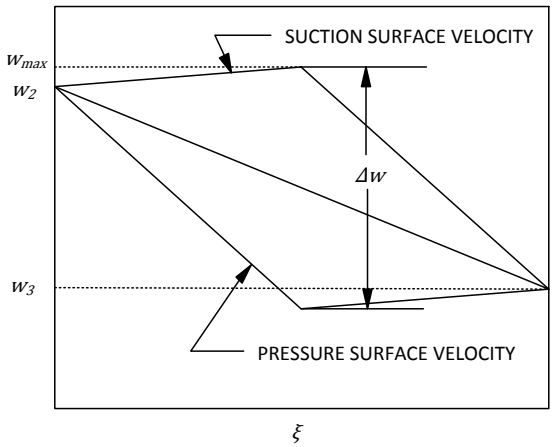

Figure 83. Blade loading model. Figure adapted from (Aungier, 2000).

The velocity distribution shown in figure 83 yields the following maximum velocity difference:

$$\Delta w = \frac{2\pi d_2\, u_2\, I_B}{z_{eff}\, L_B} \qquad \text{[Equation 4.16]}$$

Which can be implemented into the equivalent diffusion ratio developed by Lieblein (Lieblein, 1965), which is a means to evaluate the aerodynamic loading of the blades:

$$D_{eq} = \frac{w_{max}}{w_3} \quad ; \quad w_{max} = (w_2 + w_3 + \Delta w)/2 \qquad \text{[Equation 4.17]}$$

I_B is the blade work input coefficient (described later in section 4.2.3.9) while the effective number of blades is calculated by having into account the splitter blades as well: $z_{eff} = z_{FB} + z_{SB} \cdot (L_{SB}/L_{FB})$. Therefore, the blade loading loss coefficient can be calculated as:

$$\varpi_{BL} = \frac{1}{24}\left(\frac{\Delta w}{w_2}\right)^2 \qquad \text{[Equation 4.18]}$$

This latter correlation accounts for the blade loading losses which are eventually caused by the pressure gradient in the blade-to-blade direction. Nevertheless, this is not the only pressure gradient in an impeller channel even though it is the most important. There exists another pressure gradient from hub to shroud whose effect must be taken into account by an additional loss term.

This second contribution to the aerodynamic loading losses is taken into account by ϖ_{HS} which depends on the mean streamline curvature, $\overline{\kappa}_m = (\alpha_{C3} - \alpha_{C2})/L_B$, mean channel width, $\overline{l} = (l_2 + l_3)/2$, and velocity profile.

$$\varpi_{HS} = \frac{1}{6}\left(\frac{\overline{\kappa}_m \overline{lw}}{w_2}\right)^2 \qquad \text{[Equation 4.19]}$$

4.2.3.3 Mixing losses

Two separate contributions to mixing are consideredat the impeller outlet even though, in contrast to two-zone models, no secondary and primary zones are distinguished in the approach presented so far. Nevertheless, blockage is still modelled and hence the outflow is characterised by a tip blockage B_3, directly related with the well-known distortion factor:

$$\lambda = \frac{1}{1 - B_3} \qquad \text{[Equation 4.20]}$$

At non-singular operating conditions of the compressor, the boundary layer is almost removed in the inducer thanks to the flow acceleration in the convergent geometry. Hence, an almost negligible boundary layer is expected at the inlet to the blading which then builds up in the impeller channel as the relative flow is diffused. Different phenomena are the cause of this build-up: (i) wall friction, (ii) diffusion of the relative flow, (iii) hub-to-shroud aspect ratio of the impeller channel and also (iv) relative importance of the clearance gap; all these effects contribute to increasing the outlet blockage. The following model proposed by Aungier (Aungier, 1995) summons all of them.

$$B_3 = \varpi_{fr}\frac{P_{02} - P_2}{P_{03} - P_3}\sqrt{\frac{w_2\, \overline{d}_H}{w_3\, b_3}} + \left[0.3 + \frac{b_3^2}{L_B^2}\right]\frac{A_R^2\, \rho_3\, b_3}{\rho_2\, L_B} + \frac{\delta_{CL}}{2\, b_3} \qquad \text{[Equation 4.21]}$$

Where the channel area ratio is calculated as $A_R = A_3 \cos\beta_3 / (A_2 \cos\beta_{th})$ and δ_{CL} is the clearance gap size.

The first mixing process is that of the distorted flow (included in the displacement boundary layer[12]) and the core flow stream, causing pressure losses that are modelled with an abrupt expansion coefficient as proposed in (Benedict, et al., 1966).

$$\varpi_{\lambda} = \left[\frac{(\lambda - 1)\, v_{m3}}{w_2}\right]^2 \qquad \text{[Equation 4.22]}$$

The second mixing process takes place downstream of the trailing edge where the wake mixes with the channel flow. As in the previous case, this pressure loss coefficient is modelled as an abrupt expansion for which the size of the wake must be estimated. A diffusion limit of $D_{eq} = 2$ is assumed for stall-free operation in such a way that the separation velocity is calculated as follows:

$$w_{sep} = \begin{cases} w_3 & if\ D_{eq} \leq 2 \\ w_3 \dfrac{D_{eq}}{2} & If D_{eq} > 2 \end{cases} \qquad \text{[Equation 4.23]}$$

Mixing involves meridional velocities only (Aungier, 2000), which are calculated before ($v_{m3,wake}$) and after mixing ($v_{m3,mix}$).

$$v_{m3,wake} = \sqrt{w_{sep}^2 - w_{u3}^2}$$
$$v_{m3,mix} = v_{m3} \frac{A_3}{\pi\, d_3\, b_3} \qquad \text{[Equation 4.24]}$$

The destruction of absolute meridional velocity yields the wake mixing loss coefficient:

$$\varpi_{wake} = \left[\frac{v_{m3,wake} - v_{m3,mix}}{w_2}\right]^2 \qquad \text{[Equation 4.25]}$$

4.2.3.4 Clearance losses

In open impellers, there exists a flow of gas through the gap between impeller tip and shroud from the pressure to the suction side of the blades. This portion of fluid is consequently driven by the impeller whereas it does not flow out from it, thus implying an additional pressure loss. Regarding S-CO_2 turbomachinery, and given its reduced dimensions, the relative size of the gap can be noteworthy and this loos is likely to gain importance. The evaluation of clearance losses requires estimating both the pressure difference and the mass flow rate through the gap, to which aim angular momentum equilibrium is imposed:

[12] *Remember that the displacement boundary layer thickness (δ^*) is directly related with the aerodynamic blockage factor (See chapter 3).*

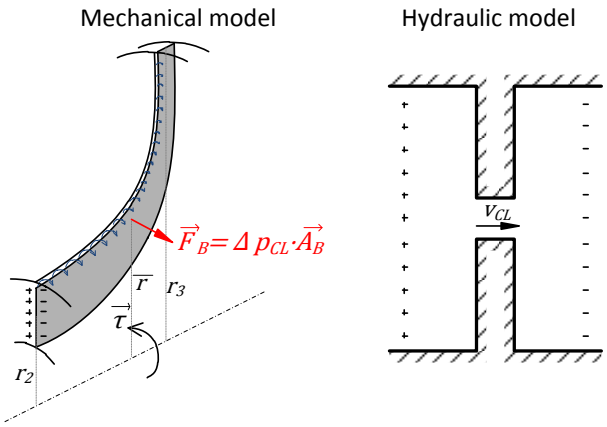

Figure 84. Gap flow model (Aungier, 2000).

$$\vec{\tau} = z_{eff}\ \vec{F}_B \times \vec{\bar{r}} \qquad \text{[Equation 4.26]}$$

What, after mathematical rearrangement, yields the pressure difference across the gap:

$$\Delta p_{CL} = \frac{\dot{m}(r_3\ v_{u3} - r_2\ v_{u2})}{z_{eff}\ \bar{r}\ \bar{b}\ L_B} \qquad \text{[Equation 4.27]}$$

On The other hand, the following flow velocity through the gap is proposed by Aungier (Aungier, 2000):

$$v_{CL} = 0.816\sqrt{2\Delta p_{CL}/\rho_3} \qquad \text{[Equation 4.28]}$$

Where the coefficient 0.816 comes from the simple hydraulic model shown in Figure 84 which comprises an abrupt contraction (from the pressure side to the gap) followed by an abrupt expansion (from the gap to the suction side).

Let CR_{CL} (defined <1) be the contraction ratio that the fluid experiences when flowing through the abrupt contraction and expansion. It is acknowledged, and it has already been said (see [Equation 4.7]), that the loss coefficient for both elements is $(1 - CR_{CL})^2$. Therefore, assuming that the density of the fluid remains constant, the application of Bernoulli's equation yields $0.816 = 1/\left[\sqrt{2}(1 - CR_{CL})\right]$, resulting in a contraction ratio equal to $CR_{CL} = 0.1334$. In other words, this means that the flow area across the gap represents around 13% of the meridional section of the impeller channel. Nevertheless, in order to provide a more general approach, a variable coefficient depending on blade heights (b_2 y b_3) and clearance gap (δ_{CL}) is used in lieu of the constant 0.816 value:

$$v_{CL} = \frac{\sqrt{\Delta p_{CL}/\rho_3}}{1 - \overline{CR}_{CL}} \quad ; \quad \overline{CR}_{CL} = \frac{1}{2}\left(\frac{\delta_{CL}}{b_2 + \delta_{CL}} + \frac{\delta_{CL}}{b_3 + \delta_{CL}}\right) \qquad \text{[Equation 4.29]}$$

The leakage flow through the gap is then:

$$\dot{m}_{CL} = \rho_3\ z_{eff}\ s\ L_B\ v_{CL} \qquad \text{[Equation 4.30]}$$

And finally the clearance loss coefficient is:

$$\varpi_{CL} = \frac{2\ \dot{m}_{CL}\ \Delta p_{CL}}{\dot{m}\ \rho_2\ w_2^2} \qquad \text{[Equation 4.31]}$$

4.2.3.5 *Supersonic flow losses*

Although the inlet and outlet relative velocities are in the subsonic range, it is possible to find local relative velocities in the supersonic region, which form shock waves incurring additional losses. These losses are evaluated with the following loss coefficient (Aungier, 2000):

$$\varpi_{cr} = \begin{cases} 0.4 \left[\frac{w_{max} - w^*}{a_2}\right]^2 & if\ w_{max} \geq w^* \\ 0 & if\ w_{max} < w^* \end{cases} \qquad \text{[Equation 4.32]}$$

Where w^* is the relative velocity at sonic conditions calculated in the inducer analysis (see page 81).

4.2.3.6 *Disk friction losses*

The disk friction work input coefficient is calculated with the classical model of Daily and Nece (Daily & Nece, Mar, 1960) (Daily & Nece, Sept, 1960), based on the plot shown in figure 85 which gives the torque coefficient (C_{M0}) as a function of the characteristic Reynolds number ($Re_{disk} = \rho\ \omega\ r_{disk}^2/\mu$) and the relative roughness (ε/r_{disk}) of the disk.

$$C_M = \frac{2\tau}{\rho\omega^2 r^5} \qquad \text{[Equation 4.33]}$$

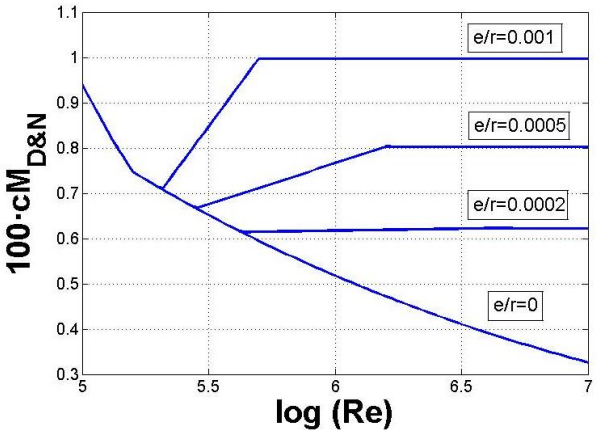

Figure 85. Daily & Nece's model to estimate the torque coefficient for disk friction calculations (Aungier, 2000).

The final torque coefficient (defined in [Equation 4.33]) results from implementing some corrections given by Aungier into the values provided by Daily and Nece (Aungier, 2000). A first correction is done to account for the leakage flow according to the following expressions:

$$C'_M = C_{M0}\frac{(1-K)^2}{(1-K_0)^2}$$

$$K_0 = \frac{0.46}{\left(1 + \frac{\delta_{disk}}{r_{disk}}\right)} \quad ; \quad K = K_0 + C_q\left(1.75\ \frac{v_{u3}}{u_3} - 0.316\right)\frac{r_{disk}}{\delta_{disk}} \quad ; \qquad \text{[Equation 4.34]}$$

$$C_q = \frac{\dot{m}_L\ Re_{disk}^{1/5}}{2\pi\ \rho_3\ r_{disk}^2 u_3}$$

This corrected coefficient is split into two due to the fact that Daily and Nece's model yields the torque coefficient at both sides of the wheel (disk and cover). These partial coefficients are given by Aunger based on experimental data:

$$\begin{cases} C_{M,disk} = 0.75\ C'_M \\ C_{M,cover} = 0.75\ C'_M\ L_B \dfrac{1-(r_{2s}/r_3)^5}{r_3 - r_2} \end{cases} \quad for\ close\ impellers \qquad \text{[Equation 4.35]}$$

Finally, disk friction losses are numerically characterised by the following work input coefficient:

$$I_{DF} = \left(C_{M,disk} + C_{M,cover}\right)\frac{\rho_3\ u_3\ r_3^2}{2\dot{m}} \qquad \text{[Equation 4.36]}$$

4.2.3.7 Recirculation flow losses

When the relative flow diffusion gets high, the risk of stall taking place must be taken into account as it would lead to partial flow recirculation back to the impeller channel. Therefore a consistent parameter for evaluating this situation is needed, which is usually taken as Lieblein's equivalent diffusion ratio [Equation 4.17] being higher than 2 (Lieblein, 1959). This into account, the following work input coefficient due to recirculation losses is obtained:

$$I_R = \left(\frac{D_{eq}}{2} - 1\right)\left(\frac{w_{u3}}{v_{m3}} - 2\tan\beta_3\right) \geq 0 \qquad \text{[Equation 4.37]}$$

The two conditions needed for recirculation to take place are (i) diffusion ratio higher than the threshold value, and (ii) deviation at impeller exit higher than:

$$\tan\alpha'_3 > 2\tan\beta_3\ (\text{as } w_{u3}/v_{m3} = \tan\alpha'_3) \qquad \text{[Equation 4.38]}$$

4.2.3.8 Leakage losses

The design of efficient labyrinth seals for high pressure turbomachinery is anything but a simple task. A thorough analysis is usually needed to balance two opposing effects. Reducing the gaps in the labyrinth leads to lower leakage flows but, at the same time, increases the potential rub and tear of the fins, hence increasing mechanical losses and reducing the reliability and useful life of the component. On top of this, too narrow gaps make it more demanding to operate the unit during (cold) start-up and shut-down when thermal strains play an important role.

This into account, any labyrinth seal will incur a certain leakage flow which reduces the performance of the turbomachine. And depends on the geometry of the seal and pressure ratio across it (in this particular case, the pressure ratio across the seal is the ratio from impeller exit to atmosphere). Based on this twofold dependence, there are two possible ways to calculate the leakage flow, depending on whether the impeller is open of covered.

For open impellers, Aungier (Aungier, 1995) assumed that "*half of the clearance gap leakage flow is re-entrained into the blade passage flow and re-energized by the impeller*".

$$I_{L,open} = \frac{\dot{m}_{CL}\ v_{CL}}{2\ u_3\ \dot{m}} \qquad \text{[Equation 4.39]}$$

However, for covered impeller, it is necessary to estimate the leakage mass flow rate, for which the classical paper by Egli (Egli, 1935) is used as proposed by Aungier (Aungier, 2000).

$$\dot{m}_L = \pi \, d_{seal} \, \delta_{seal} \, C_r \, C_t \, C_c \, \rho_3 \sqrt{RT} \qquad \text{[Equation 4.40]}$$

Where the seal contraction ratio (C_r), seal throttling coefficient (C_t) and seal carryover coefficient (C_c) depend on the geometry of the seal and the number of fins.

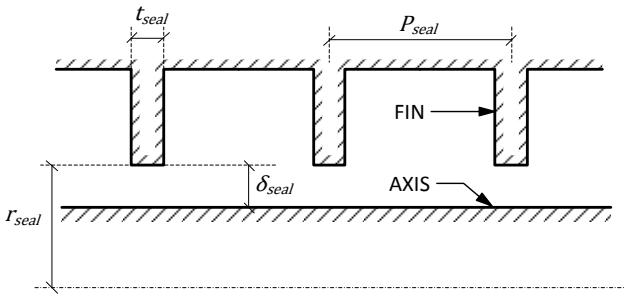

Figure 86.Labyrinth seals geometrical definition.

Thus, for covered impeller, the leakage work input coefficient is calculated by:

$$I_{L,covered} = I_B \frac{\dot{m}_L}{\dot{m}} \qquad \text{[Equation 4.41]}$$

4.2.3.9 The blade work input coefficient

The blade work input coefficient is the non-dimensional enthalpy change of the fluid across the impeller. This is well established by Euler's equation as the variation of $v_u u$ from the inlet to the outlet. For ideally guided flow ($\beta_3 = \alpha_3'$), the tangential component of the absolute velocity at impeller exit is:

$$v_{u3}^{id} = u_3 - w_{u3} = u_3 - \frac{\dot{m}}{\rho_3 A_3} \tan \beta_3 \qquad \text{[Equation 4.42]}$$

As a consequence of the pressure difference between both sides of the blade, the flow deviates from the direction of the blade trailing edge towards the suction side. This deviation effect is accounted for by the slip factor (σ), which is defined as "*the ratio between the actual blade work input and the value that would exist if the flow were perfectly guided by the blades*" (Aungier, 2000).

Another non-ideal effect is caused by the aerodynamic blockage at impeller exit, generally considered in radial machinery by means of the distortion factor (see section 4.2.3.3). Consequently, the blade work input coefficient is computed by the equation:

$$I_B = \sigma \left(1 - \frac{\dot{m} \, \lambda \, \tan \beta_3}{\rho_3 \, A_3 \, u_3}\right) - \frac{u_2 \, v_{u2}}{u_3^2} \qquad \text{[Equation 4.43]}$$

The slip factor is calculated based on Wiesner's equation (Wiesner, 1967) with the correction implemented by Aungier (Aungier, 1995). As a matter of fact, Aungier's correction makes adopts Wiesnser's factor if the meanline radius ratio ϵ is below its limiting value and a modified expression when this limiting value is exceeded:

$$\sigma_{WIESNER} = 1 - \sqrt{\cos \beta_3} \sin \alpha_{C2} \, / z_{eff}^{0.7} \qquad \text{[Equation 4.44]}$$

$$\epsilon_{lim} = \frac{\sigma_{WIESNER} - \sigma^*}{1 - \sigma^*} \quad ; \quad \sigma^* = \sin(37^o - 0.2\beta_3) \qquad \text{[Equation 4.45]}$$

$$\sigma = \begin{cases} \sigma_{WIESNER} & If\ \epsilon \leq \epsilon_{lim} \\ \sigma_{WIESNER}\left[1 - \left(\frac{\epsilon - \epsilon_{lim}}{1 - \epsilon_{lim}}\right)^{\sqrt{9^o - \beta_3/10}}\right] & If\ \epsilon > \epsilon_{lim} \end{cases} \quad \text{[Equation 4.46]}$$

4.2.3.10 Algorithm for the calculation of impeller performance

Taking the solution of the inducer flow as an input, it is possible to calculate the ideal discharge of the impeller if null deviation and isentropic flow are considered. Then, a first estimate of the flow field is obtained, which is later used to calculate the various losses and other coefficients that are necessary to calculate the real impeller flow. Moreover, as opposed to the inducer and other stationary elements, the impeller analysis is done in the relative reference frame which gives place to the following equation for the conservation of rothalpy and the calculation of total pressure losees:

$$h'_{03} = h'_{02} + (u_3^2 - u_2^2)/2$$
$$P'_{03} = P'_{03id} - f_c\,(P'_{02} - P_2)\sum_{2\to 3}\varpi_i \quad \text{[Equation 4.47]}$$

The correction factor f_c is employed to account for the fact that the losses are applied at the impeller outlet (i.e., they are applied to the total pressure at the outlet from this component) but they are defined as a fraction of the inlet dynamic head. In accordance, the factor mitigates errors caused by high pressure differences between impeller inlet and outlet and, even though the one employed by Aungier is $f_c = (\rho'_{03}T'_{03})/(\rho'_{02}T'_{02})$ (Aungier, 1995), it is herein redefined as:

$$f_c = P'_{03}/P'_{02} \quad \text{[Equation 4.48]}$$

The factor translates the relative dynamic pressure at the inlet $(P'_{02} - P_2)$ to comparable terms at the outlet, a fraction of which is later subtracted from the ideal relative total pressure at this section. It is noted here that for adiabatic and isentropic processes involving ideal gases, Aungier's original factor and the factor proposed herein are ust the same since $P'_{03}/P'_{02} = (\rho'_{03}T'_{03})/(\rho'_{02}T'_{02})$. Nevertheless, since supercritical carbon dioxide is not an ideal gas, the ratio of relative total pressures is preferred.

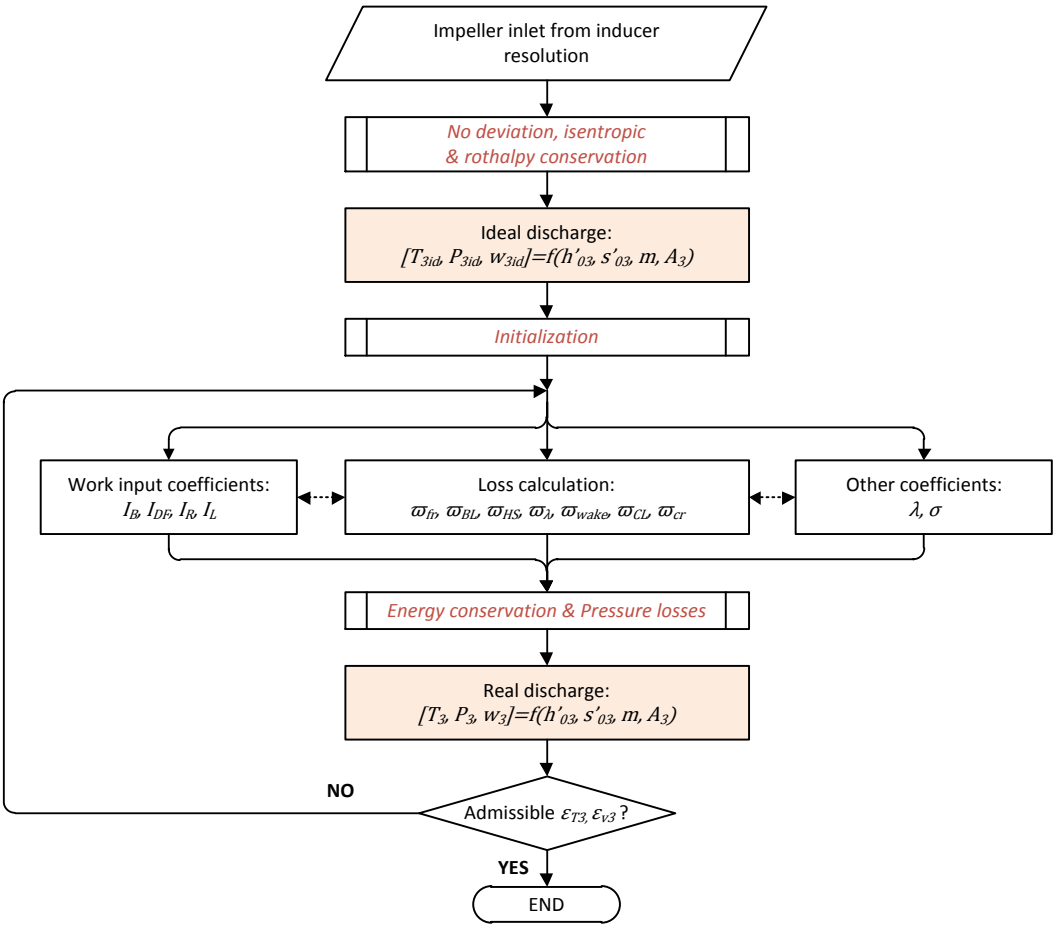

Figure 87. Flow diagram for the analysis of the impeller.

4.2.4 Vaneless space model

A vaneless space is always present in radial machines, whether it be as the only diffuser or as an intermediate passage between impeller and diffuser. Non-negligible losses can take place in this vaneless space even at small radii ratio, since the flow angle brings about streamlines that are far from being radial. Therefore, this effect has to be included in 1D models.

A simple loss model is presented in (Oh, et al., 1997) for the vaneless space, accounting for friction only. However, the one-dimensional analysis of vaneless diffusers is usually based on the differential form of conservation laws as originally exposed by Stanitz (Stanitz, 1952). Dubitsky and Japikse also proposed a model based on this approach in (Dubitsky & Japikse, 2008). Halfway between these, the approach used here is based on another classical one appearing in (Johnston & Dean, 1966) and also employed by Aungier (Aungier, 2000) because of its simplicity. The model consists of the following equations:

$$\begin{cases} \dot{m} = 2\pi\, r\, b(1-B)\, \rho\, v_m \\ b\, v_m \dfrac{d(r\, v_u)}{dm} = -r\, v\, v_u\, c_f \\ \dfrac{1}{\rho}\dfrac{dp}{dm} = \dfrac{v_u^2 \sin\alpha_C}{r} - v_m \dfrac{dv_m}{dm} - \dfrac{v\, v_m\, c_f}{b} - \dfrac{dI_D}{dm} - I_C \\ h_0 = h + \dfrac{1}{2}v^2 \end{cases} \qquad \text{[Equation 4.49]}$$

Is also noted that even though a mixing process takes place in the vaneless space, the corresponding losses are not included in this model but in the impeller's. The losses in the model of the vaneless space hence limit to friction, diffusion because of area change and streamline curvature because of changes in the inclination angle (α_C).

4.2.4.1 Boundary layer model in the vaneless diffuser

Friction is again modelled by a skin friction coefficient calculated as a function of the relative roughness and Reynolds number, the latter of which employs twice the boundary layer thickness δ as the characteristic length[13]. Let it be noted that this is the actual boundary layer thickness, which is known at the inlet from the previous calculation of the impeller flow, and not the displacement thickness δ^*.

A boundary layer model is thus necessary for the calculation of friction losses, the classical 1/7th power law being considered for both the meridional and tangential velocity profiles (Figure 88).

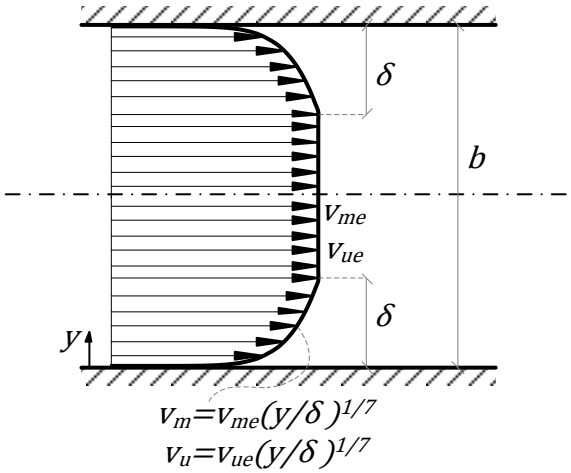

Figure 88. 1/7th power law for velocity profiles.

Assuming that there are no radial variations of the meridional component radius-wise, the integral along the height of the passage $b\int_0^b \rho v_m dy = \rho b v_{me}[1-\delta/(4b)\,]$ can be identified as $\dot{m}/2\pi r$, thus correlating with the blockage factor:

$$B = \delta/4b \qquad \text{[Equation 4.50]}$$

On other side, a mass flow averaged angular momentum is calculated for each section as:

$$r\,v_u = \frac{\int_0^b r\,v_u\,dm}{\int_0^b dm} = \frac{\int_0^b r\,v_u\,\rho\,v_m\,dy}{\dot{m}} = \frac{r\,\rho\,b\,v_{me}v_{ue}\left[1-\frac{4\delta}{9b}\right]}{\rho\,b\,v_{me}(1-B)} = \frac{r\,v_{ue}\left[1-\frac{4\delta}{9b}\right]}{(1-B)} \qquad \text{[Equation 4.51]}$$

It is easily deduced that the angular momentum in the core flow remains constant until the boundary layer thickness occupies half of diffuser height ($\delta = b/2$), and diminishes downstream.

The angular momentum of the core flow, i.e. rv_{ue}, is easily calculated with the flow field at the inlet to the vaneless space and, along with [Equation 4.50] permits closing the boundary layer model. With this information, the continuity equation can be solved and the skin friction coefficient can be calculated.

[13] *Be noticed that δ is the actual boundary layer thickness, in difference to the displacement thickness boundary layer δ*.*

4.2.4.2 *Diffusion model*

The flow diffusion model is based on an analogy to classical two-dimensional diffusers. The diffuser is divided into infinitesimal diffusers of length dm and area ratio established by the radius ratio. If constant density is assumed, which is acceptable given the very short length of the diffuser, and applying Bernoulli's equation between r and $r + dr$ where a reduction of velocity of $-dv$ takes place, the following area ratio is obtained:

$$A_R = 1 - \frac{dv}{v} \qquad \text{[Equation 4.52]}$$

Therefore, it is possible to adapt the divergence parameter defined by Reneau (Reneau, et al., 1967), D, to the annular case.

$$D = b_1(A_R - 1)/L = 2\tan\theta_C \qquad \text{[Equation 4.53]}$$

$$D = -\frac{b}{v}\frac{dv}{dm} \qquad \text{[Equation 4.54]}$$

The following threshold below which diffusion losses can be assumed negligible is then established:

$$D_m = 0.4\ (b/dm)^{0.35}\cos\alpha \qquad \text{[Equation 4.55]}$$

This value is provided by (Reneau, et al., 1967) based on experimental information and later adapted to the annular case with the factor $\cos\alpha$by Aungier (Aungier, 2000). Following the two-dimensional diffuser analogy, the efficiency of the elementary annular diffuser is calculated as:

$$E = \begin{cases} 1 & If\ D \le 0 \\ 1 - 0.2(D/D_m)^2 & If\ 0 < D < D_m \\ 0.8\sqrt{D/D_m} & If\ D \ge D_m \end{cases} \qquad \text{[Equation 4.56]}$$

The diffusion loss term included in [Equation 4.49] results:

$$\frac{dI_D}{dm} = -2\ (P_0 - P)(1 - E)\frac{1}{\rho v}\frac{dv}{dm} \qquad \text{[Equation 4.57]}$$

Which is substituted by the following one when stall takes place

$$I_D = 0.65\ (P_0 - P)\left[1 - \frac{(r\ b)_m}{r\ b}\right]\frac{1}{\rho} \qquad \text{[Equation 4.58]}$$

Where $(r\ b)_m$ is the maximum stall-free area, calculated as the outlet area of the equivalent diffuser with divergence angle of 9º.

$$(r\ b)_m = (r\ b)_3[1 + 0.16\ m/b_3] \qquad \text{[Equation 4.59]}$$

4.2.4.3 *Curvature effects*

Variations of the mean streamline angle with respect to the axis (α_C) produce total pressure losses similar to those occurring in an elbow. The effects of this curvature ($\kappa_m = -\partial\alpha_C/\partial m$) are accounted for with the following empirical correlation, presented in (Aungier, 2000):

$$I_C = \frac{\kappa_m (P_0 - P) v_m}{13\ \rho\ v}$$ [Equation 4.60]

4.2.4.4 Algorithm for the calculation of vaneless space performance

The algorithm is based on a radial discretisation of the vaneless space, where the conservation laws are solved in differential form. Firstly, the inlet section is calculated from the stagnation conditions and blockage at impeller exit, the mass flow rate and the component geometry. Secondly, the streamwise distribution of blockage, density and friction coefficient are initialised before starting the iterative loop.

The aforesaid conservation laws are solved in conjunction with the loss model and the equation of state following the steps observed in figure 89. The convergence criterion is established on the distribution of density distribution.

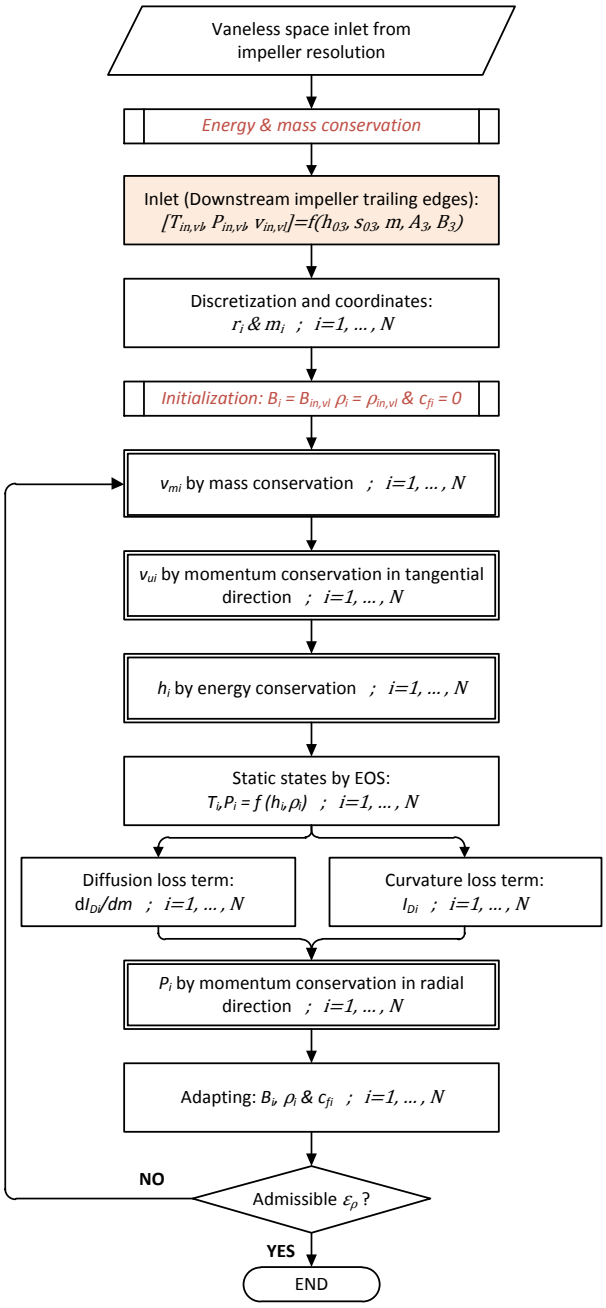

Figure 89. Flow diagram for the analysis of the vaneless space.

4.2.5 Vaned diffuser model

The kinetic energy imparted to the fluid by the impeller has to be converted into enthalpy (pressure energy) by the diffuser. This conversion can be carried out by a vaneless diffuser (section 4.2.4) but, if appropriately designed, a vaned one yields a much more efficient pressure recovery. The parameter E, introduced by Aungier (Aungier, 1988), is a useful definition to evaluate the benefits of a vaned diffuser with respect to a vaneless one.

$$E = \frac{R^2(A_R^2 - 1)}{A_R^2(R^2 - 1)} \qquad \text{[Equation 4.61]}$$

Where R is the radius ratio and $A_R$the area ratio of the vaned diffuser.

Similarly to the impeller, vaned diffuser analysis is based on conservation laws together with pressure loss coefficients coming from different contributions. Actually, in spite of imposing total enthalpy conservation is used in lieu of rothalpy conservation, the model must also be complemented with calculations regarding deviation and blockage in addition to checking critical phenomena such as stall and choking.

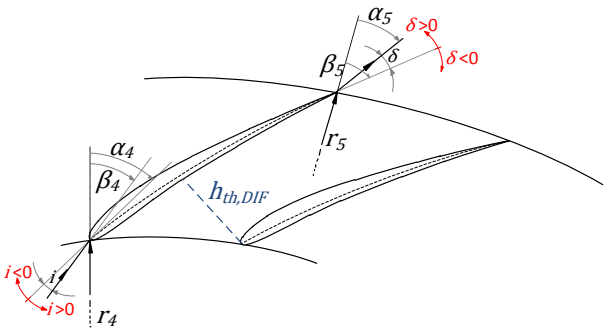

Figure 90. Vaned diffuser geometry.

Two characteristic incidences are identified by blade cascade theory: minimum loss and stall. The stall criterion is based on the parameter $K = -r\,\partial(\sin\alpha)/\partial r$, which is related with the streamline curvature. High curvatures imply high values of *K* so, as a consequence, the probability of stall increases with *K*. In practice, the value of this parameter at the inlet to the diffuser can be evaluated from the geometry of this component at the inlet and the throat:

$$K_4 = \frac{r_4}{h_{th,DIF}}\left[\frac{\sin\alpha_4}{\sin\alpha_{th,DIF}} - 1\right] \quad ; \quad \cos\alpha_{th,DIF} = A_{th,DIF}/A_4 \qquad \text{[Equation 4.62]}$$

which represents the contribution to stall by the initial part of the diffuser because of the change that it produces in the flow angle. Moreover, the total contribution to stall must account for the effect of the vaneless space also, which is evaluated by the following expression according to (Aungier, 2000):

$$K_0 = \frac{M_4^2\cos^2\beta_4\sin\beta_4}{1 - M_4^2\cos^2\beta_4} \qquad \text{[Equation 4.63]}$$

The criterion used for stall, [Equation 4.64], was established experimentally by Aungier (Aungier, 2000) and permits, once K_0 is calculated, to calculate the value of K_4at stall conditions, hence the stall angle, α_{4s}, and velocity, v_{4s}.

$$K_0 + K_4 = 0.39 \qquad \text{[Equation 4.64]}$$

$$\alpha_{4s} = \operatorname{asin}\left\{\sin\alpha_{th,DIF}\left[1 + \frac{h_{th}}{r_4}(0.39 - K_0)\right]\right\} \qquad \text{[Equation 4.65]}$$

$$v_{4s} = v_{m4}/\cos\alpha_{4s} \qquad \text{[Equation 4.66]}$$

On the opposite side, the minimum loss incidence, associated to the optimum incidence velocity (v_4^*), is defined as:

$$\cos\alpha_4^* = v_{m4}/v_4^* = \sqrt{\cos\beta_4\cos\alpha_{th}} \qquad \text{[Equation 4.67]}$$

4.2.5.1 *Incidence losses*

Following the philosophy applied for the impeller, incidence losses are the consequence of two effects: the difference between the actual flow angle and the optimum one (in terms of minimum loss), and the abrupt contraction caused by the blade leading edges (i.e, the effect of blade thickness). In addition, if the diffuser is stalled ($v_4 > v_{4s}$), a supplementary term must be introduced in this loss contribution.

$$\varpi_{inc,DIF} = \begin{cases} \varpi_{inc0,DIF} + 0.8\left(\frac{v_4 - v_4^*}{v_4}\right)^2 & If\ v_4 \le v_{4s} \\ \varpi_{inc0,DIF} + 0.8\left\{\left(\left(\frac{v_4}{v_{4s}}\right)^2 - 1\right)\left(\frac{v_{th,DIF}}{v_4}\right)^2 + \left(\frac{v_{4s} - v_4^*}{v_{4s}}\right)^2\right\} & If\ v_4 > v_{4s} \end{cases} \quad \text{[Equation 4.68]}$$

Where the minimum incidence losses in the diffuser is given by:

$$\varpi_{inc0,DIF} = 0.8\left(\frac{v_4^* - v_{th}}{v_4}\right)^2 + \left(\frac{z_{DIF} t_4}{2\pi r_4}\right)^2 \quad \text{[Equation 4.69]}$$

4.2.5.2 *Choking*

Choking losses in the diffuser are based on the same model employed for the impeller (see section 4.2.2, [Equation 4.12]). The calculation of the flow conditions at the throat is thus necessary, for which incidence losses are taken into account.

4.2.5.3 *Wall friction losses*

$$\varpi_{fr,DIF} = 4c_f \frac{L_{B,DIF}}{\overline{d}_{H,DIF}}\left(\frac{\overline{v}}{v_4}\right)^2 \left(\frac{\overline{d}_{H,DIF}}{2\delta}\right)^{0.25} \quad \text{[Equation 4.70]}$$

As observed in the equation above, friction losses are calculated as in the impeller [Equation 4.15] though affected by the factor $\left(\overline{d}_{H,DIF}/2\delta\right)^{0.25}$, which includes a correction due to the fact that boundary layers in diffusers are not fully-developed usually.

4.2.5.4 *Mixing losses*

As a consequence of the mixing process downstream of the diffuser trailing edges, a pressure loss arises. As for the impeller, this is a function of the meridional wake and mixed-flow velocities, $v_{m5,mix}$ and $v_{m5,mix}$ respectively.

$$\varpi_{mix,DIF} = \left(\frac{v_{m5,wake} - v_{m5,mix}}{v_4}\right)^2 \quad \text{[Equation 4.71]}$$

where the wake velocity is estimated from a separation velocity (v_{SEP}) and the mixed-flow velocity is given by continuity:

$$v_{m5,wake} = \sqrt{v_{SEP}^2 - v_{u5}^2} \quad \text{[Equation 4.72]}$$

$$v_{m5,mix} = v_{m5}\frac{A_5}{\pi\, d_5\, b_5} \quad \text{[Equation 4.73]}$$

The separation velocity depends on the divergence angle through the parameter C_θ, defined in section 4.2.5.5.

$$v_{SEP} = \frac{v_4}{1 + 2C_\theta} \qquad \text{[Equation 4.74]}$$

4.2.5.5 Aerodynamic blockage at vaned diffuser outlet

An empirical correlation presented in (Aungier, 1988) is used for the calculation of blockage [Equation 4.75]. It was seen in chapter 3 that flow at the outlet from the diffuser is strongly dependent upon throat conditions, especially the aerodynamic blockage. However, according to the model employed, the blockage at diffuser outlet does not depend upon the blockage at diffuser inlet, the rationale being that the acceleration of the flow from the inlet to the throat brings about a negligible boundary layer thickness at the latter section.

$$B_5 = [K_1 + K_2(\bar{C}_R^2 - 1)]\frac{L_{B,DIF}}{l_{5,DIF}} \qquad \text{[Equation 4.75]}$$

Where

$$\bar{C}_R = \frac{1}{2}\left(\frac{v_{m4}\cos\beta_5}{v_{m5}\cos\beta_4} + 1\right)$$
$$K_1 = 0.2\left(1 - \frac{1}{C_\theta\, C_L}\right) \qquad \text{[Equation 4.76]}$$
$$K_2 = \frac{2\theta_C}{125C_\theta}\left(1 - \frac{2\theta_C}{22C_\theta}\right)$$

Where the width of the flow passage is calculated as

$$W = (2\pi r\cos\beta)/Z_{DIF} - t$$

and C_θ and $C_L$are correction coefficients associated to the equivalent diffuser divergence angle ($2\theta_C$) and blade loading parameter (L), which are calculated as follows:

$$2\theta_C = 2\,\mathrm{atan}\left[\frac{l_5\, b_5/b_4 - l_4}{2L_{B,DIF}}\right]$$
$$L = \frac{\Delta v}{v_4 - v_5} = \frac{2\pi\,(r_4 v_{u4} - r_5 v_{u5})/(z_{DIF} L_{B,DIF})}{v_4 - v_5} \qquad \text{[Equation 4.77]}$$

It is worth noting that a pronounced deterioration of diffuser performance has been observed experimentally when the loading parameter exceeds 1/3 or the divergence angle is higher than 11º. Therefore, coming back to correction coefficients, they are calculated as:

$$C_\theta = \max(1, 2\theta_C/11)$$
$$C_L = \max(1, 3L) \qquad \text{[Equation 4.78]}$$

4.2.5.6 Deviation at the vaned diffuser outlet

The calculation of the outflow angle is based on Howell's work on axial blade cascades (Howell, 1947) and thus requires a transformation of the coordinate system. At the minimum-loss incidence, the deviation is:

$$\delta^* = \frac{\theta[0.92\,(a/c)^2 + 0.02\,\beta_5]}{\sqrt{\sigma} - 0.02\theta} \qquad \text{[Equation 4.79]}$$

Where the cascade parameters (relative location of maximum camber, a/c, solidity, σ, and camber angle, θ) are:

$$a/c = \frac{2 - (\bar{\beta} - \beta_4)/(\beta_5 - \beta_4)}{3}$$
$$\sigma = \frac{z_{DIF}\,(r_5 - r_4)/(2\pi r_4 \cos\bar{\beta})}{3} \qquad \text{[Equation 4.80]}$$
$$\theta = \beta_4 - \beta_5$$

But diffusers do not usually operate at the minimum-losses incidence, and therefore the effect of incidence on deviation must be computed by means of the following derivative:

$$\frac{\partial\delta}{\partial i} = \exp\{[(1.5 - \beta_4/60)^2 - 3.3]\sigma\} \qquad \text{[Equation 4.81]}$$

Finally, the glow angle at the outlet from the diffuser is calculated, at any incidence angle, as:

$$\alpha_5 = \beta_5 - \delta = \beta_5 - \delta^* - \frac{\partial\delta}{\partial i}(\beta_4 - \alpha_4) \qquad \text{[Equation 4.82]}$$

4.2.5.7 Algorithm for the analysis of vaned diffusers

As it was the case for the impeller, the vaned diffuser is initialised with ideal discharge conditions, i.e. no deviation and no-losses. Once a flow field is obtained, it is possible to compute losses and hence update the flow field at the end of each iteration. Convergence criteria are set for static pressure and velocity at diffuser outlet.

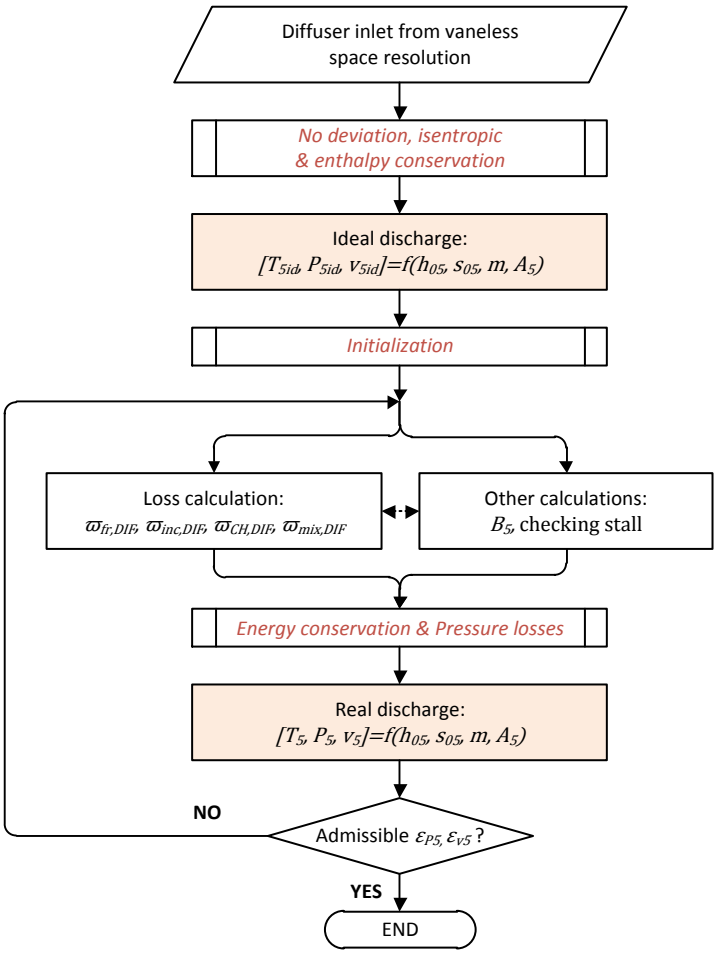

Figure 91. Flow diagram for the analysis of vaned diffusers.

4.2.6 Volute model

The high pressure fluid delivered at the diffuser outlet is collected by the volute, which still may produce a certain pressure rise thanks to flow diffusion. This process brings about three different contributions to the total loss of the compressor:

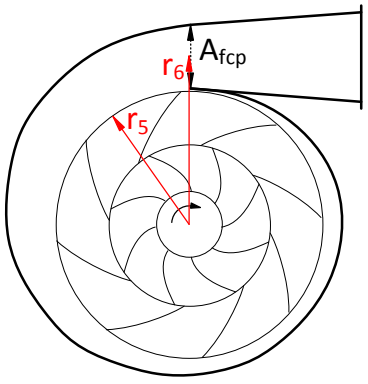

Figure 92. Volute geometry definition

- The "destruction" of the meridional component of velocity at diffuser exit, since the geometry of the volute imposes a tangential velocity in the full-collection plane (Figure 92).

$$\varpi_m = (v_{m5}/v_5)^2 \qquad \text{[Equation 4.83]}$$

- With regard to the tangential component, additional losses are generated when the angular momentum is not conserved, which is evaluated by the so-called sizing parameter:

$$SP = \frac{r_5\, v_{u5}}{r_6\, v_{u6}} \qquad \text{[Equation 4.84]}$$

$$\varpi_U = \begin{cases} \frac{1}{2}\frac{r_5\, v_{u5}^2}{r_6\, v_5^2}\left(1 - \frac{1}{SP^2}\right) & If\ SP \geq 1 \\ \frac{r_5\, v_{u5}^2}{r_6\, v_5^2}\left(1 - \frac{1}{SP}\right)^2 & If\ SP < 1 \end{cases} \qquad \text{[Equation 4.85]}$$

- And, finally, friction losses exist and they are evaluated with:

$$\varpi_{fr,V} = 4\, c_f \left(\frac{v_6}{v_5}\right)^2 \frac{L_V}{d_{H,V}}$$
$$L_V = \pi(r_5 + r_6)/2 \qquad \text{[Equation 4.86]}$$
$$d_{H,V} = \sqrt{4\, A_6/\pi}$$

4.2.6.1 *Algorithm for the analysis of the volute*

The velocity at the outlet from the volute is initialised with a default value, for instance $v_5/2$, which allows to calculate the three loss terms that participate in the volute. Then, the volute outlet flow is updated and the convergence (velocity at the volute exit in this case) criterion checked.

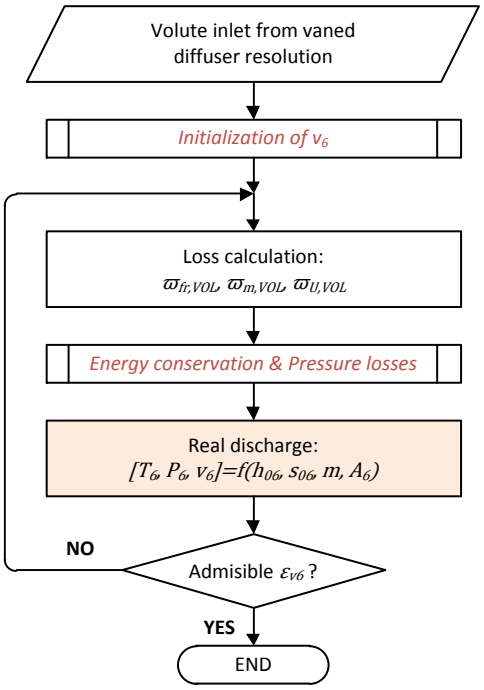

Figure 93. Flow diagram for volute analysis.

4.3 Validation of the model

The model presented in earlier sections is now validated both for supercritical carbon dioxide and air. The radial compressor existing at SANDIA National Laboratories (Wright, et al., September 2010) is taken for validation with carbon dioxide, while the NASA CC3 compressor (Tan, 2003) is used for air.

4.3.1 Validation for supercritical carbon dioxide

Table 9 presents the geometrical parameters that define the supercritical CO_2 compressor at SANDIA NL, which has been used for validation. Impeller data are explicitly indicated in the document (Wright, et al., September 2010) while for the diffuser some parameter need to be calculated from graphical information available in the same document. Additional experimental data is found in (Vilim, 2010) as well.

The geometry of the diffuser geometry is estimated by measuring the dimensions in figure 5-35 in (Wright, et al., September 2010), where the component can be seen completely (see figure 94). It is noted though that the diffuser modelled is of the vaned type (i.e. aerodynamic aerofoils) whereas the one used in the validation compressor is of the channel type; nevertheless, in order to minimise the effect of this difference, the diffuser geometry was set up with the objective of keeping the divergence angle and the area ratio identical: ∼8.5 º and ∼2 respectively.

Figure 94. Full S-CO2 turbo-compressor at SANDIA NL (Wright, et al., September 2010).

IMPELLER GEOMETRY	
Number of full blades	6
Number of splitter blades	6
Impeller inlet radius at hub	2.537585 mm
Impeller inlet radius at shroud	9.372047 mm
Impeller exit radius	18.68170 mm
Blade angle of the impeller leading edge at hub	17.88 º
Blade angle of the impeller leading edge at mean radius	37.13 º
Blade angle of the impeller leading edge at shroud	50.00 º
Blade angle of the impeller trailing edge	-50.00 º (backward)
Angle between streamlines and shaft at impeller inlet	0 º
Angle between streamlines and shaft at impeller exit	90 º
Full blade length	25.0 mm
Splitter blade length	12.5 mm
Axial length of the impeller	15.9 mm
Blade thickness at impeller leading edge	0.762 mm
Blade thickness at impeller trailing edge	0.762 mm
Blade height at impeller leading edge	1.7 mm
Clearance gap at impeller tip	0.254 mm
VANED DIFFUSER GEOMETRY	
Number of vanes	17
Diffuser inlet radius	18.5 mm
Diffuser exit radius	26.0 mm
Blade angle at diffuser inlet	71.50 º
Blade angle at diffuser exit	42.44 º
Blade height at diffuser inlet	1.8 mm
Blade height at diffuser exit	1.8 mm
Diffuser channel length	10.6 mm
Blade thickness at diffuser inlet	0.0 mm
Blade thickness at diffuser exit	3.35 mm

Table 9. Geometry employed in the simulation of the SANDIA NL compressor used for validation with S-CO_2.

Once the geometry of the component is defined, the total conditions at the inlet, mass flow rate and shaft speed are set for each validation case, whereas static pressure at impeller exit and total pressure and temperature at diffuser outlet are taken as the reference parameters to be compared against experiments. The results of the validation are presented in table 10 below, where last three points are taken from (Vilim, 2010) and the remaining ones from (Wright, et al., September 2010).

N (rpm)	T_{01} (K)	P_{01} (bar)	$\dot{m}$ (kg/s)	P_3 (bar)			P_{05} (bar)			T_{05} (K)		
				Exp.	Mod.	Dev. (%)	Exp.	Mod.	Dev. (%)	Exp.	Mod.	Dev. (%)
10000	305.5	76.76	0.454	76.76	77.40	*0.83*	79.79	77.74	*1.28*	-	-	-
20000	305.5	76.76	0.771	78.54	79.49	*1.21*	80.69	81.11	*0.53*	-	-	-
28000	305.5	76.76	1.134	82.11	82.06	*-0.06*	85.33	85.19	*-0.16*	-	-	-
39000	305.6	77.11	1.451	85.68	87.88	*2.54*	92.82	94.55	*1.86*	-	-	-
49000	306.3	78.54	1.816	94.25	95.46	*1.28*	106.39	106.18	*-0.20*	-	-	-
55000	306.4	78.90	2.043	99.96	100.53	*0.57*	113.53	114.41	*0.78*	-	-	-
56000	306.6	78.26	2.088	101.04	101.54	*0.49*	114.96	115.85	*0.77*	-	-	-
60000	306.9	79.97	2.225	102.11	105.69	*3.51*	121.39	122.37	*0.81*	-	-	-
64900	307.9	82.11	2.406	108.53	111.98	*3.18*	129.24	131.59	*1.82*	-	-	-
64384	308.71	82.86	2.860	106.7	108.94	*2.10*	119.4	108.94	*4.30*	323.82	324.17	*0.11*
29888	306.78	79.20	1.315	82.64	84.86	*2.69*	85.68	88.01	*2.72*	310.094	310.056	*-0.01*
59584	308.33	82.24	2.609	102.60	104.89	*2.23*	112.28	118.5	*5.54*	321.64	321.884	*0.08*

Table 10. Comparison of the experimental and analytical performances for supercritical carbon dioxide operation.

Given the complexity of the model, a mean deviation of 1.67 % with a peak at 5.54 % for the relevant parameters being screened, along with a deviation lower than 1 % in delivery temperature, are deemed satisfactory. Therefore, the model is considered to be suitable for its implementation into a design and optimisation tool to be used in supercritical carbon dioxide operation.

4.3.2 Validation for air

The suitability of the model to simulate the performance of radial compressors operating on air is also checked. To this aim, the NASA CC3 compressor is considered, for which data is available in (Tan, 2003) and (Landon Tarr, 2008). In this case, the comparison between the experimental and simulated performance is done for the pressure ratio and efficiency vs mass flow rate curves at constant-speed (60, 70, 80, 90 and 100 % the design value, 21798 rpm). The results of this comparison are shown graphically in figure 95, and the geometrical data is available in Table 11. As it was the case for S-CO_2, the diffuser is of the channel type and is modelled by modifying the trailing edge angle in order to keep the divergence angle in the actual case, while the leading edge angles of impeller and diffuser are set to have null incidence at the design point (21789 rpm and 4.54 kg/s).

IMPELLER GEOMETRY	
Number of full blades	15
Number of splitter blades	15
Impeller inlet radius at hub	41 mm
Impeller inlet radius at shroud	105 mm
Impeller exit radius	73 mm
Blade angle of the impeller leading edge at hub	24.8695 º
Blade angle of the impeller leading edge at mean radius	39.5336 º
Blade angle of the impeller leading edge at shroud	49.8897 º
Blade angle of the impeller trailing edge	-50.00 º (backward)
Angle between streamlines and shaft at impeller inlet	0 º
Angle between streamlines and shaft at impeller exit	90 º
Full blade length	197 mm
Splitter blade length	137.9 mm
Axial length of the impeller	133.89 mm
Blade thickness at impeller leading edge	7.58 mm
Blade thickness at impeller trailing edge	7.58 mm
Blade height at impeller leading edge	17 mm
Clearance gap at impeller tip	0.81 mm
VANED DIFFUSER GEOMETRY	
Number of vanes	24
Diffuser inlet radius	232.76 mm
Diffuser exit radius	450.813 mm
Blade angle at diffuser inlet	72.1222 º
Blade angle at diffuser exit	30 º
Blade height at diffuser inlet	17 mm
Blade height at diffuser exit	17 mm
Diffuser channel length	288.794 mm
Blade thickness at diffuser inlet	0.0 mm
Blade thickness at diffuser exit	49.99 mm

Table 11. . Geometry employed in the simulation of the CC3 compressor at NASA Glenn Research Centre with air.

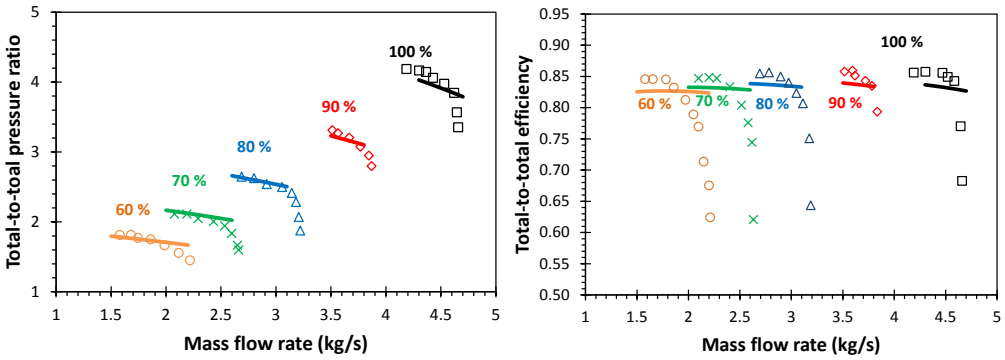

Figure 95. Comparison between numerical and experimental performance data of the CC3 compressor at NASA Glenn Research Centre (Tan, 2003) .

Having into account the difficulties founds when defining the geometry and accordingly the inherent uncertainty of this process, in the author considers that the results presented in figure 95 are acceptable, in particular for operating conditions close to the design point, i.e. far from choking (performance drop at high mass flow) and stall. The fact that this model has been developed for design purposes makes these results even more satisfactory and thus it is concluded that this research can move on to the next stage.

4.4 Design strategy for supercritical CO_2 centrifugal compressors: Inverse problem

The inverse or design problem consists of calculating the geometry that yields the desired performance a compressor given a set of operating conditions, i.e. inlet stagnation point, mass flow rate and pressure ratio for a specific gas, whether it be a pure substance or a mixture. Although the equations involved are the same as in the direct problem (see section 4.2), they have to be solved through a different algorithm, which gives place to the design strategy. This section presents a design strategy which accounts for general rules in radial turbomachinery design but also includes specific considerations for supercritical fluids.

From the concept of the power cycle to the final design of the compressor, the process can be divided into three steps:

- Firstly, the operating cycle is design for given net power, which means determining the total pressure and temperature at the inlet and outlet sections of each component and also the mass flow rate. To this aim, component efficiency and other performance parameters need to be guessed.
- The compression system can be designed once the inlet conditions, pressure ratio and mass flow rate are known. A target efficiency is also fixed by selecting appropriate values of specific speed (N_s) and diameter (D_s), which eventually yields shaft speed and impeller diameter for each compression stage.
- Finally, the geometry for each stage is obtained by solving the inverse problem.

4.4.1 Cycle definition

According to the solar-oriented application of the project, the design concept is based on an S-CO_2 power cycle for a 10 MW central receiver solar plant. The turbine inlet temperature is set to 1100 K, which is an affordable value for this type of technology (central receiver) even though the existing plants still work at a lower temperature (in the order of 850 K for a multi-megawatt application). The maximum pressure of the cycle is on the other hand limited to 250 bar which brings about a much more demanding

operating environment for the receiver in comparison with the previous temperature specification. The remaining specifications for the cycle design are the performance parameters indicated in table 12.

Isentropic efficiency of the turbine	90 %
Isentropic efficiency of the compressor	80 %
Recuperator effectiveness	95 %
Mechanical efficiency	98 %
Pressure drop in the hot side of the recuperator	1.5 %
Pressure drop in the cold side of the recuperator	0.5 %
Pressure drop in the heater	2 %
Pressure drop in the cooler	1 %

Table 12. Performance parameters for the cycle design.

The choice of compressor inlet conditions is crucial in supercritical cycles given their proximity to the saturation line. Hence, even though the total pressure and temperature at the inlet to the compressor are selected in the supercritical superheated vapour region, the local acceleration of the flow in the entry region of the impeller might sink the static properties down into the biphasic zone. The probability of encountering two-phase flow depends not only on the total properties of the flow but also on impeller geometry and inlet Mach number.

For given total inlet conditions, it is possible to calculate the isentropic static point where condensation would ideally take place (or, more precisely, where the saturation conditions would be met) by modelling an isentropic expansion of the flow down to the saturation pressure/temperature. The Mach number resulting from this isentropic expansion is termed *Acceleration Margin to Condensation* (*AMC*) and it is convenient to keep it as high as possible in order to avoid two-phase flow at the impeller throat. Figure 96 shows the variation of *AMC* with compressor inlet temperature (T_{01}) and pressure (P_{01}). As expected, increasing T_{01} and decreasing P_{01} benefits the design as it separates the inlet stagnation state from the saturation line and therefore as AMC increases

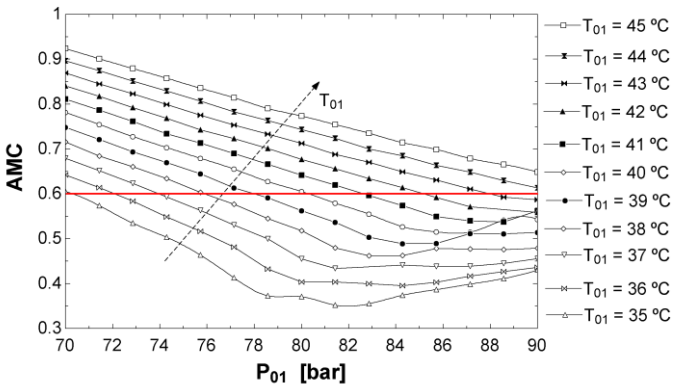

Figure 96. Compressor AMC as a function of the stagnation pressure and temperature at the inlet.

The selection of a certain *AMC* influences the efficiency of the cycle as it modifies the total conditions at the inlet to the compressor, therefore fluid compressibility and compression work, as shown in figure 97. The red lines in both figures represent the locus where AMC = 0.6, which could be an acceptable design margin.

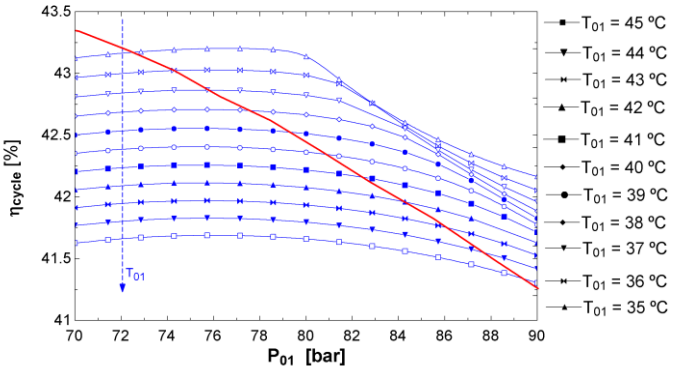

Figure 97. Cycle efficiency as a function of the stagnation pressure and temperature at the inlet.

Based on the previous figures, the total inlet pressure and temperature are set to 75 bar and 40 ºC respectively. This pressure is slightly above the critical point in order to get a purely supercritical cycle whereas temperature is selected in order to achieve a cycle efficiency higher than 40 %. The design specifications for the compression system of a 10 MW power plant are those listed in the table below.

Inlet stagnation temperature	40 ºC
Inlet stagnation pressure	75 bar
Mass flow rate	73.04 kg/s
Total-to-total pressure ratio	3.33:1
Gas	Carbon Dioxide (CO_2)

Table 13. Design specifications of the compression system.

4.4.2 Compression system design

The design of the compression system is based on the specific speed-specific diameter diagram provided by Balje (Balje, 1981) (Figure 98), where these dimensionless parameters are based on the volume flow rate ($\dot{V}$) and isentropic enthalpy change (Δh_s) of the stage.

$$N_s = \frac{N\dot{V}^{1/2}}{\Delta h_s^{3/4}}$$

$$D_s = \frac{D\Delta h_s^{1/4}}{\dot{V}^{1/2}}$$

[Equation 4.87]

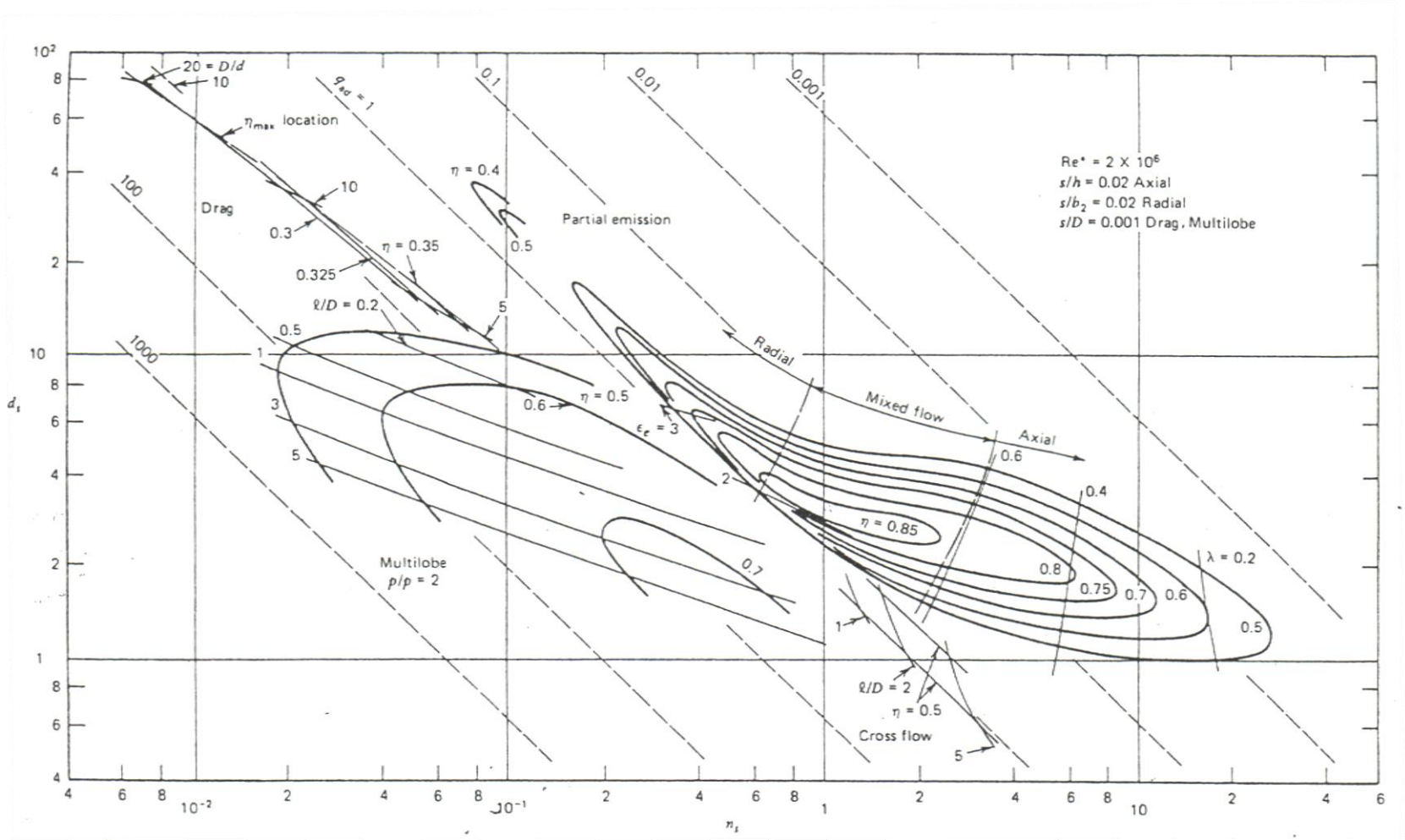

Figure 98. N_s-D_s diagram for single stage compressors (Balje, 1981).

The diagram above results from fitting curves to a vast experimental information gathered for compressors of all types and working fluids. Therefore, although supercritical carbon dioxide is an uncommon fluid with regard to turbomachinery design, it can be assumed as reported by Fuller and co-workers that the desired compression stages follow the patterns presented in the diagram (Fuller, et al., 2012).

The design aim is thus to maximise the efficiency of the stage and, at the same time, minimise shaft speed as a secondary target. It is noted that, as mentioned in (Fuller, et al., 2012), reducing shaft speed brings about a number of advantages when it comes to compressor design: higher availability, longer life, and lower Mach number at impeller throat which, in turn, reduces the risk of condensation. All these into account, it is decided to set a limit to the shaft speed at 20000-30000 rpm.

On the other hand, the optimum specific speed is identified to lie in the range 0.60-0.77 as established in (Rodgers, 1980). In consequence, for the volume flow rate that resulted from cycle design, the enthalpy change (or pressure ratio) is also limited which might result in several compression stages. Once this is solved, the selection of the appropriate specific diameter permits calculating the impeller diameter.

The common approach to distribute the duty of a multistage compressor is to assume that all the stages have the same specific work consumption. A different approach is used here though, since it is considered that it is pressure ratio which is evenly distributed amongst the various compressor stages, thus leaving the number of stages as the only unknown. A condensation-free operation is assured by eliminating all the possible designs for which the throat Mach number is lower than the AMC estimated as:

$$AMC = \frac{v_{limit}}{a_{limit}} \qquad \text{[Equation 4.88]}$$

Where the limit velocity is derived from the energy conservation and the conditions of isentropic flow, i. e. $h_0 = h_{limit} + v_{limit}^2/2$ and $s_0 = s_{limit}$. The equation of state of the fluid links both h_{limit} and s_{limit} with the speed of sound at these conditions, a_{limit}.

The next step is to produce a draft impeller geometry from which the design process could be initiated. To this aim, two radius ratios for the impeller are initially considered: inlet to outlet radius ratio and hub to shroud radius ratio at the inlet [Equation 4.89]. These ratios allow calculating an inlet flow area and therefore an inlet absolute velocity using energy conservation and isentropic flow as before. It is very important to note that these hypotheses have been considered in order to get an estimate only and they never must be taken as stage design inputs.

$$\begin{cases} r_{out}/\overline{r_{in}} = 2.8 \\ r_{in.s}/r_{in,h} = 2.5 \end{cases} \qquad \text{[Equation 4.89]}$$

Shaft speed is obtained from the specific speed selected previously and permits calculating the magnitude and angle of the inlet relative velocity if the absolute velocity assumed in the axial direction.

$$\beta_{in} = \operatorname{atan}(u_{in}/v_{in}) \qquad \text{[Equation 4.90]}$$

where v_{in} was previously obtained.

As proposed in (Aungier, 2000), throat area can be estimated as $A_{th} = A_{in}\cos\beta_{in}$, where the velocity triangle of Figure 99 applies. The flow at the throat is solved thanks to the application of mass and energy conservation along with a consideration that the flow is isentropic [Equation 4.91] and that both the blade speed and blade angle remain constant downstream of the inlet section; it is also noted that continuity makes use of the absolute velocity normal to the throat ($w_{th} - u_{th}\sin\beta_{th}$).

$$\begin{cases} h_{02} = h_{th} + \frac{1}{2} v_{th}^2 \\ \dot{m} = \rho_{th} A_{th} (w_{th} - u_{th} \sin \beta_{th}) \\ s_{02} = s_{0th} \end{cases}$$ [Equation 4.91]

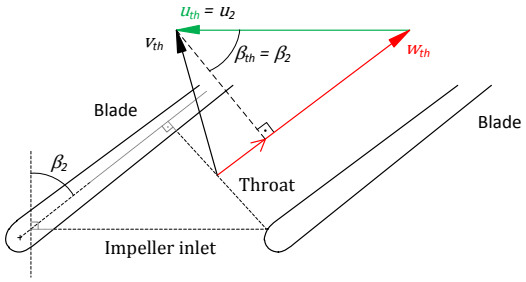

Figure 99. Velocity diagram at impeller throat.

The procedure described in the previous paragraph yields the throat Mach number which can be compared against the AMC initially calculated. This is shown in the next two tables for two and three compression stages with a specific speed of 0.7 in the first one and specific diameter of 4 for each of them.

Stage	Speed (rpm)	Impeller diameter (mm)	AMC	Throat Mach number
1	21151	185.5	0.689	0.554
2		144.2	1.290	0.394

Table 14. Two-stage compression system, N_{s1}=0.7 D_s=4.

Stage	Speed (rpm)	Impeller diameter (mm)	AMC	Throat Mach number
1	15184	207.2	0.689	0.416
2		175.2	1.113	0.336
3		149.4	1.462	0.274

Table 15. Three-stage compression system, N_{s1}=0.7 D_s=4

It must be highlighted that blade thickness is been neglected in the calculation of flow area, which is a simplification that will later be corrected in section 4.4.3, where a more precise model is generated.

As for the results, the option of three stages is more conservative regarding the margin to condensation, but has the drawback of higher costs and complexity in comparison to the two stages alternative. Moreover, Mach number is not uniform at the throat as higher blade speeds are found at the shroud which increases the risk of condensation so a further investigation of this aspect must be carried out at a later stage of the design process both for the two and three stage designs. A decision so as to which is the most suitable design will then be done.

4.4.3 Stage design

The inverse problem is solved in this last step of the design process, yielding the full geometrical definition of both impeller and diffuser for each compression stage. Stage design is divided into 5 parts in a structure similar to that of the model of performance: inducer, impeller, vaneless space, vaned diffuser and volute. The first one is designed independently, whilst the design of the remaining parts are linked to one another as shown in figure 103.

Prior to initiating any design process, there are a number of parameters whose values must be selected by the designer and which then remain constant throughout the process. These choices are based on experience and include the number of blades in each element, the thickness of these blades and the geometry of the seals. Should any of these decisions lead to inappropriate designs, the corresponding guess would need to be changed and the design process initiated again.

4.4.3.1 Inducer design

The design of the inducer is not linked to other parts of the compressor. Nonetheless, it is a crucial element as it must ensure that no condensation takes place at the throat (saturation conditions are not met) for which the *AMC* must be considered. Mass flow rate ($\dot{m}$), total inlet conditions (P_{01}, T_{01}) and shaft speed (ω) are the predefined boundary conditions to which the following two inputs must be added:

- **Shaft diameter**, or hub radius at impeller inlet (r_{2h}). It is set to constant value during the design process. However, there is a minimum shaft diameter based on mechanical integrity issues [Equation 4.92] (Loewenthal, 1984), which has to be compared with the fixed r_{2h} based on aerodynamic considerations and obtained at the end of the design. In consequence, if $2r_{2h} < d_{axis,min}$ the design must be modified.

$$d_{axis,min} = \sqrt{\frac{16\dot{W}_m}{\omega\pi\tau_m}} \qquad \text{[Equation 4.92]}$$

  Where $\dot{W}_m$ is the gross mechanical power (i.e. without considering mechanical losses) transmitted by the shaft[14] and τ_m is the shear stress limit of the material.

- The **absolute Mach number at the throat** (M_{th}) must be lower than the AMC of the stage in order to ensure condensation-free operation.

The shroud radius (r_{2s}) and the leading edge blade angle (β_2) are calculated as follows:

1. A value of r_{2s} is guessed.
2. The geometry at impeller inlet is calculated[15].
3. The velocity diagram at impeller inlet is calculated and therefore the relative flow angle which is equal to the leading edge blade angle (β_2) if null incidence is assumed.
4. Throat geometry is calculated.
5. Throat flow is solved as described at the end of section 4.4.2.
6. With the static conditions obtained previously, the absolute Mach number is calculated and compared with the desired one.

Points 1 to 6 are carried out for several values of r_{2s} and the results are then shown graphically to appreciate the variation of Mach numbers when the shroud radius varies. This is shown in Figure 100, representing these results for the first stage in the compression systems with 2 (left) and 3 (right) stages whose main characteristics were detailed in table 14 and 8.

[14] *The total mechanical power includes not only the power that the fluid absorbs, but also the losses due to leakage, disk friction and recirculation:* $\dot{W}_m = \dot{m}(I_B + I_L + I_{DF} + I_R)u_3^2$.

[15] *The area reduction because of the leading edge thickness is here considered.*

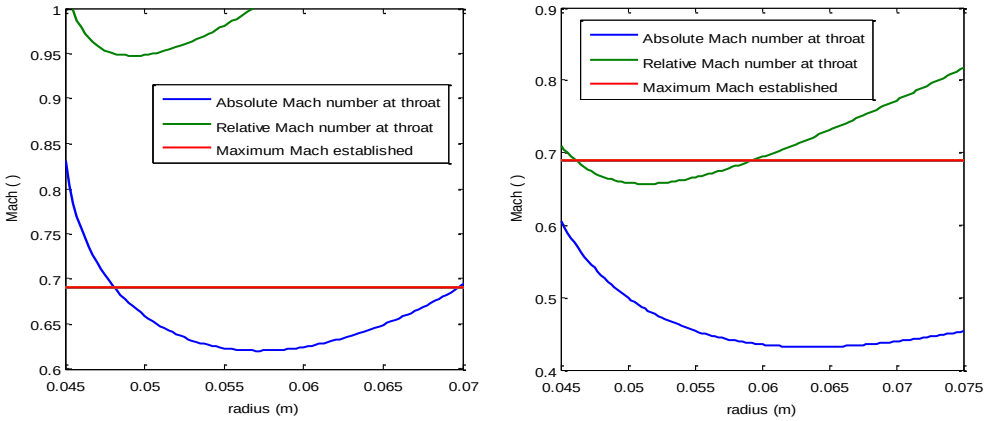

Figure 100. Absolute and relative Mach numbers at the inducer throat of the first stage of a compression system with 2 (left) and 3 (right) stages.

The two-stage system does not allow for designing the stage with a Mach number lower than 0.62 in the throat, which is risky taking into account that *AMC* = 0.689 (red line). Additionally, the relative Mach number for this alternative is always over 0.95. In contrast, when a three-stages system is adopted, it is possible to employ relative Mach numbers at the throat lower than the *AMC*. Therefore the three-stages option is finally selected.

4.4.3.2 Impeller design

Once the inlet section of the impeller has been sized in the previous section, the design of the entire impeller implies calculating the blade angle at impeller exit (β_3), for which the desired stage pressure ratio is achieved. it must be noted that even if the impeller exit radius (r_3) plays an important role in this issue as well, it is not considered as a degree of freedom for it is determined by the desired specific diameter (section 4.4.2).

It must be also noted that pressure losses occur downstream the impeller which have an impact on stage pressure ratio. Therefore, coefficients of performance of both diffusers and volute must be initially guessed prior to closing the design of the impeller. In few words, given the mutual influence between the different elements of the compressor, this draft design will later have to be refined to account for the performance of the remaining of the machine.

Summing up, impeller design provides the impeller exit angle and requires the following inputs:

- The **impeller exit radius** (r_3), imposed by the specific diameter.
  The **total-to-total efficiency** (η_{tt}) of the stage and the **total pressure loss coefficient of the system formed by diffuser and volute,** [Equation 4.93], must be guessed in order to get the desired conditions at impeller exit. The development of the design process requires to update this parameter for convergence.

$$K_{diff-vol} = \frac{P_{03} - P_{06}}{P_{03}} \qquad \text{[Equation 4.93]}$$

- The **ratio of meridional velocities between impeller inlet and outlet** is a design choice commonly set to 1.

The design loop for the impeller is as follows:

1. A value of $K_{diff-vol}$ is assumed and kept constant throughout the entire impeller design process.
2. A value of η_{tt} is initially guessed.

3. The absolute total conditions at impeller exit are defined by pressure and enthalpy, calculated by means of the following system of equations:

$$\begin{cases} h_{03} = h_{02} + \dfrac{\Delta h_{0s}}{\eta_{tt}} \\ P_{03} = \dfrac{P_{01}\, PR_{stage}}{1 - K_{diff-vol}} \end{cases} \qquad \text{[Equation 4.94]}$$

   Where Δh_{0s} is the isentropic total enthalpy change of the stage, calculated from the desired total-to-total pressure ratio. The equation for P_{03} is derived from the proper definition of $K_{diff-vol}$ taking into account that $PR_{stage} = P_{06}/P_{01}$.
4. v_{u3} is calculated with Euler's equation while the meridional component (v_{m3}) is a design choice, usually $v_{m3} = v_{m2}$.
5. The performance parameters of the impeller parameter are assumed ideal, i.e. $\sigma = \lambda = 1$ and $\sum_{2\to3} \varpi_i = 0$.
6. The impeller blade exit angle is calculated by $\beta_3 = \text{atan}[(v_{u3}/\sigma - u_3)/(\lambda v_{m3})]$
7. The velocity diagram at impeller exit is solved and, consequently, the static conditions.
8. By continuity, the blade height at impeller exit (b_3) is calculated.
9. The impeller is thus completely defined[16]. Therefore, it is simulated with the model presented in section 4.2.3 in order to update slip and distortion factors as well as losses in it. In consequence, it is necessary to iterate from points 6 to 10 to achieve convergence.
10. Once the impeller is consistently solved, the new outlet conditions can be calculated since $K_{diff-vol}$ is still the same. The total-to-total efficiency is then updated, giving place to an external iteration loop from points 3 to 10.

4.4.3.3 Vaneless space design

There usually exists a vaneless space between impeller and diffuser with the objective of homogenising the flow and produce a certain flow diffusion at the same time. The design of this part comprises the definition of the blade height (b_4), blade angle (β_4) and radius (r_4) at the leading edge of the diffuser blades. [Equation 4.95] is an empirical correlation proposed in (Aungier, 1988) to size the radius:

$$\frac{r_4}{r_3} = 1 + \frac{90 - \alpha_4}{360} + \frac{M_3^2}{15} \qquad \text{[Equation 4.95]}$$

This space provides the necessary path downstream of the impeller to reduce the distortion of the flow coming out from the latter element, thus reducing the locally high Mach number to the extent possible. An appropriate design of the angle β_4 should guarantee a wide enough stable operating range, i. e. stall-free operation. Figure 101 shows how incidence and inlet flow angle in stall conditions vary with diffuser leading edge angle for different Mach numbers and considering 20 vanes in all cases. These curves are result from solving [Equation 4.64] to [Equation 4.66] for the various cases. As a general rule of thumb, it is concluded that the lower the Mach number, the higher the stall margin, which justifies the interest of diffusing the flow before going into the diffuser. However, this parameter is not a design choice as it comes imposed by impeller design. In contrast, the diffuser leading edge angle is here a design result that is defined by incidence (typically around -1º (Aungier, 2000)). The flow angle at this point is controlled by blade height, which is a design choice constraint to:

[16] *The impeller geometry is calculated by a simple model where the blade camber line is assumed circular. More details of the method are provided in (Aungier, 2000).*

$$b_4 \leq b_3$$ [Equation 4.96]

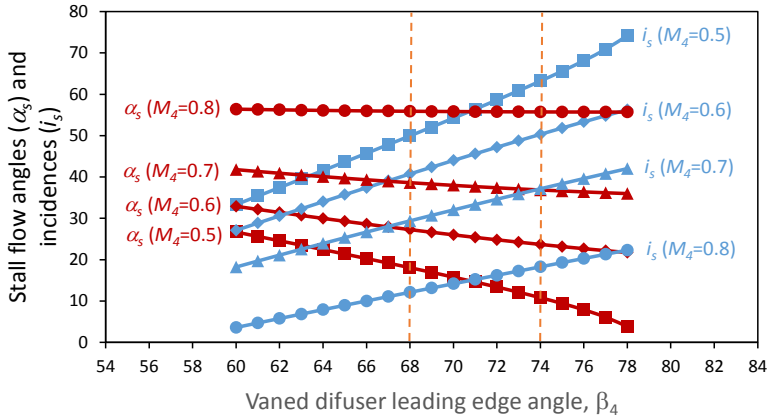

Figure 101 Effect of the diffuser leading angle and the Mach number at diffuser inlet onto the stall incidence (blue) and flow incidence angle (red) for a diffuser with 20 vanes.

Empirical observation (Aungier, 2000) shows that the most favourable diffuser leading angle designs are found for β_4 between 68 and 74 º and for the radius ratio, r_4/r_3, between 1.06 and 1.12. This region is marked with dashed lines in Figure 101.

The design loop is presented below:

1. The meridional velocity at the diffuser leading edge (v_{m4}) is guessed.
2. [Equation 4.95] is solved along with the momentum conservation equation ($r_3 v_{u3} = r_4 v_{u4}$) and velocity diagrams, yielding the flow angle α_4. An internal loop is necessary in order to solve this system of equations.
3. Mass and energy conservation is solved simultaneously with the equation of state and the total pressure loss equation[17], yielding the static conditions.
4. Loss terms are calculated. In this initial estimation, only two loss terms are considered: one due to wall friction and another due to the geometric contraction at the diffuser leading edge (Benedict, et al., 1966). The latter is modelled as:

$$\omega_{cont,VL} = \cos^2 \alpha_3 \, (1 - b_3/b_4)^2$$ [Equation 4.97]

5. In parallel, v_{m4} is updated.
6. The geometry is fully defined when iterating from points 2 to 5. Then, this component is simulated in detail with the vaneless space model presented in section 4.2.4.

4.4.3.4 Vaned diffuser design

Given that the leading edge is defined in previous design loops, designing the vaned diffuser comprises the calculation of the outlet and throat geometries only. Thus, there are three degrees of freedom that need to be specified for the full geometrical definition of the diffuser (Aungier, 2000). Thus, as opposed to other elements, the diffuser is designed by a sort of a trial-and-error process where, after defining those three degrees of freedom, the geometry is computed and the diffuser is modelled as described in section 4.2.5. Once this is completed, the parameters are checked to be within acceptable ranges and, if not, they are updated and the process is initiated again.

Following the indications in (Aungier, 2000), the most commonly employed geometrical specifications are used here: radius ratio ($R = r_5/r_4$), area ratio (A_R) and number of blades (z_{DIF}).

[17] *In the first iteration no losses are considered.*

Amongst all the combinations of this parameters, the one that provides acceptable values for the divergence angle ($2\theta_c$), diffuser loading (L) and design parameter (E), [Equation 4.61] is adopted as the final design. From a designer standpoint, the following ranges are recommended based on experience:

- A divergence angle lower than 11º: $2\theta_c \leq 11º$
- A loading parameter not higher than 1/3: $L \leq 1/3$
- And a design parameter in the range 1.5-1.7, which indicates that using the vaned diffuser really improves the performance with respect to a vaneless diffuser: $1.5 \leq E \leq 1.7$.

As opposed to the impeller, the blade camber line is not assumed circular. Instead, the method developed in (Aungier, 1988), and also described in (Aungier, 2000) is used.

4.4.3.5 Volute design

There are two different methods to design the volute:

- The **simple area schedule (SAS)** method is based on varying the cross sectional area linearly with the angular coordinate θ. The design is accordingly defined by the full-collection plane area.
- More common and more precise, the **conservation of mass and angular momentum (CAM)** approach considers area variations in such a way that these two conservation laws are satisfied. When angular momentum conservation ($rv_u = r_5 v_{u5}$) and continuity ($\rho A v = \theta \rho_5 r_5 b_5 v_{m5}$) are satisfied, the cross-sectional area at a certain angle θ of the volute is: $A = \theta r_5 b_5 / \tan \alpha_5$. Therefore, the general equation for volute sizing is:

$$A = SP\ \theta\ r_5\ b_5 / \tan \alpha_5 \qquad \text{[Equation 4.98]}$$

Where SP is the sizing parameter that controls the design, already used in section 4.2.6. It is desirable that the sizing parameter be in the range [1, 1.2], 1 being the optimum value which means that momentum is conserved.

Taking SP as the input, the second approach is implemented in this work as follows:

1. The radius of the full-collection plane is initially guessed, R_{fcp}.
2. The geometry of the volute is completed with the simple expressions:

$$\begin{cases} r_6 = r_5 + R_{fcp} \\ A_{fcp} = \pi R_{fcp} \end{cases} \qquad \text{[Equation 4.99]}$$

3. The volute is modelled as described in section 4.2.6.
4. The sizing parameter is calculated by [Equation 4.84].
5. R_{fcp} is modified if SP has a value different to the desired one.

4.4.3.6 Design overview and results

The content dedicated to stage design and presented in previous sections is finally summarised here. figure 102 and Table 16 present the result of a valid design for the first compression stage with N_s and D_s equal 0.6 and 4 respectively, which has been obtained by the methodology developed herein. A sketch of this impeller is represented in figure 103.

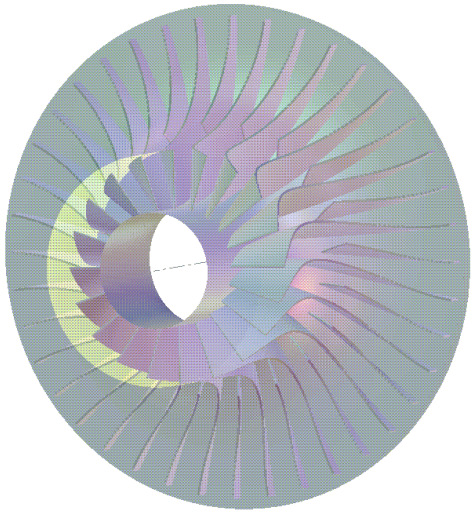

Figure 102. First stage geometry obtained with the one-dimensional design tool.

IMPELLER GEOMETRY	
Number of full blades	20
Number of splitter blades	20
Impeller inlet radius at hub	25 mm
Impeller inlet radius at shroud	50 mm
Impeller exit radius	103.6 mm
Blade angle of the impeller leading edge at hub	33.0 º
Blade angle of the impeller leading edge at mean radius	44.3 º
Blade angle of the impeller leading edge at shroud	52.4 º
Blade angle of the impeller trailing edge	-1.49 º (backward)
Angle between streamlines and shaft at impeller inlet	0 º
Angle between streamlines and shaft at impeller exit	90 º
Full blade length	72.5 mm
Splitter blade length	36.3 mm
Axial length of the impeller	66.1 mm
Blade thickness at impeller leading edge	1 mm
Blade thickness at impeller trailing edge	1 mm
Blade height at impeller leading edge	6.9 mm
Clearance gap at impeller tip	2 % of the span

Table 16. Geometry of the impeller obtained for the S-CO_2 cycle design.

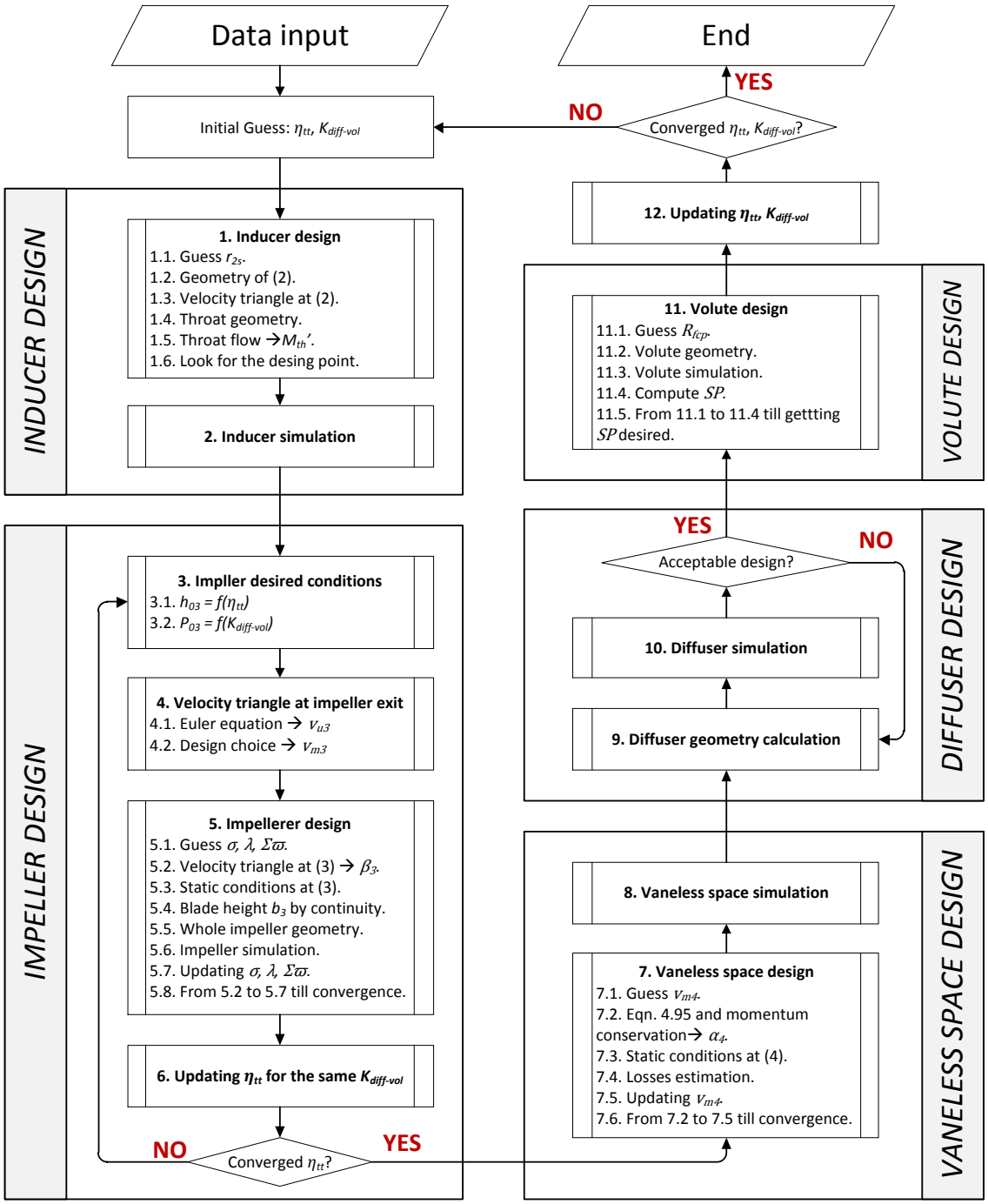

Figure 103. Loop for stage design.

4.5 Summary and conclusions

A literature review in the field of centrifugal compressor design has confirmed the importance of using one-dimensional tools in the preliminary stages of this process. After this evidence, a 1D tool has been developed which is able to provide a tentative detailed design of all the elements in such a turbomachinery: inducer, impeller, vaneless space, vaned diffuser and volute.

This 1D model of performance is presented in section 4.2 and its application to the direct problem is validated in section 4.3, both for supercritical carbon dioxide and air. The centrifugal compressor existing in the experimental S-CO2 loop at SANDIA NL was taken as reference for the first validation, whilst the NACA CC3 unit operating at the Glenn Research Center was considered for air. Good agreement was obtained for both cases and thus a tool based on the similar principles was implemented for the inverse problem (producing the geometry that yields a certain performance with the highest possible efficiency).

This design process for the inverse problem is affected by two aspects that are original for the application under analysis. These features must be bear in mind as they do not apply in standard turbomachinery using air:

- The Acceleration Margin to Condensation (*AMC*) becomes an important design parameters, in particular for the first stages. It is a way of measuring how far the flow is from meeting the saturation line (i.e. where condensation would take place theoretically), which would incur additional losses in addition to mechanical damage due to the impact of liquid droplets on the walls of the flow passage.
- Since high efficiency is desired, the compression system usually comprises multiple stages because the rotating speed of the shaft is limited by the *AMC*. A high enthalpy rise requires high rotating speeds, which would violate the *AMC* constraint. Therefore, the total pressure rise must be split into several stages.

Finally, the geometry of the first compression stage is presented at the end of the section 4.4 and will be analysed in the next chapter.

4.6 Justification of the research

Once the design process together with all related concepts have been presented, it is time to vindicate the research project presented in this dissertation. It must be acknowledged first of all that even though supercritical carbon dioxide is an original working fluid, the corresponding compressor raising its pressure is still a piece of turbomachinery and, as such, its design can be approached following conventional methodologies. Nevertheless, this being said, it must also be bear in mind that the unconventional behaviour of carbon dioxide in the vicinity of the supercritical point brings about some special features into this process. This introduces substantial differences when designing these machineries with respect to standard ones.

On one hand, regarding the operation of the exiting test rigs, there exist some operational constraints derived from the fluid nature. Thus, the condensation of the supercritical fluid in the inducer one represents an important inconvenient, since the experimentation with some existent prototypes has proven physical damage in the inducer blades when operating inside the biphasic region (below the saturation dome). Additionally, given the lower speed of sound of S-CO_2, choke is encountered earlier (at a lower fluid velocity) than in air turbomachinery. These aspects impose restrictions onto shaft speed, which generally imply larger impeller diameter for the same pressure ratio (in order to achieve high enough blade speeds at impeller outlet). However, in the light of the results presented in chapter 3, the risk of stall in the diffuser channels is higher for S-CO_2, unless the (dimensionless) length of the channel is also increased. A compromise must be thus achieved between these and other opposing effects.

In summary, the design space of a supercritical carbon dioxide compressor is modified because of the fluid nature. Moreover, the performance of this turbomachinery is expected to vary with respect to similar equipment operating on air or other conventional fluid. A sample of this is presented below in order to make it evidence to what extent the design space is influenced by the nature of the fluid.

Let the pressure ratio of a single stage radial compressor be considered as a function of the reduced pressure and temperature at the inlet (i.e. the *thermodynamic distance* from the critical point). The following assumptions are made:

- The ranges considered for the reduced inlet conditions are equivalent to assuming compressibility factors in the range from 0.24 to 0.87 approximately.
- The ratio from throat Mach number to AMC is set to 0.8 in order to avoid that avoid condensation during the initial expansion.
- The mass flow rate is kept constant at 73.04 kg/s whereas the specific speed and diameter are set to 0.7 and 4 respectively in order to increase efficiency as much as possible.

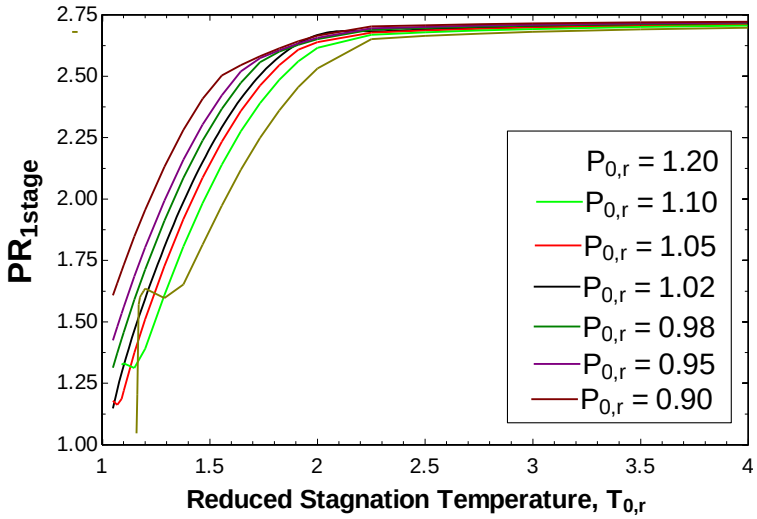

Figure 104. Effect of reduced inlet conditions on stage pressure ratio.

The results shown in figure 104 confirm the following:

- An anomalous behaviour is observed for reduced pressures over 1.05 when the reduced temperature gets close to unity. This is due to the sharp density rise with respect to temperature (see figure 16). Based on the definition of specific speed itself, the enthalpy rise decreases when density increases ($\Delta h_{0s} \propto \rho^{-2/3}$), and pressure is related with it. These points are characterised by very low values of the compressibility factor (around 0.25).
- The previous behaviour is not observed for the remaining curves as reducing the inlet temperature would give place to equilibrium condensation (coexistence of liquid and vapour in the subcritical region) rather than to a fluid with transition properties.
- As a main conclusion, it is observed that effect of the supercritical nature of carbon dioxide is translated into a limitation of the stage pressure ratio down to values around 1.2-1.7. These pressure ratios are much lower than expected from ideal gas compressors and they tend to increase with inlet temperature even if this influence vanishes as temperature increases. As a matter of fact, there is no further increase in pressure ratio for reduced temperatures higher than 2 regardless of the reduced pressure at the inlet. For higher temperatures, pressure ratio is limited by choke in the throat.
- Having into account that reducing the pressure ratio affects the specific work of the cycle, it would be necessary to increase the mass flow rate or, a rather elegant alternative, to employ multistage compressor, incurring in higher costs.

From a *thermoeconomic* standpoint, it is concluded that the working fluid sets new boundaries for the design space where the designer must make a decision between opposing effects. On one hand, using single stage compressors imply a reduction on cycle pressure ratio which impacts the performance of the system negatively. This translates into lower efficiency (regardless of power output) and higher costs for a given output (larger equipment for larger flow rates). On the other hand, should the designer

target higher efficiencies, it would be necessary to employ multiple stage turbomachinery thus incurring much higher costs.

This very simple example is just to confirm the interest of this research, which is deemed relevant for the S-CO2 community. Throughout the document, the main differences between air and supercritical carbon dioxide are discussed and design recommendations are provided whenever possible. Furthermore, the tool presented is expected to enable the development of an optimisation tool based on which design engineers will hopefully save time and money when developing turbomachinery for a particular application. Even if this tool exceeds the scope of this work, this research paves the way for its successful development in the near future.

CHAPTER 5. Three-dimensional CFD simulation of supercritical carbon dioxide turbomachinery

Before proceeding to prototype manufacturing, it is absolutely necessary to perform accurate aerodynamic simulations in order to ensure that the compressor will integrate correctly into the power cycle. One-dimensional tools like those presented in the previous chapter are useful for the rapid evaluation and global geometry definition of a number of design alternatives, but they provide limited information of the flow features within the machine stations and thus fully three-dimensional calculations are required. As illustrated in figure 72, it is also usual to employ simulations of intermediate complexity for optimisation, streamline curvature methods being the most widespread (Boyer, 2001) followed by inviscid-3D and turbulent-3D simulations.

This chapter is aimed at fully-3D simulations of the impeller that resulted from the 1D design. It means that the exact geometry of the impeller is run by CFD (using ANSYS Fluent®) considering the particular features of supercritical carbon dioxide exposed in chapter 2, including boundary layer effects. Prior to that, a coarser impeller model is run, which excludes those elements that add considerable computational burden, i.e. clearance gap and boundary layer refinement. 2D and inviscid-3D simulations are hence omitted in this project even if they are mentioned at the end of the chapter as the subject of future research at GMTS. These 2D simulations are faster than 3D CFD models and with acceptable precision, thus being excellent choices when developing optimisation studies. In fact, they are catalogued as the "*backbone of turbomachinery design*" by Denton and Dawes (Denton & Dawes, 1999).

5.1 Geometry generation

One-dimensional design provides blade angles and radii at the hub and shroud for the inlet and outlet stations of each compressor element, whereas other dimensions such as blade lengths and impeller axial length are estimated based on simple considerations proposed in (Aungier, 2000). It is worth noting that generating the full three-dimensional shape of the impeller and other elements requires extensive work, involving complex mathematical treatment of the geometry. It is nevertheless possible today to circumvent this hurdle thanks to specialised software such as the one employed in this project, ANSYS BladeGen®; which is able to create the 3D geometry apart from the parameters that follow:

- Hub and shroud radii at inlet: r_{2h} and r_{2s}.
- Radius and blade height at impeller exit: r_3 and b_3.
- Impeller axial length: L_{axial}
- Number of full and splitter blades: z_{FB} and z_{SB}
- Blade angles at hub, mean-radius and shroud in the inlet station, as well as the blade angle at impeller exit: β_{2h}, β_2, β_{2s} and β_3.
- Length ratio between splitter and full blade: L_{SB}/L_{FB}.
- Thickness at leading and trailing edge: t_2 and t_3.

Bezier curves (Casey, 1983) are the most common option employed to define the contours of hub and shroud and is here used (this is possible in ANSYS BladeGen®), Figure 105. The inlet flow is assumed in the axial direction whereas the outflow is contained in a plane normal to the shaft (purely radial machine), after which the default geometry provided by the software is assumed valid. This

geometry is based on curves given by five reference points at the hub and shroud contours (see Figure 105).

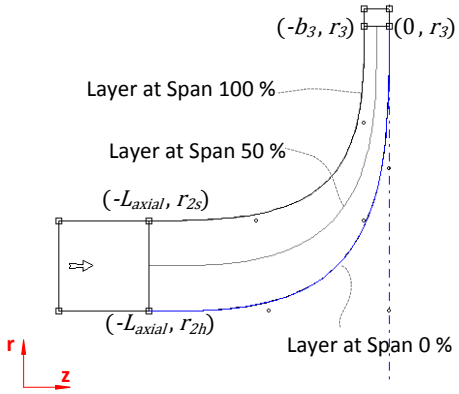

Figure 105. Impeller hub and shroud curves.

Three control layers are defined span-wise (at spans of 0, 50 and 100 %) which are later employed for the definition of blade angle and thickness. A constant value is assumed for thickness stream and span-wise whilst the angle is modelled by the option "*End Angle Definition*" for each layer (see figure 106). Four input angles are needed for this option: "*Beta*" (cyan curve in figure 106) and "*Theta*" (blue curve in figure 106), both at the inlet and outlet, define univocally a blade angle distribution which is compatible with the 1D design results.

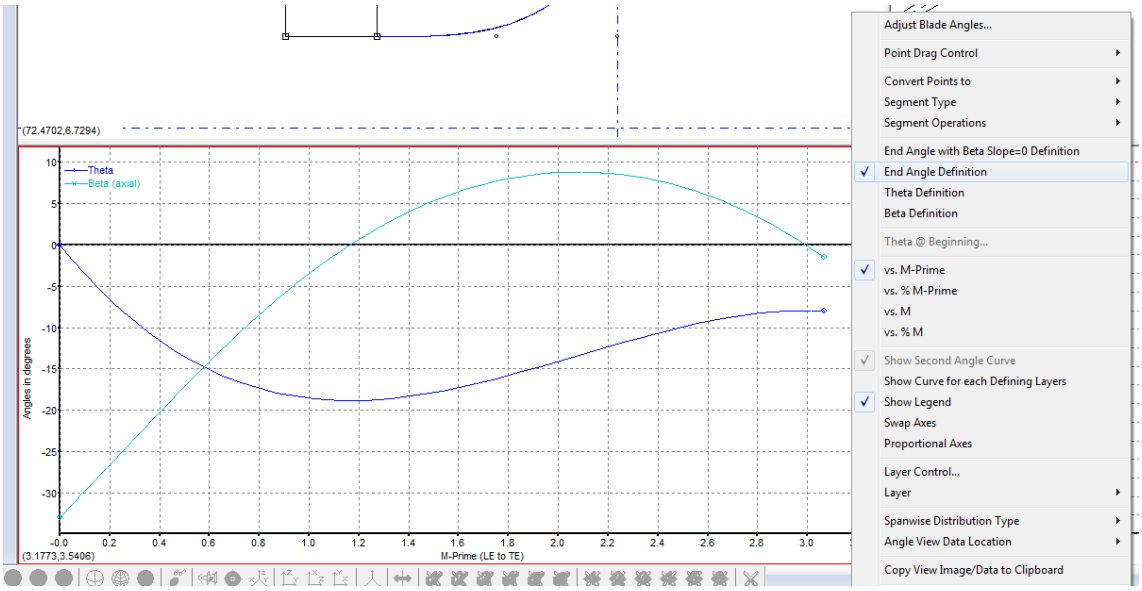

Figure 106. Window for angle definition in ANSYS BladeGen®.

The "*Beta*" angle is defined with respect to the meridional direction while the "*Theta*" angle defines the polar coordinate with respect to an origin selected. Therefore, for the same set of "*Beta*" angles, the same geometry is obtained as long as the increment in "*Theta*" is the same. Eventually, the angle distribution of a layer is defined by the following considerations:

- "*Beta*" angles coincide with those obtained from the 1D design: β_{2h}, β_2, β_{2s} and β_3.
- "*Theta*" angle at the inlet is set to 0.
- "*Theta*" angle at the outlet is modified to adjust the full blade length to the one obtained from the 1D design.

Finally, splitter blades are incorporated taking into account that the trailing edges of both splitter and full blades are located at the same meridional coordinate; the leading edge of the splitter blades is nevertheless located according to the length ratio. For both full and splitter blades, cut-off trailing edges are considered whilst an elliptic shape is used for the leading edges. Summing up, figure 102 represents the impeller geometry obtained from the 1D design, where no clearance gap has been created yet since ANSYS BladeGen® does not permit it. How the interstitial is created is explained in the next section.

5.2 The computational model

5.2.1 The mesh

A number of works have been already done in the field of numerical analysis of S-CO2 turbomachinery, showing that it is possible to use either structured (Munroe, et al., 2009) or hybrid meshes[18] (Pecnik & Colonna, 2011) (Pecnik, et al., 2012) (Rinaldi, et al., 2013) with satisfactory results. Hybrid meshes allow for varying the mesh density according to the problem needs without affecting other regions of the fluid domain. This is not the case for structured meshes though since projecting the boundary layer refinement towards the external boundaries brings about an unnecessarily large number of elements (Figure 107). This can eventually give place to high aspect ratio cells which may cause numerical divergence. This issue can be overcome by obtaining the final solution in a step-by-step method, i.e. from coarser to finer meshes including boundary layer and gap treatment.

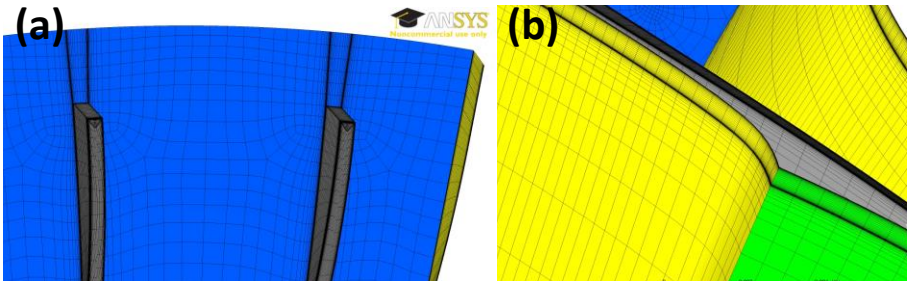

Figure 107. Detail of structured meshes: Projection of boundary layer towards external boundaries: (a) Projection of blade boundary layer downstream of the trailing edges. (b) Projection of the boundary layer in the gap towards the periodic boundaries.

Unstructured meshes based on tetra cells have also been analysed in this work, but they have been discarded because of the risk of numerical diffusion. This is observed in figure 108, where an impact of the location of the surface elements of the mesh on the absolute velocity profile is shown regardless of the size of the mesh. Due to the dissimilarity between cell shape and fluid domain geometry, a higher number of elements is required for unstructured meshes than for structured ones, meaning that the hexa cells in the latter can be adapted to the flow channel making them longer stream-wise whereas, at the same time, they are adapted pitch and span-wise in accordance to the physical requirements of the problem, i.e. near wall regions. Therefore, structured meshes are considered the most appropriate selection.

[18] *Hybrid meshes combines regions with hexa and tetra cells in the same computational domain, including the O-Grid in the boundary layer as an option.*

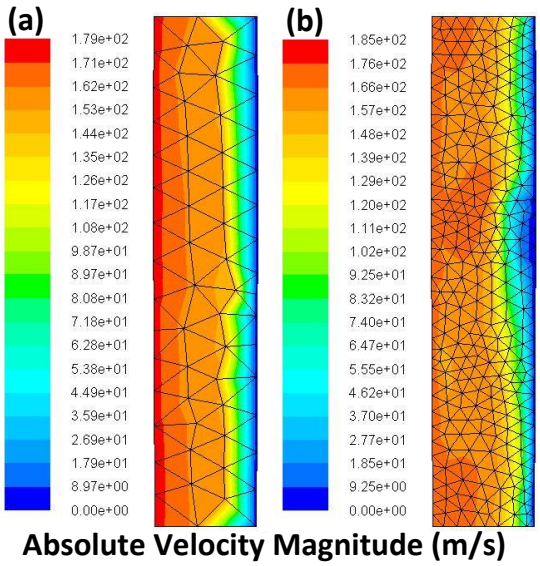

Figure 108. Detail of unstructured meshes: the velocity field at the outlet is largely affected by the mesh; results are masked by numerical diffusion. Meshes **(a)** *with 287911 elements and mesh* **(b)** *with 2523482 elements.*

The grid has been created with a dedicated software specialised in turbomachinery meshing, ANSYS TurboGrid®, which is a structured-mesh generator. Prior to mesh generation, this software allows to create the clearance gap by, for instance, specifying a percentage fraction of the span amongst other different methods. For this case, according to the 1D results, the gap size was set to 2 % of the span. Alternatively, ICEM CFD could have been employed to generate unstructured or hybrid meshes but the process is more complex, more susceptible to errors and there are no significant advantages in the mesh quality and size regarding the CFD software employed later.

General mesh parameters are kept constant for all the meshes created while a boundary layer refinement is implemented with the aim of reducing y+ progressively. As recommended in the TurboGrid's User's Guide, the selection of a certain topology results from a trial and error approach: i.e. trying all of them and verifying which exhibits a higher quality. It is nonetheless usual that the *ATM Optimised* topology achieves the best results. A global size factor of 1 is thus fixed, namely "Fine Mesh", meaning around 140000 cells without boundary layer. Span-wise mesh parameters are set in order to obtain a homogeneous grid, i.e. a proportional discretisation in comparison with the stream and pitch-wise directions.

The Reynolds number (based on the blade height) is calculated as the mean value between inlet and outlet from 1D calculation. This parameter is employed by the software, together with a desired wall y+ (namely Offset Y+, table 17), to calculate the distribution of prismatic layers in the boundary layer mesh, in such a way that the higher the Reynolds number is, the smaller the first layer will be for a same Offset Y+. In summary, once the Reynolds number is defined, the boundary layer refinement is controlled in ANSYS TurboGrid® by means of the Offset Y+.

Finally an additional factor is necessary to define the boundary layer at the cut-off trailing edges, which controls the first element size on that wall surface.

General parameter	
Topology of the mesh	ATM Optimized
Global Size Factor	1
Span-wise mesh method	Proportional
Span-wise mesh Factor	1
Shroud Tip mesh method	Match Expansion at Blade Tip
Reynolds Number	$9.4 \cdot 10^7$
Refinement variables	
Offset Y+	10^3, 10^2, 10, 1
Cut-off Edge To Boundary layer Factor	0.5, 1

Table 17. Characteristics of the structured mesh.

5.2.1.1 GCI analysis

As done in chapter 3 for 2D simulations, the *GCI* methodology is here applied to the compressor in order to find an adequate mean element size of the model. The *GCI* analysis is accordingly applied to the impeller geometry without the gap nor the boundary layer refinement, with the purpose of including afterwards these two aspects of higher accuracy modelling. Five different meshes are created in TurboGrid® by modifying the *Global Size Factor* from 0.5 to 1.8, obtaining the characteristics presented in table 18:

Mesh	Number of elements	Mean size, $\bar{h}$ (m)	Ratio, r_{ij}
1	26432	$1.446 \cdot 10^{-3}$	-
2	61921	$1.095 \cdot 10^{-3}$	1.32
3	137775	$8.396 \cdot 10^{-4}$	1.30
4	313104	$6.394 \cdot 10^{-4}$	1.31
5	700128	$4.894 \cdot 10^{-4}$	1.31

Table 18. Features of the meshes employed in the GCI analysis.

Mass-weighted average values of pressure, temperature and (absolute and relative) velocity both at the inlet and the outlet are reported in Table 19 for each simulation, using the computational model, described in this section. The GCI methodology is thus applied to the mesh groups 1-2-3, 2-3-4 and 3-4-5, from which several extrapolated values and therefore convergence indexes are calculated. Table 19 shows the extrapolated values obtained with the group of finer meshes along with other information of interest:

Mesh	$\bar{p}_{in}$ (bar)	$\bar{T}_{in}$ (K)	$\bar{v}_{in}$ (m/s)	$\bar{w}_{in}$ (m/s)	$\bar{T}_{out}$ (K)	$\bar{v}_{out}$ (m/s)	$\bar{w}_{out}$ (m/s)
Mesh 1	71.491	309.66	55.439	83.392	336.29	160.652	73.407
Mesh 2	71.413	309.65	55.566	83.486	336.32	162.039	74.703
Mesh 3	71.375	309.64	55.633	83.532	336.36	161.973	75.657
Mesh 4	71.297	309.63	55.769	83.624	336.43	162.084	76.200
Mesh 5	71.234	309.62	55.879	83.698	336.48	162.216	76.524
Extrapolated value	70.922	309.61	56.004	83.784	336.57	162.225	77.615
GCI_{45} (%)	0.546	0.004	0.281	0.128	0.032	0.007	1.791
$\varepsilon_{3,ext}$ (%)	0.638	0.011	-0.664	-0.301	-0.063	-0.155	-2.523

Table 19. Mass-averaged reports in meshes for the GCI analysis.

In the light of these results, and bearing in mind the limited computational capacity, mesh 3 is selected, whose relative error with respect to the extrapolated value is below 1 % for every averaged variable except the relative velocity at the outlet.

Regarding local results, different outlet velocity profiles are analysed at the midspan, as shown in next plots:

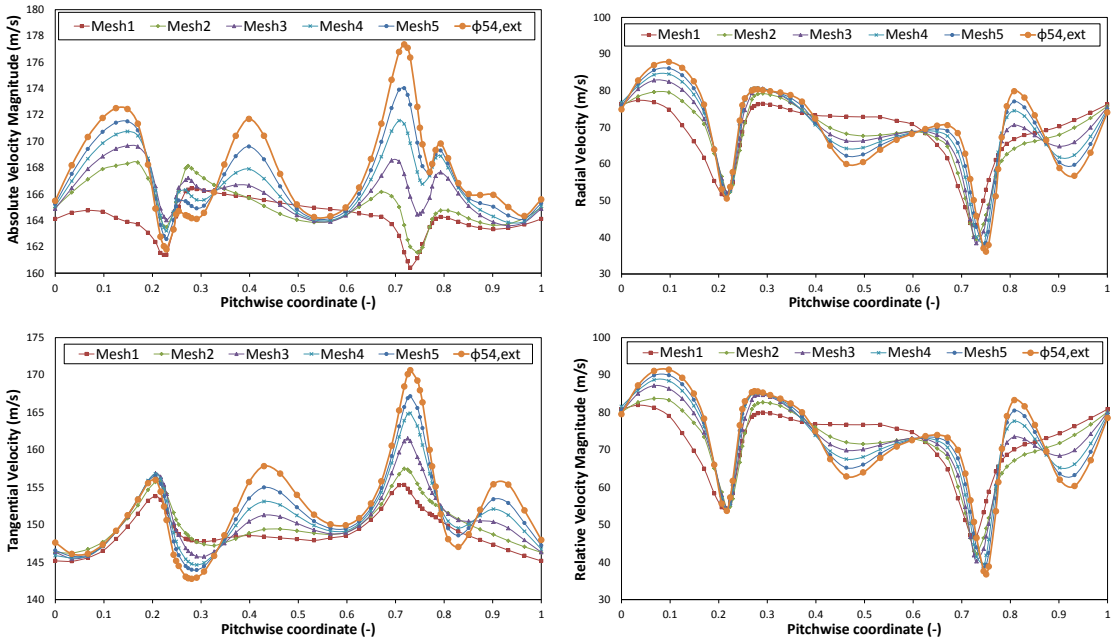

Figure 109. Absolute, radial, tangential and relative velocity profiles pitch-wise at the outlet midspan position. Data shown for meshes and extrapolated values.

In addition to the velocity profiles obtained from the five meshes, extrapolated profiles are also plot in figure 109 which have been obtained by applying the GCI methodology locally and then averaging the apparent order of the method. In spite of the satisfactory results obtained for the mean averaged values, see Table 19, appreciable differences can be observed between Mesh 3 and extrapolated profiles. Note that even if this error is balanced pitch-wise in such a way that the mean errors along the profiles between mesh 3 and the extrapolated values is -1.06, -0.51, -0.89 and -0.37 % respectively for the absolute, radial, tangential and relative velocities, the plots suggest that care must be taken when applying the results to a local flow analysis.

Better agreement exists in the pressure distribution in the stream-wise direction, plotted in Figure 110 for both sides of the full blades in the five meshes considered. No extrapolation seems to be needed based on the errors between the different meshes and hence Mesh 3 is deemed to provide satisfactory enough results.

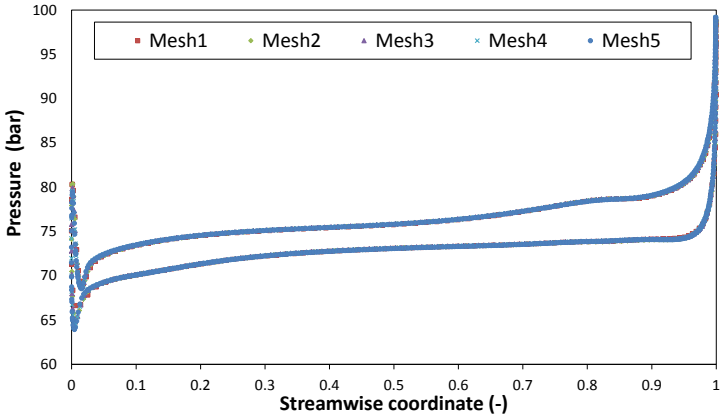

Figure 110. Pressure distribution stream-wise at blade midspan for all meshes studied.

5.2.1.2 Near wall treatment

As stated in chapter 2, near wall treatment depends on the turbulence model employed. In this regard, the adverse pressure gradient against the flow suggests that the $k-\omega$ SST model be most appropriate. Nevertheless, this turbulence model requires an important mesh refinement next to wall which becomes a large handicap given the limited computational capacity of the author and also the high Reynolds numbers of the simulation, $1.02 \cdot 10^7$ and $1.82 \cdot 10^7$ at impeller inlet and outlet respectively according to 1D estimations. The first prismatic layer thickness are calculated by estimating the friction coefficient as per the Schlichting equation (Schlichting, 1968) shown below.

$$c_f = (2\log_{10} Re - 0.65)^{-2.3} \qquad \text{[Equation 5.1]}$$

The wall shear stress is thus $\tau_w = \left(c_f/2\right)\rho V_\infty^2$, from which a friction velocity can be calculated:

$$u^* = \sqrt{\tau_w/\rho} \qquad \text{[Equation 5.2]}$$

Finally, the thickness of the first layer is a function of the desired wall y+ as deduced from the proper definition of this parameter.

$$y_0 = \frac{y_{des}^+ \mu}{\rho\, u^*} \qquad \text{[Equation 5.3]}$$

Taking the most unfavourable conditions (impeller outlet), the thickness of the first layer results $1.52 \cdot 10^{-8}$ m, which is around two orders of magnitude higher than when air is used just because of fluid properties. Therefore, mesh refinement required by S-CO_2 is much more severe than for air, which incurs a higher number of layers and/or higher growth ratio in the boundary layer.

In order to verify whether this first layer size is accurate enough to model the boundary layer, the results obtained with for a complete impeller that includes both boundary layer refinement and clearance gap it is next presented. The impeller is initially run with smooth wall boundaries, showing an acceptable wall y+ in figure 112 (a) that confirms that the first prismatic layer is inside the viscous sub-layer. However, when roughness is included in the model, wall y+ increases by three orders of magnitude due to the displacement of the wall y+ origin by $K_S^+/2$, where K_S^+ is the dimensionless roughness grain height (ANSYS, 2011).

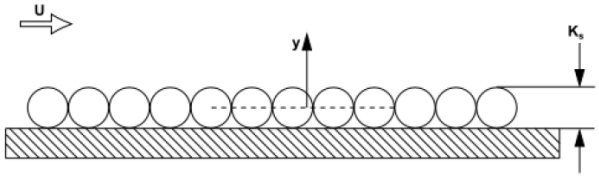

Figure 111. Representation of rough wall model in ANSYS Fluent® (ANSYS, 2011).

$$K_S^+ = \frac{\rho\, K_S\, u^*}{\mu} \qquad \text{[Equation 5.4]}$$

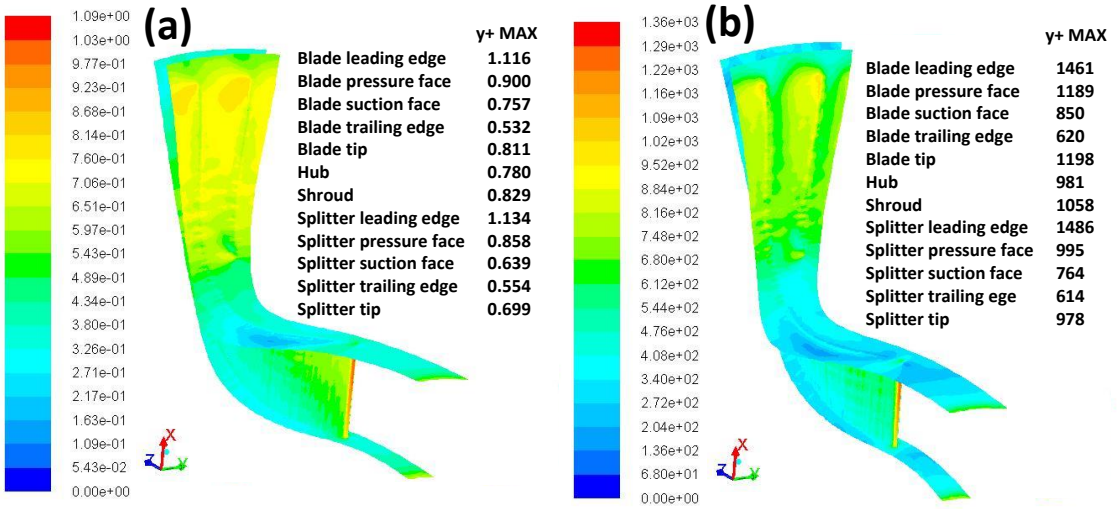

Figure 112. Wall y+ obtained in a full impeller model with smooth (a) and rough (b) wall boundary conditions. Roughness grain height 25 μm.

5.2.2 Other numerical aspects of the computational model

In addition to the main remarks given in chapter 2 for the simulation of S-CO_2 flows, this section presents the features of the numerical model that is specific for the compressor model. First of all, a Single Reference Frame (SRF) approach is used, meaning that the fluid domain is linked to a relative reference frame to which a rotational speed is imparted. Consequently, wall boundaries are set to moving rather than stationary, as required by ANSYS Fluent® when a frame motion is used. Moreover, zero velocity with respect to the relative reference frame is set for blades and hub, whilst for the shroud zero velocity is imposed with respect to the absolute frame. Finally, wall boundaries are completely defined with a mean roughness grain height of 25 μm and adiabatic condition.

Inflow and outflow boundaries are defined as mass flow inlet and pressure outlet respectively, default choices for compressible flow. Moreover, the mass flow rate at the inlet boundary is set to $\dot{m}/z_{DIF}$ in a direction normal to the inlet boundary as only one channel of the impeller is simulated. The definition of this inlet flow is completed by the static inlet temperature obtained from the 1D calculation and the following turbulence parameters: Turbulence intensity = 1.92%, Turbulence length-scale = 7 mm[19]. In contrast, only the static pressure is required at the outlet, even though other static properties like temperature and turbulence must be specified in the eventual case of backflow (reverse flow).

[19] *These turbulence parameters have been set based on ANSYS Fluent® recommendations [ANSYS UserGuide]:* $\mathrm{Tu} = 0.16\mathrm{Re}^{-1/8}$ *and* $\mathrm{l_{Tu}} = 0.07\mathrm{d_H}$.

Periodic contours close the fluid domain externally but there are other boundary conditions that need to be defined inside: the interfaces. In effect, when clearance gap is modelled, there exist surfaces that separate the pressure and suction sides of the blades and require the corresponding mesh interfaces.

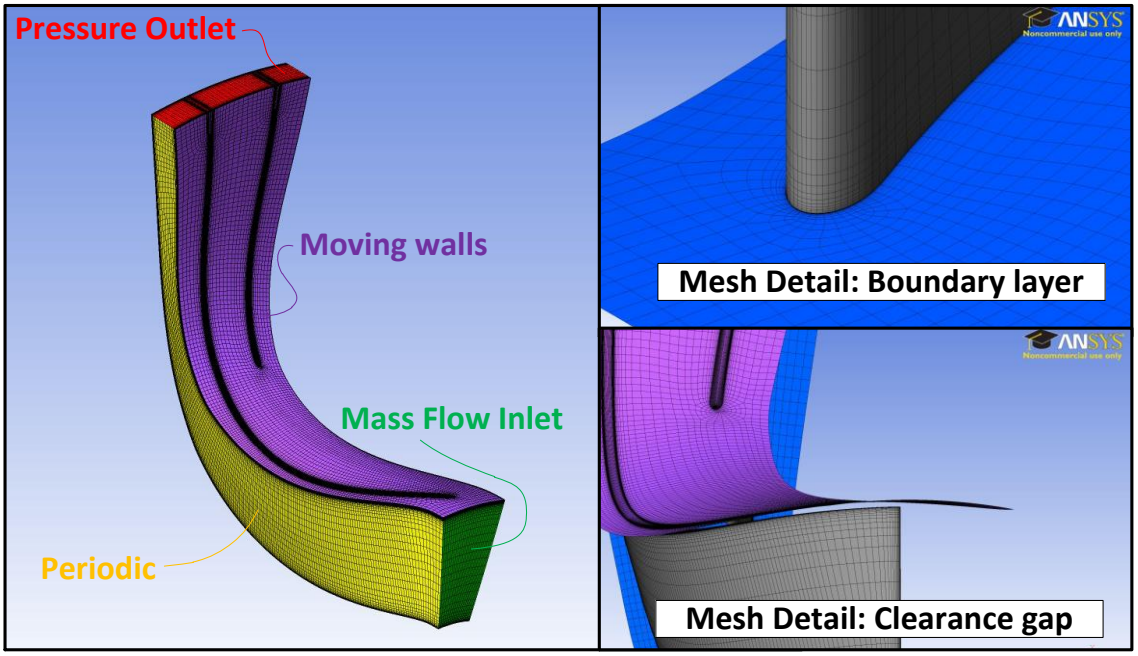

Figure 113. Impeller mesh including boundary layer refinement and clearance gap modelling.

The *Coupled* scheme is employed for the pressure-velocity coupling algorithm whereas *first order upwind* interpolation schemes have been used for each variable. Other choices regarding pressure-velocity coupling algorithms have been unsuccessfully tested, arriving at non-converged solutions. On the other hand, *fou* schemes have been used because of its computational robustness, since higher orders increase the elapsed times considerably.

As mentioned before, the final solution is obtained following a step-by-step methodology where the mean mesh size is fixed at the reference value (Mesh 3 in the *GCI* analysis) and the boundary layer is progressively refined until wall y+ lower or near 1 is achieved. Each mesh is initialised with the results from the immediately coarser mesh except for the first one, for which the *Hybrid Initialization* method implemented in ANSYS Fluent® is applied. This method requires both inlet and outlet pressure boundaries. Therefore, a total pressure inlet equal 75 bar was set up only for the hybrid initialization process, later changed to perform the simulation with the mass flow inlet boundary. Once initialized, simulations were carried out as follows:

1. Minimum pressure and temperature are limited to values above the critical point, 75 bar and 305 K respectively.
2. Simulations are started with flow equations only, i.e. continuity and momentum.
3. When the residuals show a clearly descending pattern, the Turbulence equations are activated.
4. The energy equation is activated when the difference of mass flow rates between inlet and outlet is considerably low: $\sim 10^{-3}$ kg/s.
5. At this point, there exist a large number of cells with their pressure and temperature set to the minimum values imposed in 1, but this number of cells starts to decrease at a certain point in the iterative process. When the minimum number of limited cells, both for pressure and temperature, is nearly achieved, the aforesaid limits are modified to 30 bar and 200 K, values of pressure and temperature that must not be achieved in the computational models if they are accurate enough.

5.3 CFD results

Once the uncertainties associated with the mesh are, if not removed, at least, reduced and known, the numerical model of the impeller is calibrated with a main purpose: defining general guidelines to be applied in future simulations of S-CO_2 turbomachinery. Therefore, the two main inaccuracies committed in the model employed for the *GCI* analyses should be now quantitatively evaluated. These are: (i) the boundary layer refinement and (ii) the clearance gap modelling, both of them previously omitted. Accordingly, the following analysis of four cases in parallel has been done:

- Case 1: Without gap modelling and without boundary layer refinement.
- Case 2: With gap modelling but without boundary layer refinement.
- Case 3: Without gap modelling but with boundary layer refinement
- Case 4: With gap modelling and with boundary layer refinement

Four different meshes are generated in TurboGrid® with a common mean size (that of Mesh 3 in the *CGI* analysis, section 5.2.1.1)and the boundary layer is refined by reducing the y+ offset down to 1 where necessary. Regarding turbulence models and according to the recommendation in chapter 2, two different alternatives are used: $k-\omega$ SST and $k-\varepsilon$ models depending on whether the boundary layer refinement is implemented or not. Regarding the inflow/outflow boundary conditions, these are just the same for all four cases at expected. Table 20 summarises the mass-weighted averaged values obtained in this 4-case analysis performed with ANSYS Fluent®. The values reported are measured at the inlet and outlet sections, the static pressure at the outlet being omitted for it is a boundary condition.

Case	1	2	3	4
$\bar{T}_{in}$ (K)	309.60	309.69	309.51	309.65
$\bar{P}_{in}$ (bar)	71.17	71.61	70.66	71.44
$\bar{T}_{out}$ (K)	336.53	336.00	337.08	336.06
$\bar{v}_{in}$ (m/s)	55.99	55.22	56.88	55.53
$\bar{v}_{out}$ (m/s)	161.49	163.06	161.44	163.85
$\bar{w}_{in}$ (m/s)	83.77	83.27	84.37	83.47
$\bar{w}_{out}$ (m/s)	74.29	74.90	72.07	76.30
$\bar{v}_{m,in}$ (m/s)	55.88	55.12	56.78	55.43
$\bar{v}_{m,out}$ (m/s)	68.28	69.45	66.42	70.67
$\bar{\rho}_{in}$ (kg/m^3)	221.43	224.49	217.96	223.27
$\bar{\rho}_{out}$ (kg/m^3)	276.49	278.87	273.98	278.77

Table 20. Mass-weighted averaged values for the four-case analysis.

Apart from the reported values, it is interesting to define the impeller operation by means of its main performance parameters (see chapter 4): total pressure loss coefficient ($\sum_{2\to3}\varpi_i$), total-to-total isentropic efficiency of the impeller ($\eta_{tt,imp}$) and slip (σ) and distortion (λ) factors. The simple model presented below is been created for this analysis:

- The static thermodynamic properties are calculated with the averaged temperatures and pressures directly: enthalpy $h=h(\bar{T},\bar{P})$ and entropy $s=s(\bar{T},\bar{P})$.
- The absolute and relative stagnation enthalpies are then calculated with the absolute and relative velocities: $h_0=h+v^2/2$ and $h_0'=h+w^2/2$; the corresponding entropies remain the same: $s=s_0=s_0'$.

- Stagnation temperatures and pressures are calculated with the corresponding enthalpy-entropy pairs. These values are presented in table 21, where the inlet total temperature ($\bar{T}_{0,in}$) is the same in all cases (it is a boundary condition).

Based on these variables/properties, the aforelisted performance parameters can be calculated from their definitions directly:

- The total-to-total isentropic efficiency of the impeller is calculated as:

$$\eta_{tt,imp} = \frac{h_{0,out,s} - h_{0,in}}{h_{0,out} - h_{0,in}} \qquad \text{[Equation 5.5]}$$

Where the isentropic outlet enthalpy ($h_{0,out,s}$) is obtained for the actual total pressure at the outlet and the inlet entropy: $h_{0,out,s} = h\left(\bar{P}_{0,out}, s_{0,in}\right)$.

- Calculating the distortion factor requires the aerodynamic blockage factor ($\lambda = 1/(1-B)$), which is computed with the following equation directly:

$$\dot{m} = \rho\, v_m\, A\, (1 - B) \qquad \text{[Equation 5.6]}$$

- The slip factor results from the resolution of both the actual (measured) and ideal velocity diagrams at the impeller exit, both sharing the same meridional velocity and differing in the absolute and relative flow angles (note that absolute flow angle and blade angle are the same in the ideal diagram) (Figure 114).

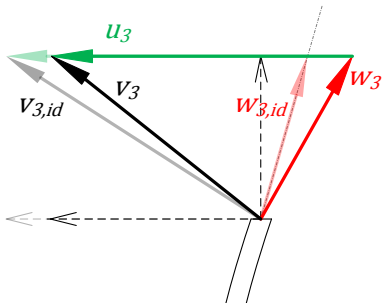

Figure 114. Ideal (transparent) vs. actual/measured velocity diagrams at impeller exit.

- Finally the total pressure loss coefficient is calculated:

$$\bar{P}'_{0,out} = \bar{P}'_{0,out,id} - \frac{\bar{P}'_{0,out}}{\bar{P}'_{0,in}}\left(\bar{P}'_{0,in} - \bar{P}_{in}\right)\sum_{2\to3}\varpi_i \qquad \text{[Equation 5.7]}$$

where the ideal discharge has the same entropy as the inlet and the same total enthalpy as the outlet.

The following conclusions are drawn from the results obtained from the model and presented in Table 21:

- No large differences are observed between cases, neither in terms of averaged variables nor performance parameters, and this situation remains when statistical information is taken into account (mean μ, variance σ^2 and standard deviation σ have been calculated for each variable in the group of four cases object of the study and included in Table 21). It

can be observed that typical variations are 1% of mean values for all the variables except for the pressure loss coefficient and the distortion factor. The former has a descendent trend when the complexity of the model increases whilst the latter does not follow any apparent trend.

- When it comes to considering whether to include the gap (case 2) or the boundary layer refinement (case 3), the first option is slightly preferred as its results are a bit more similar to the complete model in terms of performance parameter with a hardly noticeable exception for the pressure loss coefficient.
- Including the gap seems to have an important effect on flow distortion. In particular, eliminating the gap from the complete model (case 3 respect to case 4) brings about a deviation higher than 7.5% in λ, while this deviation downs to 1.6 % if the gap is modelled and the boundary layer refinement eliminated (case 2 respect to case 4). This fact suggests that case 3 exhibits a more pronounced difference with respect to case 4 than the one exhibited by case 2 in regard to the velocity profile at impeller exit.

Case	1	2	3	4	μ	σ^2	σ/μ (%)
$\bar{T}_{0,in}$ (K)	313.15	313.15	313.15	313.15	313.15	0.0000	0
$\bar{P}_{0,in}$ (bar)	74.70	75.09	74.25	74.94	74.745	0.1010	0.425
$\bar{T}_{0,out}$ (K)	362.49	362.51	362.94	362.81	362.6875	0.0373	0.053
$\bar{P}_{0,out}$ (bar)	141.36	142.64	140.95	143.04	141.9975	0.7508	0.610
$\sum_{2\to3} \varpi_i$	0.7282	0.7078	0.6932	0.5976	0.6817	0.0025	7.352
η_{t-t}	89.12	89.84	89.57	90.99	89.88	0.4768	0.768
σ	0.8414	0.8491	0.8486	0.8459	0.84625	$9.32\cdot10^{-6}$	0.361
λ	1.220	1.252	1.176	1.273	1.23025	0.0013	2.972

Table 21. Stagnation points and performance parameters for the four-case analysis.

In order to thoroughly analyse this differences, a comparison in terms of velocity profiles at the impeller outlet is made. The outcome of this comparison is summarised in figure 115, yielding the following surprising observations:

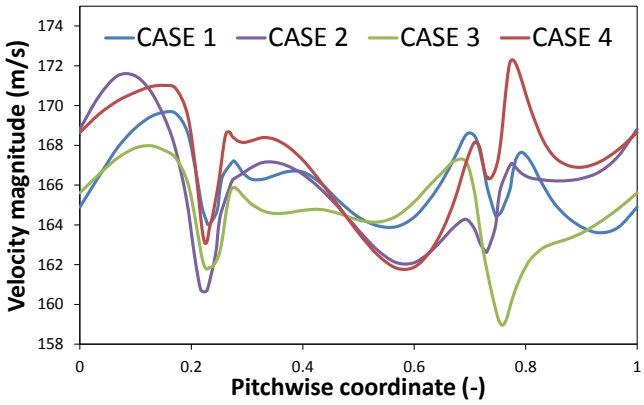

Figure 115. Absolute velocity profiles at impeller outlet for the four cases under analysis.

- The most pronounced difference, both quantitatively and qualitatively, is found between cases 3 and 4. Looking at case 3 in detail, a velocity drop is observed in the wake downstream of the pressure side of the splitter which is not found in the other cases. This

difference comes about because of the following numerical issue experienced by the cells that are adjacent to the blade tip and shroud in case 3 (where there is no interstitial gap in the mesh)::

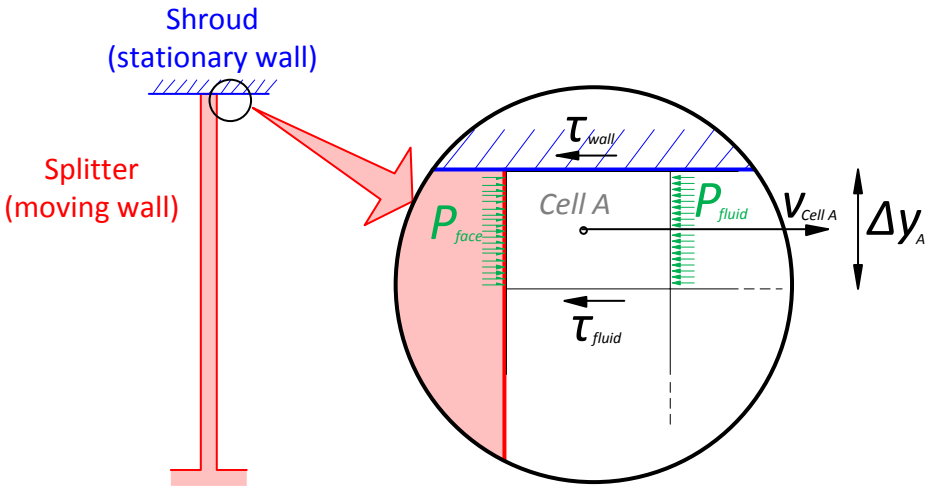

Figure 116. Detail of a cell sharing faces both with shroud and splitter surfaces.

Figure 116 summarises the boundary conditions of the aforecited cell, namely cell A. On one hand, the velocity of cells A is influenced by the velocity imparted by the splitter wall, i.e. $v_{cell\ A} \sim r \cdot \omega$, whereas in the upper face of the cell the velocity is fixed to zero given the stationary wall boundary. Therefore, the velocity gradient in the tangential direction (which affects the wall shear stress) yields:

$$\tau_{wall} \cong \mu \frac{v_{cell\ A}}{\Delta y_A / 2} \qquad \text{[Equation 5.8]}$$

On the other hand, the pressure and shear stress produced by the fluid (P_{fluid} and τ_{fluid}) surrounding the wall-free sides of cell A are related by the following simplified equation as long as the tangential velocity of the fluid is assumed constant (stationary motion in the tangential coordinate):

$$\tau_{wall} + \tau_{fluid} + P_{fluid} \Delta y_A = P_{face} \Delta y_A \qquad \text{[Equation 5.9]}$$

The main effect of a boundary layer refinement is that Δy_A is largely reduced what in turns brings about a n inverse increase in P_{face} to compensate for this effect. This is the reason why a pronounced pressure peak is observed in Figure 117.

It must be noted that this numerical issue does not take place in case 1 where the gap is not present either. The reason is that Δy_A is much larger due to the absence of mesh refinement. And neither does it occur in case 4 since type A cells are not found in the mesh due to the interstitial gap being modelled. In summary, it is the combination of boundary layer refinement and absence of interstitial gap which brings about the occurrence of the discussed numerical instability.

- In consequence, where the boundary layer is refined, the impact of implementing the gap is more visible since the phenomena around the blades are solved for rather than being implemented in the turbulence model as an overall effect. The conclusion is thus that whenever the boundary layer is refined, the gap must be also implemented. On the contrary, if the boundary layer is not refined, it is less important whether or not the

interstitial gap is also included. This is of course as far as local velocities are concerned. In terms of the global parameters, implementing the gap but not refining the boundary layer seems to be the most leveraged solution.

- This explanation is further confirmed by the static pressure distribution on the blade walls (Figure 117), which show that the high pressures typically found on the blade tips are more pronounced in case 3 (see coloured scales on the left). This pressure peak in case 3 is behind the velocity drop of the wake in figure 115.

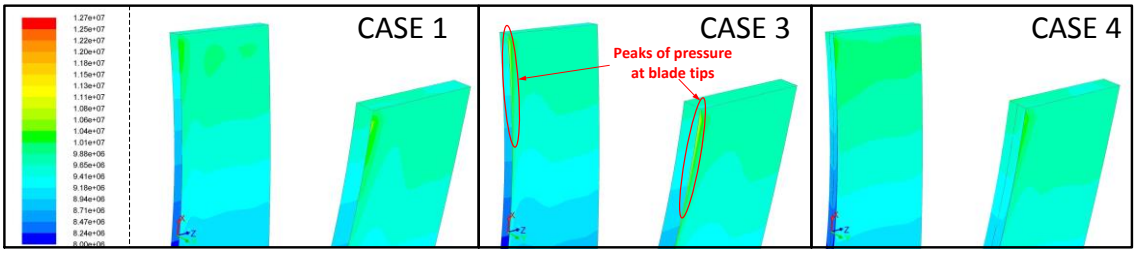

Figure 117. Pressure contours for cases 1, 3 and 4, where pressure peaks on the blade tips can be observed in case 3.

- The most difficult question to answer is whether or not the added computational burden of case 4 is worth the gain in accuracy. This is disputable and the best way to provide an answer is to ask ourselves the type of results on which we are interested. Thus, in terms of global parameters (averaged values), one would say that case 2 is most balanced. On the contrary, should the local flow phenomena at impeller outlet be of interest, then it would be necessary to select the most complex model including interstitial gap and boundary layer refinement.
- In terms of turbulence model, it seems that the *Realizable* $k-\varepsilon$ model suffices to provide satisfactory results when no boundary layer refinement is implemented whereas the more complex $k-\omega$ *SST* model must be used when the boundary layer is refined around the blades and in the wakes.

Graphical comparisons between the four cases are additionally provided in the next figures, comprising contours of entropy, pressure and velocity, streamlines and velocity vectors.

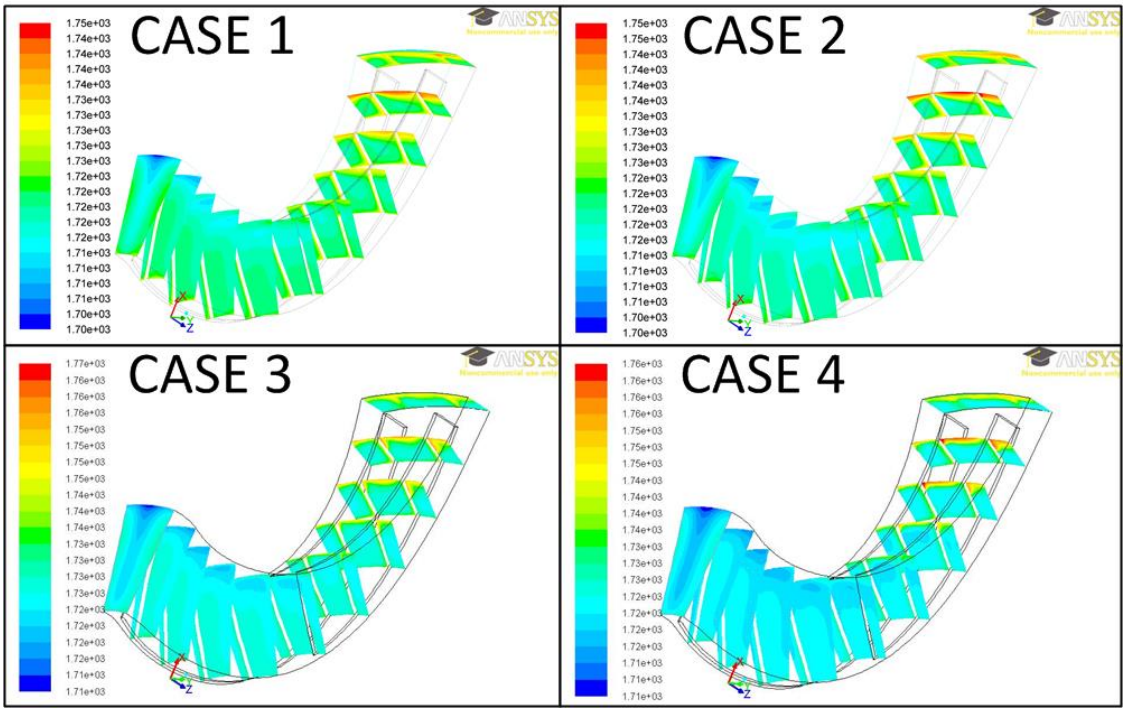

Figure 118. Contours of entropy at different meridional positions along the impeller channel.

The previous figure presents those zones where flow irreversibilities are created, generally near the walls and in the gap, and more in particular in the shroud near the impeller exit. The next figure shows pressure contours that are very similar qualitatively, with the exception of case 3 because of the aforediscussed effect, which is again visible in Figure 117.

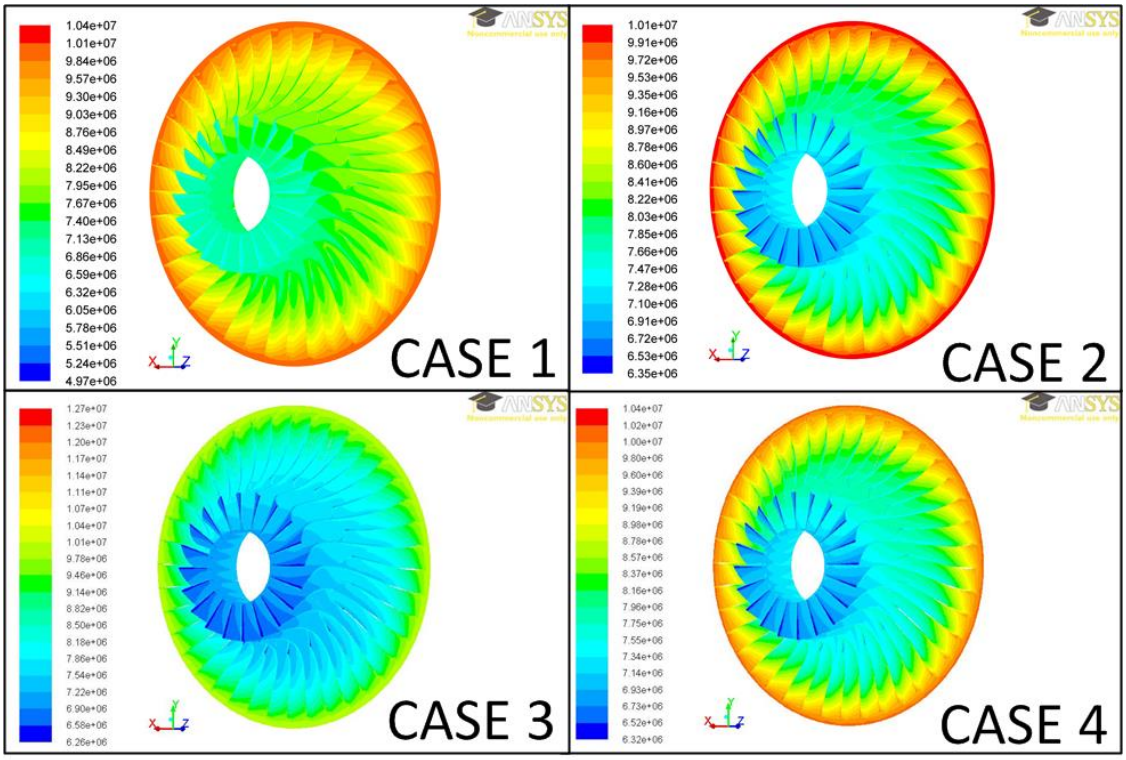

Figure 119. Static pressure contours in hub, blades and splitters.

The next figures do not reveal any appreciable difference between the four cases, as reported in the previous quantitative analysis.

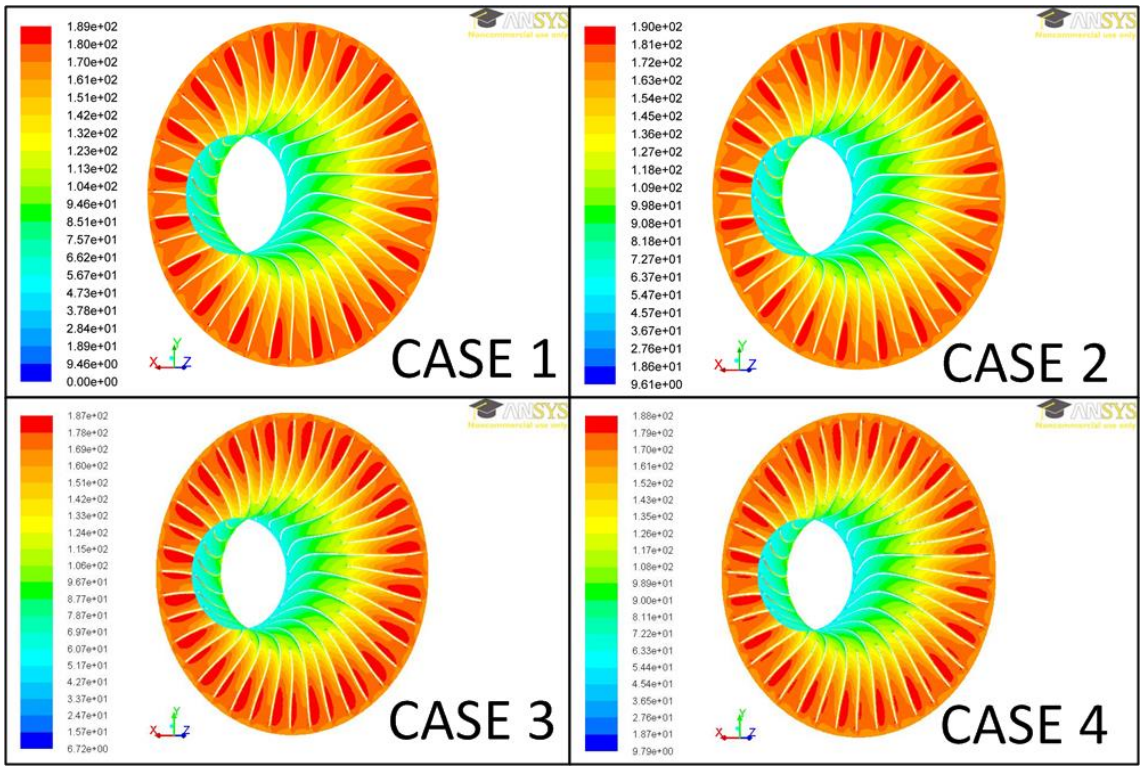

Figure 120. Absolute velocity contours on a surface located at midspan.

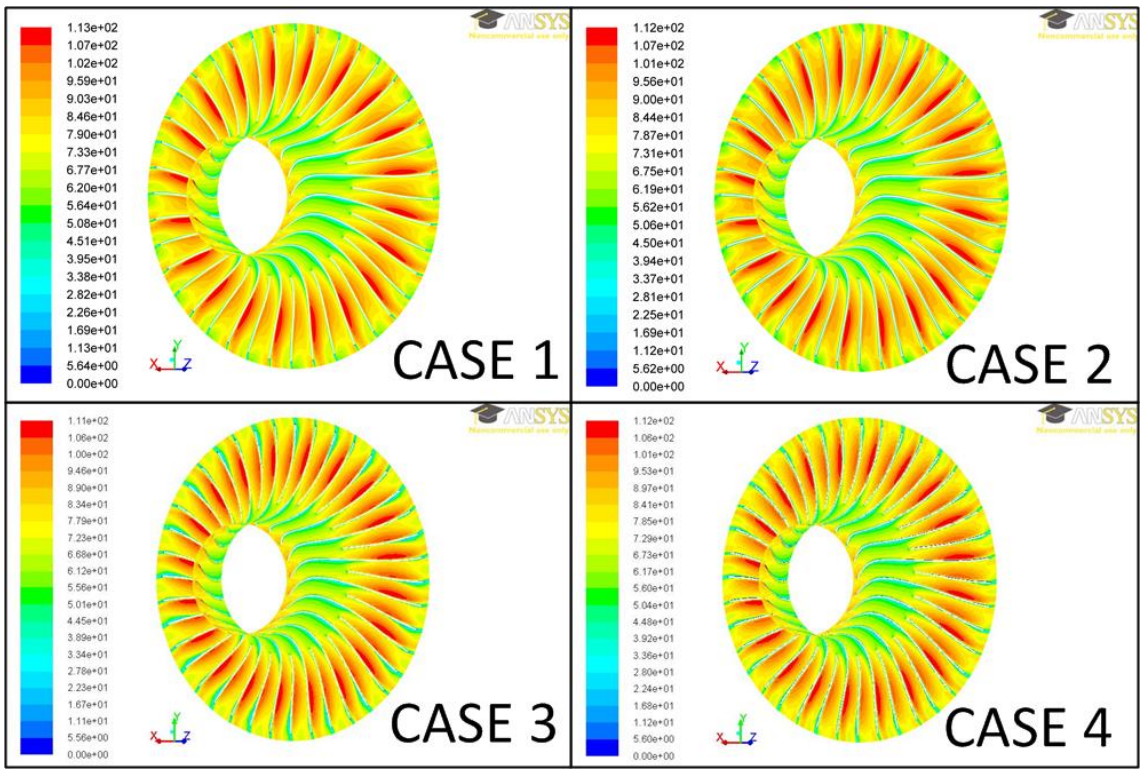

Figure 121. Relative velocity contours on a surface located at midspan.

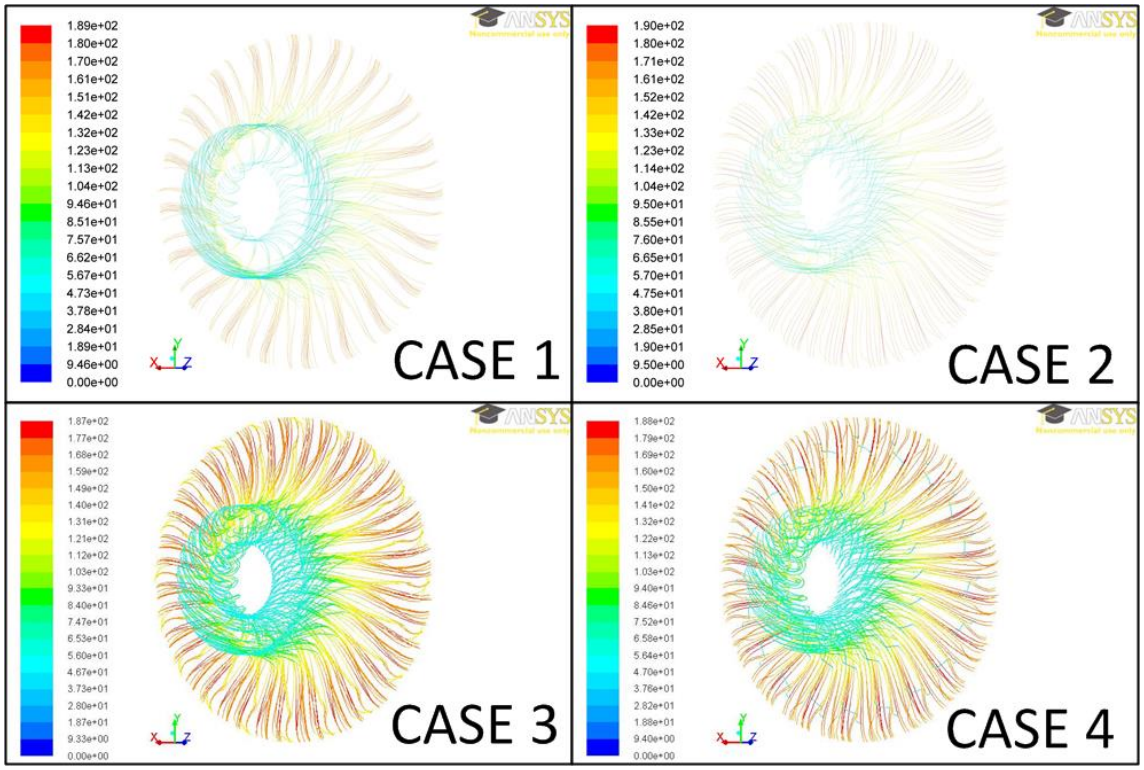

Figure 122. Streamlines starting from the inlet boundary coloured by absolute velocity.

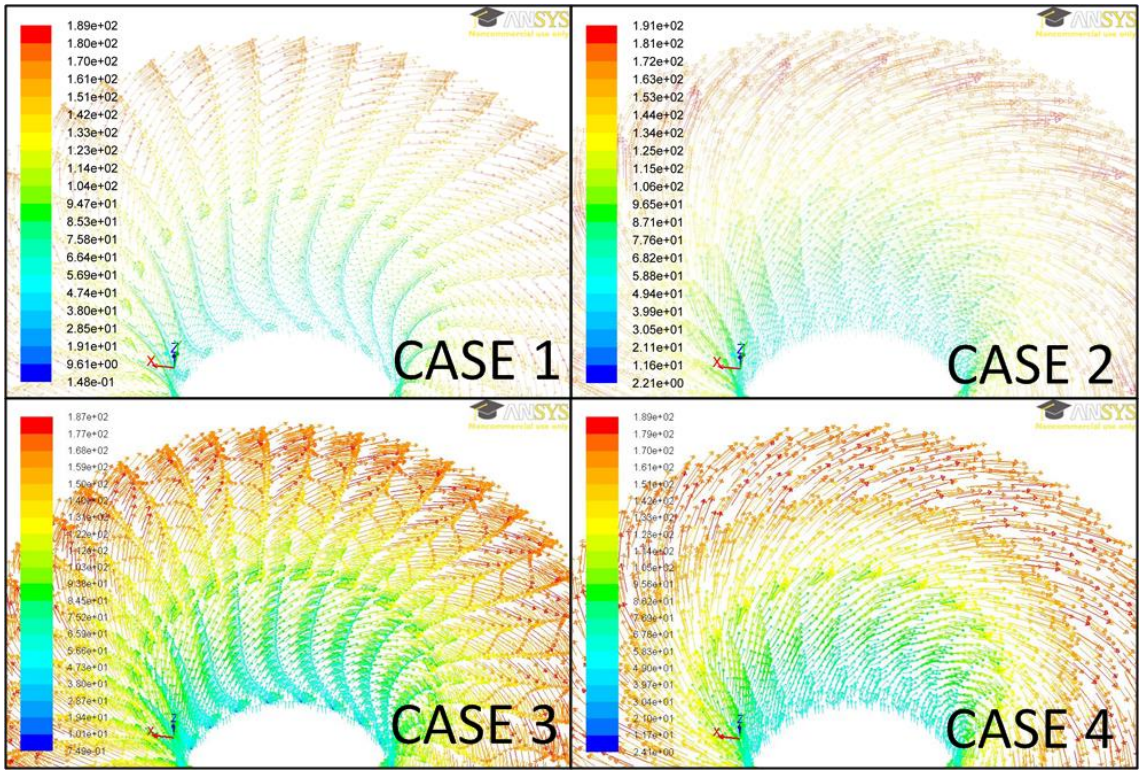

Figure 123. Vectors of absolute velocity on a surface located at midspan.

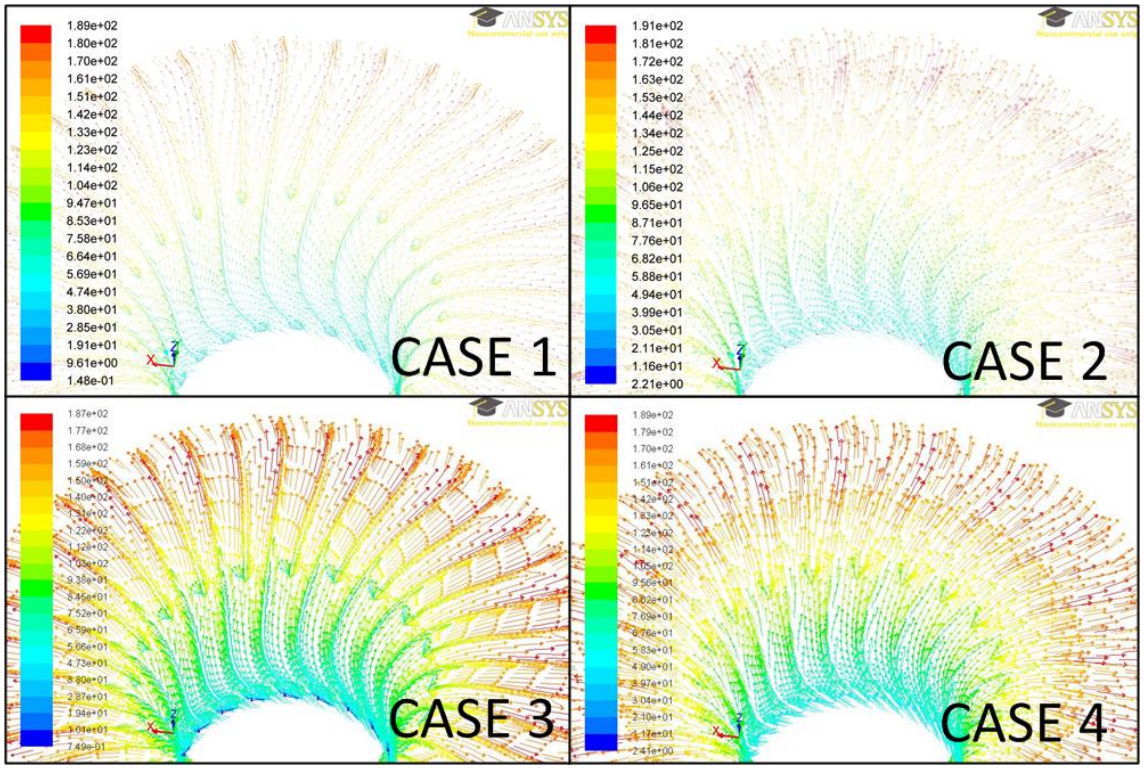

Figure 124. Vectors of relative velocity on a surface located at midspan.

5.4 Comparison between 3D-CFD and 1D results

The results from the CFD and 1D model are compared in this chapter as a definitive proof of: (i) concordance between both tools and (ii) satisfactory similarity of the simplest model (case 1) to the 1D results. Let us consider the following input data and performance parameters for a brief discussion on this issue:

- $\bar{P}_{0,in}$ = 75 bar
- $\bar{T}_{0,out}$ = 361.40 K
- $\bar{P}_{0,out}$ = 141.16 bar
- $\sum_{2\to3} \varpi_i$= 0.3982
- η_{t-t} = 93.37 %
- σ = 0.9075
- λ = 1.110

The one-dimensional results presented above show satisfactory agreement with the CFD results in table 21. Nonetheless some remarks can be extracted from the comparison:

- The most important difference is found at evaluating total pressure losses, the most complete CFD model (case 4) being more similar to the 1D evaluation; i.e. including clearance gap as well as mesh refinement next to the walls (see Figure 125).
- The slip factor is hardly affected by the choice of numerical model, as its deviation from the 1D results remains virtually keeps constant between -6.44 and -7.28 %. The peaks of pressure produced at blade tip in case 3 affect this parameter noticeably.
- Therefore, from the two previous bullet points, it is concluded that the overall losses are lower for 1D evaluations whereas the slip factor is, on the contrary, higher.

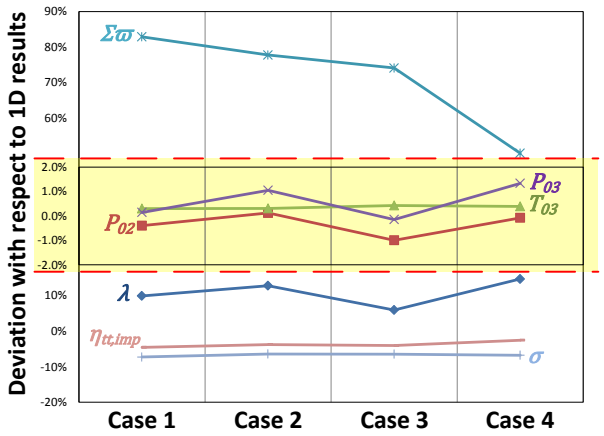

Figure 125. Deviation of the four CFD cases with respect to the 1D simulation.

Based on the conclusions extracted from this analysis, and given the similar results provided by the CFD cases 1 and 2, it is possible to create a numerical model of the entire stage (impeller and diffuser) that is affordable to solve if no clearance gap nor boundary layer refinement is implemented in the mesh. Thus, in a more advanced step, the diffuser obtained in chapter 4 is modelled and coupled to the impeller, giving place to the computation mesh shown in figure 126.

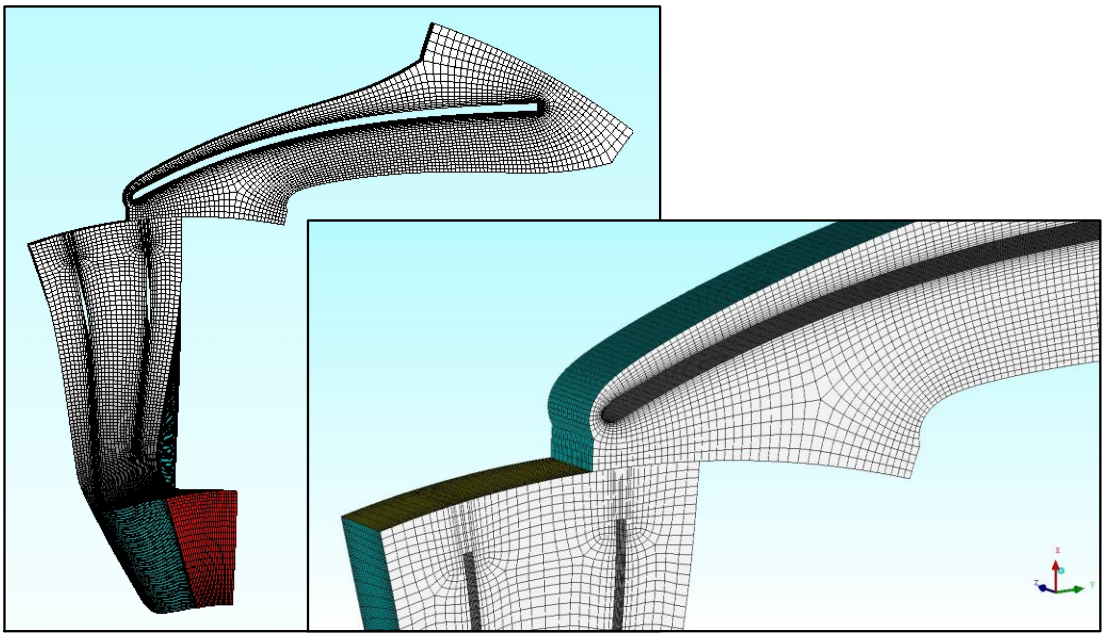

Figure 126. Mesh of the full compressor stage (impeller and diffuser). Note that there is no substantial mesh refinement around the blades.

The main difference with respect to the impeller model is that the pressure outlet boundary condition is now imposed at diffuser exit and the surface formerly acting as pressure outlet in the impeller model is now set as an interface. This interface is defined as *Periodic Repeat* and links the impeller outlet with the diffuser inlet surfaces. As the boundary layer is not refined, the Realizable $k-\varepsilon$ turbulence model is employed.

The 1D and 3D models of the full compressor are used to evaluate a number of operating conditions (off-design operation) which are then used to produce the performance map of the unit. This is shown in figure 127, where a remarkable agreement is observed except for a few cases near surge and choke operation. This is a final confirmation that the 1D and 3D models can be combined to search

optimum designs for a given set of operating conditions, as long as local flow phenomena inside the impeller are of interest.

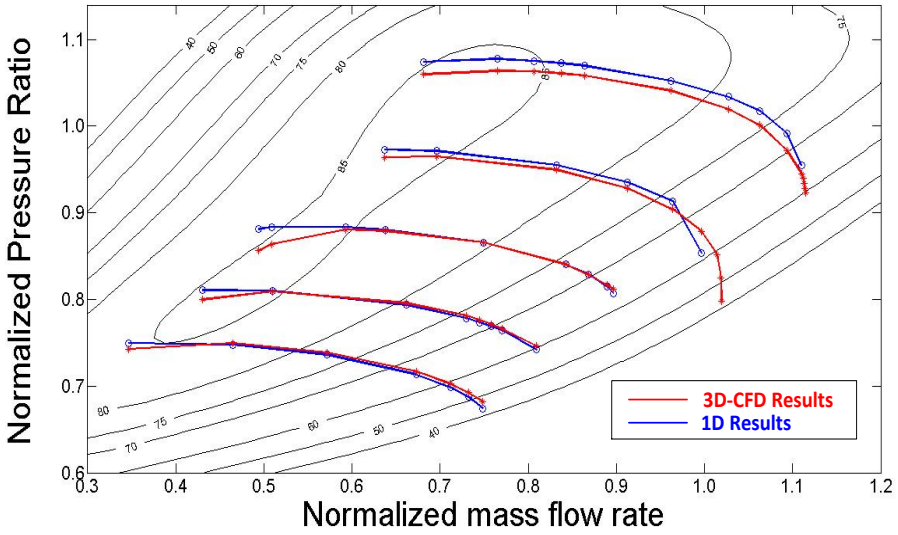

Figure 127. Comparison between 1D and 3D models in terms of the performance map of the compressor.

The performance map plots 1D and 3D results for constant speed lines (100, 90, 80, 70 and 60 % of the design speed) while the constant efficiency contours are taken from the 1D model results. The following conclusions are drawn from the analysis:

- First of all, the efficiency of the stage is within the expected range according to the selection of specific speed and diameter in section 4.4.2.
- Better agreement is found at low speed.
- For every speed, the largest differences are found near the surge line. Nevertheless, even for these operating conditions there is still good agreement.
- For 100 and 90 %, the 3D model is able to reach convergence stably. On the contrary, stability issues are encountered for the 60, 70 and 80 % rotating speeds. These convergence problems are due to the refprop function of the NIST real gas model and are linked to potential condensation of the working fluid.

5.5 Summary and conclusions

In order to gain precision in the design process as well as to be able to perform local studies, the first compression stage of the compressor designed with the one-dimensional model in the previous chapter has been herein analysed with a three-dimensional CFD model. This CFD has been implemented in ANSYS® environment using BladeGen® for the geometry generation, TurboGrid® for meshing and Fluent® for the simulations. Aiming to evaluate and reduce the main sources of uncertainties, meshes of different types and mean sizes have benn analysed, confirming the convenience of using structured meshes inasmuch as (i) their results are less affected by numerical diffusion, (ii) the required number of elements is lower than in unstructured meshes and also (iii) because of the easier manipulation of this type of meshes with TurboGrid®.

Once determined an acceptable mesh size by means of a Grid Convergence Index analysis with 5 meshes, a comparative analysis of four different cases has been done in order to investigate the impact that more accurate models would have in the results. Impeller models with and without clearance gap and boundary layer refinement have been produced to this aim. As the main conclusion from this comparison, it has been observed that there are no dramatic differences between including all of these

effects or not in terms of the mean averaged values of the thermodynamic variables of interest (which are representative of the performance of the stage).

On the contrary, the analysis of local velocities at the impeller outlet has shown that the features of the CFD model might lead to substantial differences when it comes to local flow phenomena. This has been confirmed by the outlet velocity distribution when a mesh with no clearance gap nor boundary layer refinement has been compared to other meshes either more complex or simpler. In this regard, the impeller performance parameters have proved to be more affected by the modelling, especially the overall loss coefficient for which differences larger than 20 % have been observed between the simplest and the most complex models.

The good agreement between 1D and 3D tools has also been determined by comparing both the overall performance parameters and thermodynamic variables in on-design and off-design operation. Moreover, in spite of the high differences in terms of performance parameters in on-design operation, the more complete comparison of performance maps produced with 1D and 3D models has confirmed that these tools have an extraordinary potential to be combined to yield a very flexible optimisation tool.

CHAPTER 6. Conclusions and future developments

A solid background in the field of the supercritical carbon dioxide power cycle has been built since the middle of last century, covering mostly thermodynamic and other theoretical studies. More recently, in the first decade of this century and thanks to the works of important research centres such as the Massachusetts Institute of Technology and SANDIA National Laboratories in the US or the Tokyo Institute of Technology in Asia, new impulse has been given to the technology, aimed to achieve market deployment in the next five years or so. This nevertheless requires a more practical knowledge in order to develop efficient and reliable cycle components.

Even though originally conceived as a technology of interest for large scale nuclear power stations (in particular GEN IV HTGRs), the most interesting market niche currently is the Concentrating Solar Power industry, in particular those power plants making use of a central receiver (i.e. solar towers). The market is clear and significant advantages over the conventional direct steam generation or even molten salt technologies have been claimed despite the relatively low technology readiness level of S-CO_2 technology; actually, based on API's scale ranging from 0 to 7, the current TRL of S-CO_2 is somewhere around 3, far from the minimum of 6 required for initial commercialisation. Aspects such as turbomachinery aerodynamic design, mechanical design of turbomachinery auxiliaries (seals, bearings, etc.), volumetric receivers operating at high pressure, compact heat exchangers, etc. constitute the main technological hurdles to date.

This work is focused on turbomachinery aerodynamic aspects, trying to contribute in two main directions:

- Fundamentals of supercritical diffusion processes; aimed at fully understanding the impact of the supercritical features on the performance of diffusing flows. Conical diffusers are the reference geometry for this analysis.
- Design of radial compressors; aimed at providing some conclusions and recommendations to be applied to the design of supercritical CO_2 turbomachinery. The analyses were performed numerically, firstly in one dimension and then three dimensionally.

This chapter summarises the main conclusions drawn from this work.

6.1 Conclusions from the comparative analysis of air and S-CO_2 in conical diffusers

With the purpose of investigating how differently supercritical carbon dioxide behaves with respect to air, a numerical analysis was conducted where conical diffusers operating on both fluids were studied. For air, there exist extensive databases generated experimentally during the 1950's and 1980's which have constituted an important tool in the development of efficient turbomachinery. Moreover, these empirical results have more recently been replaced by powerful numerical techniques whose results have proven satisfactory and accurate when properly applied.

Based on this experience with air, the experimental information has been found crucial to compare the performance of gaseous flows when the working fluid and operating conditions are substituted. At the same time, simple geometries have been selected based on reducing the influence of the shape of the domain on the flow phenomena observed; in this regard, conical diffusers represent the most elementary devices to rise the static pressure of a given fluid and they seem a natural stage prior to approaching the analysis of the whole compressor.

More practically, after the dimensional analysis and literature review, the parameters of influence in conical diffuser performance were identified to later develop the numerical tool for the analysis. Three categories of parameters were distinguished: (i) geometrical parameters, (ii) first order aerodynamic parameters and (iii) second order aerodynamic parameters. The main conclusions in this regard are summarised in the next subsection, though they are explained in more detail in chapter 3.

6.1.1 Effect of geometry

The effects of non-dimensional geometrical parameters were represented in the plane L/D_th-AR, in such a way that constant-divergence-angle curves became straight lines (double logarithmic scale). On these maps, contours of constant C_p were plotted, for which 30 different geometries were employed, keeping all the remaining aerodynamic conditions constant on each map. Firstly, eight maps presented the comparison between both fluids and then a total of thirty maps were generated for the supercritical fluid only, yielding the following conclusions:

- Operating with S-CO_2 is more efficient in a wider region, which is larger for lower blockage.
- The performance of a conical diffuser running on air improves can be increased if the area ratio is increased. On the contrary, the performance of a S-CO_2 diffuser will improve when increasing he non-dimensional length.

6.1.2 Effect of first order parameters

The aerodynamic blockage factor and Mach and Reynolds numbers conform the list of "first order" aerodynamic parameters because of their transversal usage in the field. The importance of aerodynamic blockage was actually proven in the 60's experimentally by Dolan and Runstadler who also confirmed that neither Mach nor Reynolds have significant influence for the usual ranges employed with air. Nonetheless, given that the working fluid is substituted for the application of interest, it was questioned whether these trends would be similar for supercritical carbon dioxide. The following conclusions regarding the impact of aerodynamic blockage were drawn:

- The simulations confirmed that the maximum C_p decreases with blockage, as expected from the results for other fluids.
- Secondly, higher C_p can be achieved with supercritical carbon dioxide, especially at low blockage factors. Air was only simulated with blockages up to 12 %, while for CO_2 this range was increased to 15 %
- The differences between both fluid vanish when blockage is augmented, in such a way that over 12 %, the C_p vs. geometry (whether AR or L/D_{th}) curves exhibit virtually identical behaviours for both fluids.
- Another expected behaviour in S-CO_2 diffusers was verified as a further increase in blockage make the geometrical parameters more determinant, i.e. the area ratio becomes more detrimental whereas the non-dimensional length becomes more beneficial.

Finally, the influence of Mach and Reynolds were found to be similar to that observed for air, i.e. hardly any influence. The only difference worth noting is the different value of the S-CO_2 critical Reynolds number beyond which this non-dimensional parameter becomes influence-less. Also, a weak dependence of this critical value upon Mach number must be mentioned.

6.1.3 Effect of second order parameters

In addition to the previous parameters, another group was formed by different aspects of the inlet velocity profile and the turbulence features of the inflow. Thus, the effects of distortion (both the axial and angular components), turbulence intensity and turbulent length scale were analysed, avoiding those effects linked to the anisotropy of the turbulent flow given the inherent limitations of the computational tool.

Regarding distortion, five different throat velocity profiles were examined in Fluent: tip jet flow, linearly distorted flow, asymmetric parabola, uniform flow and axisymmetric parabola.

- Regardless of the working fluid, the diffuser produces an amplifying effect on distortion, since λ (parameter quantifying how distorted the flow is) increases as the fluid flows through the diffuser.
- This amplifying effect is stronger for air, accentuated with the asymmetry of the velocity profile.
- Supercritical carbon dioxide exhibits a slightly higher pressure rise coefficient, the differences between fluids being emphasised for those inlet profiles for which the radial velocity gradients are higher.

As opposed to distortion, there is hardly any difference between fluids when it comes to the effect of swirl velocity, since the maximum pressure recovery for air and S-CO_2 were very similar and found for virtually the same swirl velocity angles.

Finally, the study of turbulence revealed the existence of a critical value of non-dimensional turbulence length scale around 100, meaning that the characteristic length scale of the turbulence phenomenon is on the order of magnitude of the throat diameter.

6.2 Conclusions from S-CO_2 turbomachinery design

The very intensive research and industrial activity in the field of turbomachinery has produced a large number of design guidelines and best-practice recommendations that are available in a wide variety of handbooks and computer codes. Nonetheless, some additional recommendations have to be considered when working with supercritical carbon dioxide due to some particular features of the fluid. In order account for these singularities, an integral design methodology has been developed from the conceptual design to the (not optimised) geometrical definition of each compressor stage. This initial design is obtained in three steps:

- The cycle is defined, establishing the layout of the cycle along with the total pressures and temperatures at the most important stations. In this first stage, the concept of AMC (Acceleration Margin to Condensation) is introduced. This is the Mach number at which the static conditions lie in the saturation line for a given stagnation point. The choice of the compressor inlet stagnation point requires a compromise between a high enough AMC and an acceptable thermal efficiency of the cycle, parameters that affected by total temperature at the compressor inlet in opposite directions.
- The compression system is then designed based on traditional maps of specific speed and diameter. Taking the AMC as the maximum limit for the absolute Mach number at impeller throat (where the fluid accelerates the most) along with the desired specific speed and diameter (in agreement with a high isentropic efficiency of the turbomachinery) closes the compression system design, from which the main design parameters and desired performance for each compression stage are obtained.
- Finally, the 1D tool developed is solved for the inverse problem in order to obtain a full geometrical definition of each stage. Nonetheless, this characterisation is based on mean streamline codes. Consequently, the radii, blade angles and thicknesses are only given at the main stations of the machine (inlets, outlets and throats), and no distributions or detail profiles are provided.

From a compressor design standpoint, two main features were found interesting to highlight for their novelty with respect to air compressors: (i) the importance of not exceeding the AMC restriction in order to not have two-phase flow in the compressor (and therefore avoiding instability problems and mechanical damage to the machine), and (ii) the need to use multiple stages because of the limitation on shaft speed coming from the AMC.

The geometry of the first compression stage was simulated in 3D by using the Turbosystem ANSYS® package, which comprises BladeGen® for turbomachinery geometry generation, TurboGrid® for meshing and Fluent® to run the simulation. From the adjustments done in the numerical model (Equation of state, turbulence model, degree of complexity, mesh,…), no dramatic differences were found between adopting the highest level of complexity in the compressor model, i.e. modelling the clearance gap and refining the boundary layer, and opting for the most simple model. Extraordinary agreement was also found between the 1D and 3D models, shown through the representation of compressor performance maps (mass flow vs. pressure ratio & efficiency) produced with both models.

6.3 Original contributions

Once the conclusions have been presented and before presenting the plans for future work, it is time to highlight the original contributions of this thesis. The original contributions can be seen from two different perspectives. On one hand there are those related with the applications of existent tools to fields/systems where they have not been applied previously. On the other, there are those studies, tools and methodologies that have come out from the specific development of this thesis.

- In relation with the original application of existent tools, the utilisation of a Matlab®-Fluent® coupling as presented in chapter 3 was employed to run a set of conical diffuser simulations, both for air and supercritical carbon dioxide. This somewhat novel application of a Matlab® routine allows for a fast and accurate automation of multiple and even parallel runs.
- On the other side, the novel contributions of this work are listed below:
  - ✓ Systematic analysis of the pressure recovery capacity of S-CO_2 conical diffusers incorporating not only the standard geometrical and aerodynamic parameters of influence but also other parameters that are specific to this application (i.e. compressibility factor).
  - ✓ The development of a numerical tool for the previous analysis, which allows for future extensions of the ranges herein considered.
  - ✓ Development of a design strategy for S-CO_2 compressors, from the concept of the power cycle to the production of a draft geometry/prototype. In this regard, an optimization method should be added to this development in order to complete a fully optimized design tool, as indicated in the next section devoted to future developments.

6.4 Future developments

The Thermal Power Group (GMTS) at the University of Seville has been working on the supercritical power cycle for the last five years, focusing mostly on the thermodynamic performance of the cycle and on the constraints that these features set on turbomachinery. The present work is actually the first approach of this research group to addressing the challenges faced when designing efficient S-CO2 compressors and is therefore motivated by the recurring problems experienced by the scientific community. It is not actually aimed at solving the problem that others have not been able to overcome, it is just aimed at understanding the fundamentals of supercritical carbon dioxide flows in turbomachinery and providing tools for a future optimisation of the few existing prototypes. This research has thus been developed in the context of a larger approach to S-CO2 turbomachinery development, comprising:

- Examination of the design space of S-CO_2 compressor.
- Throughflow codes for the optimisation of S-CO_2 compressor designs.
- Software development gathering 1D, 2D-Throughflow and 3D-CFD calculations aimed at the integral aerodynamic design of S-CO_2 compression systems.

It is acknowledged though that these research projects are based on numerical models only, while the main drawback associated to this technology is the scarcity of experimental data. Therefore, these proposed works may be valueless if not compared against experimental data. In consequence, it is deemed crucial to construct an experimental S-CO_2 compressor test rig to give a solid support to the numerical developments planned for the near future. This is not to say that numerical analyses are not interesting; on the contrary, this is to highlight the need to develop theoretical and numerical analyses in parallel so that they can benefit from one another and bridge the gap to commercialisation as soon as possible.

CHAPTER 7. References

Hoffman, J. A., 1981. Effects of free-stream turbulence on diffuser performance. *Journal of Fluid Engineering,* Volume 103, pp. 385-395.

Ainley, D. & R Mathieson, G., 1955. *An Examination of the Flow and Pressure Losses in Blade Rows of Axial-Flow Turbines,* London: AERONAUTICAL RESEARCH COUNCIL REPORTS AND MEMORANDA.

Angelino, G., 1969. Real Gas effects in Carbon Dioxide Cycles. *ASME Paper No. 93-GT-103.*

Angelino, G., July 1968. Carbon Dioxide Condensation Cycles For Power Production. *Journal of Engineering for Power,* pp. 287-295.

ANSYS, I., 2011. *ANSYS FLUENT Theory Guide,* s.l.: Release 14.0.

ANSYS, I., 2011. *ANSYS FLUENT User's Guide,* s.l.: Release 14.0.

Aungier, R., 1988. A Systematic Procedure for the Aerodynamic Design of Vaned Diffusers. In: A. Hamed & U. Rohatgi, eds. *Flows in Non-Rotating Turbomachinery Components.* New York: ASME, pp. 27-34.

Aungier, R., 1995. Mean Streamline Aerodynamic Performance Analysis of Centrifugal Compressors. *ASME Journal of Turbomachinery, Vol.117,* pp. 360-366.

Aungier, R., 2000. *Centrifugal Compressors: A strategy for Aerodynamic Design and Analysis.* New York: ASME Press.

Balje, O., 1970. Loss and Flow Path Studies on Centrifugal Compressors-Part I. *Journal of Engineering for Power,* 3(92), pp. 275-286.

Balje, O., 1981. *Turbomachines.* Toronto: Joun Wiley & Sons, New York.

Benedict, R., Carlucci, N. & Swetz, S., 1966. Flow Losses in Abrupt Enlargements and Contractions. *Transaction ASME, Journal of Engineering for Power,* Volume Jan, pp. 73-81.

Bölcs, A. & Tsamourtzis, V., 1991. *Quasi-Three-Dimensional Characteristics Method for a Supersonic Compressor Rotor.* Orlando, FL, US, Proceedings of the international Gas Turbine an Aeroengine Congress and Exposition, Paper No. 91-GT-81.

Boussinesq, J., 1877. Théorie de l'Écoulement Tourbillant. *Mem. Présentés par Divers Savants Acad. Sci. Inst. Fr.,* Volume 23, pp. 46-50.

Boyer, K. M., 2001. *An improved Streamline Curvature Approach for Of-Design Analysis of Transonic Compression Systems,* s.l.: Diserttation phD, Virginia Polytechnic Institute and State University..

Casey, M., 1983. A Computational Geometry for Blades and Internal Flow Channels fo Centrifugal Compressors. *ASME Journal of Engineering for Power,* Volume 105, pp. 288-295.

Celik, I. et al., 2008. Procedure for Estimation and Reporting of Discretization Error in CFD Applications. *Journal of Fluids Engineering,* Volume 130, pp. 1-4.

Chacartegui, R. et al., 2011. Alternative cycles based on carbon dioxide for central receiver solar power plants. *Applied Thermal Engineering,* Issue 31, pp. 872-879.

Chang, H. et al., 2006. *Development Od A Supercritical Carbon Dioxide Brayton Cycle: Improving VHTR Efficiency And Testing Material Compatibility,* Idaho: Idaho National Laboratory INL/EXT-06-01271.

Chang, Y., Grandly, C., Lo Pinto, P. & Konomuro, M., 2005. *Small Modular Fast Reactor Design Description,* Chicago: ARGONNE NATIONAL LABORATY, ANL-SMFR-1.

Cleveland, C., 2004. *The Energy Library.* [Online] Available at: http://www.theenergylibrary.com/node/460 [Accessed 4 Oct. 2013].

Commission, E., 2013. *Research & Innovation, Energy.* [Online] Available at: http://ec.europa.eu/research/energy/index_en.cfm [Accessed 22 1 2014].

Conrad, O., Raif, K. & Wessels, M., 1980. *The calculation of performance maps for centrifugal compressor with vane-island diffusers..* New Orleans, Louisiana, March 9-13, Proceedings of the Twenty-fifth Annual International Gas Turbine Conference and Exhibit and Twenty-second Annual Fluids Engineering Conference.

Cumpsty, N., 1989. *Compressor Aerodynamics.* New York: John Wiley & Sons, Inc..

Daily, J. & Nece, R., Mar, 1960. Chamber Dimension Effects on Induced Flow and Frictionl Resistance of Enclosed Rotating Disks. *Transactions ASME, Journal of Baisc Engineering,* pp. 217-232.

Daily, J. & Nece, R., Sept, 1960. Roughness Effects on Frictional Resistance of Enclosed Rotating Disks. *Transaction ASME, Journal of Basic Engineering,* pp. 553-562.

Dean, R. & Senoo, Y., 1960. Rotating wakes in vaneless diffusers. *Trans. ASME Journal of Basic Engineering,* Volume 82, pp. 563-74.

Deardorff, J., 1970. A numerical study of three-dimensional turbulent channel flow at large Reynolds numbers. *Journal of Fluid MEchanics,* 41(2), pp. 453-480.

Denton, J., 1993. Los Mechanisms in Turbomachinery. *Journal of Turbomachinery,* Volume 115, pp. 621-656.

Denton, J. & Dawes, W., 1999. Computational fluid dynamics for turbomachinery design. *Proceedings of the Institution of mechanical Engineers, Journal of Mechanical Engineering Science,* 213(Part C), pp. 107-124.

Dolan, F. X. & Runstadler, P. W., 1973. *Pressure recovery performance of conical diffusers at high subsonic mach numbers,* Washington, D.C.: NASA CR-2299.

Dostal, V., Driscoll, M. & Hejzlar, P., March, 2004. *A Supercritical Carbon Dioxide Cycle for Next Generation Nuclear Reactors,* s.l.: MIT-ANP-TR-100.

Dostal, V. & Kulhanec, M., 2009. *Research on the Supercritical Carbon Dioxide Cycles in the Czech Republic.* Troy, New york (US), Proceedings of the SCO2 Power Cycle Symposium 2009.

Dubitsky, O. & Japikse, D., 2008. Vaneless Diffuser Advanced Model. *Journal of Turbomachinery,* Volume 130, pp. 011020-1/10.

Eckardt, D., 1980. Flow field analysis of radial backswept centrifugal compressor impellers, Part I: Flow measurements using a laser velocimenter. In: S. Gopalakrishnan, P. Cooper, C. Grennan & J. Switzer, eds. *Performance prediction of centrifugal pumps and compressors.* s.l.:ASME.

Egli, A., 1935. The leakage of Steam Through Labyrinth Glands. *Transaction ASME,* Volume 57, pp. 115-122.

Feher, E., 1968. The Supercritical Thermodynamic Power Cycle. *Energy Conversion, Vol. 8,* pp. 85-90.

Fenghour, A., Wakeham, W. & Vesovic, V., 1998. The Viscosity of Carbon Dioxide. *Journal of Physical and Chemical Reference Data,* 27(1), pp. 31-44.

Ferziger, J. & Peric, M., 2002. *Computational Methods for Fluid Dynamics.* 3rd ed. New York: Springer.

Fox, R. K. & Kline, S. J., 1962. Flow regimes in curved subsonic diffusers. *Journal of Basic Engineering,* 84(3), p. 303.

Frigne, P. & Van Den Braembussche, R., 1979. *One dimensional design of centrifugal compressors taking into account flow separation in the impeller,* s.l.: VKI, TN 129.

Fuller, R., Noall, J. & Preuss, J., 2012. *Turbomachinery for supercritrical CO2 power cycles.* Copenhagen, Denmarck, Proceedings of the ASME Turbo Expo 2012, GT2012-68735.

Gibson, A. H., 1910. On the flow of water through pipes and passages having converging or diverging boundaries.. *Proc. Royal Soc. (London), Vol. LXXXIII, No. 563, Series A,* pp. pp. 366-378..

Haghshenas Fard, M., Hooman, K. & Chua, H., 2010. Numerical simulation of a supercritical CO2 geothermosiphon. *International Communications in Heat and Mass Transfer ,* Issue 37, pp. 1447-1451.

Harink, J., Guardone, A. & Colonna, P., 2009. The influence of molecular complexity on expanding flows of ideal and dense gases. *Physics of Fluids,* Issue 21, pp. 086101-1/14.

Houses of Parliament, 2011. *Carbon Footprint of Electricity Generation,* London: s.n.

Howell, A., 1947. *Development of the British Gas Turbine Unit.* Reprint ed. New York: ASME.

Jansen, W., 1967. A method for calculating the flow in a centrifugal impeller when entropy gradinets are present. *institution of Mechanical Engineers, Royal Society Conference on Internal Aerodynamics (Turbomachinery),* Issue 19, pp. 133-146.

Japikse, D., 1996. *Centrifugal Compressor Design and Performance.* s.l.:Concept ETI, Inc..

Japikse, D., 1996. *Centrifugal Compressor Design and Performance.* Vermont: Concepts ETI; Inc.

Japikse, D., 2009. *Turbomachinery Performance Modeling,* s.l.: Concepts NREC, 2009-01-0307.

Japikse, D. & Baines, N., 1997. *Introduction to Turbomachinery.* 2nd ed. s.l.:Concepts ETI.

Japikse, D. & Baines, N. C., 1998. *Diffuser Design Technology.* s.l.:Concepts ETI, Ic..

Johnston, J. & Dean, R., 1966. Losses in Vaneless Diffusers of Centrifugal Compressors and Pumps. *Transaction ASME, Journal of Engineering for Power,* Volume 88, pp. 49-62.

Junta de Andalucía, C. d. I. C. y. E., 2014. *Agencia Andaluza de la Energía.* [Online] Available at: http://www.agenciaandaluzadelaenergia.es/Radiacion/radiacion1.php [Accessed 18 12 2013].

Klein, A., 1981. REVIEW: Effects of inlet conditions on conical-diffuser performance. *Journal of Fluid Engineering,* Volume 103, pp. 250-255.

Kosuge, H., Ito, T. & Nakanishi, K., 1982. A Consideration Concerning Stall and Surge Limitations Within Centrifugal Compressors. *Journal for Engineering for Power,* 104(4), pp. 782-787.

Landon Tarr, D., 2008. *Scaling of Impeller Response to Impeller-Diffuser Interactions in Centrifugal Compressors,* s.l.: Massachusstes Institute of Technology.

Launder, B. & Spalding, D., 1972. *Lectures in Mathematical Models of Turbulence.* London: Academic Press.

Lemmon, E., Huber, M. & McLinden, M., 2010. *NIST Standard Reference Database 23: Reference Fluid Thermodynamic and Transport Properties-REFPROP, V 9.0.,* s.l.: National Institute of Standars and Technoogy, Standard Reference Data Program.

Lieblein, S., 1959. Loss and Stall Analysis of Compressor Cascades. *ASME Transaction, Journal of Basic Engineering,* Issue Sept, pp. 387-700.

Lieblein, S., 1965. Experimental Flow in Two-Dimensional Cascades. In: *Aerodynamic Design of Axial-Flow Compressors.* Washington DC: NASA, pp. 183-226.

Loewenthal, S. H., 1984. *Design of Power-Transmitting Shafts,* Cleveland, Ohio: NASA 1123.

López Florenciano, A., 2013. *Estudio de la influencia de parámetros aerodinámicos de segundo orden sobre las prestaciones de difusores cónicos operando con aire y CO2 supercrítico.* Sevilla: MSc Thesis.

Mahalakshmi, M., 2007. Experimental investigations of flow through conical diffusers with and without wake type velocity distortions at inlet. *Experimental Thermal and Fluid Science,* Volume 32, pp. 133-157.

Ma, Z. & Turchi, C. s., 2011. *Advanced Supercritical Carbon Dioxide Power Cycle Configurations for Use in Concentrating Solar Power Systems,* s.l.: NREL/CP-5500-50787.

Mc Donald, A. T. & Fox, R. W., 1966. An experimental investigation of incompressible flow in conical diffusers. *International Journal of Mechanical Science,* Volume 8, pp. 122-139.

Mc Donald, A. T., Fox, R. W. & Van Dewoestine, R. V., 1971. Effects of swirling inlet flow on pressure recovery in conical diffusers. *AIAA Journal,* 9(10), pp. 2014-2018.

Menter, F., 1994. Two-Equation Eddy-Viscosity Turbulence Models for Engineering Applications. *AIAA Journal,* 32(8), pp. 1598-1605.

Menter, F., Kuntz, M. & Langtry, R., 2003. Ten Years of Industrial Experience with the SST Turbulence Model. In: K. Harjalic, Y. Nagano & M. Tummers, eds. *Turbulence, Heat and Mass Transfer 4:Proceedings of the Fourth International Symposium on Turbulence, Heat and Mass Transfer.* Antalya (Turkey): Begell House, Inc..

Monje, B. et al., 2012. *Comparing the pressure rise of air and supercritical carbon dioxide in conical diffusers.* Copenhagen, Proceedings of ASME Turbo Expo 2012, Paper No. GT2012-69835.

Moore, C. A. & Kline, S. J., 1958. *Some effects of vanes and of turbulence on two-dimensional, wide-angle, subsonic diffusers,* s.l.: NACA TN-4080.

Muñoz de Escalona, J. et al., 2010. *A comparison between MCFC based hybrid systems using air and supercritical carbon dioxide Brayton cycles with state of the art technology.* Seville, Spain, s.n.

Munroe, T. et al., 2009. *FLUENT CFD Steady State Predictions of a Single Stage Centrifugal Compressor with Supercritical CO2 Working Fluid.* Troy, New York (United States), Proceedings of the S-CO2 Power Cycle Symposium 2009.

Munroe, T. et al., 2009. *FLUENT CFD Steady State Predictions of a Single Stage Centrifugal Compressor with Supercritical CO2 Working Fluid.* Troy, New York, Proceedings of the S-CO2 Power Cycle Symposium 2009.

Munroe, T. et al., 2009. *FLUENT CFD Steady State Predictons of a Single Stage Centrifugal Compressor wuith Supercritical CO2 Working Fluid.* New York, Proceedings of the S-CO2 Power Cycle Symposium 2009.

NIST, N. I. o. S. a. T., Nov. 2012. *NIST Standard Reference Data.* [Online] Available at: http://www.nist.gov/srd/ [Accessed 18 09 2013].

NREL, 2012. *10-Megawatt Supercritical Carbon Dioxide Turbine Test-Thermodynamic Cycle to Revolutionize CSP Systems.* [Online] Available at: http://www.nrel.gov/csp/supercritical_co2.html [Accessed 24 Abril 2013].

Oh, H., Yoon, E. & Chung, M., 1997. An optimum set of loss models for the performance prediction of centrifugal compressors. *Proceedings of the institution Mechanical Engineers. Journal of Power and Energy,* 211(A4), pp. 331-338.

Padilla, A. M., Elkins, C. J. & Eaton, J. K., 2011. *The effect of inlet distortion on 3D annular diffusers.* Ottawa, 7th International Symposium on Turbulence and Shear Flow Phenomena TSFP-7.

Patankar, S. & Spalding, D., 1972. A Calculation Procedure for Heat, Mass and Momentim Transfer in Three-Dimensional Parabolic Flows. *International Journal of Heat and Mass Transfer,* Volume 15, p. 1787.

Pecnik, R. & Colonna, P., 2011. *Accurate CFD Analysis of a radial Compressor Operating with Supercritical CO2.* Boulder, Colorado, Supercritical CO2 Power Cycle Sumposium.

Pecnik, R., Rinaldi, E. & Colonna, P., 2012. *Computational Fluid Dynamics of a radial compressor operating with supercritical CO2.* Copenhagen (Denmark), Paper NO. GT2012-69640, Proceedings of ASME Turbo Expo 2012.

Petr, V., Kolovratnik, M. & Hanzal, V., 1999. *On the Use of CO2 Gas Turbine in Power Engineering (in Czech),* Prague: Czech Technical University in Prague, Department of Fluid Dynamics and Power Engineering, Division of Power Engineering, Depertment report Z-530/99.

Pope, S. B., 2000. *Turbulent Flows.* Cambridge, UK: Cambridge University Press.

Prior, B., 2011. *Cost and LCOE by Generation Technology, 2009-2020,* s.l.: GTM Research.

Reneau, L., Johnston, J. & Kline, S., 1967. Performance and Design of Straight Two-Dimensional Diffusers. *Transaction ASME, Journal of Basic Engineering,* Issue Mar, pp. 141-150.

Reneau, L. R., Johnston, J. P. & Kline, S. J., 1967. Performance and design of straight two-dimensional diffusers. *Journal of Basic Engineering,* 89(1), p. 141.

Rinaldi, E., Pecnik, R. & Colonna, P., 2013. *Steady state CFD investigation of a radial compressor operating with supercritical CO2.* San Antonio, Texas (United States), Paper No. GT213-94580. Proceedings of ASME Turbo Expo 2013: Turbine Technical Conference and Exposition.

Rodgers, C., 1980. Specific speed and efficiency of centrifugal impellers. In: S. Gopalakrickrishnan, P. Cooper, C. Grennan & J. Switzer, eds. *Preformance Prediction of Centrifugal Pumps and Compressors.* New York: ASME NY, pp. 592-603.

Romero-Álvarez, M. & Zarza, E., May 2007. 21, Concentrating Solar Thermal Power. En: *Handbook of Energy Efficiency and Renewable Energy.* s.l.:Taylor & Francis Group, LLC, pp. 21-1, 21-98.

Runstadler, P. W. & Dolan, F. X., 1973. Further data on the pressure recovery of straight-channel, plane divergence diffusers at high subsonic Mach numbers. *Journal of Fluids Engineering,* Volume 95, p. 373.

Sajben, M., Kroutil, J. C., Sedrick, A. V. & Hoffman, G. H., 1974. *Experiment on conical diffuser with distorted inflow,* s.l.: AIAA-Paper 74-529.

Schlichting, H., 1968. *Boundary Layer Theory.* 6th ed. s.l.:McGraw-Hill Book Company.

Schlichting, H., 1979. *Boundary-Layer Theory.* 7th ed. New York: McGraw-Hill.

Schobeiri, M. T., 2005. *Turbomachinery Flow Physics and Dynamic Performance*. 2nd ed. s.l.:Springer.

Sheperd, D., 1956. *Principles of Turbomachinery.* 1st ed. New York: MacMillan Company.

Shimizu, Y., Kuzuhara, S. & Nagafusa, M., 1982. Effects of approaching flow on the performances of straight conical diffusers. *Bulletin of JSME,* Volume 25 (208), pp. 1506-1512.

Shur, M., Spalart, P., Strelets, M. & Travin, A., 2008. A hybrid RANS-LES approach with delayed-DES and wall-modeled LES capabilities. *International Journal of Heat and Fluid Flow,* 29(6), pp. 1638-1649.

Slater, J. W., 2008. *NPARC Alliance CFD Verification and Validation Web Site.* [Online] Available at: http://www.grc.nasa.gov/WWW/wind/valid/tutorial/spatconv.html [Accessed 25 09 2013].

Smagorinsky, J., 1963. General Circulation Experiments with the Primitive Equations. *Monthly Weather Review,* 91(3), pp. 99-164.

Smith, C. R., 1975. A note on diffuser generated flow steadiness.. *Journal of Fluids Engineering,* 97(3), p. 377.

Spalart, P. & Allmaras, S., 1992. *A one-equation turbulence model for aerodynamic flows,* s.l.: American Institute of Aeronautics and Astronautics. AIAA-92-0439.

Span, R. & Wagner, W., 1996. A New Equation of State for Carbon Dioxide Covering the Fluid Region from the Triple-Point Temperature to 1100 K at Pressures up to 800 MPa. *Journal of Physical and Chemical Reference Data,* 25(6), pp. 1509-1596.

Span, R. & Wagner, W., 1996. A New Equation of State for Carbon Dioxide Covering the Fluid Region from Triple-Point Temperature to 1100 K at Pressures up to 800 MPa. *Journal of Physical Chemical Reference Data,* Volume 25, pp. 1509-1597.

Srinivasan, P. S. & Lakshmi Narasimhan, J. L., 1978 . Incompressible flow in conical diffusers with central wake-type inlet velocity distortion. *Journal of Aeronautical Society of India,* Volume 30, pp. 75-79.

Stanitz, J., 1952. *One-dimensional compressible flow in vaneless diffusers of radial- and mixed-flow entrifugal compressors, including effects of friction, heat transfer and area change,* s.l.: National Advisory Committee for Aeronautics. Technical note 2610. Jan.

Stern, F., Wilson, R. & Shao, J., 2006. Quantitative V&V of CFD simulations and certification of CFD codes. *Internation Journal for Numerical Methods in Fluids,* Issue 50, pp. 1335-1355.

Stratford, B. S. & Tubbs, H., 1965. The maximum pressure rise attainable in subsonic diffusers. *Journal of Royal Aeronautic Society,* Volume 69.

Takagi, K. et al., 2010. Research on Flow Characteristics of Supercritical CO2 Axial Compressor Blades by CFD Analysis. *Journal of Power and Energy Systems,* 4(1), pp. 138-149.

Tan, C. S., 2003. *Effects of impeller-Diffuser Interaction on Centrifugal Compressor Performance,* Cleveland: NAG3-2732.

Tennekes, H. & Lumley, J., 1972. *A First Course in Turbulence.* Cambridge, Massachusetts and London, England: MIT Press.

Tokyo Institute of Technology, 2011. *Tokyo Institute of Technology Bulletin.* [Online] Available at: http://www.titech.ac.jp/bulletin/archives_category/topics/topics_231.html

Torresol Energy Investments, S.A., 2010. *Torresolenergy.* [Online] Available at: http://www.torresolenergy.com/TORRESOL/central-tower-technology/en [Accessed 4 Oct. 2013].

Turchi, C., Mehos, M., Ho, C. K. & Kolb, G. J., 2010. *Current and Future Costs for Parabolic Trough and Power Tower Systems in the US Market,* s.l.: NREL/CP-5500-49303.

Ulizar, I. & Pilidis, P., 2000. Handling of a Semiclosed Cycle Gas Turbine With a Carbon Dioxide-Argon Working Fluid. *Journal of Engineering for Gas Turbines and Power, Vol. 122,* pp. 437-441.

Utamura, M., 2012. Aerodynamic Characteristic of a Centrifugal Compressor Working in Supercritical Carbon Dioxide. *Energy Procedia 14,* pp. 1149-1155.

Utamura, M., Hasuike, H. & Yamamoto, T., 2010. Demonstration Test Plan of Closed Cycle Gas Turbine with Supercritical CO2 as Working FLuid. *Journal of Strojarstvo,* pp. 52 No.4: 459-65.

Van Abel, E., Anderson, M. & Corradini, M., 2011. *Numerical Investigation of Pressure Drop and Local Heat Transfer of Supercritical CO2 in Printed Circuit Heat Exchanger.* Boulder, Colorado, The Supercritical CO2 Power Cycle Symposium.

Van Abel, E., Anderson, M. & Corradini, M., 2011. *Numerical Investigation of Pressure Drop and Local Heat Transfer of Supercritical CO2 in Printed Circuit Heat Exchangers.* Boulder, Colorado, Proceedings of Supercritical CO2 Power Cycle Symposium.

Van Dewoestine, R. V. & Fox, R. W., 1966. An experimental investigation on the effeect of subsonic inlet Mach number on the performance of concial diffusers. *International Journal of Mechanical Science,* Volume 8, pp. 759-769.

Versteeg, H. & Malalasekera, W., 2007. *An Introduction to Computational Fluid Dynamics, the finite volume method.* 2nd ed. Essex, England: Pearsn Education Limited.

Vesovic, V. et al., 1990. The Transport Properties of Carbon Dioxide. *Journal of Physical and Chemical Reference Data,* 19(3), pp. 763-811.

Vilim, R., 2010. *A One-Dimensional Compressor Model for Super-Critical Carbon Dioxide Applications.* San Diego, Proceedings of ICAPP'10, Paper 10156.

Walker, M. et al., 2013. Utilization of municipal wastewater for cooling in thermoelectric power plants: Evaluation of the combined cost of makeup water treatment and increased condenser fouling. *Energy,* Volume 60, pp. 139-147.

Wang, Y., Guenettem Jr., G., Hejzlar, P. & Driscoll, M., 2004. *Compressor Design for the Supercritical CO2 Brayton Cycle.* Rhode Island, Proceeding of the 2nd International Energy Conversion Engineering Conference, AIAA 2004-5722.

Whitfield, A. & Baines, N., 1990. *Design of radial turbomachinery.* First ed. Essex: Longman Scientific & Technical.

Wiesner, F., 1967. A Review of Slip Factors for Centrifugal Impellers. *ASME Journal of Engineering for Power, Vol. 89,* pp. 558-572.

Wilcox, D., 1988. Re-assessment of the scale-determining equation for advanced turbulence models. *AiAA Journal,* 26(11), pp. 1299-1310.

Wilcox, D., 1994. *Turbulence Modeling for CFD.* 2nd ed. California: DWC Industries.

Wilcox, D. C., 1993. *Turbulence Modeling for CFD.* 1st ed. ed. La Cañada, California: DWC Industries, Inc..

Wolf, S. & Johnston, J., 1969. Effects of non-uniform inlet velocity profiles on flow regimes and performance in two-dimensional diffusers. *Journal of Basic Engineering,* Volume 91, pp. 462-474.

Wright, S. A. et al., September 2010. *Operation and Analysis of a Supercritical CO2 Brayton Cylce,* s.l.: SAND2010-0171.

Yahya, S., 2005. *Turbines Compressores and Fans.* 3rd ed. s.l.:Tata McGraw Hill.

Zamora Parra, B., 2008. *Notas sobre simulación Numérica de Flujos de Fluidos.* Cartagena: Universidad Politécnica de Cartagena.